Ultrafast time-resolved photoelectron spectroscopy of substituted benzene molecules

By Laura Elizabeth Whalley, MSci.

Thesis submitted to the University of Nottingham for the degree of Doctor of Philosophy

September 2019

Abstract

Intramolecular vibrational energy redistribution, IVR, is a non-radiative process of energy dispersal throughout polyatomic molecules through the coupling of vibrational modes. IVR is an important consideration for molecular stability and chemical reactivity. The experiments within this thesis have utilised laser pulses of ~1 ps duration, which are sufficiently short to monitor IVR dynamics that typically occur on a picosecond timescale, whilst having a sufficiently narrow bandwidth to allow (partial) resolution of vibrational levels.

In this work, the vibrational levels of *para*-fluorotoluene (*p*FT) and aniline in the first electronically excited state (S_1) have been identified using resonance enhanced multiphoton ionisation (REMPI) in combination with slow electron velocity map imaging (SEVI) which is used to investigate the cationic ground state. IVR dynamics within the S_1 electronic state of these molecules have been probed using time-resolved photoelectron spectroscopy, also utilising the technique of velocity map imaging (VMI).

IVR dynamics that occur following the excitation of two near-degenerate vibrational levels at S_1 0^0 + ~2000 cm^{-1} in *p*FT have been investigated. In both cases doorway states which mediate the IVR dynamics have been identified, and IVR lifetimes, which differ dramatically for the two levels, have been determined. The IVR dynamics associated with these two levels are concluded to be mode-specific.

A systematic study of IVR in the S_1 electronic state of aniline has been conducted. Assignments have been made for S_1 vibrational levels up to S_1 0^0 +2110 cm^{-1}. These S_1 vibrational levels were then used as intermediates in the time-resolved study. Different IVR regimes have been observed with changing wavenumber; the lowest wavenumber vibrations exhibited no time-dependence indicating that no IVR redistribution processes occurred. With increasing wavenumber, examples of restrictive IVR were apparent, where population remained localised between a few vibrational modes causing quantum beats. The highest wavenumber vibrational levels either showed quantum beats alongside overall decay, indicative of doorway states mediating the dynamics, or fast 'dissipative' energy dispersal.

Publications

1. *Complexity surrounding an apparently simple Fermi-resonance in para-fluorotoluene revealed using two-dimensional laser-induced fluorescence (2D-LIF) spectroscopy,* D. J. Kemp, **L. E. Whalley**, A. M. Gardner W. D. Tuttle, L. G. Warner and T. G. Wright, J. Chem. Phys., 2019, **150,** 064306.
2. *Effects of symmetry, methyl groups and serendipity on intramolecular vibrational energy dispersal*, W. D. Tuttle, A. M. Gardner, **L. E. Whalley**, D. J. Kemp and T. G. Wright, *Phys. Chem. Chem. Phys.*, 2019, **21**, 14133-14152*.*
3. *Direct observation of vibrational energy dispersal via methyl torsions*, A. M. Gardner, W. D. Tuttle, **L. E. Whalley** and T. G. Wright, *Chem. Sci.*, 2018, **9**, 2270.
4. *Vibrations of the p-chlorofluorobenzene cation,* D. J. Kemp, L. E. Whalley, W. D. Tuttle, A. M. Gardner, B. T. Speake and T. G. Wright, *Phys. Chem. Chem. Phys.*, 2018, **20**, 12503-12516.
5. *Probing the origins of vibrational mode specificity in intramolecular dynamics through picosecond time-resolved photoelectron imaging studies,* J. A. Davies, **L. E. Whalley** and K. L. Reid, Phys. Chem. Chem. Phys., 2017, **19**, 5051-5062
6. *Vibration and vibration-torsion levels of the S_1 state of para-fluorotoluene in the 580-830 cm^{-1} range: Interactions and coincidences*, W. D. Tuttle, A. M. Gardner, **L. E. Whalley** and T. G. Wright, *J. Chem. Phys.*, 2017, **146** 244310
7. *Torsion and vibration-torsion levels of the S_1 and ground cation electronic states of para-fluorotoluene,* A. M. Gardner, W. D. Tuttle, **L. Whalley**, A. Claydon, J. H. Carter and T. G. Wright, *J. Chem. Phys.*, 2016, **145**, 124307

Acknowledgements

First of all, I must express my gratitude to my supervisor, Professor Katharine Reid for her expertise and endless encouragement over the last four years, including throughout the writing of this thesis. I also wish to thank my second supervisor, Professor Tim Wight, for his support and providing opportunities to work on experiments in his Lab.

I have worked alongside a number of PDRA, PhD and masters students in the Phys. Chem. Department over the last few years and am forever grateful for their friendship, advice and moral support, particularly at the pub. Special thanks must go to Drs. Adrian Gardner, Nicolas Saquet and William Tuttle and who helped me settle in when I first started my PhD and got me started in the lab, showing me infinite patience! I also need to acknowledge Neil Barnes for his assistance with vacuum pumps and the chiller system over the years, his stories and Lab peculiarities were always entertaining and Dr. June McCombie for her guidance and encouragement throughout my undergraduate years and beyond.

I also need to thank my family. First of all, my parents, Kate and John Whalley, who have supported me throughout my studies. Secondly, my grandparents; Christine and Norman Simpson, who inspired me to study Chemistry and Muriel and Stan Whalley who were always so proud of everything I achieved. They always encouraged me, and I want to dedicate this to them. Finally, I also want to thank Liz Pittaway and Christina Whalley for the adventures and for always being there, for anything and everything.

Finally, I am eternally grateful to my husband, Adrian, who was an endless source of humour, support and motivation; he never lost confidence in me, even when I lost confidence in myself.

Table of contents

Table of Figures

Table of Tables

1. Introduction

1.1. Motivation

Routes for energy dispersal throughout molecules are vital for their stability following the input of localized energy, for example following photoexcitation, an excited state species may undergo a photochemical reaction or process such as dissociation. Upon photoexcitation, a number of different process may occur to redistribute the excess energy in a molecule; these include radiative pathways such as fluorescence or phosphorescence and non-radiative pathways such as intersystem crossing or internal conversion. The focus of this thesis is the dispersal of energy through molecules *via* the mixing of vibrational modes which is known as intramolecular vibrational energy redistribution (IVR).

Studying IVR in molecules and across families of molecules using time- and frequency-resolved spectroscopic techniques allows experimentalists to establish how factors such as doorway states (dark states which facilitate coupling to a large number of vibrations known as bath states), mode-dependence and molecular flexibility (further discussed in section 1.4) affect IVR rates and mechanisms. This is the first step in moving towards developing robust models of IVR which predict the rates and pathways of energy redistribution.[1] Furthermore, if IVR is significantly sensitive to molecular structure and vibrational degree of freedom this leads to the possibility of manipulating or controlling IVR and reaction pathways by designing molecules with specific photophysical characteristics.[1] For example, it may be desirable to enable the rapid dispersal of energy to increase stability of molecules. Conversely if no routes exist for IVR, photoexcitation could result in vibrational energy remaining bond-localised permitting a level of control over reactivity. If a desired bond vibration cannot be accessed through absorption of a photon, then identifying coupling to other vibrational levels through time- and frequency-resolved studies of IVR dynamics could provide a mechanism by which the desired vibrational level gains population.

1.2. Previous studies of IVR

Most of the techniques included in this section investigate IVR in excited electronic states; although there has been significant interest in probing IVR in the ground electronic state,[1] for example Ebata and co-workers used a picosecond IR-UV pump-probe technique to study the OH and OD stretching vibration of phenol as well as the vibrational relaxation of the clusters of phenol.[2] Knight and co-workers used a technique they termed 'stimulated emission pumping-single vibronic level fluorescence spectroscopy (SEP-SVLF)' to measure the collision-free lifetimes of selected vibrational levels in S_0 *para*-difluorobenzene.[3] A specific S_0 vibrational level was prepared though stimulated emission from an initially excited S_1 vibrational level and its time-dependence was probed by laser-induced fluorescence resulting from excitation, after some delay, to a specific vibrational level in S_1.

Many of the early techniques that probed IVR in excited electronic states employed fluorescence spectroscopy such as the chemical timing experiments of Parmenter and co-workers.[4,5,6,7,8] In a first study,[4] a frequency-doubled continuous-wave argon ion laser was used to first excite an S_1 vibrational level (~2191 cm^{-1}) in *para*-difluorobenzene (*p*DFB). Holtzclaw and Parmenter carried out follow up studies on a further eleven vibrational levels between 1615-3310 cm^{-1} in the S_1 electronic state using the same technique, they measured IVR lifetimes between 15 to 300 ps.[7] The time-resolution was achieved by adding an electronic quenching gas such as O_2 to the fluorescence cell which contained the *p*DFB.[4] Collisions between electronically excited *p*DFB and O_2 molecules result in non-radiative deactivation of the *p*DFB molecules to their ground electronic state. Effectively, emission was only observed from *p*DFB molecules during the interval between absorption and collision which results in the quenching of their fluorescence.[4] Carrying out the same experiment at varying partial pressures of oxygen and recording multiple spectra allowed the IVR time scale to be determined from the growth rate of congestion within the dispersed fluorescence spectrum. [4] In these experiments, when the partial pressure of O_2 was relatively high resulting in short intervals between absorption and collision, only the earliest portions of the fluorescence were emitted leading to resolved vibrational structure observed in the spectrum. As the pressure of the quenching gas was decreased, an increase in unstructured emission in the fluorescence was observed, indicative of enhanced IVR. Further chemical timing experiments by Parmenter and Stone[9] and Moss and Parmenter[10] compared IVR in *para*-fluorotoluene, *para*-fluorotoluene-d_3 and *para*-difluorobenzene, the accelerated IVR observed in *p*FT was concluded to result from the presence of the methyl group.

There are several disadvantages of employing chemical timing to study IVR: (i) it depends on the ability of the molecule to fluoresce, which is not the case for many large systems; (ii) even when an excited electronic state of a molecule is able to fluoresce, the fluorescence lifetime must be sufficiently long to allow the vibrational energy dispersal to occur; (iii) not all molecules will be quenched at precisely the same time meaning the IVR could progress further in some cases, therefore the "integrated" dispersed fluorescence spectra could be the result of a distribution of lifetimes,[11] and (iv) the observed fluorescence is integrated over time, so behaviour such as quantum beats cannot be observed which provide information on the mechanism of coupling, and will be discussed further in section 1.4.1. Furthermore, studies carried out on room temperature samples in which low wavenumber degrees of freedoms (rotations and low frequency vibrations for example) are populated in the ground electronic state, can lead to a complicated (and congested) excitation spectrum as transitions which originate from these populated levels are possible. Congestion observed in the dispersed fluorescence spectra may therefore be a result of overlapping transitions from these, and the zero-point vibrational level, severely complicating interpretation; this is discussed by Moss and Parmenter.[12] Similarly, for large and complex molecules, especially at high excitation energies, congestion may simply be a result of overlapping, but uncoupled, vibrations in S_1 and therefore not indicate the rate of energy distribution.[11] This may be unravelled through comparison with high resolution spectra which is described below. As a result of collisions between the photoexcited molecules and the quenching gas (O_2), it is also possible that an alternative energy redistribution mechanism, vibrational relaxation, may be influencing the congestion.

Zewail and co-workers improved on the chemical timing experiments by developing a time-resolved fluorescence spectroscopy technique, which they termed picosecond-jet technique.[13] In these experiments the molecule of interest was cooled in a supersonic jet expansion, which not only simplified the resulting dispersed fluorescence spectrum, by reducing the number of (ro)vibrational levels initially populated, but allows the measurements to be conducted in a collisionless environment, preventing energy redistribution through vibrational relaxation. In this technique a vibrational wavepacket in an electronic excited state was prepared using a picosecond laser pulse with ~15 ps duration and the resulting fluorescence was dispersed with a monochromator.[13,14] Through temporal gating of the detector (photomultiplier or MCP), dispersed fluorescence spectra at specific times after photoexcitation could be obtained. The changing appearance of the dispersed fluorescence spectra with increasing time following initial excitation provided information on the time evolution of the wavepacket, as changes in the wavepacket are manifested in changes in the intensities bands in the dispersed fluorescence spectrum. In an initial study of anthracene[13,14] Zewail and co-workers were able to observe quantum beats in the dispersed fluorescence upon excitation to internal energies of ≈ 1400 cm^{-1} using this technique. In later papers Felker and Zewail developed some formalism which allowed the interpretation of the manifestations of IVR in temporally resolved fluorescence spectra[15] and conducted further studies of anthracene[16,17] and *t*-stilbene[18]. This technique had the advantage that the dispersed fluorescence spectrum observed was *not* integrated over all time from the initial excitation, as is the case in the earlier chemical timing experiments, which allowed quantum beating to be observed. The temporal resolution of these experiments were limited by the detector employed to ~150 ps in the earliest study,[14] and improved to ~80 ps in later work;[16] as a result, these studies were limited to study systems which displayed relatively slow dynamics.

McDonald and co-workers developed a time-resolved fluorescence depletion (TRFD) technique in which two pulses of identical wavelength and duration (5.7 ps or 7.9 ps) were utilised; the first 'pump' pulse excites a vibrational level in the S_1 electronic state, the second pulse (as well as potentially exciting molecules which remained in the ground electronic state to S_1) causes stimulated emission from the initially prepared vibrational level in S_1 to the ground state.[19] The identical wavelength of the pulses means stimulated emission only occurs from molecules in their initially excited state. Measuring the intensity of spontaneous fluorescence as a function of time delay between the two pulses allows IVR to be monitored because if IVR occurs during the time delay between the two laser pulses causing evolution of the initially excited level, the efficiency with which the second pulse stimulates emission will decrease as more molecules will remain in the electronically excited state.[19] IVR will therefore be manifested as an increase in spontaneous fluorescence intensity.[19] In this experiment the time resolution is not limited by the response of the detector used to record the dispersed fluorescence spectra, but on the pulse width of the lasers used.[20] McDonald used this technique to study 19 vibrational levels in the S_1 electronic state of fluorene and three categories of time dependence were observed: (i) low wavenumber vibrational levels showed no strong time dependences, indicating no IVR; (II) vibrational levels between 800 – 1600 cm^{-1} exhibited quantum beating, and (iii) vibrational levels above 1600 cm^{-1} exhibited fast (dissipative) decay, for which IVR lifetimes were reported.[20]

Owing to developments in ultrafast laser systems, later studies employed time-resolved photoelectron spectroscopy, tr-PES to study IVR processes in excited electronic states of molecules. This technique is a two-colour process where the vibrational wavepacket is initially coherently prepared in an electronically excited state through absorption of a ‘pump’ photon, then a second ‘probe’ photon is used to ionise the molecule and a photoelectron spectrum is recorded. The photoelectron spectrum provides a fingerprint of the intermediate excited state populated. The delay between the pump and probe pulses may be varied by changing the optical path length, allowing photoelectron spectra to be measured as a function of time delay. Changes in the photoelectron spectrum will result from evolution of the vibrational wavepacket during the delay between the pump and probe pulses, so recording series of photoelectron spectra allows IVR to be observed and monitored. A key benefit of this technique is that the timing of the pump-probe steps is much more controllable than in some time-resolved fluorescence measurements. Furthermore, molecules can be photoionized from any state if the probe pulse is of sufficient energy, but do not necessarily fluoresce from all states.[21]

Tr-PES typically uses ultrafast lasers producing pulses in the picosecond to femtosecond range. Femtosecond lasers provide high temporal resolution allowing experiments on short-lived electronic states to be conducted, and have been used to study electronic relaxation processes such as intersystem crossing and internal conversion.[22,23,24,25,26] For Gaussian laser pulses the time-bandwidth relationship is $\Delta\nu\Delta t \geq 0.441$, which means that very short pulses on the order of femtoseconds have bandwidths of ~100 cm^{-1}.[27,28] So, the high temporal resolution in femtosecond time-resolved experiments comes at the expense of energy resolution, which means often differing vibrational bands in either electronic or photoelectron spectra are not resolved. Such *vibrational resolution* is required for the quantitative study of vibrationally mediated dynamics. Also, it is difficult to probe just a few selected levels with femtosecond pulses, especially at high energies where there is a high density of states, which will result in complicated spectra. Instead, lasers which have pulse durations of 1-10’s of picoseconds can be a compromise between sufficient time-resolution to deconvolute IVR, which typically occurs on a picosecond timescale, and achieving (at least partial) vibrational resolution in the electronic and photoelectron spectra.

A number of different techniques have been used to obtain photoelectron spectra, here, the techniques: time-of-flight (TOF), velocity map imaging (VMI) and zero kinetic energy (ZEKE) will be discussed. Reilly and co-workers developed a tr-PES technique which used field-free time-of-flight measurements.[29,30] In the time-of-flight method, the kinetic energy of the photoelectrons are determined from the time taken (t) for a photoelectron to travel a set distance (flight tube) between the interaction region and detector:

$$t = t_0 + l\sqrt{\frac{m_e}{2E_{eke}}} \qquad \text{Equation 1.1}$$

where l is the path length, m_e is the mass of an electron, t_0 is the time of incidence of the laser pulse and E_{eke} is the electron kinetic energy. In the experiments of Reilly and co-workers on trans-*p*-*n*-butylaniline, a picosecond laser producing pulse durations of 10-15 ps was used to excite the $^1B_2 \leftarrow {}^1A_1$ 1^1_0 transition.[29] The two-colour photoelectron spectra recorded using the technique evolved as the time delay between excitation and ionisation increased. The Δv = 0 peak, the photoelectron peak which has the same vibrational identity as the vibrational level initially excited, became increasingly broad and other peaks in the photoelectron spectrum, originating from transitions from the bright state, decreased in intensity as time delay was increased.[29] The time resolution of this method was limited by the duration of the laser pulses used.[29] The key disadvantage in these experiments was that only IVR processes which occur on a time-scale of significantly longer than 15 ps could be studied; Parmenter and co-workers had already determined shorter IVR lifetimes in their chemical timing studies.[5]

Later, picosecond time-of-flight photoelectron spectroscopy (TOF-PES), experiments were undertaken by Reid and co-workers who studied the S_1 0^0+ 1200 cm^{-1} energy region in jet cooled *para*-fluorotoluene.[21] In this study pulses of ~1 ps duration were used for both the pump and probe beams, the much shorter pulse duration meant IVR processes occurring on a shorter time-scale could be studied.[21] Using the 1 ps pulse simultaneously excited a C-F stretch with an S_1 wavenumber of 1230 cm^{-1} and a C-CH$_3$ stretch with an S_1 wavenumber of 1194 cm^{-1} and photoelectron spectra were monitored at eight different time delays up to 1000 ps.[21] Well-resolved ion vibrational states were observed in the photoelectron spectra at a time delay of 0 ps, with the vibrational structure lost and the spectrum increasingly congested with increasing time delay. This behaviour was concluded to be a result of a dissipative IVR process in which progressively more isoenergetic levels in S_1 were populated as time delay increased.[21] In a later study,[31] corresponding TOF photoelectron spectra were measured for four levels in S_1 toluene above 750 cm^{-1} using ~5 ns pulses and in a second experiment ~1 ps pulses. Comparison showed that limited vibrational structure was seen in the nanosecond spectra, but that in most cases many more peaks could be resolved and assigned in the early time picosecond spectra.[31] This study showed that 1 ps pulses could be used to retrieve structure in some cases where a rising base line and high levels of congestion are seen.

Zero electron kinetic energy (ZEKE) spectroscopy is a high-resolution type of photoelectron spectroscopy.[32] The principle of this technique is that following ionisation, electrons with nonzero kinetic energy quickly leave the field free interaction region, and the remaining zero kinetic energy electrons are selectively detected by applying an extraction voltage ~1 μs after the probe pulse directing these electrons to the detector.[33] In reality, as a result of stray electric and magnetic fields, even electrons with no kinetic energy leave the ionisation region, and the extraction pulse field ionises very high lying Rydberg levels, and these are the electrons detected. This is technically denoted zero electron kinetic energy pulsed field ionisation, ZEKE-PFI, however owing to the ubiquitous nature of PFI, the differentiation is not usually made, and the technique is referred to colloquially as ZEKE. To obtain ZEKE spectra, the pump wavelength is fixed and while scanning the probe laser wavelength, the "ZEKE" (ZEKE-PFI) electrons are detected; analysis of the resulting spectrum yields the vibrational frequencies in the cation. The evolution of the excited vibrational wavepacket can be monitored by measuring photoelectron spectra at different delay times. Alternatively, the pump wavelength is fixed to a specific $S_1 \leftarrow S_0$ transition, the probe wavelength is fixed allowing ionisation to a specific cation vibrational level, and the pump-probe time delay can be scanned, allowing the dependence of the electrons produced with time delay to be deduced, which is a reflection of the evolving wavepacket. Time resolved ZEKE (tr-ZEKE) spectroscopy, was utilised by Knee and co-workers who used a picosecond laser system with pulse duration ~10 ps to investigate the S_1 state of fluorene.[34] In these experiments a vibrational level at S_1 0^0 + 834 cm^{-1} was initially excited; monitoring the ZEKE signal as a function of time delay when the probe laser was fixed on two different photoelectron peaks, showed out of phase quantum beats with a period of 125 ps. When a second vibrational level at S_1 0^0 + 1707cm^{-1} was excited, the ZEKE spectrum at 0 ps showed resolved vibrational structure, whereas by 500 ps the spectrum was broad and unstructured; evidence of a dissipative IVR mechanism, with a lifetime of 80 ps determined.[34] The authors stated that the resolution of the spectra were limited to the laser bandwidth, ~6 cm^{-1}.[34]

While ZEKE is a very high-resolution photoelectron spectroscopy technique, the requirement for scanning the probe wavelength results in long acquisition times, even when spectra are measured at selected time delays. For the same reason it is difficult to cover an extensive region of ion internal energy. These problems are avoided in velocity map imaging[35] (VMI), which is employed in this work and is explained in detail in Chapter 2. Briefly, an electrostatic lens is used to focus the photoelectrons onto the position sensitive detector so that all photoelectrons with the same initial velocity are mapped onto the same point on the detector resulting in a 2D image containing a series of rings. The use of the electrostatic lens to focus the photoelectrons means there should, in principle, be close to 100% transmission reached in VMI,[35] which is a benefit over TOF spectroscopy which can suffer from lower electron transmission resulting in lower signal-to-noise and requiring longer acquisition times to measure robust relative peak intensities. Using VMI permits multiple cation vibrational levels to be monitored simultaneously meaning a photoelectron spectrum can be recorded in minutes, an advantage over time-resolved ZEKE spectroscopy where the acquisition time could be hours. Further, alongside the kinetic energies, the angular distributions of the photoelectrons can be measured simultaneously which provides additional information on the photoionisation dynamics.[22,36]

Assignment of the vibrations observed in the photoelectron spectrum allows the vibrational levels that have been populated in the S_1 electronic state to be determined. However, this highlights a key disadvantage of time-resolved photoelectron spectroscopy compared to time-resolved dispersed fluorescence spectroscopy. Whereas the vibrations observed in the dispersed fluorescence spectra may be assigned based on knowledge of the S_0 vibrational wavenumbers, cationic vibrational wavenumbers are often unknown, making assignment difficult. Complementary, high-resolution PES experiments, alongside computational studies, are required to aid identification and assignment of the cation vibrational levels. These are discussed below.

When using Fourier-Transform limited 1 ps laser pulses, with a bandwidth of > 13 cm^{-1}, the spectral resolution is limited by that of the VMI technique which depends on the spatial resolution of the electron detector and the focussing by the electrostatic lens (see Chapter 2). A variation of VMI is slow-electron velocity map imaging (SEVI) which provides a means of achieving higher energy resolution over the same internal energy range.[37,38] This technique involves recording a series of images using different probe wavelengths which are then combined to produce the full SEVI spectrum. This technique is described in further detail in Chapter 2. Hammond and Reid[38] utilised the SEVI technique combined with transform limited 1 ps laser pulses to study a number of substituted toluene molecules; the full width at half maximum, FWHM, of peaks were observed to be reduced by nearly a factor of 3 in the SEVI spectra versus VMI spectra, with photoelectron peak widths as narrow as 16 cm^{-1} reported. Additional photoelectron peaks, obscured in previous VMI spectra, were also observed, indicating the importance of obtaining an energy resolution that approaches the laser bandwidth.[38] Collecting multiple images using different probe wavelengths to produce the "full" SEVI spectra results in the collection time required for SEVI experiments being considerably longer than VMI experiments where a single probe wavelength is used to obtain a photoelectron spectrum. As a result, SEVI are usually employed for a selection of time delays and can be used to compliment VMI measurements. Generally, no major changes in experimental set up are required to produce either SEVI or VMI photoelectron spectra.

Employing ZEKE spectroscopy, utilising nanosecond pulsed lasers,[39] allows close lying cation vibrational levels to be resolved. In principle, as the spectral resolution is limited by that of the laser bandwidth, which in many cases is approximately ~0.2 cm^{-1}, even partial rotational resolution is possible for some systems.[33] At high energies, where the density of states is significant, the spectra will have similar congestion problems to those discussed in relation to dispersed fluorescence spectroscopy.

In principle, if every $S_1 \leftarrow S_0$ (ro)vibrational transition can be observed, high resolution experiments allow the coupling pathways to be determined and so can be used to study IVR. In frequency-resolved studies, observance of specific rovibrational levels is an advantage over time-resolved experiments where usually the IVR lifetimes and periods are averages over a range of rotational and other quantum states (e.g. nuclear spin states).[40] Studies by Pratt and co-workers[41] employed rotationally-resolved fluorescence excitation spectroscopy using a continuous wave laser to probe molecules such as toluene. Their work provided insight into the influence of the motion of the methyl group on the S_1 geometry and the effect of the presence of the methyl group on the IVR rate (discussed further in section 1.2.6).[41] More recently, two-dimensional laser induced fluorescence (2D-LIF) spectroscopy was demonstrated by Gascooke and Lawrance[42] to be a valuable technique with sufficient resolution to observe rovibronic transitions of polyatomic molecules and to separate features that overlap in LIF spectra. In the 2D-LIF technique the pump excitation laser is scanned over features in the excited S_1 electronic spectrum and a segment of the dispersed fluorescence spectrum is monitored, the wavenumber range of which is dependent on the spectrograph used, with the dispersed fluorescence imaged by a CCD camera. This technique was employed by Lawrance and co-workers to study the $S_1 \leftarrow S_0$ transition in fluorobenzene[42] which allowed them to determine the rotational constants with high precision and identify two electronic ground state Fermi resonances. Alongside the time required for a scan, this technique has the same drawback as the previous fluorescence spectroscopy techniques in that it can only be performed for molecules that fluoresce. This technique has recently been used by the Wright group (University of Nottingham) to study *p*FT,[43,44,45] the results will not be discussed in this thesis but relevant studies are briefly referenced in the conclusion.

In the following subsections the theory behind the coupling of vibrational levels and intramolecular vibrational energy redistribution will be introduced, the experimental approaches will be outlined and the various approximations and models which are applied in order to interpret spectra obtained within this thesis are described. Finally, the aims of the experimental work are highlighted, and an overview of the following chapters is given.

1.2. Molecular vibrations

1.2.1. Separation of the degrees of freedom

The energies (E) of quantum mechanical systems are given by the Schrödinger equation:

$$E\Psi = \hat{H}\Psi \qquad \text{Equation 1.2}$$

where Ψ is the molecular wavefunction and $\hat{H}$ is the Hamiltonian operator which has contributions from the kinetic energy and potential energy of the system. In order to solve the Schrodinger equation a number of approximations are applied. The first of these is due to the large mass difference between nuclei and electrons which results in their motions occurring on very different timescales. This is the basis of the Born-Oppenheimer approximation, which states that the electronic and nuclear motion may be considered separable, this allows the total molecular wavefunction to be separated into the electronic and nuclear parts:

$$\psi_{tot} \approx \psi_{elec}\psi_{nuc} \qquad \text{Equation 1.3}$$

Similarly, ψ_{nuc} can be further simplified by separating out the individual contributions from vibrations, rotations and nuclear spin:

$$\psi_{nuc} \approx \psi_{vib}\psi_{rot}\psi_{nspin} \qquad \text{Equation 1.4}$$

$$\psi_{tot} \approx \psi_{elec}\psi_{vib}\psi_{rot}\psi_{nspin} \qquad \text{Equation 1.5}$$

The energy can also be separated into similar contributions such that degrees of freedom can be considered separately:

$$E_{tot} \approx E_{elec} + E_{vib} + E_{rot} + E_{nspin} \qquad \text{Equation 1.6}$$

1.2.2. Harmonic Oscillator model – Normal modes and zero order states

In a vibrating diatomic molecule, the bond which undergoes stretching and compression can be treated as a spring which obeys Hooke's law. This states that when there is displacement from the equilibrium bond length there will be a proportional restoring force (F):

$$F = -\frac{dV(x)}{dx} = -kx \qquad \text{Equation 1.7}$$

where V is potential energy, k is the force constant which reflects the bond strength (the negative sign arising from the fact the restoring force is opposite to displacement), x is the displacement from equilibrium bond length ($r - r_e$ where r is the internuclear separation and r_e is the equilibrium bond length).[46] Any oscillating system satisfying Hooke's law can be described as a harmonic oscillator. Integration of equation 1.7 gives:

$$V = \frac{1}{2}kx^2 \qquad \text{Equation 1.8}$$

Which is the equation for the potential energy upon distortion of the spring or bond in a diatomic molecule. Plotting V against r gives a parabolic potential energy curve, symmetrical about the equilibrium geometry, where the potential energy goes up to infinity for both stretching and compressing. As the bond returns to its equilibrium position the potential energy is progressively converted to kinetic energy and vice versa. The vibrational energy is the total amount of energy, potential + kinetic, which is constant during the vibrational motion.

The quantum mechanical Hamiltonian for the harmonic oscillator is given by: [46]

$$\hat{H} = \frac{-\hbar^2}{2\mu}\frac{d^2}{dx^2} + \frac{1}{2}kx^2 \qquad \text{Equation 1.9}$$

where μ is the reduced mass of the nuclei determined from the masses of the two atoms involved. Substituting this into Equation 1.2, the Schrödinger equation becomes:

$$\left(\frac{-\hbar^2}{2\mu}\frac{d^2}{dx^2} + \frac{1}{2}kx^2\right)\psi = E\psi \qquad \text{Equation 1.10}$$

The quantised vibrational energies (eigenvalues) of the vibrational eigenstates within the harmonic oscillator approximation are determined by solving equation 1.10.: [46]

$$E_v = \left(v + \frac{1}{2}\right) h\nu \qquad \text{Equation 1.11}$$

Where v is the vibrational quantum number, which has integer values (0,1,2,3…) where the vibrational ground state has a value v=0, and ν is the harmonic vibration frequency which depends on the force constant and reduced mass:[46]

$$\nu = \frac{1}{2\pi}\sqrt{\frac{k}{\mu}} \qquad \text{Equation 1.12}$$

Generally, vibrational wavenumber (cm^{-1}), ω, is used rather than frequency as this is a convenient unit for spectroscopy; fundamental vibrations typically have vibrational wavenumbers of 100's-1000's cm^{-1}. So rather than energy levels, vibrational term values ($G(\boldsymbol{v})$) are reported which are related by: [46]

$$\frac{E_v}{hc} = G(\boldsymbol{v}) = \left(v + \frac{1}{2}\right)\omega \qquad \text{Equation 1.13}$$

where c is the speed of light (cm s^{-1}). The harmonic potential rises to infinity, so there are an infinite number of quantised eigenstates which are regularly spaced, the separation being $hc\omega$. The vibrational ground state v=0 has an energy of $\frac{1}{2}hc\omega$ known as the zero-point energy.[46]

In a diatomic molecule there is only one bond and so one vibrational mode, the stretching and compression of the bond linking the two atoms. Polyatomic molecules contain more than one bond, with the number of vibrations are given by 3N-5 for linear molecules and 3N-6 for non-linear molecules, where N is the number of atoms. The atomic motions that occur during the vibrations are described by the normal modes of the molecule, each of which are independent.

In a polyatomic molecule the potential energy is expressed in terms of the independent normal modes:

$$V = \frac{1}{2}\sum_i k_i Q_i^2 \qquad \text{Equation 1.14}$$

Where k is the force constant and Q is the normal coordinate which depends on the displacements of the individual atoms involved in the particular normal mode. Using normal coordinates means there are no cross terms for kinetic or potential energy, so the matrix representation of the Hamiltonian is diagonal, with the modes themselves are independent. Each of the vibrational normal modes can be treated as an independent harmonic oscillator of the form described above. Each vibrational normal mode has its own vibrational quantum number v_i and its own vibrational frequency. The total vibrational energy is given by:

$$E_v = \sum_i \left(v_i + \frac{1}{2}\right) h\nu_i \qquad \text{Equation 1.15}$$

In the vibrational ground state v=0 for each normal mode. The harmonic vibrations are also known as zero-order states (ZOS), which is a term which will be mentioned throughout this work. The zero order states and corresponding energies are exact for the harmonic oscillator, but approximate for the vibration of a real molecule.

1.2.3. Labelling schemes for the vibrations

If a molecule has n quanta in normal mode labelled X, it is said to be in the X^n vibrational state, which in principle allows the atomic motion to be completely described. However, there is more than one notation scheme which has been developed to label the vibrational modes. Perhaps some of the most common schemes used to describe the vibrations of substituted benzene molecules, which is the focus of this work, are the Mulliken/Herzberg,[47,48] Wilson,[49] Varsányi[50] schemes and that of Gardner and Wright[51,52].

Briefly, in Mulliken notation the molecule is assigned a specific point group and the vibrations are organised based on their symmetry group (e.g. A_1, A_2, B_1 and B_2 for a molecule in the C_{2v} point group) then numbered in decreasing wavenumber. As specific labels are not associated with specific atomic motions, if the wavenumbers of vibrations change across related molecules, the Mulliken labels would not necessarily correspond to the same atomic motions.

In Wilson notation, the vibrations of substituted benzene molecules are labelled in terms of those of benzene, this provides information on the atomic motion, but the form of the vibrational modes can change greatly upon substitution. Varsányi attempted to correct this issue by proposing a series of normal vibrational modes for a series of different categories of substituted benzenes. The proposed normal modes were given the same labels as in Wilson notation, including the normal modes that significantly differ from those of benzene, so confusingly some labels refer to different atomic motions in the different schemes. These normal modes also were shown to be unrepresentative of those of real molecules.[53] In the scheme proposed by Gardner and Wright, the normal modes of fluorobenzene are numbered in the same way as Mulliken, i.e. by symmetry, then by decreasing wavenumber; vibrations of all other monosubstituted benzene molecules are based on the vibrational modes of fluorobenzene. In this notation, the same label is used for the same vibrational mode (which corresponds to the same atomic motion) in different molecules, regardless of changes in energy of symmetry. In this scheme the same vibrational motions will have the same labels facilitating comparison between molecules, although notably, substituent-localised modes require a separate set of labels. For disubstituted benzene molecules, the vibrational modes of the relevant difluorobenzene are used as a basis.

1.2.4. Anharmonic oscillator

The harmonic oscillator relies on Hooke's law which is a reasonable approximation for small displacements in geometry but does not allow for the fact that real molecules dissociate at higher energies as the chemical bond will break if stretched far enough. Therefore, as internuclear separation (r) increases towards the dissociation limit, the potential should tend to zero asymptotically, rather than rising to infinity as the harmonic oscillator model predicts (see Figure 1-1).[46] Further, as r becomes shorter than r_e, the electron-electron repulsion energy increases significantly. This means the repulsive part of the potential must be steeper than the harmonic oscillator model predicts. These deviations from the behaviour predicted by the harmonic model is known as mechanical anharmonicity and will increase with increasing vibrational energy.

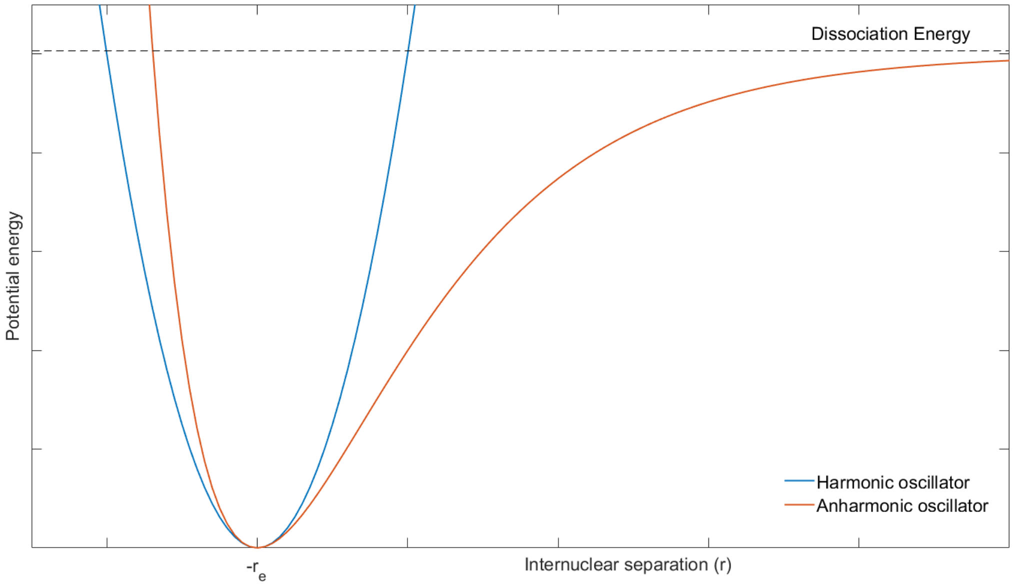

Figure 1-1: Potential energy of the anharmonic oscillator versus the harmonic oscillator.

1.2.5. Coupling of vibrational modes

Anharmonicity affects the vibrational term values (eigenvalues) and wavefunctions (vibrational eigenstates). The harmonic oscillator term values shown in equation 1.13. become the power series[46]:

$$G(v) = \omega_e \left(v + \frac{1}{2}\right) - \omega_e x_e \left(v + \frac{1}{2}\right)^2 \ldots. \qquad \text{Equation 1.16}$$

where ω_e is the harmonic vibrational wavenumber and $\omega_e x_e$ is the anharmonicity constant which decreases in value along the series $\omega_e, \omega_e x_e \ldots$[46] The anharmonicity constants cause only small perturbations to the harmonic wavenumbers of low wavenumber vibrations. However, as v increases the anharmonic correction becomes larger, resulting in increased deviation from the harmonic behaviour and predicted wavenumber position. As the anharmonic term is subtracted, this also means the vibrational levels will converge at higher energies until dissociation.

For polyatomic molecules, anharmonicity also means the independent zero order states are no longer strictly valid because off diagonal terms (known as coupling matrix elements) are now introduced when the vibrational Hamiltonian is expressed in matrix form. The result is that if vibrations have similar, near degenerate, vibrational wavenumbers (known as an accidental degeneracy) and are also of the correct symmetry then they may couple, an example of a Fermi resonance in CO_2 is described in section 1.3.1. The coupled levels are referred to as the vibrational eigenstates and the vibrational motion is better described by a linear combination of the ZOSs rather than a single ZOS. This is shown schematically in Figure 1-2 for two vibrational levels. As a result of the interaction, one of the vibrational levels will shift higher in energy and the other will shift lower in energy with respect to the harmonic ZOS wavenumbers.

The energy difference between the eigenstates depends on the off-diagonal coupling term. When anharmonicity and the off-diagonal terms are small, the harmonic normal modes and associated energies are still a fairly good approximation. When anharmonicity and the off-diagonal coupling terms are large, the ZOS are a poor approximation; this is the basis for IVR, strong coupling of the vibrational levels leads to (vibrational) energy redistribution in the molecule.

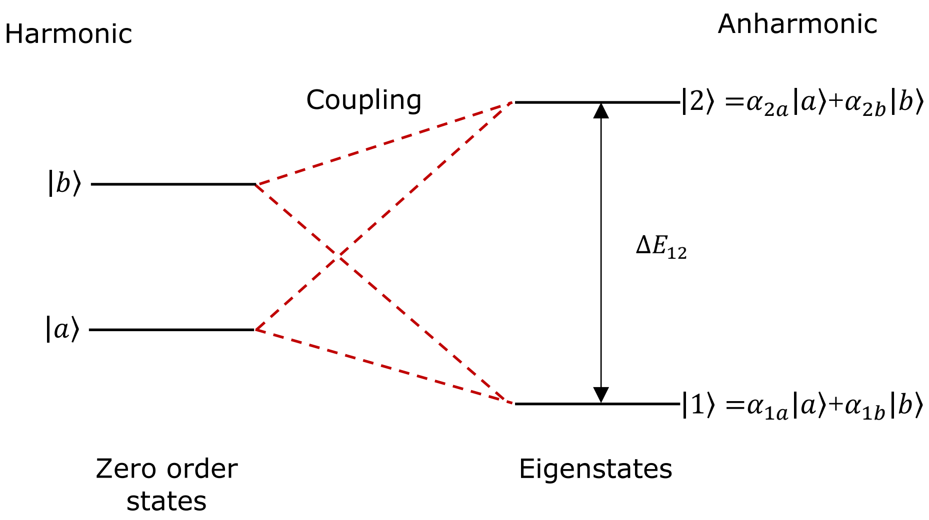

Figure 1-2: Schematic diagram of the coupling observed between two zero-order states and the resulting eigenstates. The coefficient α *is the coupling matrix element and depends on how close the ZOS is to the real eigenstate.*

The same sets of quantum numbers may be used to label both ZOS and eigenstates.[1] However, labelling the eigenstate in this way is only approximate as it only reflects the dominant ZOS which provides the largest contribution to the linear combination of ZOS which actually describes an eigenstate.[1] It will not fully describe the vibrational motion.

1.2.6. Coupling mechanisms

Following from above, for two zero-order states to anharmonically couple the following expression must be satisfied:

$$\left| \int \varphi_{v_1}^{*} V_{anh} \varphi_{v_2} d\tau \right|^2 \neq 0 \qquad \text{Equation 1.17}$$

where V_{anh} is the anharmonic potential energy function and φ_{v_1} and φ_{v_2} are the wavefunctions of the two coupled vibrational states. For equation 1.17 to be non-zero the product of the irreducible representations of φ_{v_1}, V_{anh} and φ_{v_2} must be the totally symmetric irreducible representation. As V_{anh} is totally symmetric in the relevant point group, the two zero-order states must be of the same symmetry to couple through anharmonicity. A further condition is that the two zero-order states must lie close in energy, so coupling requires an accidental degeneracy or higher energies where there is a higher density of vibrational levels. This is the main coupling mechanism discussed in this thesis.

However, there are other types of coupling; if the Born-Oppenheimer approximation breaks down and electronic and vibrational motion is inseparable, levels can interact through vibronic coupling. The symmetry of the vibronic states are the direct product of the symmetries of the constituent electronic and vibrational states, this allows ZOS to couple which do not satisfy the symmetry selection rules for anharmonic coupling. Further, if the vibrational and rotational motions become inseparable, levels may couple through Coriolis and centrifugal coupling. If a molecule is rotating, then the atoms will experience two forces. Firstly, as the degree of rotational excitation increases, the bonds are put under stress and are stretched because a centrifugal force pushes the atoms away from the centre of rotation.[54] Secondly, a Coriolis force acts perpendicularly to the direction of atomic motion during vibration and axis of rotation. Coupling strength depends on the rotational quantum number J; the greater the angular momentum the greater the molecular distortions.[12] Lawrance and Knight examined centrifugal and Coriolis coupling in relation to IVR,[55] they suggest that the rotational involvement in IVR is sensitive to the temperature of the sample. They further suggest that the influence of coupling will reduce with reduction in temperature; centrifugal coupling more so since for low J states Coriolis coupling will be the dominant mechanism and Centrifugal coupling only becomes comparable at high temperatures. *J*. Dolson and co-workers[12] measured time-resolved fluorescence spectra *via* vibrationally excited levels in S_1 *p*DFB and attempted to mimic the congestion they observed by superimposing calculated fluorescence spectra. They also concluded that rotational cooling reduces the background congestion in spectra and that "excitation of higher J states and/or a larger selection of J levels apparently allows coupling to a greater number of vibrational levels than does excitation of a small set of low J levels". McDonald and co-workers used time resolved fluorescence depletion (TRFD) to study IVR in *para*-cyclohexylaniline at different rotational temperatures.[56] They observed decreasing IVR lifetimes and quantum beat lifetimes with increasing rotational temperature, which they attributed to enhancement of either: (i) Coriolis coupling with increasing temperature or (ii) vibrational coupling due to the thermally populated low energy vibrations.

Vibrational motion can couple to internal (hindered) rotation, also known as torsional motion. This type of coupling is very important in the study of *para*-fluorotoluene due to the presence of the methyl group. Moss and Parmenter[10] used time-integrated, frequency-resolved fluorescence spectroscopy to compare the rates of IVR of comparable levels in *p*FT, *p*FT-d_3 and *p*DFB. They found the presence of the methyl group increased the rate of IVR by ~two orders of magnitude and deuteration of the methyl rotor produces a twofold further increase in the rate of IVR.[10] Moss, Parmenter and Ewing developed a model for the coupling of internal methyl torsional states and ring-based zero-order vibrational states in *p*FT which they primarily attributed to van der Waals repulsion between the methyl rotor and ring.[57] The interaction potential is periodic with respect to rotation of the methyl group and modulated by the distance between the methyl hydrogens and nearby ring atoms.[57] Therefore, vibrational motion will change the height/shape of the barrier for rotation allowing an efficient route for mixing of the vibrational and torsional levels. An alternative mechanism for torsion-vibration coupling in the S_1 state of toluene was put forward by Borst and Pratt who suggested that there is a hyperconjugative interaction between the methyl and phenyl ring π orbitals. The result is that as the methyl group rotates, the ring C-C bond adjacent to the methyl group will shorten when eclipsed by a C-H bond of the methyl group.[41] Conversely, the C-C bond will lengthen again when the methyl group is in a staggered conformation. This will also cause the other bonds in the ring to distort accordingly.[41] Therefore, the hyperconjugation interaction mixes the motion of the methyl group and distortion of the ring providing a mechanism for IVR.

1.3. Experimental probes of intramolecular vibrational energy redistribution

1.3.1. Bright and dark states

If a zero order state can be accessed through absorption of a photon, it is described as a ‘zero order bright state’ (ZOBS) and will be observed in the absorption spectrum. If optically inactive, the zero order state is described as a ‘zero order dark state’ (ZODS) and will not be observed in the spectrum. This behaviour depends on symmetry selection rules and Franck-Condon factors.

In the experiments in this thesis, vibronic transitions occur which means there is a change in both the electronic and vibrational state:

$$\int \varphi_f^* \mu \varphi_i d\tau = \int \varphi_f^* \mu_e \varphi_i d\tau + \int \varphi_f^* \mu_N \varphi_i d\tau \qquad \text{Equation 1.18}$$

where φ_i and φ_f are the wavefunctions of the initial and final states, and $d\tau$ is a volume element; this is complicated slightly in the case of ionization where the wavefunction of the final state is a product of the wavefunction of the ion and the wavefunction of the photoelectron. Applying the Born-Oppenheimer approximation allows the electronic and vibrational terms on the right-hand side of equation 1.18 to be separated:

$$\int \varphi_f^* \mu\, \varphi_i d\tau = \int \varphi_{ef}^* \mu_e \varphi_{ei} d\tau \int \varphi_{vf}^* \varphi_{vi} d\tau + \int \varphi_{ef}^* \varphi_{ei} d\tau \int \varphi_{vf}^* \mu_N \varphi_{vi} d\tau \qquad \text{Equation 1.19}$$

Integration of the second term on the right of equation 1.19 yields zero because the electronic states are orthogonal and so there is no overlap of the electronic wavefunctions. However, the first term involves vibrational levels in two different electronic states so the vibrational wavefunctions can overlap and so the term *can be non-zero*. Therefore, if the Born-Oppenheimer approximation applies the transition probability (intensity) can be described as:

$$P = \left| \int \varphi_f^* \mu\, \varphi_i d\tau \right|^2 = \left| \int \varphi_{ef}^* \mu_e \varphi_{ei} d\tau \int \varphi_{vf}^* \varphi_{vi} d\tau \right|^2 \qquad \text{Equation 1.20}$$

P depends on two integrals. For an allowed electronic transition, the first integral must be non-zero which means the product of the symmetries of the transition moment, initial and final electronic wavefunctions must be totally symmetric. The second integral is often referred to as the Franck-Condon factor or the vibrational overlap integral. Again, this term must be non-zero for an allowed transition which requires the symmetries of the initial and final vibrational states to be the same. The Franck-Condon factor dictates the propensity for changes in vibrational quantum number between the initial and final state, a transition with a high or favourable Franck-Condon factor will be relatively intense. Photoexcitation of a dark state can be prevented by symmetry selection rules and/or negligible Franck-Condon factors.

Transitions which are forbidden according to the selection rules above may be observed if the Born-Oppenheimer approximation breaks down and vibrational and electronic motion can no longer be separated. In this case vibronically allowed transitions require the product of the irreducible representations of both electronic states, both vibrational states and the vibronic transition moment to be totally symmetric. These transitions tend to be weaker than electronically allowed transitions.

While a ZODS cannot be populated directly through absorption of a photon, it is possible that a ZODS may couple to a ZOBS. This would result in two vibrational eigenstates and because both contain bright state character/contributions, two peaks would be observed in the absorption spectrum, one at each of the eigenstate energies. The most widely known example of such a two-state coupling is the CO_2 Fermi resonance observed in Raman spectroscopy. The symmetric stretching mode, v_1, is expected to appear at 1330 cm^{-1} which is close in energy to the first overtone of the bending mode, $2v_2$, expected at 1334 cm^{-1}.[58] The transition from 0^0 to 1^1 is formally allowed, where mode 1 is the symmetric stretching mode, and a very intense Raman band is expected. The 2^2 zero-order state is totally symmetric, and therefore the transition from 0^0 to 2^2 is symmetry allowed, but under the harmonic approximation it is forbidden according to the $\Delta v = \pm 1$ selection rule and so no Raman band is expected.[58] However, two bands of similar intensity at 1285 cm^{-1} and 1385 cm^{-1} appear in the Raman spectrum, shifted by ~50 cm^{-1} from the predicted wavenumbers.[58] The peaks correspond to transitions from 0^0 to the two eigenstates which result from the coupling of the 1^1 and 2^2 ZOSs. Both eigenstates contain significant character from the strongly allowed symmetric stretch which provides oscillator strength for the transitions from 0^0 to both eigenstates. The unexpected intensities mean the 2_0^2 transition is often said to have stolen intensity from the 1_0^1 transition.[58]

1.3.2. Frequency resolved vs time resolved studies

IVR resulting from the coupling of vibrational levels can be probed in either time-domain or frequency resolved experiments, however they provide different (albeit complimentary) information because the 'state' initially prepared is different. It is easiest to consider this using the simplest case of IVR which is a Fermi resonance between a fundamental and overtone vibrational level; this regime is referred to as restrictive IVR which is explained further in section 1.4.1.

1.3.2.1. Frequency-resolved experiments

Frequency resolved experiments attempt to observe and resolve all eigenstates that contain contributions from a specific ZOS.[1] Relatively narrow band lasers (sufficiently narrow to obtain eigenstate resolution) are used to excite single vibrational eigenstates. The molecular eigenstates are inherently stationary and their population is not time-dependent. The wavefunction of the vibrational state can be expressed as:

$$\varphi_n(t) = \varphi_n e^{\frac{-i(E_n)t}{\hbar}} \qquad \text{Equation 1.21}$$

where E_n is the energy of the eigenstate φ_n. The probability distribution is time-independent because the time-dependent phase factors cancel when squared; the probabilities associated with molecular eigenstates do not move. If eigenstates are resolved, therefore, IVR and coupling between zero-order states will manifest itself as observable differences in peak energies and intensities with respect to expectations from the ZOSs. In the situation of a Fermi resonance where two ZOSs couple to give two eigenstates, PES or DF spectra recorded via each eigenstate will consist of two peaks at the energies of the molecular eigenstates (see Figure 1-2) and relative intensities depend on the contribution of each ZOS involved to the vibrational wavefunction. In the event that the two levels are not coupled the vibrational eigenstate will resemble the zero-order state. Coupling to a large number of bath states in a dissipative regime is indicated by severe congestion.

1.3.2.2. Time-resolved experiments

In a time-resolved experiment, the initially excited state is not a molecular eigenstate but a zero-order bright state which can be expressed as a superposition of the eigenstates. An excitation laser is used which has a pulse duration significantly shorter than the IVR lifetime and a sufficiently large bandwidth to prepare a coherent superposition of the vibrational eigenstates with a well-defined phase relationship which will initially behave as the prepared zero-order bright state (normal mode):[a]

$$\varphi(t) = \sum_i C_i \varphi_i e^{\frac{-iE_i t}{\hbar}} \qquad \text{Equation 1.22}$$

where C_i is the coefficient describing the contribution of each eigenstate in the superposition which depends on Franck-Condon factors and the relative light intensity. However, there is a temporal evolution of the initial state or wavepacket because the relative phases/phase relationship of the individual eigenstates will change with time. This means the wavepacket will dephase then rephase and there will be constructive and destructive interference of the eigenstates, resulting in a change of the nuclear displacements. At some later time, depending the eigenstate energy separation, the phase configuration of the wavepacket will resemble the ZODS. Depending on the coupling and number of levels involved there may be a recurrence of the bright state. This can be followed in a time-resolved experiment by recording spectra at different points during the evolution. In the Fermi resonance example where a single bright ZOS couples to a single dark ZOS to give two eigenstates ($|1\rangle$ and $|2\rangle$), coherent excitation gives the wavepacket:

$$\varphi = C_1 \varphi_1 e^{\frac{-iE_1 t}{\hbar}} + C_2 \varphi_2 e^{\frac{-iE_2 t}{\hbar}} \qquad \text{Equation 1.23}$$

where E_1 and E_2 are the energies of the two eigenstates and the coefficients C_1 and C_2 take values so that at t = 0 the wavepacket resembles the bright ZOS. Any

---

[a] In picosecond time-resolved spectroscopy, the term vibrational eigenstate represents the collection of rovibrational levels associated with a single vibrational eigenstate. This assumes the Born-Oppenheimer approximation is valid.

observable monitored during the experiment depends on the square of the wavefunction, the probability, as the phase factors (which have a time-dependence) no longer cancel when the wavefunction is squared the probability distribution is now time-dependent:

$$\varphi^2 = {C_1}^2{\varphi_1}^2 + {C_2}^2{\varphi_2}^2 + C_1C_2\varphi_1\varphi_2 e^{\frac{i(E_1-E_2)t}{\hbar}} + C_2C_1\varphi_2\varphi_1 e^{\frac{i(E_2-E_1)t}{\hbar}} \qquad \text{Equation 1.24}$$

Taking the real part and applying $e^{\pm i\phi} = \cos\phi \pm i\sin\phi$ and $\cos\theta = \cos(-\theta)$, equation 1.24 can be expressed as:

$$\mathrm{Re}[\varphi^2] = {C_1}^2{\varphi_1}^2 + {C_2}^2{\varphi_2}^2 + 2C_1C_2\varphi_1\varphi_2\cos\frac{(E_1-E_2)t}{\hbar} \qquad \text{Equation 1.25}$$

Importantly, in a time-resolved experiment the squared phase factors provide information on eigenstate energy separations. In the Fermi resonance case, eventually the wavepacket will evolve to resemble the ZOBS again and monitoring the population of the bright state over the length of the experiment will show oscillations in time, with a period (τ_{osc}) depending on eigenstate energy difference ($\Delta E = \frac{h}{\tau_{osc}}$). The observed time-dependent behaviour in this situation is attributed to the evolving phase relationship between the eigenstates but is often described in terms of population redistributing between coupled ZOSs; in a Fermi-resonance it can be helpful to consider energy transferring between the bright state and the dark state due to their coupling.

In order to observe the time-dependent evolution of the initially prepared bright state, the bandwidth of the excitation pulse must encompass all eigenstates resulting from the coupling of the ZOSs.

1.4. Rationalisation and models of IVR

1.4.1. Regimes of IVR

Energy redistribution in molecules is often assigned to a regime based on the type of time-dependent behaviour observed. The distinctive behaviour typical of each regime depends on the strength of the coupling and the number of zero order states involved in the coupling mechanism. However, it is important to be careful in the interpretation of time-dependent behaviour because the results also depend on the laser bandwidth. Any observed time-dependence will only reflect the full IVR process if the bandwidth of the excitation pulse is large enough to encompass all the eigenstates resulting from coupling of the bright and dark states. It follows that the absence of any observed time-dependence may not always indicate that there is no IVR occurring. Incidentally, oscillations in intensity may not necessarly evidence that IVR has occurred; instead this time dependence can occur from the coherent excitation of two uncoupled ZOBS, the vibrational wavepacket would include the eigenstates contributing to each ZOS and there would still be an evolving phase relationship although there would be an absence of any out of phase oscillations. This is demonstrated by Stolow and co-workers in their time-resolved photoionisation study on I_2.[59] High resolution experiments where perturbations in the energies of rovibrational levels could be identified would be vital here such as the work of Gascooke and Lawrance[60].

The restricted IVR regime occurs when only a few zero-order vibrational states are coupled, such as in the Fermi resonance example used earlier. As the name suggests, IVR is restricted in that energy does not irreversibly redistribute from the bright state, but oscillates between a small number of zero-order states, with periodic recurrences to the initially prepared bright state over the lifetime.[15] In a frequency-resolved ZEKE-PFI or dispersed fluorescence (DF) experiment, in which eigenstates can be resolved, the observed spectrum will be well structured, enabling the determination of intensities and energies of the molecular eigenstates. In a time-resolved experiment, restricted IVR is identified by oscillations/quantum beats in bright state (and dark state) population with time.

In the dissipative or statistical IVR regime numerous zero-order dark states are coupled to the zero-order bright state. Over the timescale of the experiment, there is irreversible flow of energy out of the initially prepared bright state into the large number of coupled ZOS. The dephasing of the wavepacket is such that there is no full recurrence of the configuration resembling the bright state. As this type of IVR requires a large number of closely spaced ZOS of the correct symmetry to be able couple, it is generally only observed in high energy regions in which the density of states is high. In a time-resolved experiment, an exponential decay in bright state population would be observed as energy irreversibly flows out of the ZOBS. A PES or DF spectrum recorded during a frequency-resolved experiment would show only a broad, unresolved feature due to the numerous eigenstates resulting from the coupling of the ZOBS to multiple ZODS.

The restrictive and dissipative regimes are two extreme behaviours, but there also exists an intermediate type of behaviour. In this regime the bright state couples strongly to a few critical dark states, some of which are known as 'doorway states'. The doorway states are so-named because they themselves are coupled to a large number of other dark states, known as 'bath' states. As the coupling between the bright state and the doorway state(s) is relatively strong, and the coupling between the doorway state(s) and the bath states is stronger than between the bright state and the bath states, the doorway state is considered to facilitate IVR directing the flow of energy into the bath states. A tier model is often used in these situations to explain the hierarchical coupling scheme controlling the energy flow.[1] In this model the ZOS are organised into tiers as shown in Figure 1-3, with a progressive set of tiers with increasing density of states with progressively weaker coupling to the bright state.[1]

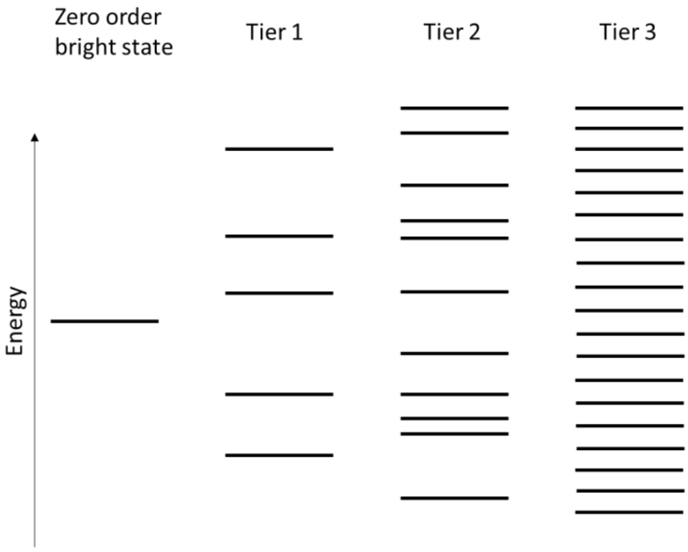

Figure 1-3: Schematic diagram of the tier model which shows the sequential energy flow in intermediate IVR. Dark states are organised into a hierarchy according to coupling strength to the bright state which gives a progressive set of tiers with increasing density of states. Based on Figure 3. in Ref 1.

In a time-resolved experiment, IVR in the intermediate regime would cause the bright state population to show quantum beats, as energy flows between a few strongly coupled ZOS, with this beating superimposed on an exponential decay, as energy redistributes irreversibly into numerous bath states. In a frequency-resolved experiment, PES or DF spectra recorded would likely contain a few well resolved peaks, attributable to eigenstates that result from the strongly coupled ZOS, which are superimposed on a broad, raised baseline, resulting from the large number of weaker coupled ZOS.

1.4.2. Density of states

Density of states arguments are often used to explain the existence of the different regimes observed in the section above. If a zero-order bright state is in a region of low density of states, then there will be few close lying levels to which it could couple meaning restricted or even no IVR is most likely, with energy remaining localised. Conversely, when the density of states is high many near degenerate zero order states are available for coupling to the bright state meaning IVR may become dissipative with short lifetimes measured.

The density of states depends partly on the structure of the molecule, (molecules that have low frequency vibrational modes have an inherently higher density of states) and is also energy dependent. The density of states will increase with increasing internal energy because of the many possibilities for vibrational states involving combinations and overtones, and so the DOS is often used to explain the existence of a threshold energy or IVR onset energy. Smalley and co-workers measured dispersed fluorescence spectra of a series of jet-cooled n-alkylbenzenes following photoexcitation of several ring modes in the S_1 electronic state.[61,62] When the alkyl chain length was short, the fluorescence spectrum showed sharp bands as the chain length was increased the features were broadened (more unstructured emission), indicating IVR (on a subnanosecond timescale).[61,63] Further, when the higher energy vibrational level was excited (12^1 at 933 cm^{-1} compared to $6b^1$ at 530 cm^{-1}), the IVR process was observed for molecules with even shorter chain lengths.[61] They concluded that the density of chain states and number of effectively coupled levels increased as the alkyl chain length is increased.[61] Similar results were also seen in dispersed fluorescence spectra measured for alkylanilines following photoexcitation of level I^2 in the S_1 electronic state.[61]

Moss and Parmenter[10] used the Fermi golden rule expression as a guideline or rationale for the different IVR rates in systems such as *para*-fluorotoluene and *para*-difluorobenzene.[10] The expression for the non-radiative rate constant (IVR rate) can be written as:[10,54]

$$k_{IVR} = \frac{2\pi}{\hbar} V^2 \rho_{eff} \qquad \text{Equation 1.26}$$

This expression shows that the rate depends on two parameters; i) V, the average coupling matrix element of the Hamiltonian matrix between the initially excited zero-order state and the levels to which it is coupled and ii) ρ_{eff}, the density of effectively coupled levels which is a subset of the total density of states. The expression indicates that IVR rate will be proportional to ρ_{eff}, but only if all the coupled states have similar coupling strength to the bright zero order state.

Nesbitt and Field commented that if the total density of states increased by adding modes which are increasingly weakly coupled to the bright state, this would decrease the mean square coupling matrix element V^2.[1] So, if IVR dynamics are dominated by 'local couplings', Fermi's golden rule would predict little or no change in IVR lifetime if the overall density of states were increased.[1] This can be observed in a high-resolution infrared study of McIlroy and Nesbitt in which the C-H stretch ($v_{CH} = 1$) was excited in the series of molecules propyne, 1-butyne and gauche/cis 1-pentyne. In 1-butyne the density of states was 22 per cm^{-1} and the IVR lifetime was calculated to be 270 ps, whereas in 1-pentyne, with a state density of 2400 cm^{-1}, the IVR lifetime for the gauche isomer was 240 ps and 440 ps for the trans isomer.[1,64] Lehmann and co-workers studied further terminal acetylenes and found $(CF_3)_3$C-CCH had a much larger density of states of 10^{11} per cm^{-1} yet an observed IVR rate of 60 ps, within 1 order of magnitude of the other systems.[1,65] The fact that the IVR lifetimes are relatively insensitive to the difference in state density suggests that the prepared C-H stretching zero order state has very weak or no coupling with the bath of states which are introduced by changing the substitution group.[1] Therefore, an increased density of states will only affect the IVR rate if mechanisms exist by which coupling can occur between these states.

1.4.3. Flexibility

Perry and co-workers have suggested that molecular flexibility plays a role in accelerating the rate of IVR.[66,67,] In earlier work[66] these authors compared the IVR lifetimes for two hydride stretching fundamental vibrational modes in 1-pentyne, ethanol and propargyl alcohol. In each species internal rotation about a C-C or C-O bond connects the gauche and trans conformers. The IVR lifetimes were determined from line shapes, positions and intensities from the frequency-resolved spectra of other authors.[66] In each of the three molecules the population loss was more rapid from the vibrational state associated with the mode closer to the centre of flexibility, COF, which was defined 'as a bond about which hindered internal rotation can occur'.[67] The authors found that this trend is supported by the comparison of IVR lifetimes following the excitation of similar vibrational modes in other flexible molecules, such as hydrogen peroxide, 1-butene, n-butane, methyl formate, and propargyl amine.[66] The longest lifetime (250 ps, 400 ps) in this group is observed when the acetylenic C-H mode in propargyl amine is excited.[66] This mode is distant from the centre of flexibility. Conversely the shortest observed lifetime (4 ps) was for hydrogen peroxide following excitation of the O-H stretch which is adjacent to the O-O bond about which internal rotation can occur.[66] For 'rigid' molecules, the IVR lifetimes were predicted to be as long or longer as in cases where the mode excited is far removed from the centre of flexibly. The IVR lifetimes of the rigid molecules isobutane, propyne, trans-2-butene, and tert-butylacetylene were reported between 132 ps – 2650 ps.[66]

In a later study, Perry and co-workers proposed that when exciting a vibrational mode close to the centre of flexibility, the IVR lifetime will increase as the height of the torsional barrier increases.[67] The authors compared IVR lifetimes of hydride stretches, which were adjacent to the COF, in a variety of molecules with different torsional barrier heights. The authors found that the IVR lifetimes in ethanol and hydrogen peroxide, which have torsional barriers of ~ 380 cm^{-1}, were fast between 4-26 ps.[67] Conversely, the molecules 1–butyne, 2-fluoroethanol and 1,2-di-fluoroethane (CH), which have much larger torsional barriers (1100 to 1700 cm^{-1}), had much longer IVR lifetimes (270 to 565 ps).[67] In a study by Wright, Reid and co-workers the critical influences on the rate of IVR were discussed through comparatives studies of the dynamics resulting from excitation of the C–CH_3 stretching mode, in the S_1 electronic states of toluene, toluene-d_3 and *p*FT.[39] The dynamics were probed through time-resolved photoelectron spectroscopy and comparisons were made to REMPI and ZEKE spectra measured using nanosecond laser pulses.[39] The authors noted that for toluene derivatives the C–CH_3 bond represents a centre of flexibility, the relationship proposed by Perry and co-workers therefore suggests that IVR should be accelerated in toluene relative to *p*FT because the barrier height for *p*FT is around 35% higher due to the influence of the fluorine substituent.[39] The hyperconjugation theory of Borst and Pratt (section 1.2.6), where rotation of the methyl group modulates the ring structure and disrupts the conjugation, also predicts a longer lifetime for *p*FT compared with toluene, because the fluorine atom stabilises the hyperconjugated structure.[41,39] Conclusions on the role of the methyl group are sometimes contradictory; in a study by Moss and Parmenter, the authors compared the IVR lifetimes following excitation of the C-F stretching mode in S_1 *p*FT and *meta*-fluorotoluene (*m*FT) and they found the IVR lifetime of *m*FT was shorter by a factor of twelve compared to the IVR lifetime of *p*FT.[39,68] The torsional barrier is four times larger in *m*FT compared to *p*FT, the authors suggested that IVR was promoted by the stronger interaction between the methyl rotor and ring for *m*FT.[39,68] According to this theory, the larger barrier in *p*FT should facilitate IVR compared to toluene which is contradictory to the prediction of Perry that substantial barriers to internal rotation hinder IVR. Wright, Reid and co-workers observed significantly shorter IVR lifetimes of 12 and 15 ps for the C-CH_3 stretching vibrations in toluene and toluene-d_3, compared to an IVR lifetime of 50 ps for *p*FT.[39] This is in apparent agreement with Perry and co-workers, however the shorter IVR lifetimes are attributed to doorway states mediating the IVR process in toluene and toluene-d_3 but not in *p*FT rather than the result of a large difference in barrier height. This indicates the importance of understanding the IVR mechanism(s) operating in each molecule and the difficulty in predicting IVR behaviours and rates.

1.4.4. Mode-dependence

The impact of the vibrational mode on IVR was highlighted by Knight and co-workers who studied IVR in S_1 *p*-difluorobenzene using single vibronic level (SVL) fluorescence spectroscopy.[69] They compared the ratio of unstructured (U) to structured (S) emission in SVL dispersed fluorescence spectra obtained following the excitation of a series of levels, some of which involved excitation of the low-frequency, out-of-plane CH mode v_{30} (in Mulliken notation), and some that did not. This comparison showed that the U/S ratios obtained following excitation of vibrational states involving mode 30 were significantly higher than those without. The authors concluded from the data that excitation of mode 30 promotes IVR in S_1 pDFB. Furthermore, it was found that excitation of the state $5^2 30^2$ (where mode 5 is a ring breathing mode) at an internal energy of 1882 cm^{-1} gave rise to a U/S ratio that was 30% greater than that found for the level $3^1 5^1$ (mode 3 is a CF stretch) which lies at 2069 cm^{-1}. This led the authors to conclude that the onset of intramolecular vibrational energy redistribution in the S_1 electronic state of *p*DFB was dependent on the mode excited.

1.4.5. Competition of IVR with other processes

The experiments described in this work involve excitation of molecules into their first electronic excited state. The capabilities of the equipment (a delay stage on a computer-controlled motor which can extend or shorten the probe path length) allow the ‘population’ of the bright state to be monitored over a 500 ps timescale following excitation. IVR is not the only event which can occur following photoexcitation, there are several processes through which bright state population can be lost (see Figure 1-4). Generally, these can be split into radiative transitions (fluorescence and phosphorescence) and non-radiative transitions, with the latter including internal conversion from the S_1 to the S_0 electronic state, intersystem crossing from S_1 to a triplet state and vibrational relaxation. Vibrational relaxation which is collisionally induced can be disregarded in the experiments described in this thesis because molecules are probed in a collision free environment.

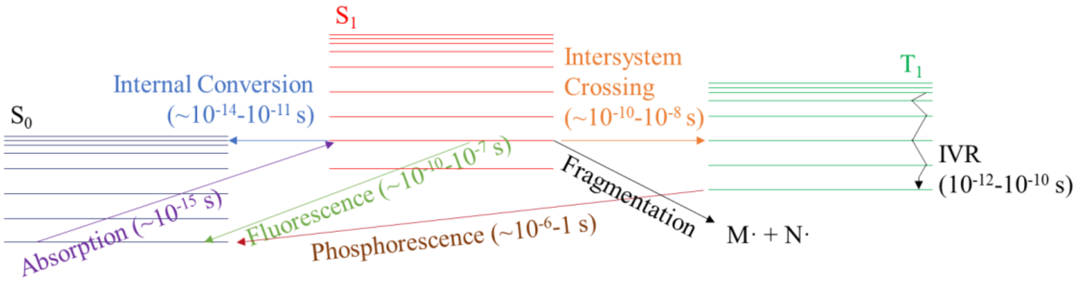

Figure 1-4: Jablonski diagram showing the processes which could occur following photoexcitation to an excited state along with approximate time scale for these processes. Internal conversion and intersystem crossing are shown by horizontal arrows because they involve redistribution of internal energy rather than decay or loss. Timescales taken from Ref. 23

Processes occurring on a substantially longer lifetime than IVR are unlikely to significantly affect experimental results which measure the first 500 ps; for example, we choose to study molecules with fluorescence lifetimes of many nanoseconds. Any processes occurring over a similar timescale to IVR which cause an observable loss of bright state population could complicate time-resolved studies of IVR, although internal conversion and intersystem crossing could be identified through a reduction in the measured photoelectron yield due to changes in the Franck-Condon factors for ionisation.

1.5. Aims and overview

1.5.1. Aims

The aim of this work was to conduct systematic studies into how the prepared S_1 vibrational states evolve as a function of time, in order that the IVR dynamics of 1) different initially prepared vibrations within an individual molecule and 2) different structurally related molecules could be compared. Slow electron velocity map imaging (SEVI) and time-resolved velocity map imaging (tr-VMI) were utilised to follow the energy dispersal dynamics upon excitation of multiple S_1 vibrational levels in aniline and *para*-fluorotoluene (*p*FT), which themselves were identified by resonance enhanced multiphoton ionisation (REMPI) spectroscopy. A comparative study could reveal insights on factors which affect energy dispersal. For example, the effect of the substituent group on IVR dynamics can be observed;

whereas *p*FT contains a methyl group and low energy torsional levels, aniline has an NH_2 group whose vibrations lie higher in energy. Further, information on mode-dependent IVR dynamics can be gained through comparison of similar modes in different molecules, in this work *p*FT spectra was compared to previous work on *para*-difluorobenzene.[70]

1.5.2. Chapters overview

The aim of this Chapter was to introduce the relevant background and theory required for following the subsequent Chapters. Chapter 2 is organised into three sections; firstly, the theory and principles of each technique are discussed, secondly the experimental set up is described and thirdly the data analysis procedures are outlined. Chapters 3, 4 and 5 present SEVI and time-resolved photoelectron spectra recorded via S_1 vibrational levels in aniline. Chapter 3 focusses on S_1 vibrational levels lying <1000 cm^{-1} which exhibit either restrictive IVR or no time-dependence. Calculated frequencies for the vibrations of aniline in the S_1 and D_0^+ states are shown here. Chapter 4 discusses the complex time-dependence of vibrational levels in the ~1100-1700 cm^{-1} region of the S_1 electronic state. Chapter 5 discusses the photoexcitation of the highest energy S_1 vibrational levels above ~1700 cm^{-1} and shows examples of dissipative IVR. Chapter 6 shows the analysis of two close lying S_1 vibrational levels in *para*-fluorotoluene, the raw data of which were recorded previously by Dr Julia Davies. In Chapter 7, the conclusions of previous chapters are summarised and comparisons are made between studies of different molecules. The appendix which is Chapter 8 shows the individual photoelectron spectra used to produce the SEVI spectra and calculated normal mode diagrams of relevant *p*FT and aniline modes.

1.6. References

---

[1] D. J. Nesbitt and R. W. Field., *J. Phys. Chem.*, 1996, **100**, 12735-12756

[2] Y. Yamada, Y. Katsumoto and T. Ebata, *Phys. Chem. Chem. Phys.,* 2007, **9**, 1170-1185

[3] S. H. Kable, J. W. Thoman, S. Beames and A. E. W. Knight, *J. Phys. Chem.,* 1987, **91**, 1004-1006

[4] R. A. Coveleskie, D. A. Dolson, and C. S. Parmenter., *J. Chem. Phys.*, 1980, **72**, 5774-5775

[5] R. A. Coveleskie, D. A. Dolson, C. S. Parmenter., *J. Phys. Chem.*, 1985, **89**, 645-654

[6] R. A. Coveleskie, D. A. Dolson, C. S. Parmenter*., J. Phys. Chem.*, 1985, **89**, 655-665

---

[7] K. W. Holtzclaw and C. S. Parmenter., *J. Chem. Phys.*, 1986, **84**, 1099-1118

[8] C. S. Parmenter, *Faraday Discuss. Chem. SOC.*, 1983, **75**, 7-22

[9] C. S. Parmenter and B. M. Stone., J. *Chem. Phys.*, 1986, **84**, 4710–4711.

[10] D. B. Moss and C. S. Parmenter., *J. Chem. Phys*., 1993, **98**, 6897-6905

[11] D. Boyall and K. L. Reid*, Chem. Soc. Rev.,* 1997, **26**, 223-232

[12] D. A. Dolson, K. W. Holtzclaw, D. B. Moss, and C. S. Parmenter., *J. Chem. Phys.*, 1986, **84**, 1119-1132

[13] A. H. Zewail., *Faraday Discuss. Chem. Soc*., 1983, **75**, 315-330

[14] W. R. Lambert, P. M. Felker and A. H. Zewail, *J. Chem. Phys.,* 1981, **75**, 5958-5960

[15] P. M. Felker and A. H. Zewail, *J. Chem. Phys.*, 1985, **82**, 2961-2974

[16] P. M. Felker and A. H. Zewail, *J. Chem. Phys.*, 1985, **82**, 2975-2993

[17] P. M. Felker and A. H. Zewail, *J. Chem. Phys.,* 1985, **82**, 2994-3002

[18] P. M Felker, W. R. Lambert, and A. H. Zewail., *J. Chem. Phys.*, 1985, **82**, 3003-3010

[19] M. J. Côté, J. f. Kauffman, P. G. Smith and J. D. McDonald, *J. Chem. Phys.,* 1989, **90**, 2865-2873

[20] J. f. Kauffman, M. J. Côté, P. G. Smith and J. D. McDonald, *J. Chem. Phys.,* 1989, **90**, 2874-2891

[21] J. A. Davies, K. L. Reid, M. Towrie and P. Matousek., *J. Chem. Phys.*, 2002, **117**, 9099-9102

[22] D. M. Neumark, *Annu. Rev. Phys. Chem.,* 2001, **52**, 255-277

[23] H. H. Fielding and G. A. Worth., *Chem. Soc. Rev*., 2018, 47, 309-321

[24] A. Stolow and J. G. Underwood, *Adv. Chem. Phys*., 2008, 139, 497–583

[25] T. J. Penfold, R. Spesyvtsev, O. M. Kirkby, R. S. Minns, D. S. N. Parker, H. H. Fielding and G. A. Worth., *J. Chem. Phys*., 2012, **137**, 204310

[26] R. S. Minns, D. S. N. Parker, T. J. Penfold, G. A. Worth and H. H. Fielding., *Phys. Chem. Chem. Phys*., 2010, **12**, 15607–15615

[27] K. L. Reid, *Int. Rev. Phys. Chem.,* 2008, **27**, 607-628

[28] R. Spesyvtsev, J. G. Underwood and H. H. Fielding, Time-Resolved Photoelectron Spectroscopy for Excited State Dynamics. In: R. de Nalda and L. Bañares (eds), *Ultrafast Phenomena in Molecular Sciences, Springer Series in Chemical Physics,* 2014, **107**, 99-117

[29] X. Song, C. W. Wilkerson Jr, J. Lucia, S. Pauls and James P. Reilly, *Chem. Phys. Lett*., 1990, **174**, 377-384

[30] J. T. Meek, S. R. Long and J. P. Reilly, J. Phys. Chem., 1982, **86,** 2809-2811

[31] P. T. Whiteside, A. K. King, J. A. Davies, K. L. Reid, M. Towrie and P. Matousek., J. Chem. Phys, 2005, **123**, 204317,

[32] G. Reiser, W. Habenicht, K. MüLLER-Dethlefs and E. W. Schlag, *Chem. Phys. Lett.,* 1988, **152**, 119-123

[33] A. M. Ellis, M. Feher, and T. G. Wright, Electronic and Photoelectron Spectroscopy Fundamentals and Case Studies (Cambridge University Press, Cambridge, 2005

[34] J. M. Smith, C. Lakshminarayan, and J. L. Knee., *J. Chem. Phys*., 1990, **93**, 4475-4476

[35] A. T. J. B. Eppink and D. H. Parker., *Rev. Sci. Instrum.*, 1997, **68**, 3477-3484

[36] K. L. Reid, *Annu. Rev. Phys. Chem.,* 2003, **54**, 397-424

[37] A. Osterwalder, M. J. Nee, J. Zhou and D. M. Neumark, *J. Chem. Phys*., 2004, **121**, 6317–6322.

[38] C. J. Hammond and K. L. Reid, *Phys. Chem. Chem. Phys*., 2008, **10**, 6762–6769.

[39] J. A. Davies, A. M. Green, A. M. Gardner, C. D. Withers, T. G. Wright and K. L. Reid., *Phys. Chem. Chem. Phys*., 2014, **16**, 430-443

[40] K. K. Lehmann, G. Scoles and B. H. Pate, *Annu. Rev. Phys. Chem*., 1994, **45**, 241-74

[41] D. R. Borst and D. W. Pratt, *J. Chem. Phys*., 2000, **113**, 3658–3669

---

[42] J. R. Gascooke, U. N. Alexander and W. D. Lawrance., *J. Chem. Phys*., 2011, **134**, 184301

[43] A. M. Gardner, W. D. Tuttle, L. E. Whalley and T. G. Wright, *Chem. Sci.,* 2018, **9**, 2270-2283

[44] D. J. Kemp, L. E. Whalley. A. M. Gardner, W. D. Tuttle, L. G. Warner, and T. G. Wright, *J. Chem, Phys.,* 2019, **150**, 64306

[45] D. J. Kemp, W. D. Tuttle, A. M. Gardner, L. E. Whalley and T. G. Wright, *J. Chem. Phys.,* 2019, **151**, 64308

[46] J. M. Hollas, Modern Spectroscopy (John Wiley and Sons Ltd., Chichester, England, 2004)

[47] R. S. Mulliken., *J. Chem. Phys*., 1955, **23**, 1997

[48] G. Herzberg, Molecular Spectra and Molecular Structure II: Infrared and Raman Spectra of Polyatomic Molecules (van Nostrand, New York, 1945)

[49] E. B. Wilson, *Jr, Phys. Rev*., 1934, **45**, 706.

[50] G. Varsanyi, *Assignments for Vibrational Spectra of Seven Hundred Benzene Derivatives*. (Wiley, New York, 1974).

[51] A. M. Gardner and T. G. Wright*., J. Chem. Phys*, 2011, **135**, 114305

[52] A. Andrejeva, A. M. Gardner, W. D. Tuttle and T. G. Wright., *J. Mol. Spec*., 2016, **321**, 28-49

[53] A. M. Gardner, *Ph.D. thesis*, University of Nottingham. 2013

[54] P. W. Atkins and R. S. Friedman, *Molecular Quantum Mechanics*, Oxford University press, 4th Edition, 2005

[55] W. D. Lawrance and A. E. W. Knight, *J. Phys. Chem*., 1988, **92**, 5900–5908

[56] P. G. Smith and J. D. McDonald., *J. Chem. Phys.,* 1990, **93**, 6350-6456

[57] D. B. Moss, C. S. Parmenter and G. E. Ewing., *J. Chem. Phys*., 1987, **86**, 51-61

[58] C. N. Banwell and E. M. McCash, Fundamentals of molecular spectroscopy, McGraw-Hill, London, 4th ed., 1994.

[59] I. Fischer, M. J. J. Vrakking, D. M. Villeneuve and A. Stolow, *Chem. Phys.,* 1996, **207,** 331-354

[60] J. R. Gascooke, E. A. Virgo, W. D. Lawrance., *J. Chem. Phys*., 2015, **143**, 44313

[61] R. E. Smalley, *J. Phys. Chem.,* 1982, **86**, 3504-3512

[62] J. B. Hopkins, D. E. Powers, S. Mukamel and R. E. Smalley, *J. Chem. Phys.,* 1980, **72**, 5049-5061

[63] J. B. Hopkins, D. E. Powers and R. E. Smalley, *J. Chem. Phys.,* 1980, **73**, 683-687

[64] A. McIlroy and D. J. Nesbitt, *J. Chem. Phys*., 1990, **92**, 2229-2243

[65] J. E. Gambogi, K. K. Lehmann, B. H. Pate, G. Scoles, X. J. Yang, *J. Chem. Phys.,* 1993, **98**, 1748-1749

[66] G. A. Bethardy, X. L. Wang and D. S. Perry, *Can. J. Chem*., 1994, **72**, 652-659

[67] D. S. Perry, G. A. Bethardy and X. L. Wang, *Ber. Bunsenges. Phys. Chem*., 1995, **99,** 530-535

[68] P. J. Timbers, C. S. Parmenter and D. B. Moss, *J. Chem. Phys*., 1994, **100**, 1028-1034

[69] S. H. Kable, W. D. Lawrance and A. E. W. Knight, *J. Phys. Chem*., 1982, **86**, 1244-1247

[70] J. Midgley, J. A. Davies, K. L. Reid., *J. Phys. Chem. Lett*., 2014, **5**, 2484-2487

2. Experimental techniques, apparatus and analysis

2.1. Overview

In this chapter the various experimental techniques utilised in the investigations reported in this thesis are discussed, followed by subsections which describe the apparatus employed, and the methodology for analysis of the acquired data. Three experimental techniques are used; firstly two-colour resonance-enhanced multiphoton ionization (REMPI) spectroscopy is used to study the $S_1 \leftarrow S_0$ electronic transition of aniline and *para*-fluorotoluene (*p*FT) with the resulting spectra used to identify vibrational levels of interest within the excited electronic state. Secondly the S_1 vibrational levels of interest are used as the intermediate excited states in (1+1′) slow electron velocity map imaging (SEVI) experiments in order to study the vibrational structure of the D_0^+ cationic ground states of these molecules. Finally (1+1′) time-resolved photoelectron velocity-map-imaging (tr-VMI) studies are used to study the vibrational dynamics which occur in S_1.

2.2. Experimental techniques

2.2.1. Resonance-enhanced multiphoton ionisation (REMPI) spectroscopy

REMPI experiments have been carried out using a picosecond laser system (with pulses of ~1 ps duration) and a velocity map imaging spectrometer which are described in sections 2.3.1 and 2.3.2 respectively. In REMPI spectroscopy molecules are first excited to a specific vibronic (or (ro)vibronic if higher resolution, long pulse duration lasers are employed) intermediate level through the absorption of one (or more) photon(s). The molecule is then ionized through the absorption of a second photon (or photons), and the number of ions (or electrons) produced is monitored. In the experiments discussed in this thesis a single UV photon drives each of the $S_1 \leftarrow S_0$ excitation and $D_0^+ \leftarrow S_1$ ionisation steps (so two photons in total). If both photons have the same wavelength the technique is known as (1+1) or one colour REMPI. If the two wavelengths are different this is known as (1+1′) or two colour REMPI. In this thesis (1+1′) REMPI spectra are shown meaning two laser beams are used; the ionization laser wavelength is fixed while the excitation laser wavelength is scanned. These processes are illustrated in Figure 2-1.[1]

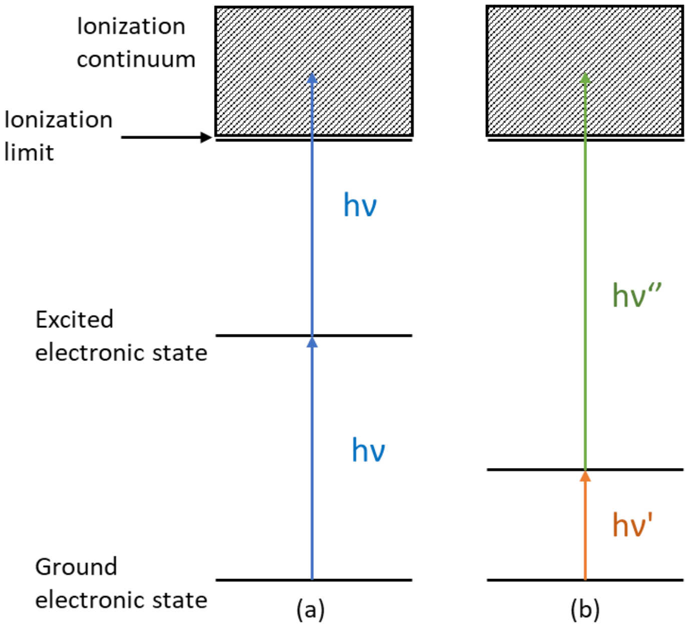

Figure 2-1: Adapted from reference 1. (a) One colour and (b) two colour resonance enhanced multiphoton ionization process.

Each time the excitation laser wavelength is tuned to be resonant with an allowed transition to a vibronic level, the ionization probability increases dramatically. This results in a peak in a plot of ion yield *vs* wavelength; with such a plot referred to as a "REMPI spectrum". In principle these vibronic transitions can originate from any vibrational level which is thermally populated, resulting in complicated spectra being obtained. To avoid this a molecular beam is used, this is described in section 2.3.4.

2.2.2. Photoelectron spectroscopy

Two techniques have been utilised which provide spectroscopic information on the molecular cation; time-resolved photoelectron imaging which allows the dynamics of the excited electronic states of molecules to be studied and SEVI spectroscopy which provides higher spectral resolution of the cation electronic ground state.

a) Time-resolved studies - VMI

The time-resolved experiments described in this thesis utilise velocity map imaging (VMI). In this technique a picosecond laser pulse is used to excite a specific vibrational level in the S_1 electronic state, a pulse from a second laser beam then ionises the molecule and the kinetic energies (and angular distributions) of the resulting photoelectrons are measured. VMI utilises an electrostatic lens to focus the photoelectrons onto a dual microchannel plate assembly, which amplifies the number of electrons through an electron cascade mechanism, before being accelerated onto a phosphor screen, where they are converted to photons, at which point their positions and intensities are recorded by a CCD camera (the apparatus is described in more detail in section 3.2).

In VMI the excitation and ionisation wavelengths are fixed; ionisation to a cation vibrational level which has higher internal energy will produce slower photoelectrons, and conversely, ionisation to lower energy cation vibrational levels will produce faster photoelectrons. Photoelectrons with different velocities are focussed onto different positions on the detector but collected simultaneously giving rise to characteristic rings in the recorded image with photoelectron kinetic energy proportional to the square of the radius (example of images are shown in Figure 2-8 and Figure 2-9). The simultaneous collection means that an image (and therefore a spectrum, see section 2.4.1) can be collected in a few minutes; this is important as images need to be recorded at multiple time delays in experiments designed to follow time evolution.

Dynamic information on the molecule of interest is gained through monitoring the evolution of the photoelectron spectrum as a function of the time delay between the excitation and ionisation laser pulses, this evolution results from the changing character of the vibrational wavepacket in the S_1 electronic state. Figure 2-2

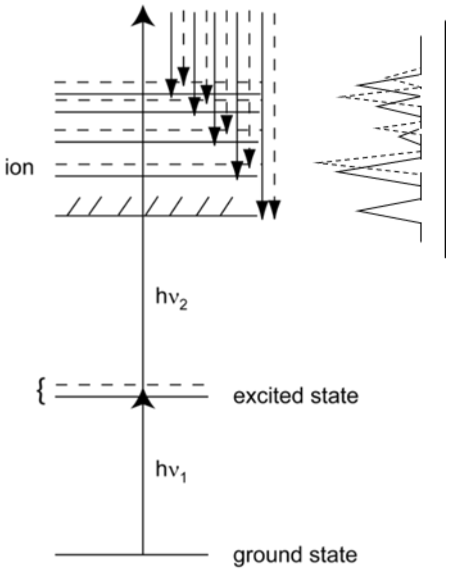

Figure 2-2: Schematic, taken from reference 2, demonstrating changes to the photoelectron spectrum when the probe pulse is delayed.

demonstrates the changes occurring with time delay.[2] When there is no delay between the excitation and ionisation pulses, aka t=0, a Franck-Condon projection of the initially excited vibrational state (bright state) onto the cation vibrational levels is shown in the photoelectron spectrum, in Figure 2-2 this process is represented by the solid lines. When the probe pulse is delayed by some time (depending on the eigenstate energy separation), if the S_1 vibrational state has changed, the Franck-Condon factors to the cation will be different and a different photoelectron spectrum will result. This is shown by the dashed lines. Quantitative information on the time-dependent behaviour such as lifetimes or eigenstate separations can be calculated through fits of the changing peak intensities.

The spatial (and therefore spectral) resolution of the VMI detection method can be a limitation in experiments using longer duration laser pulses, which have narrower linewidths, this includes the ~1 ps pulses which are employed herein.[3] The resolution of VMI depends on the accuracy (Δr) with which photoelectrons colliding at two different radial distances (r) on the detector can be distinguished.[3] This is dependent on a number of factors such as pixel size of the CCD camera, blurring caused by the MCP electron cascade, size of the image and number of pores in the MCP. In principle this means the resolution is constant across the detector. However, since photoelectron kinetic energy is proportional to the square of the radius, photoelectrons with different kinetic energies appear closer together as kinetic energy increases, leading to a deterioration in the spectral resolution. This means the energy resolution is much better for photoelectron peaks/rings closer to the centre of the image, which correspond to slow moving electrons, than for peaks/rings further from the centre, which correspond to faster moving electrons.

b) Slow electron velocity map imaging

As resolution deteriorates with increasing photoelectron kinetic energy, to improve resolution, longer wavelengths/lower energy photons would be required to generate slower photoelectrons, however, this would reduce the number of cation vibrational levels which can be accessed.

In the Slow Electron Velocity map Imaging or SEVI technique a series of spectra are collected using different probe wavelengths (same extraction voltages) and spliced together to produce the final SEVI spectrum. This process is described in section 2.4. This means shorter wavelengths can be used to access vibrational levels at higher cation internal energies without sacrificing peak resolution at lower internal energy. Figure 2-3 demonstrates this, shown are spectra that were recorded using 6 different probe wavelengths, each with a pump-probe time delay of 0ps, for the molecule *para*-fluorotoluene via the $13^1 1^1$ level.

In Figure 2-3 the photoelectron spectrum recorded with the shortest wavelength, 280.3 nm, shows the most photoelectron peaks because the shorter the wavelength allows more cation vibrational states to be accessed. On examination, it can also be seen that the peaks in this spectrum are very broad at low internal energy, whereas the spectra recorded using the longer wavelengths give progressively better resolved spectra at lower internal energies. Also shown in Figure 2-3 is the final spectrum, which is created by normalising the intensities of the different spectra and then splicing the spectra together.

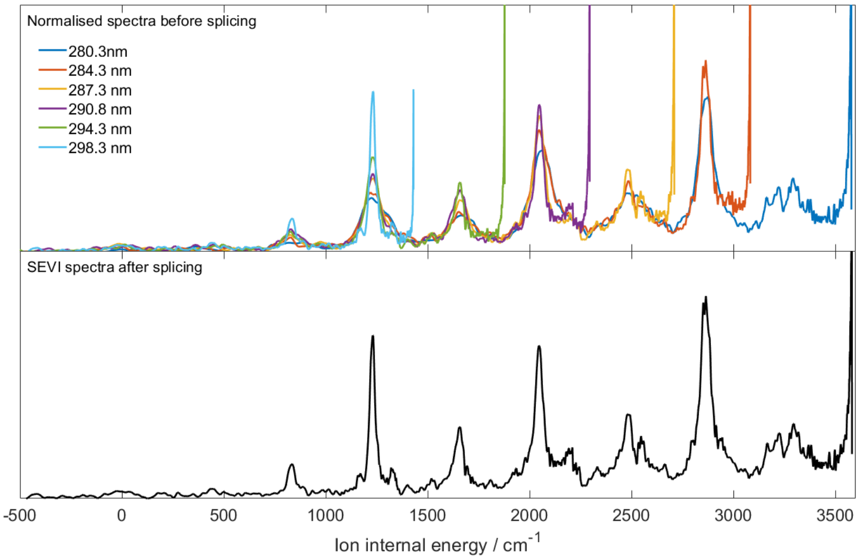

Figure 2-3: The top plot shows spectra taken at six wavelengths after the normalisation step and the bottom plot shows the final SEVI spectrum with more resolved peaks at lower wavenumbers which is produced by splicing together the six initial plots.

Unfortunately collecting spectra at multiple probe wavelengths increases the time taken to acquire data. For this reason, SEVI spectra are generally only collected for few significant time delays, such as to generate well-resolved photoelectron spectra characteristic of a bright state and a doorway state/dark state.

2.3. Experimental apparatus

2.3.1. Picosecond laser system and TOPAS

The picosecond laser system used for the time-resolved experiments consists of a regeneratively amplified Ti:sapphire seed laser (oscillator), two parallel single pass amplification stages (Coherent) and two optical parametric amplifiers (TOPAS, Light Conversion); these are described in more detail below and a schematic of the laser system is shown in Figure 2-4. The output of the system is two tuneable beams in the wavelength range 240 – 1140 nm with pulse durations of ~ 1 ps.

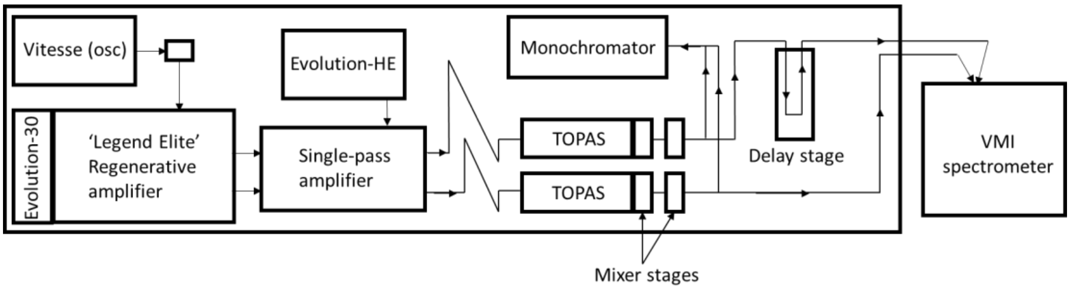

Figure 2-4: Schematic of the picosecond laser system.

The *Vitesse* seed laser is a mode-locked Ti:sapphire laser which is pumped by a *VERDI* diode laser and produces pulses of light at 800 nm with a duration of 100 fs and a repetition rate of 80 MHz. The *Vitesse* seed pulse then passes into the *Legend Elite* regenerative amplifier which works on the principle of chirped pulse amplification (CPA). The *Legend Elite* houses a pulse stretcher, mask and a Q-switched *Evolution-30* Nd:YLF laser which pumps the regenerative amplifier. First the pulse is stretched using a diffraction grating which disperses the different frequencies of the laser pulse so each wavelength travels a slightly different optical pathlength. This stretches the pulse to ~ 200 ps which serves to reduce the peak intensity, allowing for safe amplification without damage to other optical components. The beam also passes through a mask in this stage which blocks some of the extreme wavelengths dispersed by the diffraction grating to reduce the spectral bandwidth ensuring a pulse duration of ~ 1 ps, as required in these experiments, can be recovered in the compression step. The actual regenerative amplifier uses a Nd:YLF pumped Ti:sapphire crystal in a z-shaped resonant optical cavity. A single pulse is confined, by polarisation using Pockels cells, in the z-shaped cavity where it makes ~ 20 trips. The amplification occurs as the pulse passes through the crystal, and the multi-pass cavity allows for an amplification of greater than 10^6 before the pulse is ejected. The output from the regenerative amplifier is then passed through a beam splitter in order to create two beam paths.

In the single-pass amplifier (SPA) unit shown in Figure 2-5, there are two Ti:sapphire crystals, each pumped by an *Evolution-HE* Nd:YLF diode laser.[4] There is one crystal in each beam path, meaning each beam is then further amplified by passing through the Ti:sapphire crystal a single time. This single pass amplifier ensures sufficient power while maintaining beam quality. Finally, the pulses are then compressed, using gratings, to ~ 1 ps for both arms.

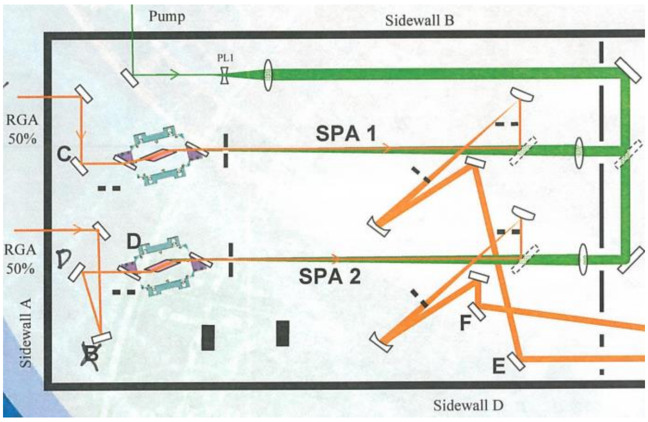

Figure 2-5: Taken from reference 4. Schematic showing the Single-pass amplifier stage.

Upon leaving the two SPAs there are two beams, both with a wavelength of 800 nm, a repetition rate of 1 kHz and powers of around 3 W. Each beam is then sent into an optical parametric amplifier or *TOPAS* (Light Conversion) which performs wavelength conversion in order to generate two UV beams which become the 'pump' or excitation beam and the 'probe' or ionisation beam. The operation of the TOPAS unit involves non-linear crystals which generate two IR photons in the range 1100-2950 nm, known as the signal and the idler, from the input 800 nm beam. The signal and idler then enter two mixer stages containing BBO crystals which are used to produce a range of wavelengths in the UV *via* sum frequency and higher harmonic generation. These interactions allow wavelengths in the range 240 – 1140 nm to be produced, the experiments in this thesis involved the use of wavelengths ~270-360 nm. The use of two TOPAS systems allows the wavelengths of the pump and probe beams to be tuned independently. The power of the pump and probe pulses were controlled using neutral density filters; the powers used for data collection were always chosen and optimised based on signal however, generally the pump was ~4 mW and the probe was ~35 mW.

Optics are set up which allow both beams to be aligned into the monochromator in order to obtain calibrated pump and probe wavelengths. At the time of these experiments the bandwidth of the pump laser was determined to be ~34 cm^{-1} at FWHM. Calibration of spectra is further discussed in section 2.4.

Finally, the probe laser is sent through a delay stage which consists of a retroreflector on a motorised delay stage which can be moved back and forth to vary the optical path length and delay the probe pulse relative to the pump pulse by up to 500 ps (corresponding to a path difference of 15 cm). At t=0 ps the pump and probe pulses are temporally overlapped (the delay stage position at which t=0 ps is determined based on signal), at negative time delays the probe pulse arrives before the pump pulse and at positive time delays the probe pulse arrives after the pump pulse.

Both beams are then focussed into the VMI spectrometer using a 1 m focussing lens in a co-propagating arrangement so that they intersect in the centre of the chamber. The beams are vertically polarised.

2.3.2. VMI spectrometer

Velocity map imaging (VMI) provides a means of determining the velocity distributions of the photoelectrons generated upon ionisation. An electrostatic lens, based on the design of Eppink and Parker[5], focuses photoelectrons with the same initial velocity onto the same point on the position sensitive detector (see later). This gives an image with a series of spherical rings; the outer ring corresponding to the fastest moving photoelectrons and the inner ring corresponding to the slowest photoelectrons.

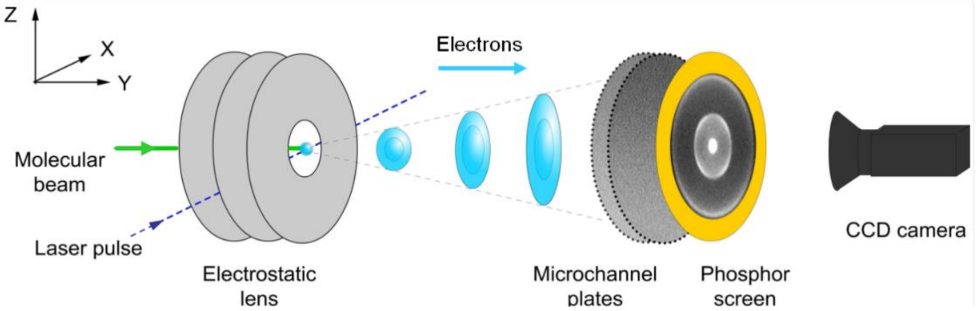

Figure 2-6: Schematic of the velocity map imaging (VMI) spectrometer

A schematic of the VMI spectrometer is shown in Figure 2-6. The electrostatic extractor lens is made up of three circular stainless-steel plates: the repeller plate, the extractor plate and the ground plate (0 V). The molecular beam intersects with the laser beams in between the extractor and repeller plates and each plate has a hole in the centre which allows the molecular beam to pass through. The extractor voltage is initially held at ~70% of the repeller voltage, by varying this voltage ratio whilst observing the image, the focus and shape of the image on the position sensitive detector can be optimised. The absolute values of the voltages determine the ‘size’ of the image on the detector and the voltages are chosen so that the outer ring in the image with the largest radius (resulting from the fastest electrons) is as large as possible while fitting completely on the detector. Negative voltages are used to extract the photoelectrons.

The detector consists of microchannel plates (MCPs) and a phosphor screen. The MCPs generate a cascade of electrons each time a single photoelectron impinges on them; the MCPs have a number of small channels meaning information of the position of the initial position is retained. When the cascade of electrons hits the phosphor screen it causes a spot on the phosphor screen to phosphoresce, allowing a 2D image of the 3D photoelectron velocity distribution to be captured by a CCD camera placed behind the phosphor screen.

To improve the signal to noise ratio, the detector is gated by stepping the voltage to the MCP only when the pulse valve fires (the pulse valve was operated at 40 Hz, see section 2.3.4); this results in higher voltage only being applied to the detector when the molecular beam is present. The detector then only amplifies photoelectrons produced from the gas pulse, and not background electrons produced from the laser entering the chamber.

The VMI spectrometer can also be set up to detect ions, this mode was used for measuring the REMPI spectroscopy shown in this thesis, by changing the voltages applied to the electrostatic lens and time-gate. Positive voltages are instead applied to the extractor and repeller plates to extract the ions and focus them towards the detector. Unless the ion fragments there will be no rings in the image, so the camera is left running and the integrated signal is recorded as a function of excitation laser wavelength.

2.3.3. Vacuum chamber

The vacuum chamber used in the VMI experiments consists of two parts. The VMI spectrometer described above is held in the second 'detection' chamber which is connected by a skimmer to the first 'source' chamber into which the sample is injected *via* the pulsed valve (described in section 2.2.4.). These two chambers are differentially pumped by diffusion pumps to maintain a high vacuum of around 9x10^{-6} mbar in the source chamber (when pulse valve operational) and 1x10^{-7} mbar in the detection chamber. This setup is shown in Figure 2-7.

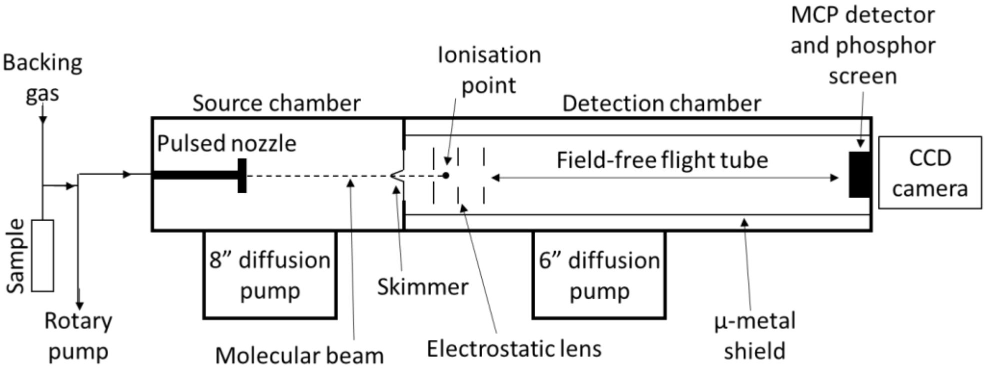

Figure 2-7: Schematic of the vacuum chamber in which the VMI spectrometer is mounted.

To ensure the photoelectrons generated are not subject to any external magnetic fields which would interfere with their trajectories, a double μ-metal shield surrounds the drift region.

2.3.4. Pulsed valve

The sample of interest is introduced into the source chamber through a pulsed valve (General Valve series 9) with an inert backing gas of helium (~2 bar,) producing a supersonic jet expansion which cools the molecules. The pulsed valve is controlled by a delay generator which synchronizes the valve opening with the laser pulse. The valve has a very small orifice (diameter ~0.5 mm), so the high pressure backing gas expands into the source chamber which is at a much lower pressure (10^{-7} mbar maintained by diffusion pumps) forming a supersonic jet expansion of He atoms seeded with sample molecules. The collisions that occur between the He atoms and the molecule of interest as they pass through the orifice and during expansion result in a directed gas flow with a narrow distribution of speeds and cools the internal degrees of freedom of the molecule.[1,6] The collision frequency reduces as the molecules move away from the nozzle enabling measurements to be made in a collision-free regime. The molecules studied are vibrationally and rotationally cold with a rotational temperature of around 10-20 K, this was determined by recording the S_1 origin peak with nanosecond pulses and using PGOPHER[7] to simulate the rotational width of the peak.

If the molecule of interest is not cooled in this way a greater number of rotational and low frequency vibrational levels would be populated. The resulting transitions from each of these levels may result in congested spectra and unresolved structure depending on the spectral resolution. Cooling the sample simplifies the spectrum because it reduces the number of initially populated states.

To keep pressure low the VMI chamber also contains a skimmer which only allows the coldest central region of the supersonic jet expansion through into the detector chamber, which forms a molecular beam, blocking the rest which is then pumped away. An Iota One General Valve controller (Parker Hannifin) is used to drive the nozzle at 40 Hz.

2.4. Data analysis

2.4.1. Producing the photoelectron spectra

To produce a spectrum of photoelectron counts *vs* ion internal energy from the images recorded using the CCD camera, several data analysis steps are required which are described in detail below.

a) Recovering photoelectron spectra from the velocity map images

Photoelectron spectra can be determined from the measured photoelectron images through the Abel inversion technique as implemented by the *Basex* program developed by the Reisler group.[8] This technique can be used because the distribution of photoelectrons produced is cylindrically symmetrical as a consequence of the vertical polarization of both the pump and probe lasers. This enables the reconstruction of the 3D velocity distribution of the photoelectrons from the recorded 2D image. *Basex* takes a slice through the 3D distribution and from this a spectrum showing photoelectron intensity versus radius from the image centre is plotted (see Fig. Figure 2-8).

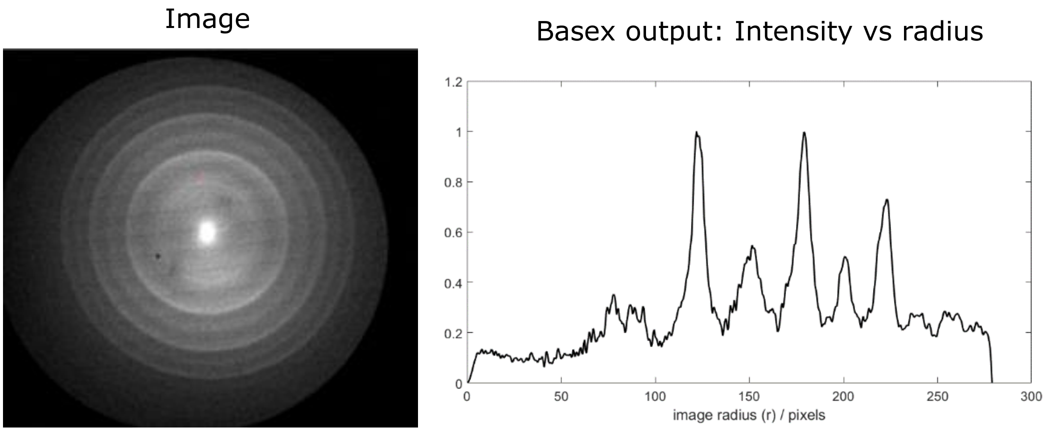

Image

Basex output: Intensity vs radius

Figure 2-8: Example of FITS image and resulting output spectrum from Basex

b) Distortion correction

Ideally a photoelectron image should have perfectly circular rings, however in practice the images may have a slight distortion caused by flaws in the electrostatic lens set up as seen in Figure 2-9. This distortion results in broader peaks in the photoelectron spectrum produced when the data reconstructed using *Basex*. The distortion in the images can be corrected computationally by stretching the images horizontally to the pixel aspect ratio which give spherical rings and the narrowest peaks, this is found through trial and error. An example of a corrected image is shown in Figure 2-9.

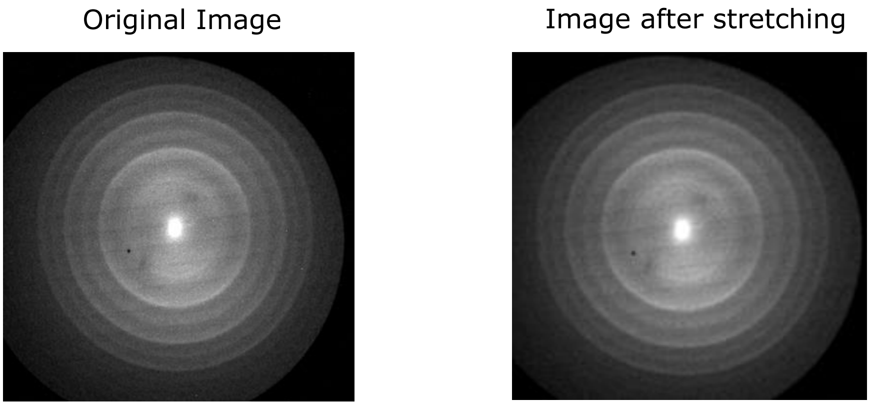

Original Image

Image after stretching

Figure 2-9: Example of the distorted image and corrected stretched image

c) Background subtraction

In tr-PES experiments the photoelectron spectrum of interest results from two-colour ionisation; excitation by the absorption of one photon from the pump laser followed by ionisation through absorption of a photon from the probe laser. However, ionisation can also occur via one-colour processes involving the absorption of multiple pump photons or probe photons, this signal needs to be subtracted out as it is not dependent on pump-probe time delay. To do this a 'background' is recorded at -10 ps, i.e. the probe pulse intersects the molecular beam 10 ps before the pump pulse; and this is subtracted from the image leaving only the two-colour pump-probe signal. The result of a background subtraction is shown in Figure 2-10.

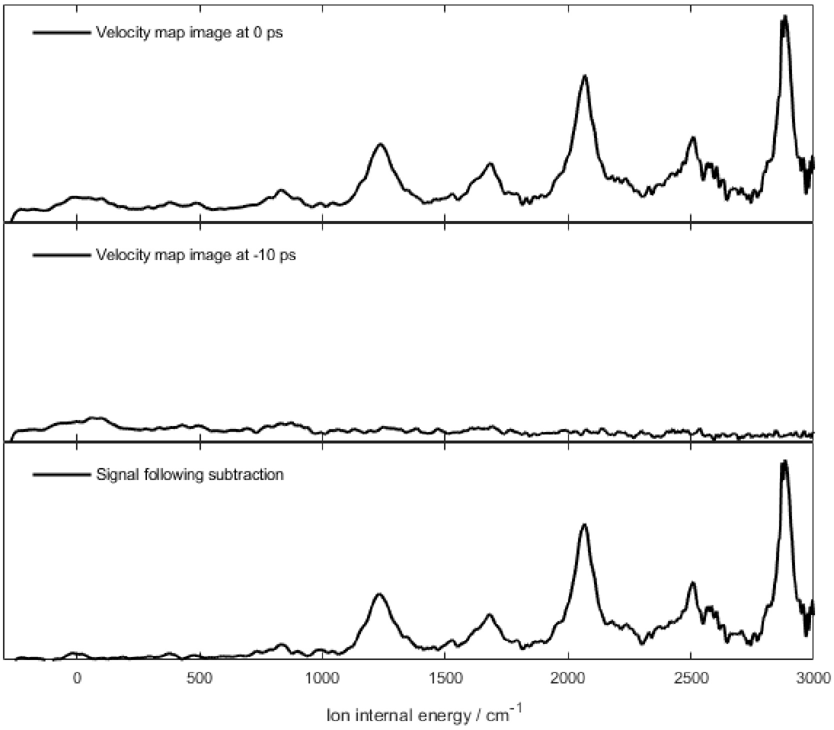

Figure 2-10: Example of a background subtraction. Recording an image at a pump-probe time delay of -10 ps provides a background.

d) Calibration

The output of *Basex* is a spectrum showing photoelectron intensity versus the radial distance, r, from the centre of the image in pixels. The square of the radius is related to the photoelectron kinetic energy by:

$$eKE = Kr^2 \qquad \text{Equation 2.1}$$

where *K* is a calibration constant that depends on the voltages applied to the extractor and repeller plates and eKE is the photoelectron kinetic energy. A plot of photoelectron intensity vs photoelectron kinetic energy therefore requires knowledge of the value of K. In this thesis photoelectron spectra are generally plotted as a function of ion internal energy. This can be determined through knowledge of the photon energies, the ionization potential and the photoelectron kinetic energy:

$$h\nu_{pump} + h\nu_{probe} = eKE + IP + E_{int} \qquad \text{Equation 2.2}$$

$$K = \frac{h\nu_{pump} + h\nu_{probe} - IP - E_{int}}{r^2} \qquad \text{Equation 2.3}$$

Equation 2.3 can be used to calculate the calibration constant K by either using a photoelectron peak for which E_{int} is already known, e.g. an origin peak at 0 cm^{-1} which would correspond to the peak at the largest radius, or by using a series of probe wavelengths and plotting $h\nu_{probe}$ against r^2 to give a straight line with gradient K. It is important to assign key fundamental peaks and compare to energies in literature or calculations to ensure the correct ion internal energy scale. The photoelectron intensity values must then be divided by r to maintain the correct peak areas on a scale that is proportional to r^2.

2.4.2. Producing SEVI spectra from photoelectron spectra

In order to produce the SEVI spectrum from the individual photoelectron spectra measured with different probe wavelengths it is important to ensure the photoelectron peaks in individual spectra are aligned in ion internal energy, then match the intensities of the individual spectra. This is achieved by normalising the individual spectra using the integral of a photoelectron peak, determined using the trapezium rule, which is observed in each spectrum; for example the ion origin peak. Following normalisation, the spectra can be spliced together at points in the baseline where no features exist, see Figure 2-3. It is important in this step not to introduce or exclude a feature in the spectrum. Details of the SEVI spectra included in this thesis are included in the appendix.

2.4.3. Assignment of spectra.

In molecules which have similar geometries in the S_1 and D_0^+ electronic states, an intense peak originating from the Δv=0 transition from S_1 to the ion is expected in the photoelectron and SEVI spectra along with a number peaks originating from

Franck-Condon allowed transitions from S_1. Importantly this "$\Delta v=0$ propensity rule" can aid assignment of the vibrational levels because the experimental cation and S_1 vibrational wavenumbers can be compared to calculated wavenumbers and those from literature. This propensity rule is used throughout the studies reported in this thesis to aid assignment of the S_1 vibrations excited.

When referring to S_1 vibrational levels, if a subscript is not shown in the label the transition results from the S_0 vibrational ground state. When referring to cation vibrational levels, unless stated otherwise, the transition results from the specified vibrational level in the S_1 electronic state. These conventions apply in the following chapters.

2.4.4. Extracting IVR lifetimes and oscillation periods.

From the time-resolved photoelectron spectra it is possible to extract the IVR lifetimes and oscillation periods which provide information on couplings. The steps required to get this information are outlined below. The intensity of each photoelectron peak must first be measured at each time delay by calculating the integral of the feature. In some cases there may be a lot of intensity in the baseline underneath the peak and/or the intensity in the baseline may increase with increasing time delay due to increasing population of bath states. In this situation it is then necessary to subtract this signal when measuring the intensity of the peak originating from the bright state; it will be noted in the following chapters when this has been done. Additionally, the peak integrals used in the time profiles in the following chapters are in fact an average of two integrals determined using two cation internal energy ranges: at the base of the peak and at close to the full width at half maximum of the peak. Error bars have been estimated based on the difference of these integrals, meaning they will be somewhat conservative especially for broad peaks, these are not included in the curve fitting procedure.

Next, the integrated intensity of each peak in the photoelectron spectrum must be plotted as a function of time delay. If the peak intensities show sustained or recurring changes with time, they are fit to a relevant expression which depends on the type of behaviour shown. If quantum beats are observed, indicative of restrictive IVR, then equation 2.4 is used:

$$A + Be^{\frac{-t}{\tau_1}} \cos \frac{2\pi t}{\tau_{osc}} \qquad \text{Equation 2.4}$$

If the intensity shows exponential decay, which could occur under a dissipative regime, in which coupling to numerous bath states occurs, then equation 2.5 is used:

$$A + Be^{\frac{-t}{\tau_1}}$$

Equation 2.5

If intermediate type energy dispersal occurs whereby the photoelectron peaks show oscillations in intensity superimposed upon an exponential decay then equation 2.6 is used in the fitting:

$$A + Be^{\frac{-t}{\tau_1}} + Ce^{\frac{-t}{\tau_2}} \cos \frac{2\pi t}{\tau_{osc}}$$

Equation 2.6

In instances in which increasing congestion is observed in photoelectron spectra as a result of the increasing population of bath states in S_1; time profiles are fit to equation 2.7:

$$A + B(1 - e^{\frac{-x}{\tau_1}})$$

Equation 2.7

In some occasions not all the data points will be included in the fits; for example data points at later time delays may be excluded if the peaks lose all their initial intensity quickly and are no longer visible. This is because any variation in intensity after the peak has decayed will just be changes baseline noise.

2.5. References

---

[1] A. M Ellis, M. Feher and T. G. Wright, *Electronic and Photoelectron spectroscopy Fundamentals and Case Studies* (Cambridge University Press, Cambridge, 2005).

[2] Professor Katharine Reid

[3] C. J. Hammond and K. L. Reid, *Phys. Chem. Chem. Phys.*, 2008, **10**, 6762–6769

[4] Laser manual, Coherent

[5] A. T. J. B. Eppink and D. H. Parker, *Rev. Sci. Instrum.*, 1997, **68**, 3477-3484

[6] J. M. Hollas, *Modern Spectroscopy*, (John Wiley and Sons Ltd., Chichester, England, 2004)

[7] PGOPHER, A Program for Simulating Rotational, Vibrational and Electronic Spectra, C. M. Western, *Journal of Quantitative Spectroscopy and Radiative Transfer*, **186** 221-242 (2016).

[8] V. Dribinski, A. Ossadtchi, V. A. Mandelshtam, and H. Reisler, *Rev. Sci. Instrum.*, 2002, **73**, 2634-2642

3. Investigation of the low wavenumber vibrations in the S_1 electronic state of aniline

3.1. Chapter overview

In this chapter the $S_1 \leftarrow S_0$ Resonance-Enhanced Multiphoton Ionisation (REMPI) spectrum of aniline (structure shown in Figure 3-1) is discussed alongside Slow-Electron Velocity Map Imaging (SEVI) spectra and time-resolved photoelectron spectra that have been measured following the excitation of REMPI features below S_1 0^0 + ~1100 cm^{-1}.

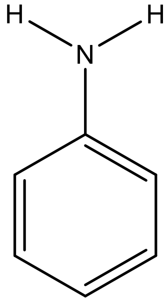

Figure 3-1: Structure of aniline.

3.2. The region of interest

The two-colour $S_1 \leftarrow S_0$ REMPI spectrum of aniline is shown in Figure 3-2; a relative S_1 internal energy scale is shown with the S_1 vibrationless origin at 0 cm^{-1}. All S_1 wavenumbers reported in this chapter (and throughout this thesis) will be relative the vibrationless origin. The focus of this chapter is the three broad REMPI features with S_1 wavenumbers of ~490 cm^{-1}, ~800 cm^{-1} and ~950 cm^{-1}. SEVI spectra at 0 ps were measured at selected wavenumbers across these three broad REMPI features and *via* the S_1 vibrationless origin; these will be discussed in the following subsections. Time-resolved spectra were measured at the four wavenumber positions indicated on Figure 3-2. The discussion of assignments and time-dependent behaviour have been divided into two subcategories according to whether the vibrational levels excited exhibited no time-dependent behaviour (including spectra recorded *via* the origin) or quantum beats indicative of restrictive IVR.

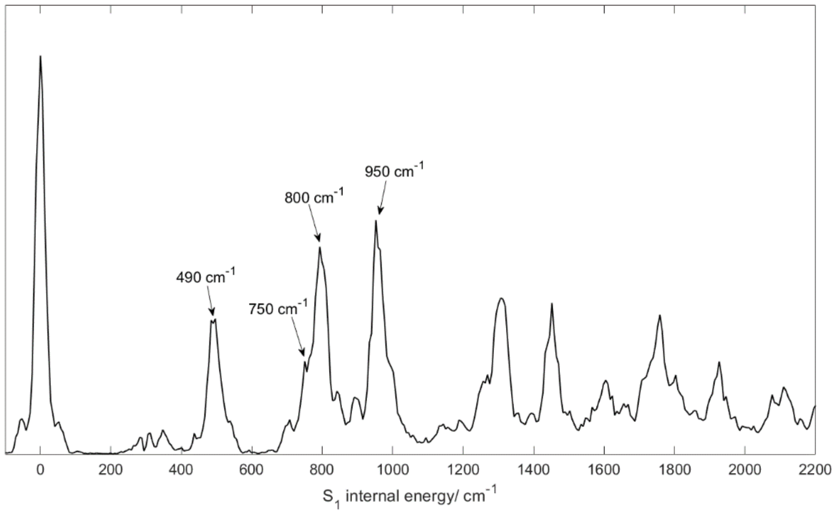

Figure 3-2: REMPI spectrum showing the first 2200 cm^{-1} *above the* S_1 *origin in aniline. Experimental wavenumbers rounded to nearest 10 cm*$^{-1}$.

3.3. Calculated vibrational wavenumbers

Assignment of peaks observed in the photoelectron and REMPI spectra to vibrational levels have been aided by comparison to calculated vibrational wavenumbers which are shown in Table 3-1. The calculations were performed with the assistance of Dr Adrian Gardner. The vibrational wavenumbers listed in Table 3-1 were calculated using the GAUSSIAN09 programme[1] and the calculated normal modes were assigned labels in the Varsányi notation. Density functional theory (DFT) was employed for the S_0 and D_0^+ states, with time-dependent density functional theory (TD-DFT) employed for the S_1 state. The calculations used the ωB97-xD functional and the aug-cc-pVTZ basis set which have been found to work well in similar molecules. A scaling factor of 0.97 was applied to the calculated vibrational wavenumbers. Calculated normal mode diagrams of these vibrations are shown in figure 8.17 and figure 8.18 in the appendix.

It is generally agreed in the literature that aniline in its ground electronic state is non-planar,[2,3,4,5] and that the aniline cation in its ground electronic state is planar.[6,7,8,9,10] There is some disagreement over the geometry of aniline in its S_1 electronic state, with some studies suggesting the S_1 excited state is essentially planar or quasi-planar, while others suggest the molecule is bent. [2,3,4,6,7,8,9,10,11,12,13,14,15,16,17] The disparity was highlighted by Stavros and co-workers, their calculations indicated that the S_1 electronic state was not planar; however, they noted that their calculations do not take the energy barrier to inversion into account.[18] These authors suggested that if the barrier was small ”a time averaged quasi-planar structure” could be experimentally observed.[18] The calculations conducted in the present work predict a planar equilibrium geometry in both the S_1 electronic state and cation ground state, meaning that aniline can be treated as having C_{2v} symmetry. In Table 3-1, the vibrations are classified according to symmetry then ordered by decreasing calculated wavenumber.

Where available, experimental fundamental vibrational wavenumbers are shown in Table 3-1 alongside the calculated wavenumbers. In these cases there is generally good agreement between calculated and experimental wavenumbers. Therefore, when experimental wavenumbers are unavailable assignments are made according to calculated wavenumbers alone. Two notable exceptions to this are (a) the wavenumber of the 16a vibration in S_1 (calculated value 149 cm^{-1} and experimental value 177 cm^{-1}), and (b) the wavenumber of the 15 vibration in the ion (calculated value 385 cm^{-1} and experimental value ~550 cm^{-1}). In the latter case the experimentally determined wavenumber was based on the assignment of a photoelectron peak to 15^2.[6,17] There is some disagreement in literature so it is possible this peak may have been incorrectly assigned; this is briefly discussed in section 3.5.1. In previous studies it has been noted that when levels of theory similar to those adopted here are used the wavenumbers calculated for vibrations of a_2 and b_1 symmetry in S_1 are less reliable than those of a_1 or b_2 symmetry.[19,20] The discrepancy in the calculated wavenumber of 16a has been highlighted, however, in Table 3-1 it can be seen that the two vibrations of b_1 symmetry for which experimental wavenumbers are known within the S_1 electronic state are in good agreement with the calculated wavenumbers.

The assignment of the 8/9 and 18/19 mode pair labels in Table 3-1 were made according to the work of Gardner and Wright who highlighted inconsistencies in the previous labelling of benzene modes, which would also impact work involving substituted benzenes.[21,22] Through comparison of their calculated normal modes to those given by Varsányi[23] and Herzberg[24], Gardner and Wright assigned the Mulliken modes 13 and 14 to the Wilson/Varsányi modes 19 and 18 and the Mulliken modes 16 and 17 to the Wilson/Varsányi modes 8 and 9 respectively. However, they found the corresponding calculated vibrational wavenumbers were reversed for each mode pair with respect to those given by Herzberg. To correct for this the associated wavenumbers of modes i) 8 and 9 and ii) 18 and 19 need to be reversed in work which uses the Wilson/Varsányi mode labels.

	S_1		D_0^+	
Varsányi	Calc	Expt.	Calc	Expt.
a_1				
D	3514		3468	
20a	3142		3143	
2	3112		3126	
7a	3096		3115	
C	1610		1643	
9a/8a	1519		1607	1593^{a}/1594^{h}/1581^{d}
18a/19a	1453	1434^{b}/1437^{f}	1496	1436^{d}
13	1316	1311^{b}/ 1308^{g}/1309^{f}	1378	1388^{a}/1385^{h}/1347^{d}
8a/9a	1132		1184	1187^{a}/1188^{h}/1170^{d}
19a/18a	988		991	993^{a}/996^{h}
12	965	956^{a}/955^{b}/954^{c}	972	983^{a}/ 976^{d}
1	808	800^{a}/$798^{b/c}$	810	807^{a} 798^{d}
6a	506	$492^{a/b/c/f}$	519	521^{a}/ 516^{d}
a_2				
17a	559		987	
10a	625		802	
A	274		568	577^{h}
16a	149	177^{a}/188^{f}	353	355^{a}/347^{d}/356^{h}
b_1				
5	875		997	
17b	687		927	963^{h} (tentative)
11	636		785	790^{h}
4	544		620	629^{h}
16b	382	387^{e}	441	445^{h}
I	313	335^{a}/352^{b}	630	656^{a}/ 645^{d}/658^{h}
10b	184	174^{a}/177^{e}/179^{h}	176	177^{a}/179^{h}
b_2				
E	3639		3582	
7b	3134		3138	
20b	3106		3116	
8b/9b	1444		1526	
19b/18b	1406		1449	
3	1356		1352	
9b/8b	1304		1340	
14	1132		1157	
18b/19b	1037		1108	
B	951		1009	
6b	526		579	582^{h}
15	378	381^{a}/351^{b}/352^{c}/ 350^{e}	385	551^{a}/373^{c}/549^{h}

Table 3-1: Calculated and experimental vibrational wavenumbers (cm^{-1}) for the S_1 and D_0^+ electronic states of aniline. Calculated values scaled by 0.97. a) Ref 6, b) Ref 13, c) Ref 8, d) Ref 7, e) Ref 16, f) Ref 2, g) Ref 3, h) Ref 17. Vibrational labels 4 and 16b from Ref 17 are switched due to better agreement with calculated wavenumbers.

3.4. S_1 vibrational levels exhibiting no time-dependent behaviour

As only a few S_1 vibrational levels have low wavenumbers, many of those observed are relatively isolated in energy and have little opportunity for coupling. Therefore, it is not unexpected that many of the low energy vibrational levels do not show any time-dependence. Alongside the S_1 origin, this subsection includes photoelectron spectra measured following excitation of the two REMPI features at ~490 cm^{-1} and 950 cm^{-1} in the S_1 electronic state. Despite the fact that no time-dependence was observed at these S_1 positions, the S_1 vibrational modes assigned in this section are observed as combination levels at higher wavenumbers (see chapter 4 and 5) and experimental vibrational wavenumbers can be determined for the cation vibrational levels, making their study pertinent to this thesis.

3.4.1. Photoelectron spectra *via* the S_1 origin 0^0

The 0 ps SEVI spectrum measured *via* the S_1 origin level is shown in Figure 3-3. The most intense SEVI peak is at 0 cm^{-1}, this is the vibrationless origin level, 0^0, in the cation which is consistent with the $\Delta v = 0$ propensity rule and implies that the ion and excited state neutral geometries are similar.[7]

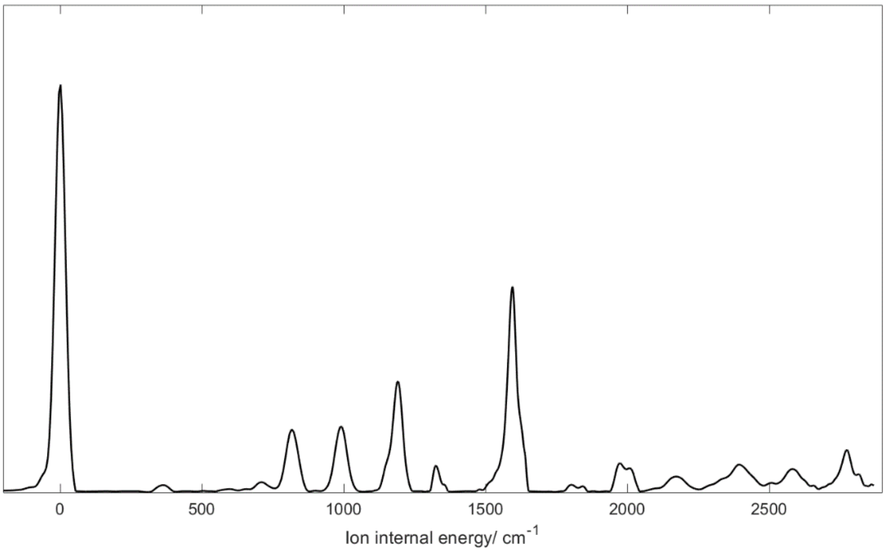

Figure 3-3: 0 ps SEVI spectrum measured via the S_1 origin 0^0.

Four other relatively intense SEVI peaks lie below ~1800 cm^{-1} in the spectrum, these are all assigned to a_1 fundamental vibrations through comparison to calculated wavenumbers and/or experimentally derived wavenumbers from literature, these are shown in Table 3-2.

Ion internal energy / cm^{-1}	Cation vibrational level assignment	Predicted wavenumber of cation vibrational level/ cm^{-1}
0	0^0 ($\Delta v=0$)	0
810	1^1	807^a, 810^b,
990	12^1	983^a, 972^b
1190	$8a^1$	1187^a, 1184^b
1590	$9a^1$ 1^2	1593^a, 1607^b 1614^a, 1620^b
1990	12^2 $1^1 8a^1$	1966^a, 1944^b, 1959^d $1994^{a,b}$, 1968^c, 2001^d
2170	$8a^1 12^1$	2170^a, 2156^b
2400	$1^1 9a^1$ $6a^2 13^1$ 1^3	2400^a, 2417^b 2430^a, 2416^b 2421^a, 2430^b
2580	$9a^1 19a^1$ $9a^1 12^1$ $1^2 12^1$ $8a^1 13^1$	2586^a, 2598^b 2576^a, 2579^b 2597^a, 2592^b 2575^a, 2562^b
2770	$1^1 12^2$ $8a^1 9a^1$ $1^2 8a^1$	2773^a, 2754^b 2780^a, 2791^b 2801^a, 2804^b

Table 3-2: Vibrational level assignments for peaks in the SEVI spectrum and their predicted wavenumbers based on fundamental wavenumbers from a) Ref 6, b) calculations (Table 3-1) and wavenumbers from c) Ref 7, d) Ref 17. Experimental wavenumbers rounded to nearest 10 cm^{-1}.

The photoelectron peaks that lie above ~2000 cm^{-1} in the SEVI spectrum are quite weak but very broad, suggesting they could be the result of several unresolved ion states. Several vibrations have predicted wavenumbers in good agreement to the wavenumbers of these peaks and these are all included in Table 3-2. Notably, all the potential assignments are combinations or overtones of a_1 fundamentals, many involving the vibrations 1, 12, 8a and 9a which were observed at low energies; progressions in these vibrations are therefore expected in the photoelectron spectra measured *via* other intermediate vibrational levels. Vibrations involving the inversion of the NH_2 group have not been observed in the SEVI spectrum, such inactivity of this mode is evident of a similar geometry of this substituent group in both the S_1 and D_0^+ electronic states, consistent with the planar structure obtained from the calculations outlined in section 3.3.

3.4.2. Photoelectron spectra *via* S_1 0^0 + ~490 cm^{-1}

3.4.2.1. Assignment of vibrational levels

Figure 3-4 shows the 0 ps SEVI spectrum measured *via* 490 cm^{-1} in the S_1 electronic state, this is the next major peak in the REMPI spectrum (Figure 3-2).

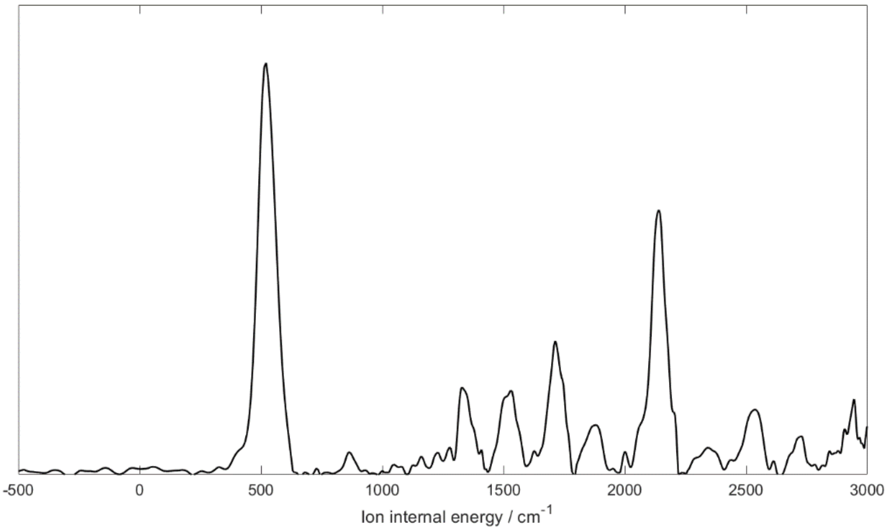

Figure 3-4: 0 ps SEVI spectrum measured via ~490 cm^{-1} in S_1.

The most intense peak in the SEVI spectrum is at ~520 cm^{-1}, similar to the S_1 wavenumber excited. Based on the intensity, this peak is attributed to the $\Delta v=0$ transition between S_1 and the ion. These experimental vibrational wavenumbers are in very good agreement to the predicted wavenumbers of the 6a fundamental vibration in the S_1 and ion states which are 492 cm^{-1} and 521 cm^{-1} respectively.[6] Therefore an assignment of $6a^1$ is concluded, this level has previously been assigned in the literature.[3,6,7,13,17]

In Table 3-3 vibrational level assignments are suggested for the other main peaks which are observed above ~1000 cm^{-1} in the SEVI spectrum in Figure 3-4. All assignments are to totally symmetric fundamental, combination or overtone levels, many involving $6a^1$ as expected. Based on their observed peak wavenumber, some SEVI peaks have multiple possible assignments; given the broadness of some of the SEVI peaks there is the possibility of unresolved vibrational levels. Notably combination bands involving modes 1, 12, 8a and 9a with the 6a vibration are observed, as predicted based on the activity observed in the SEVI spectrum resulting from initial excitation of the S_1 vibrationless origin. The non-observance of a SEVI peak at 0 cm^{-1} which is assignable to the vibrationless origin is consistent with the fact the SEVI spectrum measured at the S_1 origin level (Figure 3-3) does not show an ion peak assignable to level $6a^1$.

Ion internal energy / cm^{-1}	Cation vibrational level	Predicted wavenumber of cation vibrational level/ cm^{-1}
520	$6a^1$ ($\Delta v=0$)	519[a], 521[b]
1330	1^16a^1	1329[a], 1328[b], 1314[c], 1335[d]
1520	$6a^112^1$ $6a^119a^1$	1491[a], 1504[b] 1510[a], 1514[b]
1710	$6a^18a^1$	1703[a], 1708[b,] 1711[d]
1880	$6a^113^1$ 1^16a^2	1897[a], 1909[b/d], 1863[c] 1848[a], 1849[b], 1856[d]
2140	1^26a^1 $6a^19a^1$	2139[a], 2135[b], 2112[c], 2147[d] 2126[a], 2114[b]
2530	$1^16a^18a^1$ $6a^119a^2$ $6a^218a^1$	2513[a], 2515[b] 2501[a], 2507[b] 2534[a], 2468[c]
2940	12^219a^1 $1^16a^19a^1$ $6a^313^1$ 1^36a^1	2935[a], 2959[b] 2936[a], 2921[b] 2935[a], 2951[b] 2949[a], 2942[b]

Table 3-3: Vibrational level assignments for peaks observed in the SEVI spectrum alongside the predicted wavenumbers based on fundamental wavenumbers from a) calculations (Table 3-1), b) Ref 6, c) Ref 7 and wavenumbers from d) Ref 17. Experimental wavenumbers rounded to nearest 10 cm^{-1}.

3.4.2.2. Time-resolved photoelectron spectra

Photoelectron spectra were measured *via* ~490 cm^{-1} in S_1 at multiple time delays between 0 ps and 500 ps to investigate any time-dependence; several of these spectra are shown in Figure 3-5 and the three most intense peaks are labelled A,

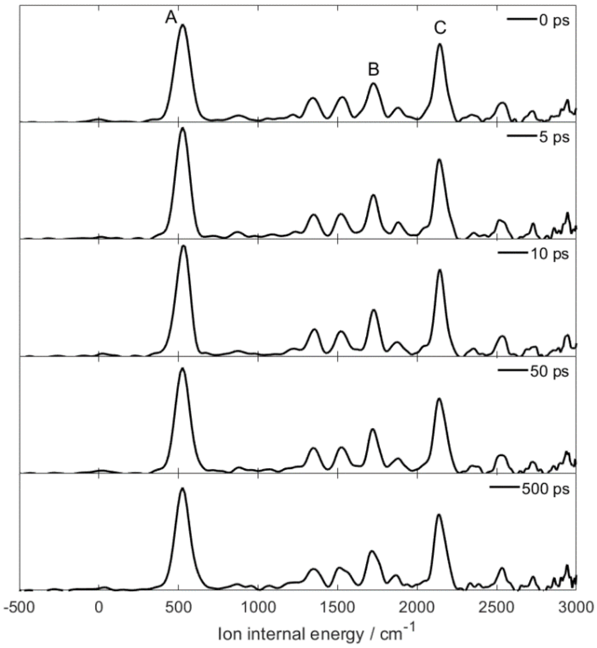

Figure 3-5: Photoelectron spectra measured via ~490 cm^{-1} in S_1 at time delays of 0 ps, 5 ps, 10 ps, 50 ps and 500 ps.

B and C. Inspection reveals that the peaks at 0 ps, including A which results from the Δv=0 transition from S_1, are still observed by 500ps with the spectra remaining well-resolved. This suggests that the bright state is still populated at 500 ps.

In Figure 3-6 are the time profiles showing the intensity of photoelectron peaks A-C as a function of time delay. For each peak there are some very weak irregular fluctuations in intensity within error bars but, on average the intensity of the peaks do not change with increasing time delay. The lack of recurring oscillations or sustained changes in peak intensity outside the experimental error indicates that there is no restrictive energy redistribution which in turn suggests that the $6a^1$ is not coupled to another vibrational level in S_1.

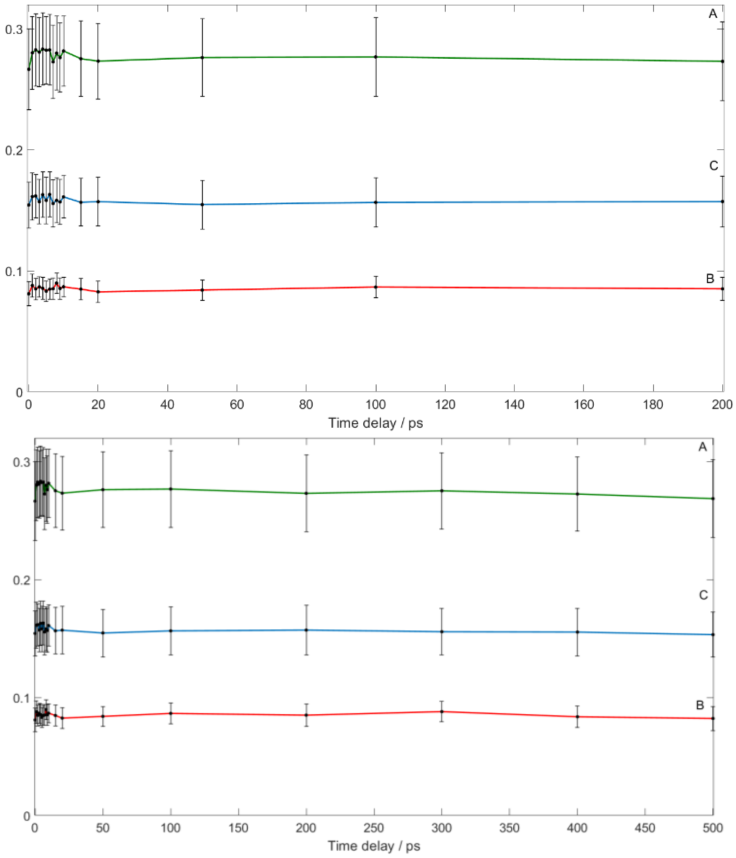

Figure 3-6: Time-dependent intensity of photoelectron peaks A, B, C. Top: 0 ps - 200 ps. Bottom: 0 ps - 500 ps. Labels correspond to peak measured.

Figure 3-7 shows the S_1 REMPI spectrum recorded using picosecond laser pulses (black line) alongside a higher resolution 1 + 1 REMPI spectrum (red line) recorded using nanosecond laser pulses. The smaller bandwidth of the nanosecond laser permits better resolution of close lying vibrational levels in the S_1 electronic state.

Comparison of the nanosecond and picosecond REMPI spectra reveals that, other than a very weak higher wavenumber band, no other intense peaks lie close in wavenumber to the S_1 6a^1 absorption band. Given the lack of close lying vibrational levels in S_1, the lack of time-dependence observed in this study is expected.

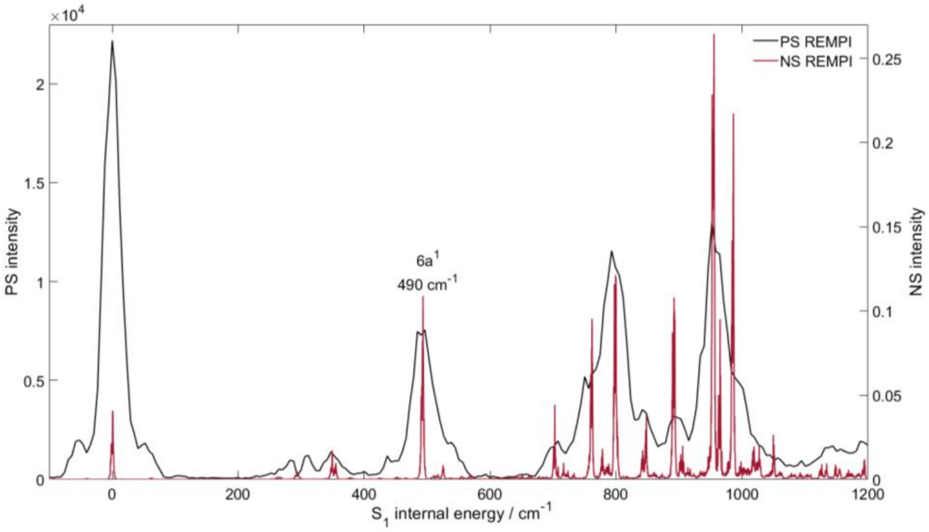

Figure 3-7: REMPI spectra recorded using nanosecond (red) and picosecond (black) pulses. The peak assigned to vibrational level 6a^1 is labelled.

3.4.3. Photoelectron spectra *via* S_1 0^0 + ~950 cm^{-1}

3.4.3.1. Assignment of vibrational levels

Figure 3-8 shows the 0 ps SEVI spectrum measured *via* ~950 cm^{-1} in S_1, this is the fourth major peak in the REMPI spectrum in Figure 3-2. The SEVI peak at ~980 cm^{-1} is more than double the intensity of the other peaks so according to the propensity rule, this peak is assigned to the $\Delta v=0$ transition from S_1.

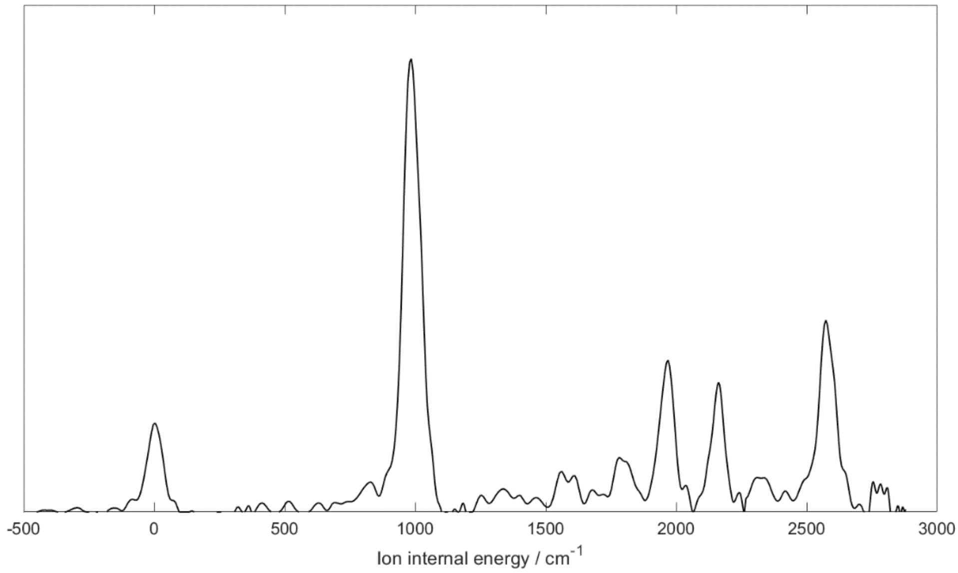

Figure 3-8: 0 ps SEVI spectrum measured via ~950 cm^{-1} in S_1.

Vibrational level 12^1 has predicted S_1 and ion state wavenumbers of 956 cm^{-1} and 983 cm^{-1} respectively (Table 3-1), in good agreement to the experimental vibrational wavenumbers determined from the REMPI and SEVI spectra. Additionally, this level has been assigned in literature.[6,7,17] So it is concluded that the S_1 12^1 vibration has been prepared.

Table 3-4 shows vibrational level assignments for the other intense peaks in the SEVI spectrum in Figure 3-8. All assignments are to vibrational levels with overall a_1 symmetry and combination levels involving modes 1, 12, 8a, 9a with the initially prepared vibration, v_{12}; the peak at ~1970 cm^{-1} can be assigned to the overtone, 12^2. An origin peak is observed, which is consistent with the fact that the 12^1 ion state is observed in the SEVI spectrum measured following excitation of the S_1 vibrationless origin (Figure 3-3).

Ion internal energy / cm^{-1}	Cation vibrational level	Predicted wavenumber of cation vibrational level/ cm^{-1}
0	0^0	0
980	12^1 (Δv=0)	972[a], 983[b]
1790	$1^1 12^1$	1782[a], 1790[b], 1793[c]
1970	12^2	1944[a], 1966[b], 1959[c]
2160	$8a^1 12^1$	2156[a], 2170[b], 2165[c]
2580	$9a^1 12^1$ $1^2 12^1$	2579[a], 2576[b] 2592[a], 2597[b]

Table 3-4: Vibrational level assignments for the peaks in the SEVI spectrum alongside the predicted wavenumbers of the vibrational levels based on fundamental wavenumber from a) calculations, b) Ref 6 and wavenumbers from c) Ref 17. Experimental wavenumbers rounded to nearest 10 cm^{-1}.

3.4.3.2. Time-resolved photoelectron spectra

Photoelectron spectra were measured at multiple time delays between 0 ps and 100 ps with several of these shown in Figure 3-10. There does not appear to be a change in the relative intensity of any of the peaks with increasing time delay and the spectra also remain well resolved up to 100 ps. This suggests no energy dispersal from the bright state on the timescale of the experiment and therefore no coupling between the 12^1 vibration and other vibrational levels in S_1. To confirm this hypothesis, the intensity of the origin peak A and the two most intense photoelectron peaks B and C are plotted as a function of time delay in Figure 3-9.

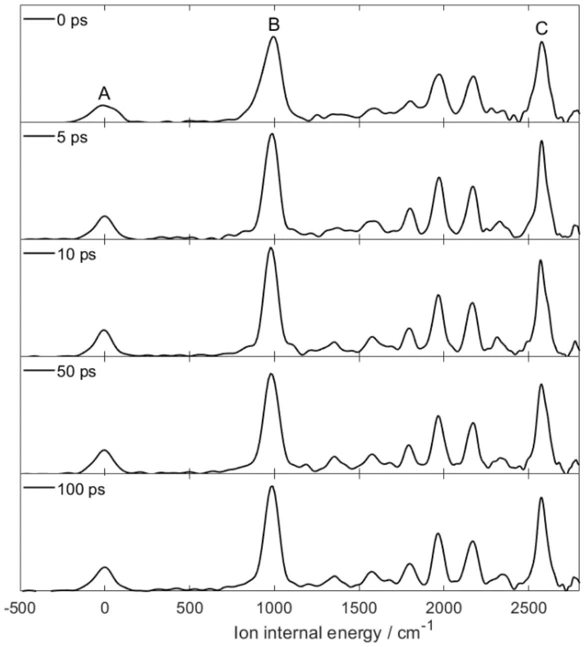

Figure 3-10: Photoelectron spectra measured via ~950 cm^{-1} in S_1 at time delays of 0 ps, 5 ps, 10 ps, 50 ps and 100 ps.

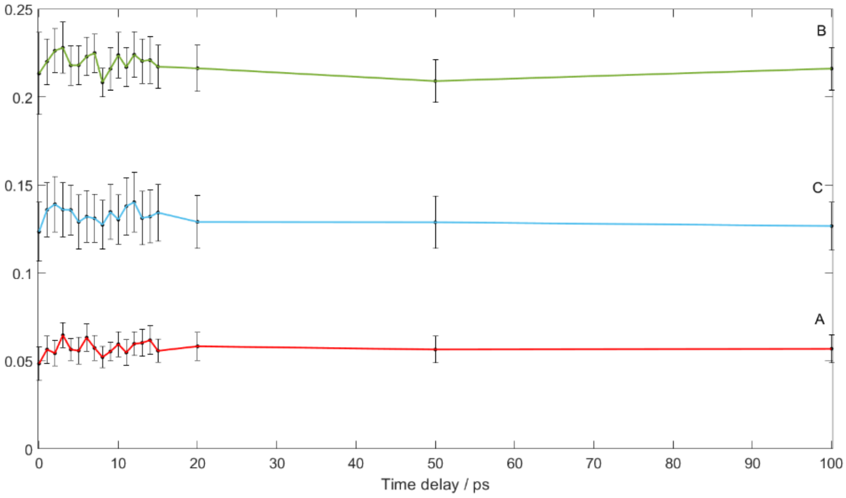

Figure 3-9: Time profiles showing the time-dependent intensity of photoelectron peaks A, B, C in Figure 3-10. Labels correspond to the photoelectron peak measured.

As expected, the time profiles in Figure 3-9 do not show any sustained changes or recurring oscillations in intensity outside the experimental error for any of the three photoelectron peaks A-C. The non-observance of any time-dependent behaviour means there is no evidence of the 12^1 vibration coupling.

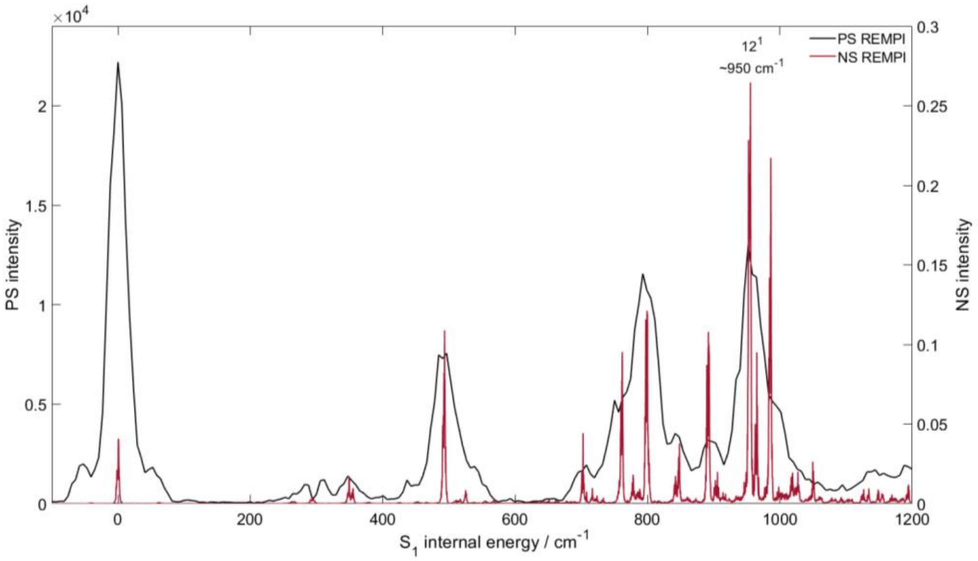

Figure 3-11: REMPI spectra recorded using nanosecond (red) and picosecond (black) pulses. The peak corresponding to vibrational level 12^1 is labelled.

Figure 3-11 shows S_1 REMPI spectra recorded using both nanosecond (red line, 1 + 1 REMPI spectrum) and picosecond (black line) pulses. Unlike level S_1 $6a^1$ at ~490 cm^{-1} which is isolated in wavenumber, Figure 3-11 shows multiple vibrational levels relatively close in wavenumber to the S_1 12^1 vibration. These levels are not resolved in the picosecond REMPI spectrum so only a broad feature is observed. As there appears to be opportunity for level S_1 12^1 to couple, it is curious that no time dependent behaviour was observed during the experiment. To investigate, photoelectron spectra (at delays of 0 ps) were measured while stepping the pump laser over the broad S_1 REMPI feature at ~950 cm^{-1}. The intermediate S_1 wavenumber positions excited are indicated in Figure 3-12 by dotted lines.

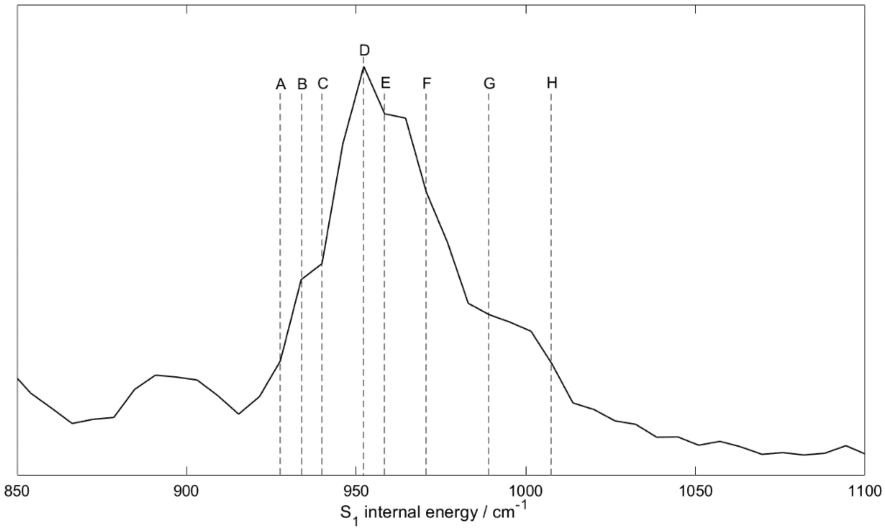

Figure 3-12: Expanded region of the S_1 REMPI spectrum in Figure 3-2, dotted lines A-H indicate the intermediate wavenumbers excited by the pump laser.

Figure 3-13 shows the resulting photoelectron spectra, spectra are labelled A-H corresponding to the intermediate position excited by the pump laser. The photoelectron spectra all appear very similar in terms of peak position and relative intensity, the peak at ~980 cm^{-1} which originates from the $\Delta v = 0$ transition from S_1 always remains the most intense. Spectra F, G and H do have a lower intensity vibrational origin peak at 0 cm^{-1} and for spectra H especially, the main photoelectron peaks all appear weaker in intensity and there is more intensity in the baseline. However, this could be attributed to the pump laser exciting close to the base of the S_1 REMPI peak so intensity is low (see Figure 3-12). The similarities between the photoelectron spectra in Figure 3-13 suggests that each spectrum may be a Franck-Condon projection of the same S_1 vibrational state, 12^1, which would mean the initially excited state is not changing with excitation wavenumber and at each position the pump laser overlaps the 12^1 vibration.

The almost identical appearance of the photoelectron spectra is somewhat unexpected considering the intensity of some of the other bands at ~950 cm^{-1} in the nanosecond REMPI spectrum in Figure 3-11. Considering this, an alternative

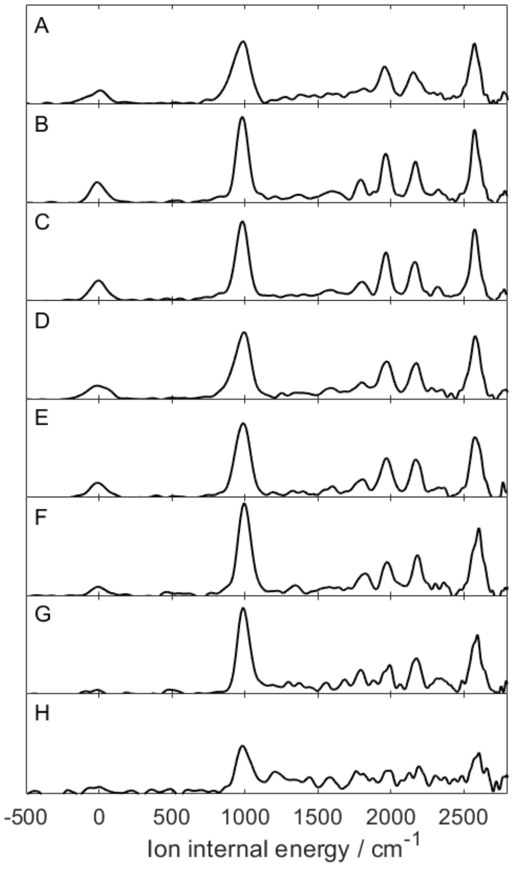

Figure 3-13: Photoelectron spectra measured when stepping the pump laser in S_1 wavenumber. Labelled A-H corresponding to positions A-H in Figure 3-12.

explanation is that the vibrations observed in this wavenumber range of the S_1 electronic state all have similar vibrational wavenumbers in the cation, which cannot be resolved in the photoelectron spectra in Figure 3-13. Notably, the shape of the most intense feature observed at ~1000 cm^{-1} in these spectra does appear to change in shape with changing excitation wavenumber. Further, inspection of the origin peak in Figure 3-13 shows an apparent change in intensity with excitation wavenumber. These observations may be indicative of the presence of at least two vibrations which are unresolved in the broad S_1 feature observed in Figure 3-11.

In their fluorescence excitation spectrum, Mikami and co-workers assigned a feature at 985 cm^{-1} to $6a^2$;[13] Scheps et al. also assigned $6a^2$ at 987 cm^{-1}.[2] When exciting at positions G and H (see Figure 3-12), wavenumbers in which the $6a^2$ vibration is expected to be most active based on these previous studies, a tail on the blue edge of the most intense feature of the photoelectron spectra in Figure 3-13 is observed. This tail agrees with the expected wavenumber of the $6a^2$ vibration in the cation of ~1042 cm^{-1}.[6] A further potential assignment of the feature observed at ~985 cm^{-1} in the ns-REMPI spectrum is to S_1 $19a^1$. The fundamental vibrational wavenumbers of the S_1 19a and S_1 12 vibrations are remarkably similar, and therefore would not be resolved in the present study. However, mode 19 has not generally been assigned in literature.

Further work where photoelectron spectra are measured using a narrower bandwidth laser would be useful in providing conclusive assignment of any additional vibrations. Also limited time delays were measured here, scanning the delay stage while monitoring the intensity of a particular ion peak would provide significantly more data points. Through Fourier Transform of these data points, a high-resolution frequency spectrum may be obtained where peaks correspond to the energy separation between eigenstates thus providing information on how many vibrations are prepared. This technique was used previously in a study of *para*-difluorobenzene.[25,26] Using this information in tandem with the photoelectron spectra above, which are necessary to provide information of the nature of the vibrations excited, could allow conclusions to be drawn on the S_1 vibrational levels prepared in these experiments.

3.5. S₁ vibrational levels exhibiting restrictive IVR

3.5.1. Probing the broad S₁ REMPI feature at 600-900 cm⁻¹

In Figure 3-14 is the 600-900 cm^{-1} region of the $S_1 \leftarrow S_0$ REMPI spectrum which contains the broad irregular feature which peaks at ~800 cm^{-1}. The profile of this feature strongly implies that unresolved vibrational levels are contributing to the overall intensity. This was confirmed through comparison to a higher resolution REMPI spectrum measured using nanosecond pulses shown in Figure 3-11; four relatively intense peaks are resolved in the spectrum, two appearing as shoulders. To investigate these close lying S_1 vibrational levels, the pump laser was stepped over the profile of the feature in the picosecond REMPI spectrum and multiple intermediate positions were excited; in Figure 3-14 the S_1 wavenumber positions excited are shown by dotted lines and labelled A-I.

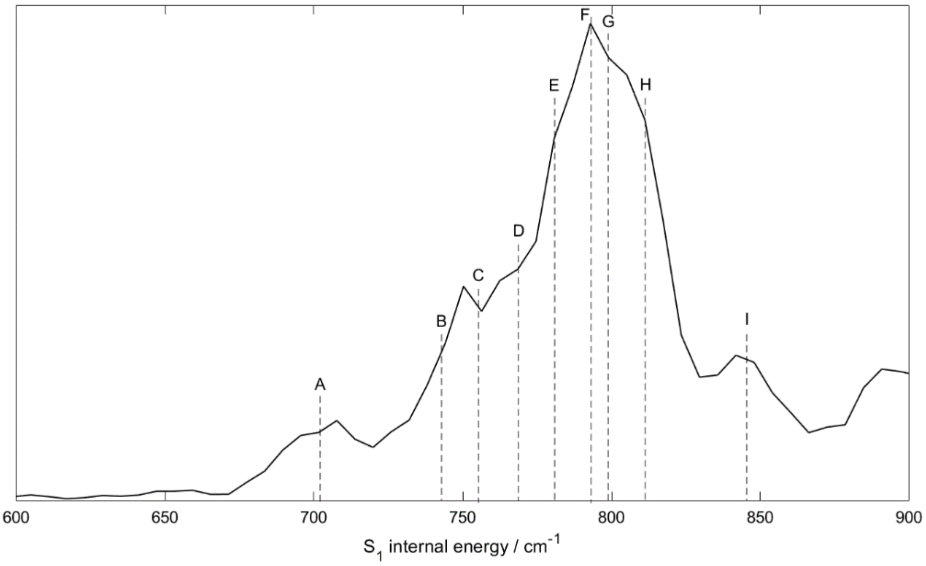

Figure 3-14: 600-900 cm^{-1} region of the S_1 REMPI spectrum, dotted lines and labels show each position excited by the pump laser.

The resulting photoelectron spectra are shown in Figure 3-15, they are labelled A-I corresponding to the pump laser position in Figure 3-14. Comparison shows that as excitation wavenumber changes, the profile of the spectrum changes, in both wavenumbers and relative intensities of bands observed. At least three distinct spectra can be identified based on the position of the most intense photoelectron peak, which appears at ~1150 cm^{-1} in spectrum A, ~1340 cm^{-1} in spectra B and C and ~810 cm^{-1} in spectra E-H. According to the propensity rule these peaks likely originate from the Δv = 0 transition from the initially prepared S_1 level which suggests that at least three different vibrational levels were prepared in S_1 as the pump laser was stepped in wavenumber. Photoelectron spectrum I suffers from poor signal to noise and apparent lower resolution so no conclusive behaviour can be determined from this spectrum.

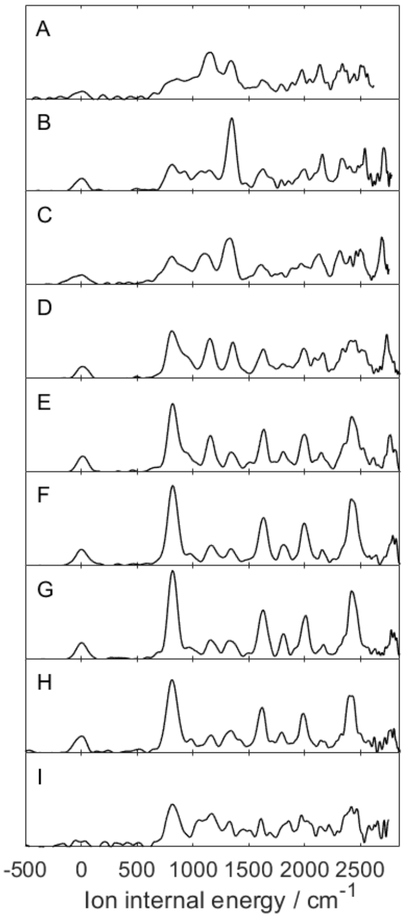

Figure 3-15: Photoelectron spectra A-I measured via different intermediate wavenumbers in S_1 (refer to Fig. 3-14). Each recorded at time delays of 0 ps.

SEVI spectra and time-resolved photoelectron spectra have been measured via the S_1 wavenumbers of i) ~800 cm^{-1} and ii) ~750 cm^{-1}; analysis and assignment of these spectra is discussed in the following sections. Photoelectron spectrum A in Figure 3-15 was measured at ~700 cm^{-1} in the S_1 electronic state; while the spectral differences (discussed above) and inspection of Figure 3-14 and Figure 3-16 suggests a different S_1 vibrational level excited, further SEVI and time-resolved spectra have not been measured. This was due to the level of congestion observed, particularly in the 500 cm^{-1} – 1500 cm^{-1} region of the photoelectron spectrum, combined with the low intensity of the intermediate level. So this vibrational level can only be discussed in relation to previous studies in literature.

In their fluorescence excitation spectrum of the first singlet transition, Mikami and co-workers assigned the 15^2 vibration at 702 cm^{-1}.[13] Knee and co-workers assigned a peak at 703 cm^{-1} in the S_1 electronic state to vibrational level 15^2; in that work two intense features at 1102 cm^{-1} and 1154 cm^{-1} were observed in the ZEKE spectrum measured *via* this intermediate level.[6] The more intense 1102 cm^{-1} feature was assigned to level 15^2 in the cation but the 1154 cm^{-1} feature was not assigned.[6] Reilly and co-workers suggested the 1154 cm^{-1} feature may correspond to the A^2 level where mode A is an out-of-plane C-NH_2 torsion.[17] In Table 3-1 the A vibration is the lowest wavenumber NH_2 localised vibration, calculations suggest vibrational wavenumbers of 276 cm^{-1} and 567 cm^{-1} in the S_1 and cation states respectively. This means the overtone, A^2, is predicted at 1134 cm^{-1} in the cation, in good agreement with the experimentally observed peak, but only 552 cm^{-1} in S_1 so the vibration could not be excited in S_1 at this position of the pump laser. Wallace and co-workers suggested wavenumbers of 373 cm^{-1} and 724 cm^{-1} for vibrational levels 15^1 and 15^2 respectively in the cation.[8] Later Wallace recorded photoionization efficiency spectra *via* an intermediate level assigned as 15^2 and they assigned a band at 724 cm^{-1} to level 15^1 in the cation.[9] Neither of these are in agreement with the work of Knee and co-workers. Comparison to the calculated wavenumber of mode 15 of 385 cm^{-1} suggests that assignment of the vibration observed at either 1102 or 1154 cm^{-1} in the cation to the 15^2 is possibly incorrect.

Photoelectron spectrum A was measured *via* a similar S_1 wavenumber to that excited in the studies of Knee and Wallace although direct comparison to the photoelectron spectroscopy in literature in some cases is not straightforward because of the larger bandwidth of the picosecond laser here. In photoelectron spectrum A there is a lot of intensity between 500 cm^{-1} and 1500 cm^{-1}. The most intense peak is at ~1150 cm^{-1} in photoelectron spectrum A, which given the resolution of the experiment, could be the same peak observed at either ~1102 cm^{-1} or 1154 cm^{-1} by Knee,[6] no vibrational levels were found which have predicted S_1 and ion state wavenumbers within 60 cm^{-1} of 700 cm^{-1} in S_1 and 1150 cm^{-1} in the cation. There is another intense photoelectron peak at ~1340 cm^{-1} which was not mentioned in previous studies. A possible assignment of the ~1340 cm^{-1} SEVI feature is to the $16a^1 17a^1$ combination band which has a predicted wavenumber of ~1342 cm^{-1} in the ion state (based on Ref 6 for mode 16a). As $16a^1 17a^1$ has a predicted wavenumber of 736 cm^{-1} in the S_1 electronic state (based on Ref 6 for mode 16a), the SEVI peak could originate from the $\Delta v = 0$ transition from this level. However, there is also a feature at similar wavenumbers in photoelectron spectra obtained at other intermediate wavenumbers, notably in spectra B – D in Figure 3-15. As will be discussed in the following sections, in these cases, the inversion mode I^2 has been assigned which is predicted 1323 cm^{-1} in the cation.[6] Despite better agreement of the predicted wavenumber of the $16a^1 17a^1$ vibration with the 1340 cm^{-1} SEVI peak, based on the expected activity of the inversion of the NH_2 group owing to changing geometry of aniline upon electronic excitation, an assignment of the ~1340 cm^{-1} feature to the I^2 is preferred here too. However, Knee assigned the I^2 vibration at 762 cm^{-1} in the S_1 electronic state meaning this vibration is assigned to the higher wavenumber nanosecond band at ~761 cm^{-1} in Figure 3-16, rather than the lower wavenumber nanosecond band at ~702 cm^{-1}. This means while the I^2 vibration in S_1 could have been prepared, another unidentified $S_1 \leftarrow S_0$ transition is likely excited as well. Based on the observed peaks a definitive assignment for the S_1 vibrational level has not been found.

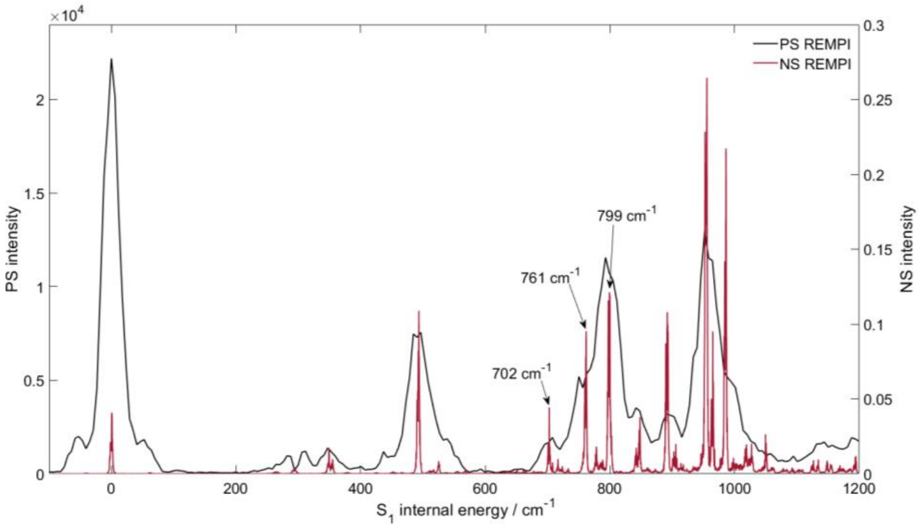

Figure 3-16: REMPI spectra measured using nanosecond (red) and picosecond (black) pulses. The wavenumbers of relevant peaks are shown.

3.5.1.1. Assignment of vibrational levels at S_1 0^0 + ~800 cm^{-1}

Figure 3-17 shows the 0 ps SEVI spectrum measured *via* ~800 cm^{-1} in the S_1 electronic state. According to the propensity rule, the most intense peak at ~810 cm^{-1}, most likely originates from the $\Delta v = 0$ transition from S_1 to the ion. These experimental vibrational wavenumbers are in very good agreement to the predicted vibrational wavenumbers of level 1^1 which are 800 cm^{-1} and 807 cm^{-1} in the S_1 and ion states respectively.[6] So it is concluded that the S_1 1^1 vibration was excited, this level has previously been assigned in the literature.[3,6,7,13,17]

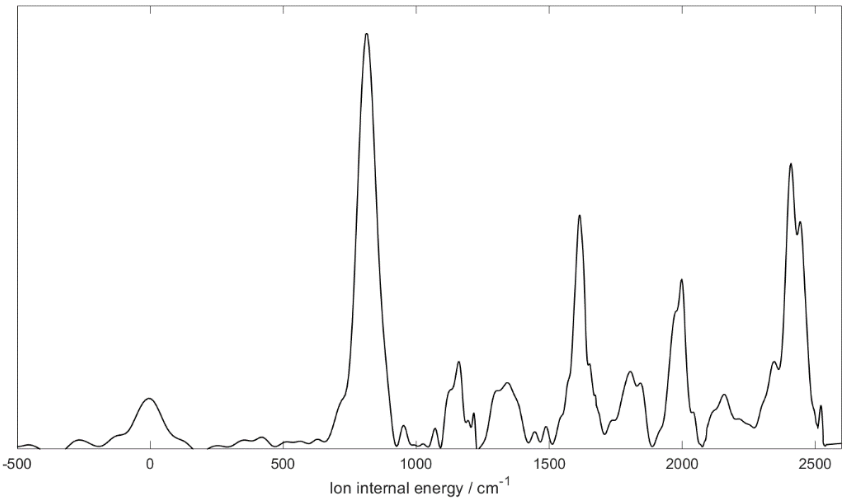

Figure 3-17: 0 ps SEVI spectrum measured via ~800 cm^{-1} in S_1.

Assignments for other SEVI peaks in Figure 3-17 are shown in Table 3-5. In some cases, especially at higher internal energies, multiple vibrational levels have predicted wavenumbers in good agreement to the observed wavenumber of the SEVI peak; this combined with the width of some of the SEVI bands suggest there may be multiple unresolved cation vibrational levels present. All assignments shown are to totally symmetric fundamental, combination or overtone levels and many involve mode 1. Notably, the peaks at ~810 cm^{-1}, ~1610 cm^{-1} and 2410 cm^{-1}, which are the three most intense features, can be assigned to vibrational levels 1^1, 1^2 and 1^3 respectively.

Ion internal energy / cm^{-1}	Cation vibrational level	Predicted wavenumber of cation vibrational level/ cm^{-1}
0	0^0	0
810	1^1	810[a], 807[b]
1160	$8a^1$ * $I^1 6a^1$ $1^1 10b^2$	1184[a], 1187[b] 1177[b], 1161[c] 1169[d]
1330	$1^1 6a^1$ $16a^1 17a^1$ *I^2	1329[a], 1328[b], 1335[d] 1342[a,b] 1323[b], 1315[c], 1325[d]
1610	1^2	1620[a], 1614[b]
1810	$1^1 19a^1$ $1^1 12^1$	1801[a], 1800[b], 1807[d] 1782[a], 1790[b], 1793[d]
1990	$1^1 8a^1$ $19a^2$	1994[a/b], 2001[d] 1982[a], 1986[b]
2410	1^3 $1^1 9a^1$	2430[a], 2421[b] 2417[a], 2400[b]
2810	$1^2 8a^1$	2804[a], 2801[b]

*Table 3-5: Assignments for SEVI peaks in Figure 3-17, the predicted wavenumbers are based on fundamental wavenumbers from a) calculations, b) Ref 6, c) Ref 7 and wavenumbers from d) Ref 17. Experimental wavenumbers rounded to nearest 10 cm^{-1}. *$6a_0^1 I_1^1$ transition, see following section.*

3.5.1.2. Assignment of vibrational levels at S_1 0^0 + ~750 cm^{-1}

The 0 ps SEVI spectrum measured *via* ~750 cm^{-1} in the S_1 electronic state is shown in Figure 3-18. SEVI peak Z at ~1340 cm^{-1} is the most intense so is assigned to the $\Delta v = 0$ transition from the S_1 electronic state. There are relatively few vibrational levels which exhibit such a large wavenumber difference between S_1 and ion states. As discussed briefly in section 3.5.1, it is concluded that level I^2 is excited in S_1 at this wavenumber, where I is the inversion mode, based on the good agreement between the experimental vibrational wavenumbers and the predicted wavenumbers in the S_1 and ion states as shown in Table 3-6. The large difference in the wavenumber of this level I^2 upon ionisation has been attributed to the phenyl-N bond developing double bond character upon ionization.[7]

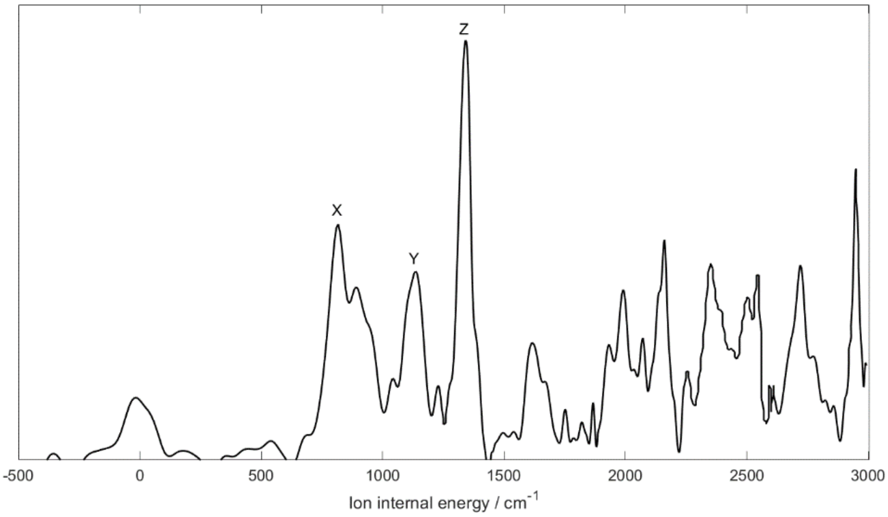

Figure 3-18: 0 ps SEVI spectrum measured via ~750 cm^{-1} in S_1. The SEVI peaks labelled X, Y, Z are discussed in the text.

$S_1 \leftarrow S_0$ Vibronic Transition	Predicted wavenumber in the S_1 electronic state relative to 0_0^0 transition / cm^{-1}	$D_0^+ \leftarrow S_1$ Vibronic Transition	Predicted wavenumber in the ion state / cm^{-1}
I_0^2	762^b, 760^c,	I_2^2	1323^b, 1315^c,
1_0^1	807^a, 800^b, 798$^{c/d}$	1_1^1	810^a, 807^b, 798^c
$\mathrm{I}_1^1 6\mathrm{a}_0^1$	786^b, 785^c, 782^d	$\mathrm{I}_1^1 6\mathrm{a}_1^1$	1177^b, 1161^c

Table 3-6: Predicted wavenumbers of vibronic transitions I_0^2, 1_0^1 and $I_1^1 6a_0^1$ relative to the 0_0^0 transition and corresponding transitions to the ion based on fundamental wavenumbers from a) Calculations, b) Ref 6, c) Ref 7, d) Ref 3.

Meek and co-workers used a time-of-flight method to measure the photoelectron spectrum via the I^2 level, they found the spectrum contained unexpected peaks which were not readily assignable.[7] This was attributed to the excitation of more than one $S_1 \leftarrow S_0$ transition as a result of 'substantial overlap between closely spaced vibronic bands' in the ultraviolet absorption spectrum of aniline.[7] A study of the first ultraviolet band system of aniline by Brand and co-workers showed that the rotational profiles of the 12^1_0, $\mathrm{I}^1_1 6\mathrm{a}^1_0$ and I^2_0 bands substantially overlap, comparison of the experimental vibrational wavenumbers shows that vibration 12^1 in the work of Brand and co-workers which was assigned to a band at 798 cm^{-1} in the S_1 electronic state corresponds to the 1^1 vibration in our notation and in the study by Meek et al.[7,3] $\mathrm{I}^1_1 6\mathrm{a}^1_0$, unlike the other transitions listed, does not originate from the vibrationless ground state in S_0, I^1_1 is a hot band transition, which originates from the first excited level of the inversion mode in the ground electronic state; the subscript and superscript relate to the ground state and S_1 excited electronic state respectively. Relative to the 0^0_0 transition, the I^1_1 transition occurs at 293 cm^{-1};[3] with the $\mathrm{I}^1_1 6\mathrm{a}^1_0$ transition expected at ~785 cm^{-1} (Table 3-6). The SEVI spectrum in Figure 3-18 is similar in appearance to the I^2 spectrum presented by Meek and co-workers,[7] this suggests that multiple $S_1 \leftarrow S_0$ transitions, possibly $\mathrm{I}^2_0, 1^1_0$ and $\mathrm{I}^1_1 6\mathrm{a}^1_0$, have been excited in these experiment also. Table 3-6 shows the predicted S_1 and ion state wavenumbers of relevant vibrational levels.

In the previous section, the SEVI spectrum measured at ~800 cm^{-1} in the S_1 electronic state was discussed. Based on excellent agreement between predicted and observed wavenumbers, the intense SEVI peak at ~810 cm^{-1} and the S_1 vibrational level initially excited were assigned to the fundamental v_1 vibration. Figure 3-19 shows there is also a peak at ~810 cm^{-1} (labelled X) in the SEVI spectrum measured via ~750 cm^{-1} in S_1. It is likely X is also the 1^1 vibration in the

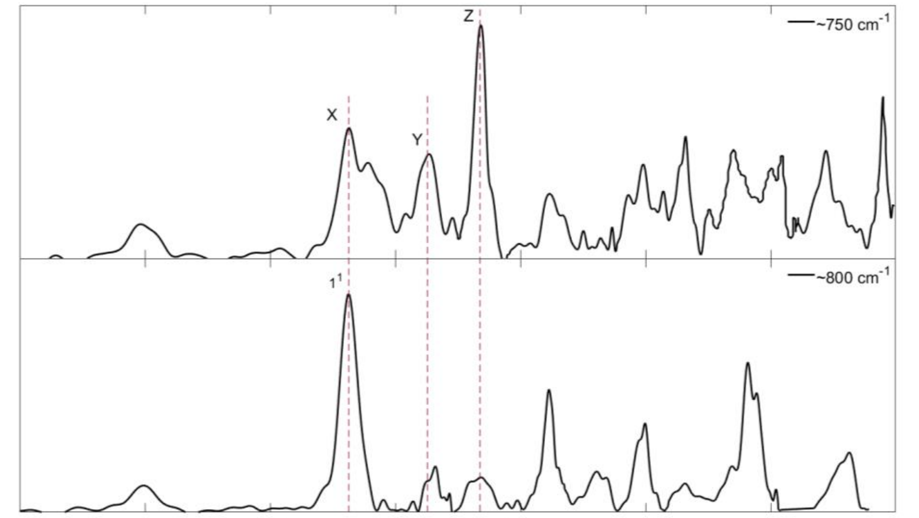

Figure 3-19: 0 ps SEVI spectra measured via ~750 $\mathrm{cm}^{-1}$and ~800 cm^{-1} in S_1.

cation. SEVI peak Y in Figure 3-19 has a wavenumber of ~1130 cm^{-1}, given the resolution, this is in reasonable agreement to the vibrational wavenumber of ~1160-1180 cm^{-1} predicted for $I^1 6a^1$ based on experimentally derived fundamental wavenumbers (see Table 3-6). Considering that all three vibrations: I^2, 1^1 and $I^1 6a^1$, are assigned in the SEVI spectrum obtained with a pump-probe delay of 0 ps, and that the peaks are all relatively intense, it is probable that both the 1_0^1 and $I_1^1 6a_0^1$ $S_1 \leftarrow S_0$ transitions were actually excited alongside the I_0^2 transition.

Further evidence the SEVI peaks X, Y, Z are attributable to three different $S_1 \leftarrow S_0$ transitions is that as the pump laser is tuned across this broad S_1 REMPI feature, the relative intensities of the three SEVI peaks change, this can be seen in Figure 3-15. In the spectrum recorded *via* B and C, the ~1340 cm^{-1} feature, assigned to I^2 is most intense; when exciting at D, the three ion peaks are of comparable intensity, when exciting at positions E – H, the 810 cm^{-1} feature dominates.

Assuming vibrational levels I^2, 1^1 and $I^1 6a^1$ are all excited in S_1 by the pump pulse, then that would make the SEVI spectrum in Figure 3-18 a superposition of the individual photoelectron spectra which would be measured via each vibrational level in S_1. This makes assignment difficult because the other SEVI peaks could be overtone or combination levels resulting from any of the three S_1vibrational levels. Furthermore, many of the SEVI peaks are broad with unresolved shoulders, particularly above ~1500 cm^{-1}, so contributions from multiple cation vibrational levels are likely. Possible vibrational level assignments for the more intense peaks in the SEVI spectrum are suggested in Table 3-7.

The assignments are based on comparison to predicted wavenumbers and the behaviour of each SEVI peak with changing excitation wavenumber. Figure 3-15 shows the SEVI peak assigned to vibration 1^1 increases in intensity as excitation wavenumber increases. The same behaviour is observed for the SEVI peak at ~1620 cm^{-1}, based on this, and the fact this peak is at double the wavenumber of vibration 1^1, this level is assigned to the overtone 1^2. The SEVI peaks at ~2150 cm^{-1} and ~2350 cm^{-1} in Figure 3-15 decrease in intensity similar to the behaviour observed for the peak at ~1340 cm^{-1} assigned to vibration I^2 suggesting they may all originate from transition from I^2 in S_1. To be conclusive about these assignments it would be valuable to record higher resolution photoelectron spectra with the aim of resolving more features and providing more precise wavenumbers.

Ion internal energy / cm^{-1}	Cation vibrational level	Predicted wavenumber of cation vibrational level/ cm^{-1}
0	0^0	0
X – 810	1^1	810[a], 807[b]
890	4^2 $16b^2$	889[d] 882[a], 890[d]
Y – 1130	I^16a^1	1177[b], 1161[c]
Z – 1340	I^2 1^16a^1	1323[b], 1315[c] 1329[a], 1328[b]
1620	1^2	1620[a], 1614[b]
1990	1^18a^1 $19a^2$ A^21^1 1^210b^2	1994[a/b] 1982[a], 1986[b] 1968[d] 1986[d]
2150	I^21^1	2130[b], 2113[c]
2350	I^219a^1	2316[b]
2720	I^4 I^213^1	2646[b], 2630[c] 2711[b], 2662[c]
2950	I^29a^1 12^119a^2	2916[b], 2896[c] 2954[a], 2969[b]

Table 3-7: Vibrational level assignments for the main SEVI peaks in Figure 3-18. Predicted wavenumbers are based on fundamental wavenumber from a) calculations, b) Ref 6, c) Ref 7, d) Ref 17. Experimental wavenumbers rounded to nearest 10 cm^{-1}. Mode A is an out of plane CN torsion. In Ref 7 Meek commented they observed a 'remarkably harmonic progression' in the inversion mode in the cation so the wavenumber of I^4 is estimated as 2x the I^2 value.

3.5.2. Analysis of time-resolved photoelectron spectra

The observation of peaks at similar wavenumbers but different relative intensities in the SEVI spectra *measured via* ~800 cm^{-1} and ~750 cm^{-1} in the S_1 electronic state, could be an indication of coupling between the S_1 vibrational levels assigned I^2, 1^1 and I^16a^1. Time-resolved photoelectron spectra were measured via ~800 cm^{-1} and ~750 cm^{-1} in S_1 to examine this possibility and coupling to other states.

3.5.2.1. Time-resolved photoelectron spectra *via* S_1 0^0 + ~800 cm^{-1}

Photoelectron spectra were measured at multiple pump-probe time delays between 0 ps and 500 ps, several of these are shown in Figure 3-20. Changes in peak intensity with time delay can be seen; arrows have been added in Figure 3-20 to three relatively intense peaks to highlight this. However, up to 500 ps the photoelectron spectra remain well resolved and no obvious increase in the intensity of the baseline underneath the peaks is observed. Also, notably the photoelectron peak at ~810 cm^{-1} which results from the $\Delta v = 0$ transition from S_1, still shows similar intensity compared to early time delays. This suggests that a dissipative type energy dispersal is not occurring during the experiment.

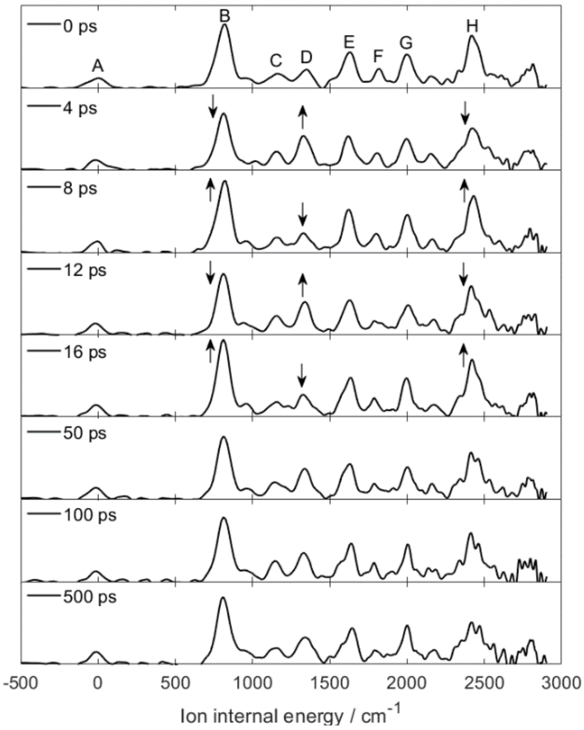

Figure 3-20: Photoelectron spectra measured via ~800 cm^{-1} in S_1 at multiple pump-probe time delays between 0 ps and 500 ps. Arrows indicate an increase or decrease in peak intensity between spectra.

The intensity (measuring the full area) of the main photoelectron peaks A – H have been plotted as a function of time delay to give the time profiles shown in Figure 3-21; the data points (0-50 ps) have been fit to equation 2.4 (see chapter 2). The time profiles show oscillations in intensity for all peaks measured indicating restrictive IVR, although some appear much weaker than others. Further, peaks A, B, E, F, G and H all show maximum intensity at 0 ps and a minimum at ~4 ps. Whereas peaks C and D oscillate out of phase to the rest, showing minimum intensity at 0 ps increasing up to ~4 ps. This suggests peaks A, B, E, F, G and H reflect the population of the initially prepared bright vibrational level, 1^1, but the intensity oscillations of peaks C and D reflect the population of a different vibrational level which is dark and strongly coupled to level 1^1 in S_1.

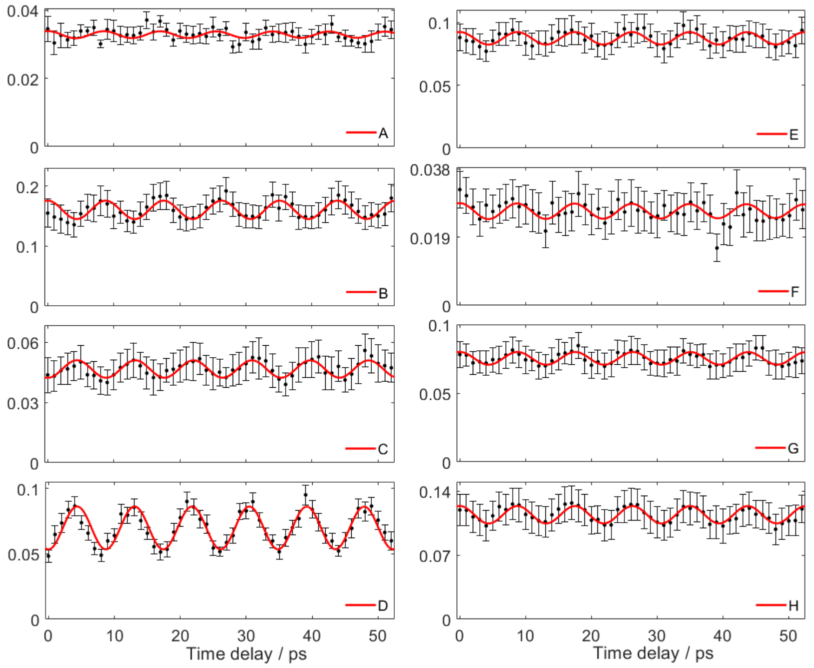

Figure 3-21: Time profiles showing fits to the time-dependent intensity of photoelectron peaks A-H.

	Coefficients			
Peak/plot	**A**	**B**	τ_{osc}	**Rsq**
A	0.20	0.01	8.51 ± 0.28	0.17
B	1.00	0.10	8.77 ± 0.10	0.59
C	0.29	-0.03	8.83 ± 0.09	0.67
D	0.43	-0.1	8.70 ± 0.05	0.85
E	0.55	0.03	8.73 ± 0.12	0.53
F	0.16	0.01	8.70 ± 0.20	0.28
G	0.47	0.03	8.77 ± 0.09	0.64
H	0.71	0.06	8.75 ± 0.08	0.73

Table 3-8: Results of the fits to the time-dependent intensity of peaks A-H which are shown in Figure 3-21. Column A and B are normalised.

The results from the fits are shown in Table 3-8, from these an average oscillation period of 8.72 ± 0.21 ps is calculated. The excellent agreement between all eight τ_{osc} values and the small associated error bars suggest a single oscillation period indicating the involvement of a single dark state. From the oscillation period an eigenstate separation of 3.83 ± 0.09 cm^{-1} is determined. Some of the fits, particularly A and F, have a low Rsq value but this is attributed to the fact that peaks A and F in Figure 3-20 are the weakest and it is difficult to measure and fit such small changes in intensity against error because the oscillation periods are in good agreement to the other peaks. The τ_1 coefficient in equation 2.4 models any decay in the oscillations, notably all the $\boldsymbol{\tau_1}$ values determined from the fits are very long, range between hundreds to thousands of picoseconds and the error bars are extremely large. This suggests that there is no clear decay occurring over the timescale of the experiments, which is expected for restrictive energy dispersal where population flows reversibly between only the bright and dark state. Due to this the τ_1 values have not been included in Table 3-8 as they do not impact the oscillation period.

It was concluded above that peaks C and D reflect dark state population because they oscillate with minimum intensity at 0 ps. Figure 3-22 shows spectra at 0 ps and 4 ps, roughly half the average oscillation period shown above. Only peaks C and D appear more intense at 4 ps versus 0 ps indicating overlapping transitions from the dark state in S_1, although a shoulder on the photoelectron peak at ~2500 cm^{-1} may be more prominent, however, neither are the most relatively intense. Peak B at ~810 cm^{-1} is the most intense peak in both the 0 ps and 4 ps spectra.

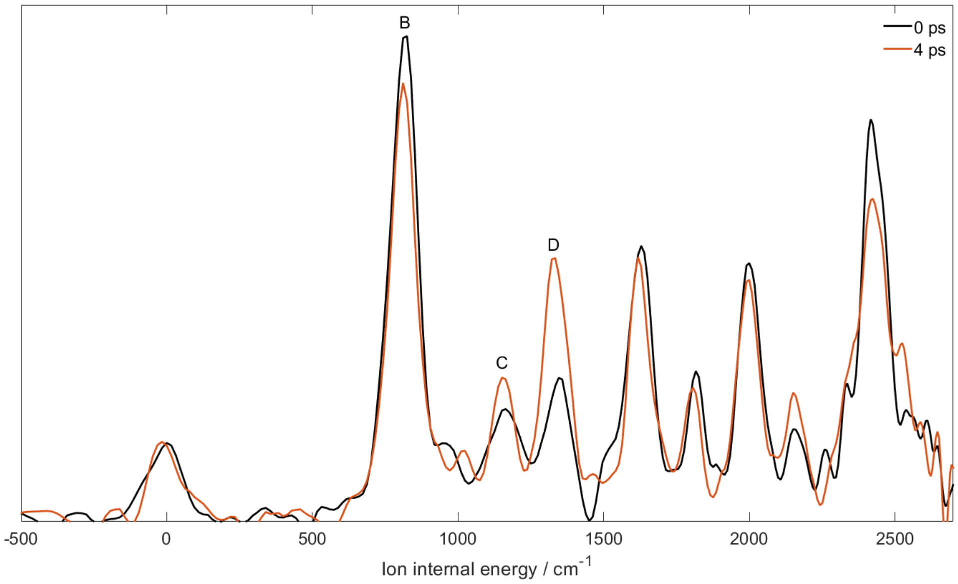

Figure 3-22: Photoelectron spectra measured via ~800 cm^{-1} in S_1 at pump-probe time delays of 0 ps and 4 ps.

As the photoelectron spectrum at 4 ps should largely reflect a Franck-Condon projection of the dark state in S_1 onto the cation vibrational levels, it is most likely then that either peak B, C or D originates from the $\Delta v=0$ transition from S_1. In the case of peak B it would mean that the $\Delta v = 0$ transitions from both the bright and dark states in S_1 have coincident wavenumbers, within the experimental resolution. Currently SEVI spectra have only been recorded at 0 ps; recording SEVI spectra at later time delays may be able to capture any small shifts in peak wavenumber that occur at later time delays compared to those at 0 ps. This would confirm the changing vibrational character of cation vibrational levels which has been inferred/proposed from the tr-PES.

Assuming the dark state has a vibrational wavenumber of ~800 cm^{-1} in the S_1 electronic state and a vibrational wavenumber of either ~810 cm^{-1} (peak B), ~1160 cm^{-1} (peak C) or ~1330 cm^{-1} (peak D) in the ion state, a search has been conducted for vibrational levels with predicted wavenumbers in agreement with these experimental vibrational wavenumbers within ± 65 cm^{-1} to account for error in the calculated wavenumbers. Table 3-9 shows vibrational levels which match the above energy constraints, the vibrational levels are ordered according to the change in vibrational quanta, ΔN, relative to vibrational level 1^1, only $\Delta N \leq 3$ shown. As ΔN increases coupling strength is predicted to decrease.[27,28,29] For the $\Delta v = 0$ transition to result in peaks C or D at 4 ps, the vibrational level in question would require a large difference in wavenumber between the S_1 and ion states. There are relatively few vibrational levels that show such large wavenumber differences.

Vibrational level	Predicted S_1 wavenumber / cm^{-1}	ΔE to the experimental wavenumber ~800 cm^{-1}	Predicted cation wavenumber / cm^{-1}	ΔE to the experimental wavenumber ~810 cm^{-1} (peak B)	ΔN relative to 1^1
15^2	756[a], 762[b]	44 38	770[a], 1102[b], 1098[e]	40, 292, 288	3
				ΔE to the experimental wavenumber ~1160 cm^{-1} (peak C)	
$10a^1 16a^1$	802[a,b]	2	1157[a,b]	3	3
				ΔE to the experimental wavenumber ~1330 cm^{-1} (peak D)	
I^2	762[b], 760[d]	38 40	1323[b], 1315[d]	7 15	3
$16a^1 17a^1$	736[a,b]	64	1342[a,b]	12	3

Table 3-9: Vibrational level assignments for the dark state in S_1. Predicted wavenumbers are based on fundamental wavenumbers taken from a) calculations, b) Ref 6, c) Ref 8, d) Ref 7, e) Ref 17. 15^2 is included due to calculated wavenumbers, discrepancy between predicted wavenumbers of vibrational level 15^2 is briefly discussed in section 3.5.1.

Of the four vibrational levels shown in Table 3-9, all involve a change in vibrational quanta of 3 relative to vibrational level 1^1 which is the lowest ΔN found. One of these vibrational levels is I^2; notably, in section 3.5.1.2 it was concluded that both vibrational levels I^2 and 1^1 were prepared when the pump laser was fixed at ~750 cm^{-1} in the S_1 electronic state. However, in the time-resolved spectra measured at ~750 cm^{-1} in the S_1 electronic state, which is discussed in the next section, ~8.7 ps oscillations in intensity are not observed. If vibrational levels 1^1 and I^2 were coupled in S_1 this should be evident from the time-resolved spectra. Of the three remaining vibrational levels, two are assignments for photoelectron peaks C or D which oscillate out of phase (peak B shows maximum intensity at 0 ps), this means there is more reason to support these assignments for the dark state, especially considering the uncertainty around mode 15. The combination level $16a^1 17a^1$ has a predicted wavenumber in agreement with peak D at ~1330 cm^{-1}, which is more intense than peak C however, as can be seen from the next subsection, this vibration is the only assignment for the other dark state. The remaining vibrational level $10a^1 16a^1$ shows excellent agreement between predicted wavenumbers and experimental vibrational wavenumbers in the S_1 state and for peak C in the ion state although the predicted wavenumbers rely on calculations for mode $10a^1$. The process of elimination seems to suggest that peak C is the result of the $\Delta v = 0$ transition from the dark state. However, as shown in Figure 3-22 peak C is weak particularly compared to photoelectron peaks B and D. This is unexpected considering that in the majority of the aniline photoelectron spectra measured at different S_1 wavenumbers there is generally an intense $\Delta v = 0$ transition observed. As a result, the dark state is only tentatively concluded to be $10a^1 16a^1$ ($\Delta v = 0$ peak C) and the changing intensity of the ~1330 cm^{-1} band (peak D) is attributed to an allowed $\Delta v \neq 0$ transition from the initially excited $10a^1 16a^1$ vibration in S_1. The $16a^1 17a^1$ vibration is a likely assignment, this combination level involves two vibrations of a_2 symmetry, one of which is the 16a vibration, so it would be expected to have good overlap from the S_1 level $10a^1 16a^1$.

3.5.2.2. Time-resolved photoelectron spectra *via* S_1 0^0 + ~750 cm^{-1}

The data above provided evidence that vibrational level 1^1 was coupled to a dark state in S_1 which was tentatively assigned $10a^1 16a^1$. Given that level 1^1 is also excited at ~750 cm^{-1} in S_1 (alongside I^2 and $I^1 6a^1$, refer to section 3.5.1.2), it is possible that manifestations of this coupling will be seen again here. However, this would require both vibrational levels to still be overlapped by the pump pulse at S_1 ~750 cm^{-1}. If not the coupling would not be reflected in the time-dependence.

To investigate the time-dependent behaviour, photoelectron spectra were measured *via* ~750 cm^{-1} in S_1 at a series of pump-probe time delays between 0 ps and 500 ps; several are shown in Figure 3-23. The peaks at 0 ps are still present up to 500 ps with similar intensity to early time delays. Further, there doesn't appear to be an obvious increase in intensity in the baseline underneath the peaks. So there is no evidence of coupling between the bright state and bath states resulting in dissipative energy dispersal. Considering that the pump laser is exciting a relatively low wavenumber region in S_1 when density of states is expected to be low this type of behaviour would not be expected.

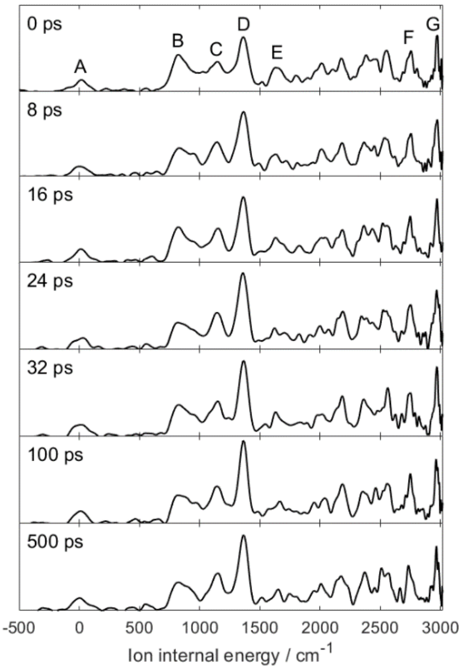

Figure 3-23: Photoelectron spectra measured via ~750 cm^{-1} in S_1 at multiple time delays between 0 ps and 500 ps. Peaks involved in time-resolved analysis are labelled A-G.

The full intensity of the main photoelectron peaks A-G have been plotted as a function of time delay and where appropriate fit (between 0-50 ps) to equation 2.4 (chapter 2), with the resulting the time profiles shown in Figure 3-24 and Figure 3-25. The plots, labelled A-G corresponding to the photoelectron peak measured, are divided into two separate figures due to different time-dependent behaviours shown. Features are broader in the ~2000 cm^{-1} - 2500 cm^{-1} region of the spectrum, likely owing to overlapping vibrational levels, thus features in this region have not been measured.

The time profiles in Figure 3-24 show the intensity of photoelectron peaks C, F and G as a function of time delay. None of the plots show any recurrences or continuous loss of intensity outside of experimental error so they have not been fitted. One explanation for the absence of any time-dependent behaviour is that photoelectron peaks C, F and G originate from a vibrational level in S_1 which is not coupled so no energy redistribution can occur, this could be level $6a^1I^1$ since in section 3.5.1.2, photoelectron peak C was assigned to the $\Delta v=0$ transition from this level in S_1. However, given that three $S_1 \leftarrow S_0$ transitions were excited, it is not unexpected that there may be overlapping transitions from S_1 to the ion. An alternative explanation for the non-observance of time dependence is that multiple coincident vibrational levels contribute to the intensity of peaks C, F or G with the result that conflicting time-dependent behaviours mask or dampen intensity changes or recurrences in peak intensity. There are perhaps some very weak fluctuations in intensity observed in the plots in Figure 3-24 which may be consistent with this explanation but these are not statistically significant enough to conclude this.

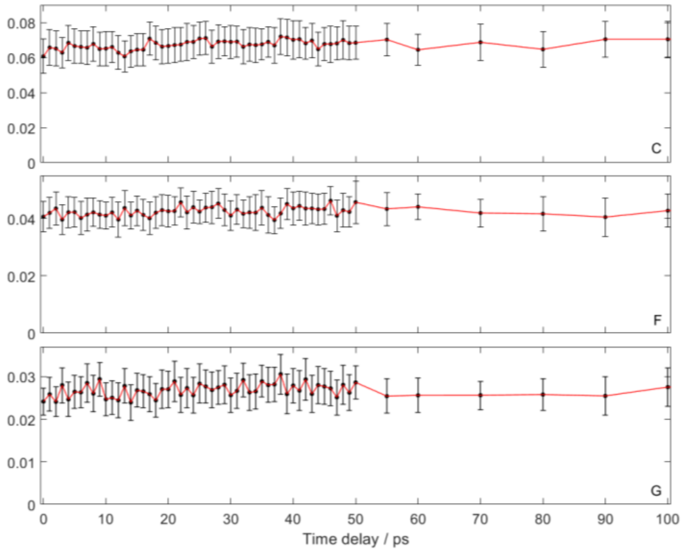

Figure 3-24: Time profiles showing the intensity of photoelectron peaks C, F and G as a function of increasing time delay.

Figure 3-25 shows the time profiles of photoelectron peaks A, B, D and E, with the results of the fits in Table 3-10. Weak oscillations in intensity with increasing time delay are seen, an average oscillation period of 15.90 ± 0.22 ps is determined from the four individual τ_{osc} values which are in good agreement. Oscillations in intensity result from population transfer indicating that one of the initially excited vibrations is coupled to another vibration in S_1. The oscillation period corresponds to an eigenstate separation of 2.10 ± 0.03 cm^{-1}. The τ_1 parameter was included to measure any decay, however in the fits all the τ_1 values are very long with large error bars, this is attributed to the fact that very little decay is actually observed in the oscillations indicating that population remains relatively localised during the experiment which is known as restrictive IVR. Thus, the τ_1 values are not shown in Table 3-10.

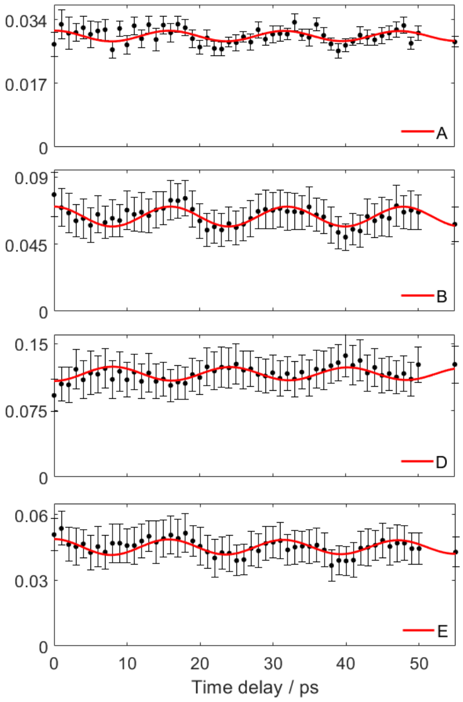

Figure 3-25: Time profiles of showing the intensity of photoelectron peaks A, B, D and E as a function of increasing time delay.

	Coefficients			
Peak	**A**	**B**	τ_{osc}	**Rsq**
A	0.26	0.01	15.80 ± 0.75	0.25
B	0.55	0.06	15.97 ± 0.34	0.62
D	1.00	-0.07	16.12 ± 0.52	0.46
E	0.39	0.03	15.71 ± 0.44	0.49

Table 3-10: Values of the parameters resulting from fits to the time profiles for peaks A, B, D, E

The time profiles of photoelectron peaks A, B and E oscillate in intensity, showing maximum intensity at 0 ps then decreasing up to ~8 ps. So they must reflect the population of the initially excited S_1 bright state. In section 3.5.1.2, A, B, E were assigned to cation vibrational levels 0^0, 1^1 and 1^2 respectively, this suggests that the S_1 vibrational level involved in coupling and therefore responsible for the time-dependence is 1^1. The time profile of peak D shows oscillations out of phase with A, B, E, with minimum intensity at 0 ps increasing up to ~8 ps. This indicates a feature overlapping peak D which originates from the dark state coupled to S_1 1^1.

Given the larger oscillation period (~15.90 ps compared to 8.72 ps), the time-dependence cannot be a manifestation of the coupling between vibrational levels 1^1 and $10a^1 16a^1$ in S_1 which was discussed in the previous section. The 1^1 vibration must couple to another S_1 level which is overlapped now the pump pulse is centred at ~750 cm^{-1} in S_1. Since D is the only photoelectron peak with maximum intensity at ~8 ps (see time profiles) in addition to being the most relatively intense peak in the 8 ps spectrum (shown in Figure 3-23) which should largely show a Franck-Condon projection of the dark S_1 state, it is likely that peak D at 8 ps originates from the $\Delta v = 0$ transition from the dark vibrational level in S_1.

In the 0 ps photoelectron spectrum, peak D at ~1340 cm^{-1} was assigned to the I^2 vibrational level in section 3.5.1.2. Given the energy resolution it is difficult to observe small wavenumber changes in peak positions occurring with increasing time delay which would indicate a different vibrational level, recording further SEVI spectra at key time delays would be useful here, but it is unlikely that peak D at 8 ps is still I^2 and it follows that it is unlikely that 1^1 and I^2 are coupled. Not only because of the out of phase oscillations of peak D but because the previous section discussed time-resolved spectra measured *via* 1^1 at ~800 cm^{-1} in the S_1 electronic state, if vibrational levels 1^1 and I^2 were coupled in S_1 then as long as the pump pulse at ~800 cm^{-1} overlapped both vibrational levels, 15 ps oscillations should have also been observed in those time profiles. However, this was not the case. If the pump pulse at ~800 cm^{-1} did not overlap both S_1 vibrational levels, then a photoelectron peak corresponding to the I^2 vibration would be expected at all time delays. However, in the 0 ps SEVI spectrum measured at ~800 cm^{-1} there is only a very weak feature at ~1330 cm^{-1}.

It is likely then that the $\Delta v = 0$ transition from the dark state in S_1 is just coincident with the $\Delta v = 0$ transition from I^2 in S_1 (given the experimental resolution) at peak D. So a search was conducted for other vibrational levels within ± 60 cm^{-1} of ~750 cm^{-1} in the S_1 electronic state and ~1340 cm^{-1} (peak D) in the ion state to account for small wavenumber shifts in peak position with time delay and error in calculated wavenumbers. The relatively large wavenumber difference means only one vibrational level was found which matches these observed S_1 and ion state wavenumbers. So the possibility that peak D originates from a $\Delta v \neq 0$ transition from the dark state in S_1 was considered and the search was extended to include vibrational levels with a predicted wavenumber within 60 cm^{-1} of peak B at ~810 cm^{-1} and peak C at ~1130 cm^{-1} given that there is a lot of intensity in this region of the spectrum at 8 ps. These vibrational levels are also shown in Table 3-11.

Vibrational level	Predicted S_1 wave-number / cm^{-1}	ΔE to the experimental wavenumber ~750 cm^{-1}	Predicted cation wave-number / cm^{-1}	ΔE to the experimental wavenumber ~810 cm^{-1} (peak B)	ΔN relative to 1^1
15^2	756^a, 762^b	6 12	770^a, 1102^b	40, 292	3
$4^1 10b^1$	$718^{a,b}$	32	$797^{a,b}$, 808^d	13, 2	3
				ΔE to the experimental wavenumber ~1130 cm^{-1} (peak C)	
$10a^1 16a^1$	$802^{a,b}$	52	$1157^{a,b}$	27	3
				ΔE to the experimental wavenumber ~1340 cm^{-1} (peak D)	
$16a^1 17a^1$	$736^{a,b}$	14	$1342^{a,b}$	2	3

Table 3-11: Assignments for the dark state in S_1. Predicted wavenumbers are based on fundamental wavenumbers from a) calculations, b) Ref 6, c) Ref 8, d) Ref 17. 15^2 is included due to calculated wavenumbers, discrepancy between predicted wavenumbers of level 15^2 in the ion is discussed in section 3.5.1.

Of the four vibrational levels shown in Table 3-11 only three can be potential dark state assignments because vibrational level $10a^1 16a^1$ was assigned in the previous section as the dark vibrational level coupled to 1^1 in S_1 resulting in the ~8 ps oscillations. Therefore, it cannot also be the cause of the ~16 ps oscillations here. The three remaining vibrational levels all involve ΔN = 3 relative to level 1^1 however, there is nothing to recommend the assignments for peaks B or C over D whereas the time-dependent behaviour of D (out of phase oscillations) does support the assignment. So given that there is also good agreement between the predicted and experimental S_1 and ion state wavenumbers, the dark state in S_1 is assigned to $16a^1 17a^1$.

3.6. Summary and conclusion

SEVI and time-resolved photoelectron spectra have been recorded *via* multiple intermediate S_1 wavenumbers below ~1000 cm^{-1} in order to assign vibrational levels and probe energy dispersal. The S_1 bright vibrational levels excited at each position of the pump laser are shown in Figure 3-26 and pertinent normal vibrational modes are shown in Figure 3-27.

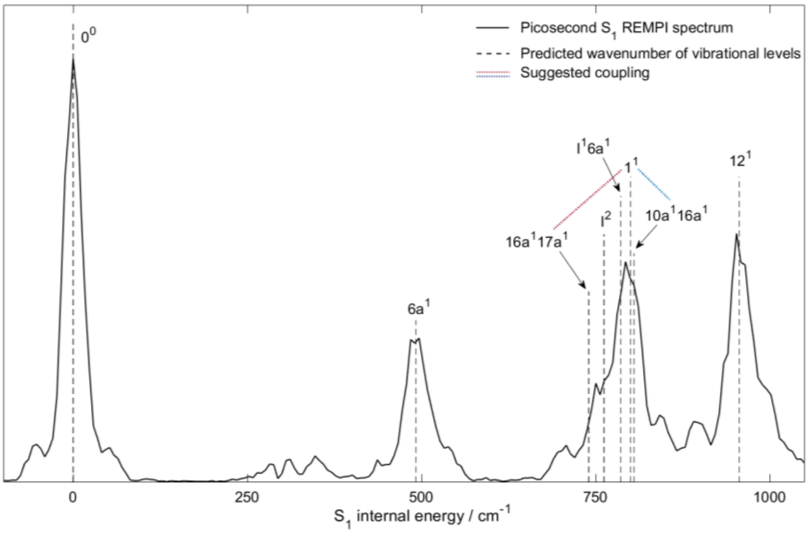

Figure 3-26: Summary of the vibrational levels below S_1 0^0 + ~1000 cm^{-1} which were excited in this study and the suggested couplings.

Only restrictive IVR or no time dependence was observed in these data sets, in line with expectations for low energy vibrations. The two vibrational levels exhibiting no time-dependence were S_1 $6a^1$ and S_1 12^1 at ~490 cm^{-1} and ~950 cm^{-1} in the S_1 electronic state respectively. The lack of time-dependence means there is no evidence for coupling and the transfer of energy in either case. Notably, restrictive energy redistribution was observed via the lower wavenumber S_1 1^1 vibration emphasising that restrictive IVR is heavily dependent on coincidental vibrational wavenumbers. The time-resolved photoelectron spectra measured following excitation at 800 cm^{-1} in S_1 showed oscillations with an average period of 8.72 ± 0.21 ps, this was attributed to coupling between level 1^1 and a dark vibrational level tentatively assigned as $10a^1 16a^1$. When the pump laser was fixed at ~750 cm^{-1} in S_1, multiple $S_1 \leftarrow S_0$ transitions were excited which were assigned to 1^1_0, $\mathrm{I}^1_1 6a^1_0$ and I^2_0. The corresponding time-resolved photoelectron spectra showed two types of behaviour, some peaks showed no time-dependence whereas peaks assigned 0^0, 1^1 (Δv = 0) and 1^2 showed intensity oscillations with an average period of 15.90 ± 0.22 ps. This was attributed to coupling between S_1 level 1^1 and a dark vibrational level tentatively assigned S_1 $16a^1 17a^1$. There is no evidence to suggest the other S_1 vibrational levels, resulting from the $I^1_1 6a^1_0$ and I^2_0 transitions, are coupled. The suggested coupling interactions are also shown on Figure 3-26.

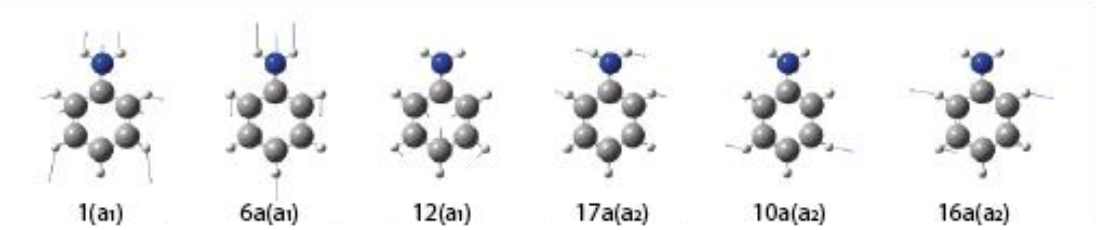

Figure 3-27: Pertinent normal vibrational modes.

3.7. References

---

[1] M. J. Frisch, G. W. Trucks, H. B. Schlegel, G. E. Scuseria, M. A. Robb, J. R. Cheeseman, G. Scalmani, V. Barone, B. Mennucci, G. A. Petersson, H. Nakatsuji, M. Caricato, X. Li, H. P. Hratchian, A. F. Izmaylov, J. Bloino, G. Zheng, J. L. Sonnenberg, M. Hada, M. Ehara, K. Toyota, R. Fukuda, J. Hasegawa, M. Ishida, T. Nakajima, Y. Honda, O. Kitao, H. Nakai, T. Vreven, J. A. Montgomery, Jr., J. E. Peralta, F. Ogliaro, M. Bearpark, J. J. Heyd, E. Brothers, K. N. Kudin, V. N. Staroverov, R. Kobayashi, J. Normand, K. Raghavachari, A. Rendell, J. C. Burant, S. S. Iyengar, J. Tomasi, M. Cossi, N. Rega, J. M. Millam, M. Klene, J. E. Knox, J. B. Cross, V. Bakken, C. Adamo, J. Jaramillo, R. Gomperts, R. E. Stratmann, O. Yazyev, A. J. Austin, R. Cammi, C. Pomelli, J. W. Ochterski, R. L. Martin, K. Morokuma, V. G. Zakrzewski, G. A. Voth, P. Salvador, J. J. Dannenberg, S. Dapprich, A. D. Daniels, Ö. Farkas, J. B. Foresman, J. V. Ortiz, J. Cioslowski, and D. J. Fox, *Gaussian 09* (Gaussian, Inc., Wallingford CT, 2009).

[2] R. Scheps, D. Florida, and S.A. Rice, *J. Chem. Phys.*, 1974, **61**, 1730-1747.

[3] J. C. D. Brand, D. R. Williams and T. J. Cook, *J. Mol. Spec.*, 1966, **20**, 359-380.

[4] W. E. Sinclair and D. W. Pratt, *J. Chem. Phys.*, 1996, **105**, 7942-7956.

[5] M. Quack and M. Stockburger, *J. Mol. Spec.*, 1972, **43**, 83-116.

[6] X. Zhang, J.M. Smith, J. L. Knee, *J. Chem. Phys*, 1992**, 97**, 2843-2860.

[7] J. T. Meek, E. Sekreta, W. Wilson, K.S. Viswanathan and J.P. Reilly, *J. Chem. Phys.*, 1985, **82**, 1741-1749.

[8] M. A. Smith, J. W. Hager, S. C. Wallace, *J. Chem. Phys.*, 1984, **80**, 3097-3105.

[9] J. Hager, M. A. Smith and S. C. Wallace, *J. Chem. Phys.*, 1986, **84**, 6771-6780.

[10] B. Kim and P. M. Weber, *J. Phys. Chem.*, 1995, 99, 2583-2588.

[11] J. M. Hollas, M. R. Howson, T. Ridley, and L. Halonen, *Chem. Phys. Lett.*, 1983, **98**, 611-614.

[12] Y. Honda, M. Hada, M, Ehara and H. Nakatsuji, *J. Chem. Phys.*, 2002, **117**, 2045-2052.

[13] N. Mikami, A. Hiraya, I. Tujiwara, and M. Ito, *Chem. Phys. Lett.*, 1980, **74**, 531-535.

[14] J. Christoffersen, J. M. Hollas and G. H. Kirby, *Mol. Phys.*, 1969, **16**, 441-452.

[15] Z. Qu, Z. Qin, X. Zheng, H. Wang, G. Yao, X. Zhang, Z. Cui., Spectrochimica Acta Part A: Molecular and Biomolecular Spectroscopy, 2017, **173**, 432-438.

[16] D. A. Chernoff, S. A. Rice., *J. Chem. Phys.*, 1979, **70**, 2511-2520.

[17] X. Song, M. Yang, E. R. Davidson and J. P. Reilly, *J. Chem. Phys.*, 1993, **99**, 3224-3233.

[18] G. M. Roberts, C. A. Williams, J. D. Young, S. Ullrich, M. J. Paterson and V. G. Stavros, *J. Am. Chem. Soc.*, 2012, **134**, 12578-12589.

[19] A. M. Gardner, W. D. Tuttle, L. E. Whalley and T. G. Wright, *Chem. Sci.*, 2018, **9**, 2270-2283.

---

[20] W. D. Tuttle, A. M. Gardner, L. E. Whalley and T. G. Wright, *J. Chem. Phys.*, 2017, **146**, 244310.

[21] A. M. Gardner and T. G. Wright, *J. Chem. Phys*. 2011**, 135**, 114305.

[22] A. M. Gardner, Ph.D thesis, 2013.

[23] G. Varsányi, Assignments of the Vibrational Spectra of Seven Hundred Benzene Derivatives (Wiley, New York, 1974), Vols. I and II.

[24] G. Herzberg, Molecular Spectra and Molecular Structure II: Infrared and Raman Spectra of Polyatomic Molecules (Krieger, 1945)

[25] J. Midgley, J. A. Davies and K. L. Reid, *J. Phys. Chem. Lett.*, 2014, **5**, 2484-2487.

[26] Jonathan Midgley, PhD. Thesis, 2013.

[27] A. M. Gardner, W. D. Tuttle, L. E. Whalley, T. G. Wright., *Chem. Sci*., 2018, **9**, 2270-2283.

[28] J. R. Gascooke and W. D. Lawrance, *J. Chem. Phys*., 2018, **138**, 134302.

[29] J. A. Davies, A. M. Green, A. M. Gardner, C. D. Withers, T. G. Wright and K. L. Reid, *Phys. Chem. Phys. Chem*., 2014, **16**, 430-443

4. Investigating the 1200-1650 cm^{-1} region of the S$_1$ electronic state of aniline

4.1. Chapter overview

This chapter focuses on the ~1200-1650 cm^{-1} region of the $S_1 \leftarrow S_0$ REMPI spectrum of aniline; the pump laser was used to excite four positions: (i)~1260 cm^{-1}, (ii)~1300 cm^{-1}, (iii)~1450 cm^{-1} and (iv)~1600 cm^{-1} and these positions are labelled in Figure 4-1. SEVI spectra and time-resolved photoelectron spectra measured *via* each position are presented in the following subsections; refer to figure 8.17 in the appendix for normal mode diagrams.

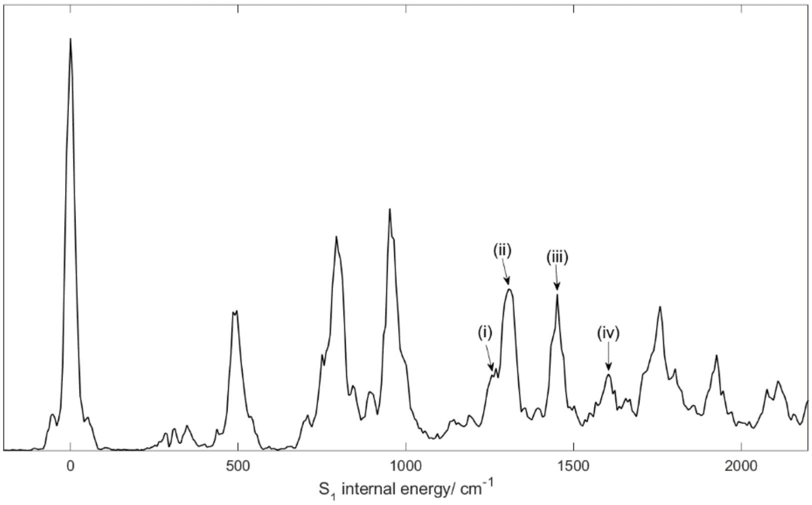

Figure 4-1: $S_1 \leftarrow S_0$ REMPI spectrum of aniline. The REMPI features at (i)~1260 cm^{-1}, (ii) ~1300 cm^{-1}, (iii) ~1450 cm^{-1} and (iv) ~1600 cm^{-1} were excited. Wavenumbers are rounded to nearest ~10 cm^{-1}.

4.2. S$_1$ feature at ~1200-1400 cm^{-1}

The broad lowest wavenumber feature in the ~1200-1400 cm^{-1} region of the REMPI spectrum has an obvious shoulder indicative of unresolved vibrational levels. Therefore, photoelectron spectra were measured *via* both the maximum of the REMPI feature at ~1300 cm^{-1}, labelled position (ii), and the shoulder at ~1260 cm^{-1}, labelled position (i). This subsection includes assignment and analysis of both sets of spectra; the spectra measured at position (ii) at ~1300 cm^{-1} are somewhat simpler so will be discussed first.

4.2.1. Photoelectron spectra via position (ii) / S_1 0^0 + ~1300 cm^{-1}

4.2.1.1. Assignment of vibrational levels

Figure 4-2 is the 0 ps SEVI spectrum measured *via* ~1300 cm^{-1}/position (ii) in the S_1 REMPI spectrum in Figure 4-1. Five relatively intense peaks appear in the SEVI spectrum between ~1000 - 3000 cm^{-1}; by far the most intense is the peak centred at ~1330 cm^{-1} which is assigned to the $\Delta v = 0$ transition from S_1.

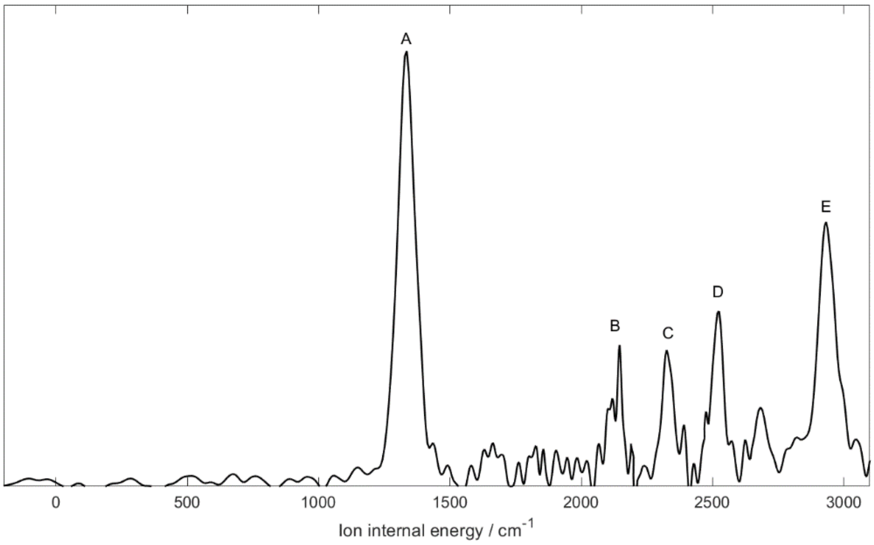

Figure 4-2: 0 ps SEVI spectrum measured via ~1300 cm^{-1} (position (ii)) in S_1.

At lower wavenumbers in the REMPI spectrum, the strong features at ~490 cm^{-1} and ~800 cm^{-1} were assigned to the $6a^1$ and 1^1 vibrational levels respectively (see Chapter 3). Thus, the combination level $1^1 6a^1$ should be expected at ~1290 cm^{-1} in S_1, this is in good agreement with the experimental vibrational wavenumber of the REMPI feature at ~1300 cm^{-1}. A vibration around this wavenumber has been assigned to this combination band in S_1 in previous work.[1,2,3] Furthermore, as shown in Table 4-1, combination level $1^1 6a^1$ is expected at ~1328-1335 cm^{-1} in the photoelectron spectrum,[1,4] this is in excellent agreement with SEVI peak A at ~1330 cm^{-1}. The wavenumbers of SEVI peaks A-E in Figure 4-2 are included in Table 4-1 alongside assignments to vibrational levels. Notably, the bright state assignment is supported by the assignment of the SEVI peaks at ~2130 cm^{-1} and ~2930 cm^{-1} to $1^2 6a^1$ and $1^3 6a^1$ respectively, showing a progression in mode 1. However, although Δv_1=+1 and Δv_1=+2 are observed, there is no obvious Δv_1=-1 peak, meaning no strong feature assignable to either level $6a^1$ or level 1^1.

There is an alternative possibility, the S_1 feature at ~1300 cm^{-1} could be assigned to the 13^1 level. This would be consistent with the work of Meek et al. who assigned a REMPI feature at 1308 cm^{-1} to the $S_1 \leftarrow S_0$ 13^1_0 transition.[5] In their resulting photoelectron spectrum, which has a similar profile to that shown in Figure 4-2, the strongest feature was a peak at ~1347 cm^{-1} which was assigned to the 13^1 vibrational level.[5] This is consistent with the wavenumber of the strongest peak in Figure 4-2 which is at ~1330 cm^{-1}. Other studies have assigned 13^1 in the $S_1 \leftarrow S_0$ excitation spectrum alongside level $1^1 6a^1$.[1,2,3,6] If this assignment is correct, the photoelectron peaks at ~1330 cm^{-1}, ~2130 cm^{-1} and ~2930 cm^{-1} in Figure 4-2 could be assigned to the progression 13^1, $13^1 1^1$, $13^1 1^2$, also a progression in mode 1. However, as shown in Table 4-1, the predicted wavenumbers of these levels show poorer agreement to the experimental wavenumbers of peaks A, B and E compared to the $1^1 6a^1$, $1^2 6a^1$, $1^3 6a^1$ progression. Based on the SEVI spectrum alone, it cannot be determined whether 13^1 or $1^1 6a^1$ is the more likely assignment or whether both have been excited; examination of the time-dependent photoelectron spectra in section 4.2.1.2 will be used to probe this in more detail.

Ion Internal energy / cm^{-1}	Cation vibrational level	Predicted wavenumber of cation vibrational level / cm^{-1}
A - 1330	$\mathbf{1^1 6a^1}$ 13^1	1328[a], 1329[b], 1323[c], 1335[d] 1378[b], 1347[c], 1385[d]
B - 2130	$\mathbf{1^2 6a^1}$ $1^1 13^1$ $6a^1 9a^1$ $8a^1 12^1$	2135[a], 2139[b], 2121[c], 2147[d] 2188[b], 2145[c], 2197[d] 2114[a], 2126[b], 2113[c], 2115[d] 2156[a], 2170[b]
C - 2330	$1^1 6a^1 19a^1$ $1^1 6a^1 12^1$ $12^1 13^1$ $8a^2$	2321[a], 2320[b], 2328[d] 2311[a], 2301[b], 2315[d] 2371[a], 2350[b], 2315[c], 2365[d] 2374[a], 2368[b], 2339[c], 2374[d]
D - 2520	$1^1 6a^1 8a^1$ $6a^2 18a^1$ $8a^1 13^1$ $6a^1 19a^2$	2515[a], 2513[b], 2492[c], 2522[d] 2534[b], 2468[c] 2575[a], 2562[b], 2516[c], 2572[d] 2507[a], 2501[b]
E - 2930	$\mathbf{1^3 6a^1}$ $1^1 6a^1 9a^1$ $1^1 8a^1 12^1$ $1^2 13^1$ $12^2 19a^1$ 12^3 $12^1 19a^2$	2942[a], 2949[b], 2928[c], 2961[d] 2936[a], 2921[b] 2966[a], 2977[b] 3002[a], 2998[b], 2952[c], 3011[d] 2959[a], 2935[b], 2954[d] 2949[a], 2916[b], 2895[c], 2940[d] 2969[a], 2954[b], 2968[d]

Table 4-1: Suggested assignments for peaks A-E in Figure 4-2. Predicted wavenumbers are determined from fundamental wavenumbers from a) Ref 4, b) calculations, c) Ref 5 and wavenumbers from d) Ref 1. Reported wavenumbers are rounded to nearest ~10 cm^{-1}.

4.2.1.2. Analysis of time-resolved photoelectron spectra

Photoelectron spectra were measured *via* ~1300 cm^{-1} in S_1 at a series of time delays between 0 ps and 500 ps; six of these are shown in Figure 4-3. While each peak, including the Δv = 0 peak at ~1330 cm^{-1} (peak A), is still observed with significant intensity up to 500 ps, changes can be seen in the relative intensities of the peaks with time delay; this is particularly noticeable for the three adjacent peaks in the ~2000-2600 cm^{-1} region of each spectrum.

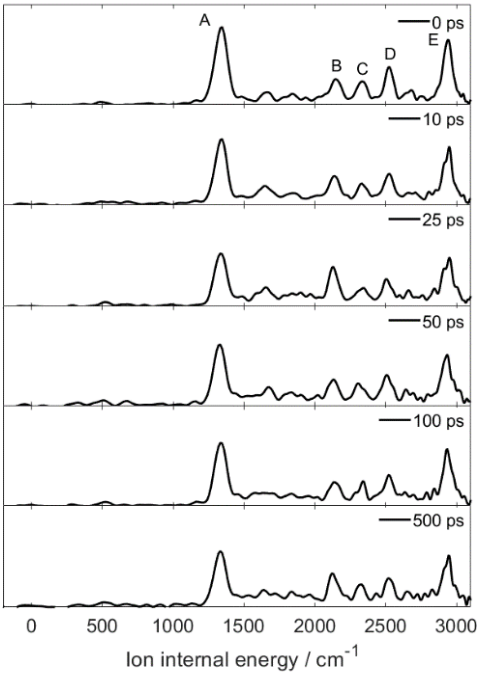

Figure 4-3: Photoelectron spectra measured via ~1300 cm^{-1} (position (ii)) in S_1 at six different time delays.

To investigate the time-dependence, the intensities of photoelectron peaks A-E have been plotted as a function of pump-probe time delay to give the plots in Figure 4-4; from which two main deductions can be made. Firstly, because the average intensity of the photoelectron peaks is similar at early time delays and >200 ps, this suggests the bright state is still populated by 500 ps meaning it is unlikely the bright state is coupled to bath states as this would lead to the continual loss of population (dissipative energy dispersal). Consistent with this is the absence of any apparent increase in baseline intensity or congestion underneath the peaks. Secondly, peak B shows clear oscillations in intensity; the period of which is ~50 ps. Unfortunately due to the long oscillation period, the data points only capture 1-2 oscillations (the data points between 50-100 ps are at larger intervals). The changes in intensity occurring with time delay for peak A, C, D and E are a lot less obvious, especially peaks D and E. A weak loss of intensity can be seen with increasing time delay from 0 ps for these peaks, but a small recurrence in intensity above ~25 ps is only noticeable for peaks A and C; the error bars, which are not included in the fits, are conservative due to the width of the base of the peaks compared to FWHM (see Chapter 2). The most likely rationale, given the time profile of peak B, is that restrictive IVR is occurring but the intensity oscillations of peaks A, C, D and E are very shallow and not noticeable especially because there are few data points after 50 ps. This must be the case because otherwise peak B would not be able to oscillate and gain intensity with time delay after 0 ps, population must be transferring from another state. The lack of clear oscillations could occur for different reasons; for example a photoelectron peak may result from overlapping out of phase transitions (within the resolution of the experiment) or a cation vibrational level may have similar Franck-Condon factors to both the bright and dark state.

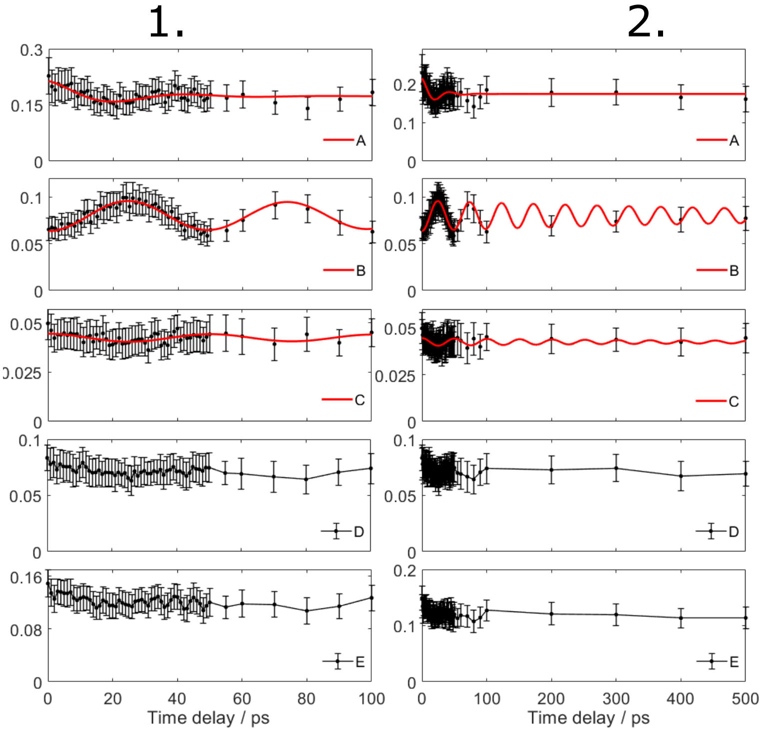

Figure 4-4: Time profiles showing the fits of the time-dependent intensities of photoelectron peaks A-C and the time-dependent intensities of peaks D and E. Column 1: 0 - 100 ps and column 2: 0 - 500 ps.

To extract an oscillation period, the time-dependent intensities of peaks A-C up to 500 ps were fit to equation 2.4. (see chapter 2), fitting oscillations was not possible for peaks D and E as the intensity changes are particularly weak. Table 4-2 contains the results of the fits shown in Figure 4-4, as decay/loss of intensity is not apparent the τ_1 values are not shown as they are large with large associated error bars. The oscillation periods determined for photoelectron peaks A-C are consistent within error bars and give an average period of 48 ± 4 ps which corresponds to an eigenstate separation of 0.7 ± 0.1 cm^{-1}. Ideally, further work should involve recording additional spectra at time delays after 50 ps, this could serve to reduce the error bar associated with the oscillation periods.

Peak/ Plot	A	B	τ_{osc}	Rsq
A	1.00	0.23	44 ± 6	0.57
B	0.46	-0.09	49 ± 1	0.92
C	0.24	0.01	50 ± 5	0.33

Table 4-2: Values determined from the fits shown in Figure 4-4. Column A and B are normalised.

The fact that peak B shows minimum intensity at 0 ps, with maximum intensity at ~24 ps suggests the growth of a photoelectron peak resulting from the coupled dark state in S_1 which gains population with increasing time delay after 0 ps. The other photoelectron peaks A,C,D,E show intensity losses from 0 ps suggesting they reflect population of the bright state. Figure 4-5 shows photoelectron spectra measured at 0 ps and 24 ps; the spectrum at ~24 ps (half the oscillation period) should show transitions from the dark state in S_1. Peak B is at ~2130 cm^{-1} so while it is relatively intense at 24 ps and more intense at 24 ps than 0 ps, it is unlikely to result from the $\Delta v = 0$ transition from the dark state in S_1. This is because the dark state must have a wavenumber of around 1300 cm^{-1} in S_1 in order to couple to the bright state and it is unlikely that a vibration will show a wavenumber change of ~1300 cm^{-1} to 2130 cm^{-1} upon ionization. A more likely scenario is that the $\Delta v = 0$ $D_0^+ \leftarrow S_1$ transition from both the bright and dark state vibrations are overlapped (within experimental resolution) at peak A, although this peak shows maximum intensity at 0 ps, it remains the most intense at 24 ps.

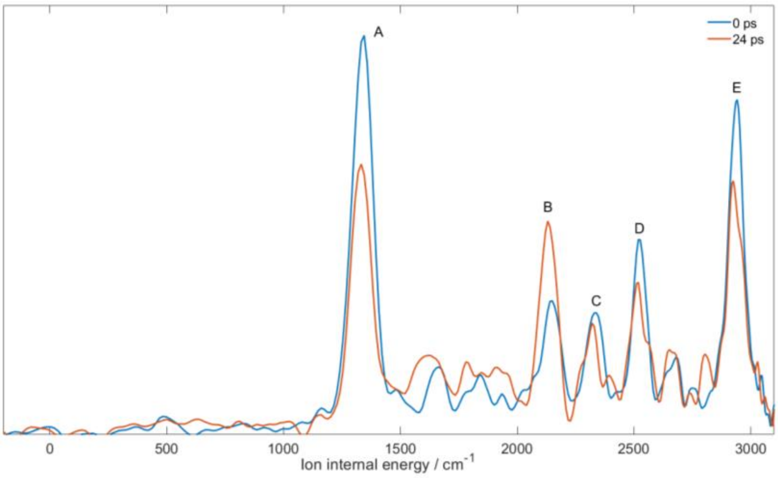

Figure 4-5: Photoelectron spectra measured via ~1300 cm^{-1} in S_1 at time delays of 0 ps (blue) vs 24 ps (red).

By the same token, peak B (which also has significant intensity at 0 ps) probably results from two overlapping out of phase transitions. Assuming the dark state is a vibration with an S_1 wavenumber of ~1300 cm^{-1} and a cation wavenumber of ~1330 cm^{-1}, a search has been conducted. Vibrational levels found which match the energy constraints ± 60 cm^{-1} are shown in Table 4-3. As anharmonic coupling strength is expected to decrease as change in the total number of vibrational quanta (ΔN) increases,[7,8] the levels are ordered by ΔN relative to the levels 1^16a^1 and 13^1 which are the two most likely assignments for the bright state (4.2.1.1).

Vibrational level	Predicted S_1 wavenumber / cm^{-1}	ΔE relative to ~1300 cm^{-1}	Predicted cation wavenumber / cm^{-1}	ΔE relative to ~1330 cm^{-1}	ΔN relative to 1^16a^1	ΔN relative to 13^1
1^16a^1	1314[a], 1292[b], 1291[d],	14, 8, 9	1329[a], 1328[b], 1323[c], 1335[f]	1, 2, 7, 5	-	3
13^1	1316[a], 1308[c], 1311[d],	16, 8, 11	1378[a], 1388[b], 1347[c], 1385[f]	48, 58, 17, 55	3	-
$6a^115^2$	1262[a], 1254[b], 1194[d],	38, 46, 106	1289[a], 1623[b], 1620[f], 1269[e]	41, 293, 290, 61	3	4
$10b^219a^1$	1336[a,b]	6	1343[a], 1347[b], 1352[f]	13, 17, 22	5	4
$10b^212^1$	1304[b],	4	1324[a], 1337[b], 1338[f]	6, 7, 8	5	4

Table 4-3: Assignments for the dark state. Predicted wavenumbers are determined from fundamental wavenumbers from a) calculations, b) Ref 4, c) Ref 5, d) Ref 2, e) Ref 9, f) Ref 1.

Three levels were found showing $\Delta N = 3$ which was the lowest change in quanta found, these were 1^16a^1, 13^1 and $6a^115^2$. Although, there is some doubt over an assignment of $6a^115^2$ because there is some discrepancy over the fundamental vibrational wavenumber reported for mode 15. Further, the bright state was assigned as either 1^16a^1 or 13^1, removing one of the three vibrational levels as a potential assignment for the coupled dark level. Based on ΔN, ΔE_{S1} and ΔE_{ion} the more likely assignment appears to be either level 1^16a^1 or 13^1 (depending on which level is assigned as the bright state); both are of A_1 symmetry so could couple anharmonically. Importantly, if two bright states were coherently excited, the wavepacket would be expected to evolve with time, however, in this case all peaks would be expected to oscillate with the same phase. The fact that the photoelectron peak at ~2130 cm^{-1} shows out of phase oscillations in intensity, indicates the transfer of vibrational population between two levels with one being dark. So if this time-dependent behaviour is a manifestation of coupling between S_1 1^16a^1 and S_1 13^1, both cannot be 'bright' and one of the following must be true;

either the bright state is $S_1\ 1^1 6a^1$ and the dark state is $S_1\ 13^1$, or the bright state is $S_1\ 1^1 6a^1$ and the dark state is $S_1\ 13^1$. In either case the intensity of peak A would result from both the bright and the dark state at different times.

In section 4.2.1.1 it was discussed that the photoelectron peaks A, B and E, at ~1330 cm^{-1}, ~2130 cm^{-1} and ~2930 cm^{-1} could be assigned to the progression $1^n 6a^1$ (n = 1, 2, 3) and/or the progression $1^n 13^1$ (n = 0, 1, 2). If it is the projection of level $S_1\ 1^1 6a^1$ onto the cation vibrational levels that gives rise to the observed progression in the $1^n 6a^1$ (n = 1, 2, 3) vibrations, then the non-observance of the $6a^1$ band (and to some extent the 1^1 vibration) is unexpected. However, if projection of the $S_1\ 13^1$ level onto the cation vibrational levels is responsible for the progression $1^n 13^1$ (n = 0, 1, 2), then non-observance of either the fundamental $6a^1$ or 1^1 is perhaps expected. By 24 ps, B has gained significant intensity so that peaks A, B and E, which are the most intense, are of comparable intensity. This, combined with the apparent non-observance of a band with similar intensity for the $6a^1$ vibration suggests level $1^1 13^1$ is the more likely assignment for photoelectron peak B at 24 ps. For these reasons, level 13^1 is tentatively assigned as the dark state and level $1^1 6a^1$ tentatively assigned as the bright state; this would result in the assignments given Table 4-4. In line with this, when comparing the spectra at 0 ps *vs* 24 ps in Figure 4-3 and Figure 4-5, a very weak band slightly above the noise level in the baseline, is highlighted in the 0 ps spectrum at ~500 cm^{-1}, in agreement with the fundamental wavenumber of the 6a mode. More confidence in these conclusions would be gained if small changes in peak position could be observed and overlapping transitions better resolved in the photoelectron spectrum; recording SEVI spectra at 24 ps would be the first step in working towards this.

Photoelectron peak	Ion internal energy / cm^{-1}	Assignment at 0 ps	Assignment at 24 ps
A	~1330	$1^1 6a^1$	13^1
B	~2130	$1^2 6a^1$ $6a^1 9a^1$ $8a^1 12^1$	$13^1 1^1$
E	~2930	$1^3 6a^1$ $1^1 6a^1 9a^1$ $1^1 8a^1 12^1$ $12^2 19a^1$ 12^3 $12^1 19a^2$	$13^1 1^2$

Table 4-4: Potential assignments for the photoelectron peaks A, B and E at 0 ps versus 24 ps. Reported wavenumbers are rounded to nearest ~10 cm^{-1}.

4.2.2. Photoelectron spectra via position (i)/ S_1 0^0 + ~1260 cm^{-1}

4.2.2.1. Assignment of vibrational levels

Figure 4-6 is the 0 ps SEVI spectrum measured *via* ~1260 cm^{-1} in S_1. Identifying the peak resulting from the $\Delta v = 0$ transition from S_1 is somewhat complicated here because there are three relatively intense SEVI peaks lying at ~1330 cm^{-1}, ~1610 cm^{-1} and ~1840 cm^{-1}, any of which could reasonably result from a $\Delta v = 0$ transition. More congestion is apparent in the baseline of this spectrum compared to Figure 4-2; the presence of congestion/unresolved structure in a 0 ps photoelectron spectrum, particularly at higher wavenumbers, could be an indication that eigenstates resulting from coupling of the bright zero order state lie outside the bandwidth of the pump laser. It could also result from the excitation of multiple bright states leading to overlapping Franck-Condon projections populating numerous close lying ion states.

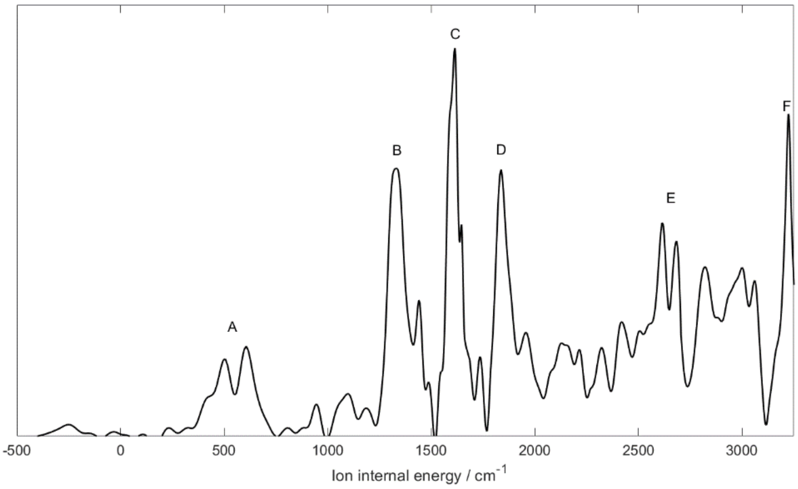

Figure 4-6: 0 ps SEVI spectrum measured via ~1260 cm^{-1} in S_1.

In Chapter 3, I^2 was assigned at ~760 cm^{-1} in the S_1 REMPI spectrum, the S_1 band excited here lies ~500 cm^{-1} above I^2, this difference is in good agreement with the wavenumber of level S_1 $6a^1$ which is ~492 cm^{-1}.[4] Therefore, the combination level $I^2 6a^1$, if present, would be observed in this region of the REMPI spectrum, this level has been assigned in fluorescence excitation spectra.[2,3] Consistent with this assignment, $I^2 6a^1$ is expected at ~1844 cm^{-1} in the cation, in good agreement to SEVI peak D at ~1840 cm^{-1} in Figure 4-6. Therefore, $I^2 6a^1$ is assigned.

SEVI peak B at ~1330 cm^{-1} in Figure 4-6 is at the same wavenumber as the most intense peak in the 0 ps SEVI spectrum in Figure 4-2 which was measured *via*

~1300 cm^{-1} in S$_1$. It is likely that both peaks could be the same vibrational level; therefore SEVI peak B is also assigned to $1^1 6a^1$ (refer to section 4.2.1) However, here, B could result from either a $\Delta v = 0$ (meaning multiple bright states are excited) or $\Delta v \neq 0$ transition. Pertinently, Brand and co-workers showed that the rotational profiles of the 1^1_0, $\mathrm{I}^1_1 6\mathrm{a}^1_0$ and I^2_0 bands substantially overlap.[5,6] This was also observed in this work (Chapter 3), photoelectron peaks were observed as a result of D$_0$ ← S$_1$ $\Delta v = 0$ transitions from both 1^1 and I^2 following excitation at ~750 cm^{-1}. It follows then that the transitions $1^1_0 6\mathrm{a}^1_0$ and $\mathrm{I}^2_0 6\mathrm{a}^1_0$ could overlap, which would be consistent with the SEVI peaks at ~1330 cm^{-1} and ~1840 cm^{-1} assigned $1^1 6a^1$ and $\mathrm{I}^2 6a^1$ respectively, both being relatively intense. The possibility of also exciting $\mathrm{I}^1_1 6\mathrm{a}^2_0$ was considered; however while the exciting pump pulse at ~1260 cm^{-1} could have overlapped $\mathrm{I}^1 6a^2$ based on the predicted S$_1$ wavenumbers shown in Table 4-5, the absence of a clear peak in the SEVI spectrum at ~1700 cm^{-1} means there is no evidence of this occurring.

Vibrational level	Predicted S$_1$ wavenumber / cm^{-1}	Predicted cation wavenumber / cm^{-1}
$\mathrm{I}^2 6a^1$	1254[a], 1250[b], 1247[d], 1246[e]	1844[a], 1831[b], 1848[c]
$1^1 6a^1$	1292[a],1290[b], 1288[c/f], 1291[d/e]	1328[a], 1315[b], 1335[c]
$\mathrm{I}^1 6a^2$	1278[a], 1266[e], 1269[f]	1698[a], 1677[b]

Table 4-5: Predicted S$_1$ and ion vibrational wavenumbers for levels discussed in the text based on fundamental wavenumbers from a) Ref 4 , b) Ref 5 and wavenumbers from c) Ref 1, d) Ref 2, e) Ref 3, f) Ref 6

SEVI peak C at ~1610 cm^{-1} is the most intense of the three SEVI peaks seen in Figure 4-6. Suggested assignments are shown in Table 4-6, but relatively few vibrational levels can account for a wavenumber in the cation which is ~350 cm^{-1} higher than in the S$_1$ electronic state, with many aniline vibrations displaying similar energies in the S$_1$ and ion electronic states. Only two of the vibrational levels listed in Table 4-6, $10a^2$ and 11^2 , would be observed in the cation owing to a $\Delta v=0$ transition from S$_1$. The fundamental wavenumbers of these vibrations have not been assigned in literature so calculated wavenumbers are reported in Table 4-6, with level 11^2 showing poorer agreement to the experimental wavenumbers. The other two possible assignments for peak C, 1^2 and $9a^1$, could not have been excited in S$_1$ at this position of the pump laser and would only be observed as $\Delta v \neq 0$ transitions from an S$_1$ bright state with a different vibrational identity, either $1^1 6a^1$ or $\mathrm{I}^2 6a^1$ based on the discussions above. While the modes involved might make 1^2 or $9a^1$ seem like more reasonable assignments over $10a^2$ and 11^2, in fact an assignment of either 1^2 or $9a^1$ is currently less likely because the intensity of peak C relative to the other peaks in the SEVI spectrum is consistent with C originating from a $\Delta v = 0$ transition from S_1. Further, the time-resolved photoelectron spectra, which will be introduced in section 4.2.2.2, also supports the theory that a third $S_1 \leftarrow S_0$ transition was excited.

Vibrational levels	Predicted S_1 wavenumber / cm^{-1}	Predicted cation wavenumber / cm^{-1}
$10a^2$	1250^a	1604^a
11^2	1272^a	1570^a
1^2	1616^a,	1620^a, 1614^b, 1605^c, 1627^e
$9a^1$	1519^a,	1607^a, $1593^{b/e}$, 1581^c

Table 4-6: Assignments for the SEVI peak at ~1610 cm^{-1} in Figure 4-6. Predicted wavenumbers are determined from fundamental wavenumbers from a) calculations and b) Ref 4, c) Ref 5, d) Ref 3, e) Ref 1.

Table 4-7 contains vibrational level assignments for the other SEVI peaks A,E,F in Figure 4-6, above 2000 cm^{-1} there is quite a lot of intensity but little resolved structure so only the more intense, resolved features have been focussed on.

Ion internal energy / cm^{-1}	Cation vibrational level	Predicted cation wavenumber / cm^{-1}
A - 500	**$6a^1$**	519^a, 521^b, 522^c
A - 610	$10b^1 16b^1$	617^a, $618^{a,b}$,624^c
B - 1330	**$1^1 6a^1$**	1329^a, 1328^b, 1335^c
B - 1440	$18a^1$ $1^1 10b^1 16b^1$ $5^1 16b^1$	1496^a 1427^a, 1442^c 1438^a
C - 1610	$10a^2$ 1^2 $9a^1$ 11^2	1604^a 1620^a, 1614^b, 1627^c 1607^a, $1593^{b/c}$, 1581^d 1570^a
D - 1840	**$I^2 6a^1$** $1^1 6a^2$	1844^b, 1848^c 1848^a, 1849^b, 1857^c
E - 2620	I^4 $1^2 19a^1$ $1^2 12^1$ $6a^2 9a^1$	2646^b, 2650^c 2611^a, 2607^b, 2622^c 2592^a, 2597^b, 2607^c 2645^a, 2635^b, 2637^c
E - 2680	$1^2 6a^2$ $8a^1 18a^1$	2658^a, 2656^b, 2669^c 2680^a, 2606^c
F - 3220	$10a^4$ 1^4 $I^2 12^2$ $9a^2$ 11^4 (combinations of levels at 1610 cm^{-1})	3208^a 3240^a, 3228^b, 3254^c 3289^b,3284^c 3214^a, $3186^{b/c}$, 1570^a

Table 4-7: Assignments for SEVI peaks in Figure 4-6 and predicted wavenumbers based on fundamentals from a) calculations, b) Ref 4 and wavenumbers from c) Ref 1, d) Ref 5. Wavenumbers are rounded to nearest ~10 cm^{-1}.

4.2.2.2. Analysis of time-resolved photoelectron spectra

Figure 4-7 shows photoelectron spectra measured *via* ~1260 cm^{-1} in S$_1$ at six different time delays between 0 ps and 500 ps. With increasing time delay there is a noticeable change in the relative intensities of the three intense peaks B, C and D as well as region G which is between photoelectron peaks C/D and indicates a peak which is not fully resolved. Given that above 2000 cm^{-1} there is not much resolved structure, even in the 0 ps spectrum, it is difficult to identify an increase in baseline or loss of peak intensity in this region.

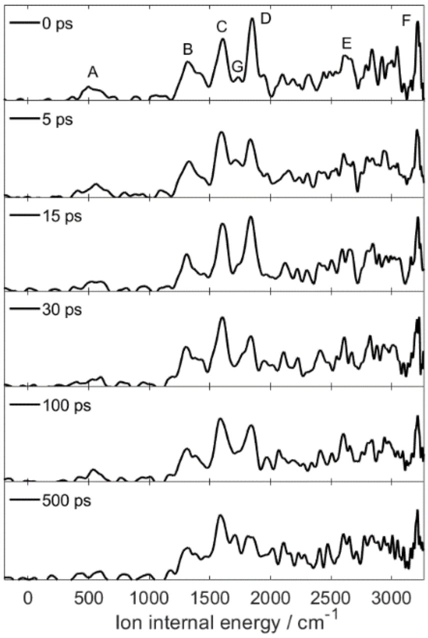

Figure 4-7: Photoelectron spectra measured via ~1260 cm^{-1} in S$_1$ at six different time delays.

Analysis of the time-resolved spectra is shown below however it has proven difficult, largely because multiple S$_1$ ← S$_0$ transitions were excited at 1260 cm^{-1} meaning that each photoelectron spectrum measured was a combination of the individual photoelectron spectra that would be measured for each S$_1$ vibrational level. This complicated analysis for a number of reasons; firstly, (as shown in the following pages) more than one of these S$_1$ bright states was involved in coupling to other states, meaning different time-dependent behaviour for different peaks. Secondly, some photoelectron peaks appeared to result from two or more overlapping transitions originating from different bright states in S$_1$ complicating the time-dependent behaviour displayed. Thirdly, it proved difficult to measure the intensity of some "peaks" or features because of the congestion/unresolved structure in the photoelectron spectrum. Lastly, it was hard to identify any intensity which should be associated with the changing "baseline" so it was not possible to subtract this contribution from the peak intensity.

Figure 4-8 shows the intensities of features A-G (up to 500 ps) plotted as a function of time delay and fit to equations 2.4, 2.5, or 2.6 in chapter 2 depending on the time-dependent behaviour shown. The fit results are shown in Table 4-8. Unfortunately, there are insufficient data points to confidently model all behaviour at long time delays; for example, although it is apparent whether the peak loses intensity overall or not, it is not possible to conclude whether oscillations continue to 500 ps in all cases. Therefore, for peaks showing only oscillations, with no apparent loss of overall intensity, t_{osc} values are reported and for peaks showing decay, t_1 values are reported (alongside t_{osc} values if appropriate). Future work would focus on collecting data at longer time delays at shorter intervals.

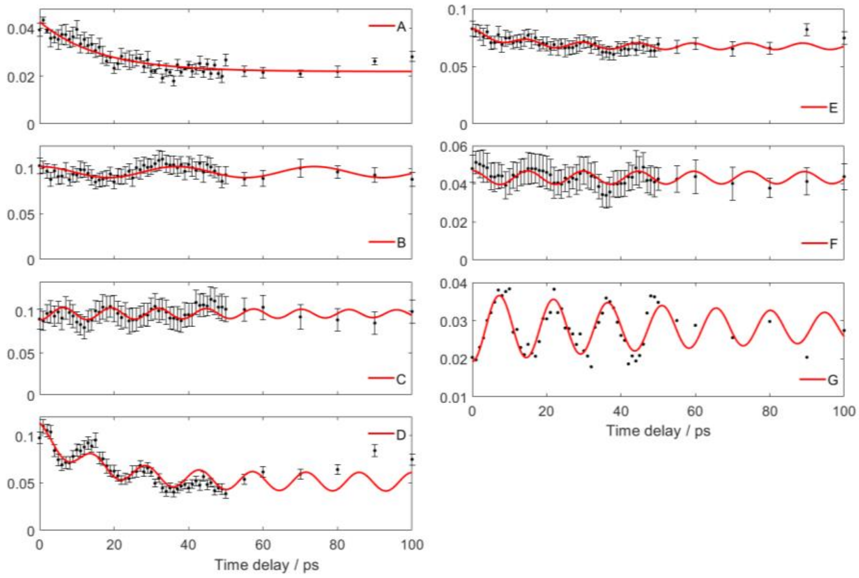

Figure 4-8: Time profiles showing fits of time-dependent intensities of photoelectron peaks A-G. Plots labelled A-G corresponding to relevant peak.

Peak/ Plot	A	B	C	τ_1	τ_{osc}	Rsq
A	0.23	0.21		16 ± 4		0.82
B	0.99	0.06			36.9 ± 0.7	0.45
C	1.00	-0.08			12.8 ± 0.2	0.38
D	0.53	0.54	0.10	15 ± 6	14.3 ± 0.3	0.74
E	0.70	0.13	0.03	11 ± 6	14.8 ± 0.1	0.59
F	0.45	0.04			14.9 ± 0.2	0.41
G	0.29	-0.09			14.6 ± 0.2	0.74

Table 4-8: Values determined from fits shown in Figure 4-8. Columns A, B and C are normalised.

In Figure 4-8, there are three types of time-dependent behaviours: i) A shows an overall loss of intensity, ii) B, C, F and G show oscillations in intensity without any overall/irreversible loss of intensity and iii) D and E show oscillations in intensity accompanied by an overall loss of intensity. That some features in the photoelectron spectrum show an overall loss of intensity and some do not is evidence of: i) the preparation of multiple bright states in S_1, only some of which are coupled to bath states and ii) different photoelectron peaks resulting from transitions from these different bright states in S_1.

The intensity of B in the photoelectron spectrum oscillates with a period of 36.9 ± 0.7 ps, more than double the other τ_{osc} values listed in Table 4-8. The peak displays maximum intensity at 0 ps and does not appear to lose intensity over the course of the experiment. These observations suggest that feature B reflects the population of a different S_1 bright state compared to the other photoelectron features A, C-G. The S_1 bright state in question is most likely $1^1 6a^1$ because in section 4.2.2.1 SEVI peak B at ~1330 cm^{-1} was assigned to the $\Delta v = 0$ transition from $1^1 6a^1$ in S_1. The intensity oscillations imply a restrictive IVR scheme where coupling to a dark state occurs, however, no other photoelectron peaks were found to oscillate out of phase with feature B with a similar period meaning none of the photoelectron peaks/features measured reflected the population of this dark state. In the photoelectron spectrum *via* ~1300 cm^{-1} (section 4.2.1), the peaks exhibited oscillations in intensity with an average period of 48 ± 4 ps, this was tentatively concluded to be due to coupling between S_1 levels $1^1 6a^1$ and 13^1. From the oscillation period, an eigenstate separation of 0.7 ± 0.1 cm^{-1} was determined, if level $1^1 6a^1$ was encompassed by the excitation pulse at both ~1260 cm^{-1} and ~1300 cm^{-1} then it is possible both the vibrations (bright and dark) involved in the time dependent wavepacket could have been encompassed by the excitation pulse at ~1260 cm^{-1} and ~1300 cm^{-1}. This would mean that the oscillations observed for feature B here could also be a manifestation of the coupling between the levels tentatively assigned to $1^1 6a^1$ and 13^1. Although, the oscillation period determined for feature B here (36.9 ± 0.7 ps) is not consistent with the average oscillation period reported in section 4.2.1 (48 ± 4 ps). It is possible that the shorter oscillation period for B may result from the difficulty of measuring and fitting the time-dependent intensity because of the level of congestion and complicated multiple coincident cation vibrational levels.

In Figure 4-8 the time profiles of photoelectron features C, D, E, F and G, all show oscillations in intensity; an average τ_{osc} value of 14.3 ± 1.5 ps is determined from all five fits. While features D, E, F show maximum intensity at 0 ps, indicating that they reflect the population of a bright state, features C and G show minimum intensity at 0 ps which increases up to ~7 ps, suggesting that ion states resulting from population of the dark state in S_1 are growing in at these positions. Figure 4-9 shows the photoelectron spectrum recorded at 0 ps versus the spectrum recorded at 7 ps (half the oscillation period). Of peak C (at ~1610 cm^{-1}) and G (at ~1730 cm^{-1}), at 7 ps peak C is relatively more intense so has more to recommend it as the $\Delta v = 0$ transition from the dark state in S_1. As peak C also has significant intensity at 0 ps, which is indicative of a bright state character, this could mean that transitions from both the bright and dark states in S_1 have coincident wavenumbers (within the experimental resolution) of peak C.

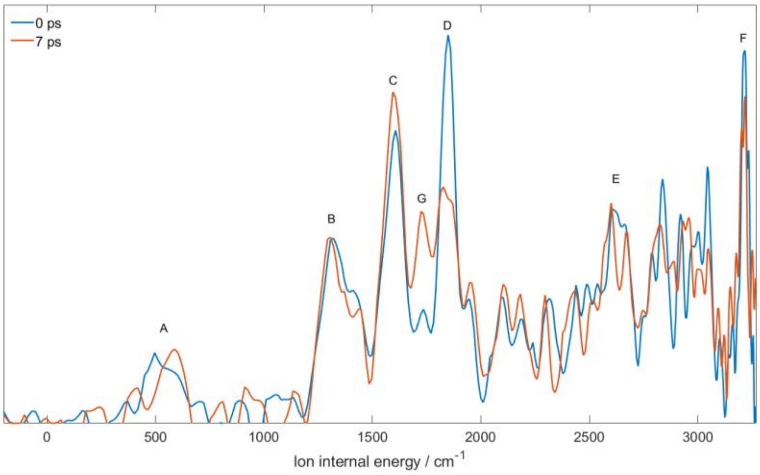

Figure 4-9: Photoelectron spectra measured via ~1260 cm^{-1} in S_1 at 0 ps and 7 ps.

Assignment of the observed time-dependent behaviour to a specific S_1 bright state is difficult; based on the analysis of the 0 ps SEVI spectrum in section 4.2.2.1, both features C and D originate from $D_0^+ \leftarrow S_1$ $\Delta v = 0$ transitions. D was assigned to $I^2 6a^1$ and C was suggested to be either $10a^2$ or 11^2. Any of these S_1 levels could be the bright state responsible for the observed oscillations in intensity here. For assignment of the dark state, Table 4-9 shows vibrational levels with S_1 wavenumbers of ~1260 cm^{-1} ± 60 cm^{-1} and ion state wavenumbers of either ~1610 cm^{-1} (wavenumber of feature C) or ~1730 cm^{-1} (wavenumber of feature G) ± 60 cm^{-1}. Also shown is the required change in vibrational quanta (ΔN) between possible coupling partners. The search code usually relies on inputted calculated frequencies but due to poor agreement of the calculated and experimental S_1 wavenumbers of mode 16a (see Chapter 3), assignments involving this mode will be based on the experimental S_1 value.[4]

Vibrational level	Predicted S_1 wavenumber / cm^{-1}	Predicted cation wave-number / cm^{-1}	ΔN to potential bright states		
			ΔN relative to $10a^2$	ΔN relative to 11^2	ΔN relative to $I^2 6a^1$
Δv=0 transition coincident with photoelectron feature C (~1610 cm^{-1})					
$10a^2$	1250^a	1604^a	-	4	5
11^2	1272^a	1570^a	4	-	5
Δv=0 transition coincident with photoelectron feature G (~1730 cm^{-1})					
$11^1 17b^1$	1323^a	1712^a	4	2	5
$6a^1 10a^1 16a^1$	$1294^{a,b}$	$1678^{a,b}$	3	5	4

Table 4-9: Potential assignments for the S_1 dark state. Predicted wavenumbers are based on fundamental wavenumbers from a) calculations, b) Ref 4, c) Ref 5, d) Ref 3.

Plausible assignments exist for both C and G meaning it is not obvious what the dark state is and which feature originates from the $D_0^+ \leftarrow S_1$ $\Delta v = 0$ transition; for example if either level $10a^2$ or 11^2 is the S_1 dark state, then feature C would originate from the $\Delta v = 0$ transition, meaning feature G would be a $\Delta v \neq 0$ allowed transition. Alternatively, if either level $11^1 17b^1$ or $6a^1 10a^1 16a^1$ is the S_1 dark state then feature G would originate from the $\Delta v = 0$ transition, meaning feature C would be a $\Delta v \neq 0$ allowed transition. Consistent with the latter, is that fact that the smallest changes in ΔN are shown by the coupling pairs $10a^2$ - $6a^1 10a^1 16a^1$ and 11^2 – $11^1 17b^1$. However, a decision on the most reasonable assignment of the dark state requires a conclusive assignment of the bright state which is not possible from the evidence available, although comparison to literature shows that only $I^2 6a^1$ has been assigned by other authors. Moreover, there may be more than one set of coupled bright and dark states, although, the similarity of the oscillation periods suggests this is unlikely.

There is another layer of complexity which was ignored in the discussion above. Photoelectron features C, D, E, F and G, do not all show the same behaviour at longer time delays. The time profiles of D and E show an overall loss of intensity alongside the oscillations. In Table 4-8, the fits of D and E give τ_1 lifetimes of 15 ± 6 ps and 11 ± 6 ps respectively which agree within error bars with the τ_1 lifetime of 16 ± 4 ps determined from the fit of feature A whose time profile only shows a small exponential loss of intensity. Together these give an average lifetime of 14 ± 3 ps. Notably, features A, D and E each lose less than half their initial intensity.

One explanation for the different behaviour at longer time delays is that there is an additional bright state, |*b*$_2$>, which couples weakly to numerous bath states. Population would then be irreversibly lost from |*b*$_2$> during the experiment. In the remaining discussion the bright state discussed in the above paragraph (and responsible for the ~14 ps oscillations observed for photoelectron features C-G) will now be referred to as |*b*$_1$>. In this scenario feature A, which displays only a decrease in intensity, must originate only from ionization of |*b*$_2$>. Feature E, which shows oscillations and an overall loss of intensity, must result from $\Delta v \neq 0$ transitions from both |*b*$_1$> and |*b*$_2$>. Feature D, which also shows oscillations alongside overall decay must result from overlapping transitions from |*b*$_2$> and |*b*$_1$>. Of the three photoelectron features showing decay, only D was assigned to a $\Delta v = 0$ transition from S_1 (see section 4.2.2.1.) with the S_1 bright state assigned as $I^2 6a^1$. This suggests that D results from a $\Delta v = 0$ transition from |*b*$_2$> and a $\Delta v \neq 0$ transition from |*b*$_1$> which would mean |*b*$_2$> is assignable to $I^2 6a^1$. If this is correct, this would then remove $I^2 6a^1$ as a potential assignment for |*b*$_1$> (refer to above paragraph and Table 4-9). Notably, although a decrease in intensity is observed for features A, D and E, suggesting dissipative energy redistribution, there is not an obvious increase in the intensity of the baseline with time delay which is expected to accompany this type of energy dispersal. However, this could be because significant congestion is already present in the spectrum at 0 ps.

Owing to the appearance of numerous overlapping transitions, further experiments would be necessary to come up with a conclusive coupling pathway for this wavenumber region. Where there are features which are suspected to result from overlapping transitions from different S_1 bright states, it would be worth trying to record higher resolution time-resolved spectra (using Fourier Transform limited 1 ps pulses) with the aim of separating out the time-dependent behaviour of the constituent cation vibrations. Also, an increasing baseline might emerge if higher resolution SEVI spectra were measured at longer time delays.

4.3. Photoelectron spectra via position (iii)/ S_1 0^0 + ~1450 cm^{-1}

4.3.1. Assignment of vibrational levels

Figure 4-10 shows the 0 ps SEVI spectrum measured *via* ~1450 cm^{-1} in S_1. The 1450 cm^{-1} S_1 feature excited lies 500 cm^{-1} above another REMPI peak which was assigned to 12^1 in chapter 3. Given that a difference of 500 cm^{-1} is in good agreement to the vibrational wavenumber of level S_1 $6a^1$ which is 492 cm^{-1},[4] the combination level $6a^1 12^1$ seems a likely assignment for the S_1 feature at ~1450 cm^{-1}, this level has been assigned in literature.[2,3,6] In the cation, level $6a^1 12^1$ is predicted to lie ~1491-1504 cm^{-1} (see Table 4-10) making it a reasonable assignment for peak A which is at ~1500 cm^{-1} in Figure 4-10. Peak A is the most intense peak in the spectrum which is consistent with it originating from the $\Delta v = 0$ transition from S_1 to the ion.

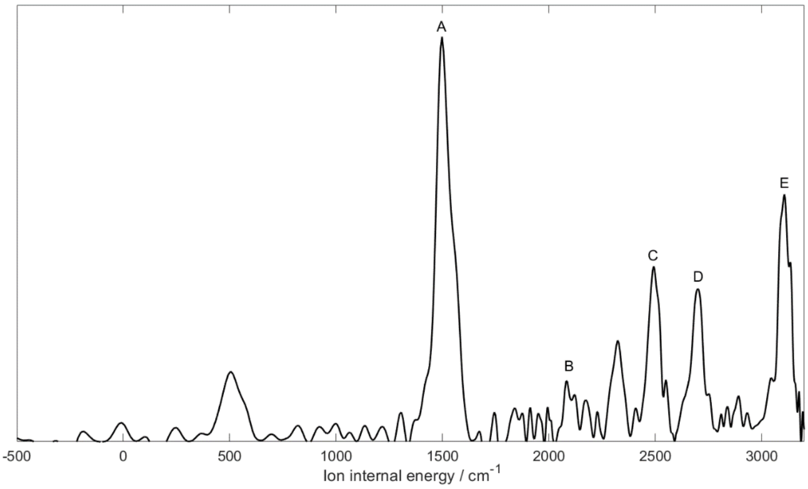

Figure 4-10: 0 ps SEVI spectrum measured via ~1450 cm^{-1} in S_1.

Vibrational level	Predicted S_1 wavenumber / cm^{-1}	ΔE relative to ~1450 cm^{-1} / cm^{-1}	Predicted cation wavenumber / cm^{-1}	ΔE relative to ~1500 cm^{-1} / cm^{-1}
$18a^1$	1453[a], 1437[d], 1434[e]	3, 13, 16	1496[a], 1436[c]	4, 64
$6a^1 12^1$	1471[a], 1448[b], 1445[c], 1449[d], 1446[e/g]	21, 2, 5, 1, 4	1491[a], 1504[b], 1500[c], 1502[f]	9, 4, 0, 2
$6a^1 19a^1$	1494[a], 1480[a,b]	44, 30	1510[a], 1514[b],	10, 14

Table 4-10: Predicted wavenumbers of levels $18a^1$, $12^1 6a^1$ and $19a^1 6a^1$ in the S_1 electronic state and ion state based on a) Calculations, b) Ref 4, c) Ref 5 and wavenumbers from d) Ref 3, e) Ref 2, f) Ref 1, g) Ref 6.

Two alternative assignments exist, $6a^1 19a^1$ and $18a^1$, the predicted vibrational wavenumbers of these levels are shown in Table 4-10. However, these are considered less likely because (i) there is better agreement between the predicted and experimental vibrational wavenumbers for level $6a^1 12^1$, (ii) both the constituent fundamental vibrations 6a^1 and 12^1 were assigned in literature and at lower wavenumbers in this work, (iii) 19a^1 has not been assigned in the REMPI spectrum at lower wavenumbers in this work, and has not been assigned in literature, with 6a^{1}19a^1 also unassigned in S$_1$ in literature, (iv) the three photoelectron peaks at ~510 cm^{-1}, ~1500 cm^{-1} and ~2490 cm^{-1} can be assigned to the progression 6a^{1}12^n where n=0,1,2. Possible assignments for the other peaks in the SEVI spectrum in Figure 4-10 are suggested in Table 4-11.

Ion internal energy / cm^{-1}	Cation vibrational level	Predicted cation wavenumber / cm^{-1}
510	**6a^1**	519^a, 521^b, 522^c
A - 1500	**6a^{1}12^1** 6a^{1}19a^1 18a^1	1491^a, 1504^b, 1502^c 1510^a, 1514^b 1496^a, 1436^d
B - 2100	6a^{1}9a^1 13^{1}16a^2	2126^a, 2114^b, 2115^c, 2097^d 2084^a, 2099^b, 2094^c,
2320	1^{1}6a^{1}12^1	2301^a, 2311^b, 2315^c
C - 2490	**6a^{1}12^2** 6a^{1}19a^2 6a^{2}18a^1	2463^a, 2487^b, 2481^c 2501^a, 2507^b 2534^a
D - 2700	**6a^{1}8a^{1}12^1** 6a^{1}8a^{1}19a^1	2675^a, 2691^b, 2689^c 2694^a, 2701^b, 2707^c
E - 3110	6a^{1}9a^{1}12^1 6a^{1}9a^{1}19a^1 1^{2}6a^{1}12^1 1^{2}6a^{1}19a^1	3098^a, 3097^b, 3096^c 3117^a, 3107^b, 3111^c 3111^a, 3118^b, 3129^c 3130^a, 3128^b, 3142^c

Table 4-11: Assignments for peaks in the SEVI spectrum and their predicted wavenumbers based on fundamental wavenumbers from a) calculations, b) Ref 4, c) Ref 1, d) Ref 5. Wavenumbers are rounded to nearest ~10 cm^{-1}.

4.3.2. Time-resolved photoelectron spectra

Photoelectron spectra were measured *via* ~1450 cm^{-1} in S$_1$ at several time delays between 0 ps and 500 ps, Figure 4-11 shows five of these spectra. A number of changes are apparent with increasing time delay; firstly a small increase in baseline intensity above ~1500 cm^{-1} can be seen, although by 500 ps a significant amount of structure still remains in the spectrum with SEVI peak A (the Δv = 0 transition) remaining relatively intense. Secondly, recurring changes in intensity are noticeable for some peaks. To investigate the time-dependence, the intensities of features A-E (determined from the full area of each feature) have been plotted as a function of time delay to give the time profiles in Figure 4-12 and Figure 4-13; the data points up to 500 ps were fit to equation 2.6 (see chapter 2) and the results of the fits are shown in Table 4-12. Although B is very weak in Figure 4-11, it has been included because it is more prominent in the SEVI spectrum and shows clear time-dependent behaviour.

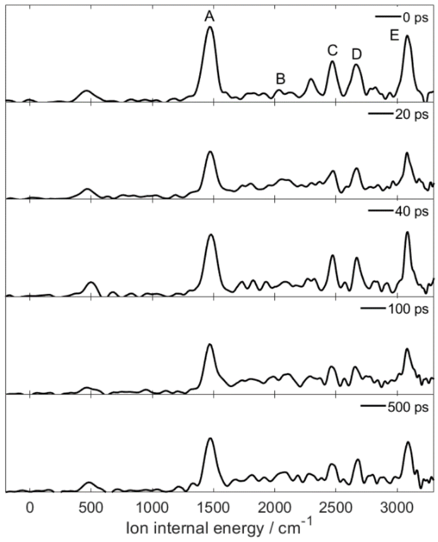

Figure 4-11: Photoelectron spectra measured via ~1450 cm^{-1} in S_1 at five different pump probe time delays.

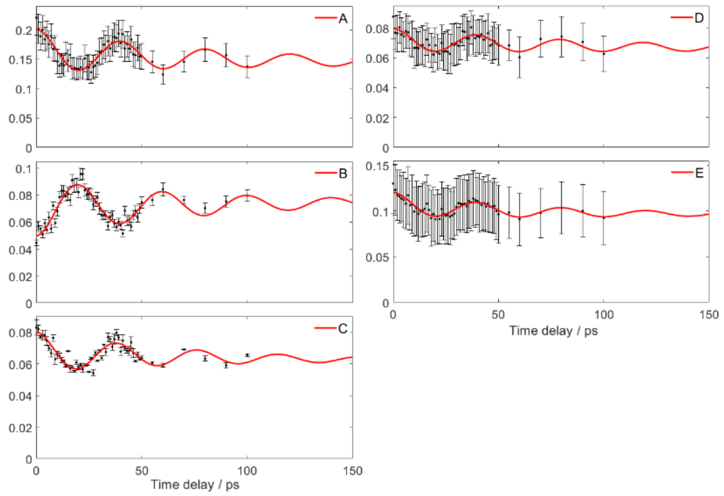

Figure 4-12: Time profiles showing fits to the time-dependent intensities of photoelectron peaks A-E up to 150 ps. Plots labelled A-E corresponding to photoelectron peaks A-E.

Peak /plot	A	B	C	τ_1	τ_2	τ_{osc}	Rsq
A	1.00	0.15	0.25	73 ± 85	100 ± 74	40.3 ± 1.2	0.84
B	0.54	-0.05	-0.14	194 ± 669	84 ± 47	40.0 ± 1.1	0.86
C	0.43	0.04	0.01	85 ± 145	76 ± 56	38.4 ± 1.3	0.78
D	0.46	0.04	0.05	85 ± 114	129 ± 151	39.7 ± 1.5	0.71
E	0.67	0.08	0.09	48 ± 40	93 ± 85	40.1 ± 1.5	0.80

Table 4-12: Values determined from the fits of the time-dependent intensity of features A-E. Columns A, B and C are normalised.

The time profiles in Figure 4-12 show the time-dependent behaviour of the photoelectron peaks up to 150 ps, initially the discussion will focus only on shorter time delays. Oscillations in intensity are apparent for each photoelectron feature and as shown in Table 4-12, all five τ_{osc} values agree within error bars, giving an average τ_{osc} value of 39.7 ± 1.3 ps which corresponds to an eigenstate separation of 0.84 ± 0.03 cm^{-1}. This signifies coupling between the bright state and a dark state. Comparison of the individual profiles in Figure 4-12 shows that the intensity oscillations of A, C, D and E are out of phase with those of B. As features A, C, D and E show a maximum intensity at 0 ps, it is likely they reflect the population of the bright state, 6a^{1}12^1. As B oscillates out of phase, showing maximum intensity at ~20 ps, it indicates a feature growing in that results from population of the dark state.

Feature B is at ~2100 cm^{-1} in the photoelectron spectrum (see Figure 4-11), given its very weak intensity, it is unlikely to result from the $\Delta v = 0$ transition from the dark state in S_1 to the ion, but rather from a $\Delta v \neq 0$ transition. Supporting this is the fact that no vibrational levels (with the correct S_1 and ion state wavenumbers) were found which had a change in quanta of $\Delta\mathrm{N} < 5$ relative to 6a^{1}12^1 (see Table 4-13) suggesting coupling is unlikely.

Vibrational level	Predicted S_1 wavenumber / cm^{-1}	ΔE relative 1450 cm^{-1}	Predicted cation wavenumber / cm^{-1}	ΔE relative 2100 cm^{-1}	ΔN relative to 12^{1}6a^1
15^{2}16a^{1}17a^1	1464[a], 1498[a,b]	14, 48	2110[a], 2444[a,b]	10, 344	6
6b^{1}15^{1}A^2	1452[a]	2	2100[a], 2284[c]	0, 184	6
16a^{2}16b^{1}17b^1	1423[a,b]	27	2074[a], 2084[a,c]	26, 16	6
10b^{4}16a^{1}17a^1	1432[a,b]	18	2044[a], 2057[a,c]	56, 43	8
10b^{3}16b^{1}A^2	1482[a], 1452[a,b]	32, 2	2105[a], 2135[c]	5, 35	8
10b^{4}16a^4	1404[b]	46	2130[b], 2138[c]	30, 38	10

Table 4-13: Vibrational levels with predicted wavenumbers of ~1450 cm^{-1} in the S_1 electronic state and ~2100 cm^{-1} in the cation. Wavenumbers are based on fundamental wavenumbers from a) calculations, b) Ref 4, c) Ref 1. Discrepancy over wavenumber of mode 15 in the cation is discussed in chapter 3.

Owing to the non-observance of a photoelectron peak displaying clear out of phase (minimum at 0 ps) oscillations in intensity which can be assigned to a $\Delta v = 0$

transition from the dark state in S$_1$, it is difficult to assign the dark state conclusively. In Figure 4-11, the most intense photoelectron peak at both 0 ps and 20 ps is A at ~1500 cm^{-1}, with no other strong peaks in the vicinity; so it is possible that the cation vibrational levels resulting from the $\Delta v = 0$ transitions from the bright and dark states are coincident, within the resolution of the experiment, at ~1500 cm^{-1}. If true then it should be possible to find a reasonable assignment, therefore a search was conducted for vibrational levels at ~1450 cm^{-1} ± 60 cm^{-1} in the S$_1$ electronic state and ~1500 cm^{-1} ± 60 cm^{-1} in the cation. Vibrational levels matching these criteria are shown in Table 4-14, these are ordered according to the value of ΔN relative to $6a^{1}12^{1}$ which was concluded to be the assignment of the bright state in section 4.3.1. Only $\Delta N \leq 4$ are shown.

Vibrational level	Predicted S$_1$ wavenumber / cm^{-1}	ΔE relative 1450 cm^{-1}	Predicted cation wavenumber / cm^{-1}	ΔE relative 1500 cm^{-1}	ΔN relative to $12^{1}6a^{1}$
$6a^{1}19a^{1}$	1494[a], 1480[a,b]	44	1510[a], 1514[b]	10, 14	2
$18a^{1}$	1453[a], 1437[d], 1434[e]	3, 13, 16	1496[a], 1436[c]	4, 64	3
$6a^{1}6b^{1}15^{1}$	1410[a], 1399[b]	40, 51	1483[a], 1653[f]	17, 153	3
$15^{1}18b^{1}$	1415[a], 1418[a,b]	35, 32	1493[a], 1659[a,b]	7, 159	4

Table 4-14: Possible assignments for the dark state. Predicted wavenumbers are based on fundamental wavenumbers from a) calculations, b) Ref 4, c) Ref 5, d) Ref 3, e) Ref 2, f) Ref 1. Discrepancy over mode 15 is discussed in chapter 3.

Many of the vibrational levels in Table 4-14 show large differences, $\Delta E \geq 30$, between the predicted S$_1$ and cation wavenumbers and the experimental vibrational wavenumbers. However, most of the predicted values rely on calculated wavenumbers for one or more vibrational modes as the fundamental and combination levels have not been assigned in the literature. Further, it should be noted that conflicting cation vibrational wavenumbers have been reported for mode 15 as discussed in Chapter 3. Therefore, a tentative assignment of $6a^{1}19a^{1}$ is made based on ΔN; coupling between this level and $6a^{1}12^{1}$ would require a change of ΔN = 2 (the lowest found) and the levels could couple anharmonically. Recording higher resolution SEVI spectra to get more precise wavenumbers at later time delays would be useful to assign the vibrations involved in this region of the S$_1$ REMPI spectrum. Especially if further features exhibiting out of phase oscillations in intensity could be seen.

So far, time-dependent behaviour at longer time delays has been neglected. The intensities of the photoelectron features up to 500 ps are shown in Figure 4-13; it can be seen that the amplitude of the oscillations decay over time. This is most pronounced for peaks A, B and C.

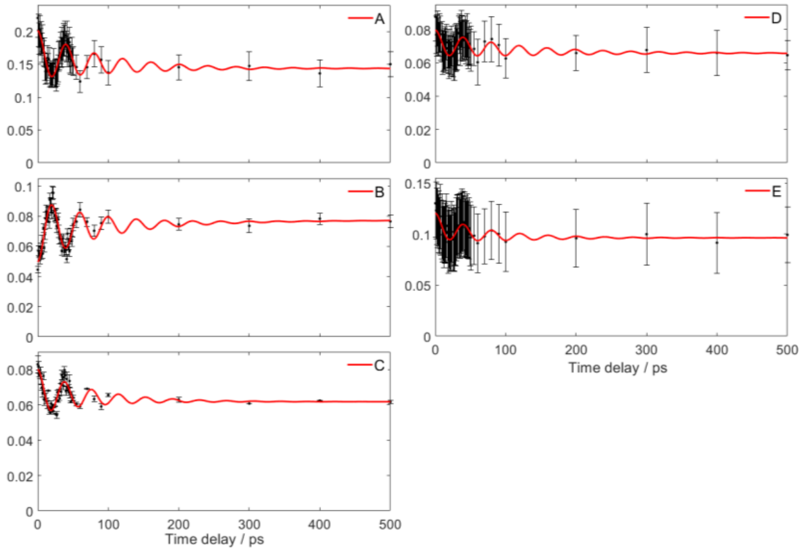

Figure 4-13: Time profiles showing the fits of the time-dependent intensities of photoelectron peaks A-E up to 500 ps. Plots are labelled A-E corresponding to the photoelectron peak measured.

Decaying oscillations can be the result of an intermediate IVR mechanism where the dark state acts as a doorway state. As doorway states facilitate coupling to multiple bath states, this leads to population irreversibly leaving the bright state. In this situation the time profiles of photoelectron peaks show oscillations in intensity superimposed on an exponential decay curve. None of the time profiles in Figure 4-13 show an exponential loss of intensity, the photoelectron peaks have similar intensities on average at 0 ps and at > 200 ps, therefore the IVR process is concluded to be restrictive, with the oscillation amplitude decaying as a consequence of another mechanism, such as rotational dephasing. This can occur because different rotational constants may be associated with each vibrational state populated in the S_1 wavepacket.[10,11] Notably, the dephasing is more rapid than is usually expected for this effect; such rapid dephasing may be caused by a rotationally dependent anharmonic coupling matrix element.[12] For rotational dephasing, on a longer timescale, recurrences in oscillation amplitude are anticipated although measurements at such long time delays can be challenging to perform. If the returning oscillations could be captured, this would support the theory of rotational dephasing.

4.4. Photoelectron spectra *via* position (iv)/ S_1 0^0 + ~1600 cm^{-1}

4.4.1. Assignment of vibrational levels

Figure 4-14 shows the 0 ps SEVI spectrum measured *via* ~1600 cm^{-1} in S_1. The S_1 REMPI feature at ~1600 cm^{-1} lies at double the wavenumber of another REMPI feature at ~800 cm^{-1} which was assigned to level 1^1 in Chapter 3. This suggests the overtone level 1^2 as an assignment here, this combination level has been assigned in higher resolution excitation spectra in literature suggesting it is bright.[2,3,6] The predicted wavenumber of 1^2 in the cation is ~1614-1627 cm^{-1} (see Table 4-15), this is in good agreement with SEVI peak B, the intense peak at ~1610 cm^{-1} in Figure 4-14. Consistent with this assignment, SEVI peaks A and D at ~800 cm^{-1} and ~2420 cm^{-1} could be assigned to the fundamental 1^1 and overtone 1^3 respectively (Table 4-16) meaning a progression of mode 1.

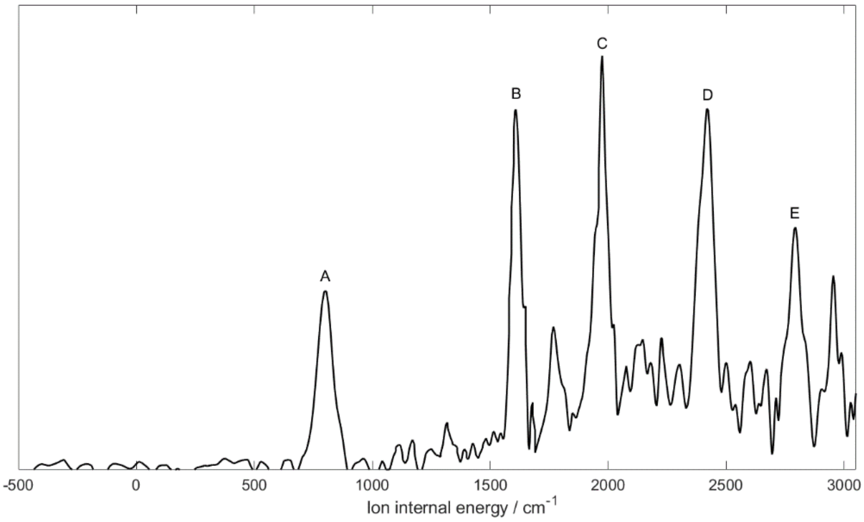

Figure 4-14: 0 ps SEVI spectrum measured via ~1600 cm^{-1} in S_1

Peak B is relatively intense, which is consistent with it originating from a $\Delta v=0$ transition from the bright state in S_1. However, SEVI peak C at ~1970 cm^{-1} is of similar intensity, while it is slightly more intense than B it also sits on a higher baseline, so it is possible that either or both peaks correspond to a $\Delta v = 0$ transition from S_1 to the ion. Four vibrational levels were found to have predicted wavenumbers in reasonable agreement with the experimental wavenumbers of ~1600 cm^{-1} in the S_1 electronic state and ~1970 cm^{-1} in the cation (peak C), these are also shown in Table 4-15. Compared to level 1^2, there is less evidence to suggest any of these four vibrational levels should be bright and observed in S_1; while totally symmetric, these are combination/overtone levels which involve nontotally symmetric modes and involve at least one mode not assigned in the REMPI spectrum at lower wavenumbers in this work or literature. The combination levels themselves are not assigned in literature either. While 1^2 appears to be the more likely assignment, if multiple vibrational levels are excited in S_1 this should be evident from time-resolved spectra which will be discussed in the next section.

Vibrational level	Predicted S_1 wavenumber / cm^{-1}	ΔE relative to ~1600 cm^{-1} / cm^{-1}	Predicted cation wavenumber / cm^{-1}	ΔE relative to B/~1610 cm^{-1} / cm^{-1}
1^2	1616^a, 1600^b, 1593^c, 1590^d	16, 0, 7, 10	1620^a, 1614^b, 1627^e	10, 4, 17
				ΔE relative to C/~1970 cm^{-1} / cm^{-1}
$10b^2 11^2$	1620^{a,b}	20	1924^{a,b}	46
$10a^2 10b^2$	1598^{a,b}	2	1958^{a,b}	12
$10b^1 16b^2 17b^1$	1625^{a,b}	25	1986^{a,b}	16
$1^1 10a^1 16a^1$	1602^{a,b}	2	1964^{a,b}	6

Table 4-15: Predicted wavenumbers of vibrational levels in the S_1 electronic state and ion state based on fundamental wavenumbers in a) calculations, b) Ref 4, c) Ref 3, d) Ref 2, e) Ref 1.

Wavenumbers and assignments for the other SEVI peaks are shown in Table 4-16; the preferred assignments, considering a bright state assignment of 1^2, involving the mode 1 progression are bolded.

Ion internal energy / cm^{-1}	Cation vibrational level	Predicted cation wavenumber / cm^{-1}
A - 800	**1^1**	810^a, 807^b, 814^c
B - 1610	**1^2** $9a^1$	1620^a, 1614^b, 1627^c 1607^a, 1593$^{b/c}$
C - 1970	$1^1 8a^1$ $1^2 10b^2$ $10b^2 11^2$ $10a^2 10b^2$ $10b^1 16b^2 17b^1$ $1^1 10a^1 16a^1$	1994$^{a/b}$, 2001^c 1972^a, 1968^b, 1986^c 1924^{a,b} 1958^{a,b} 1986^{a,b} 1964^{a,b}
D - 2420	**1^3** $1^1 9a^1$	2430^a, 2421^b, 2440^c 2417^a, 2400^b, 2407^c
E - 2790	$1^2 8a^1$ $1^3 10b^2$ $8a^1 9a^1$ $1^1 19a^2$ $1^1 12^2$	2804^a, 2801^b, 2814^c 2782^a, 2775^b, 2798^c 2791^a, 2780$^{b/c}$ 2792^a, 2793^b, 2804^c 2754^a, 2773$^{b/c}$
2960	$12^2 19a^1$ 12^3 $12^1 19a^2$	2935^a, 2959^b, 2954^c 2916^a, 2949^b, 2940^c 2954^a, 2969^b, 2968^c

Table 4-16: Assignments for SEVI peaks and their predicted wavenumbers based on fundamental wavenumbers from a) calculations and b) Ref 4, c) Ref 19. Wavenumbers are rounded to nearest ~10 cm^{-1}.

4.4.2. Time-resolved photoelectron spectra

Photoelectron spectra were measured *via* ~1600 cm^{-1} in S_1 at selected pump-probe time delays between 0 ps and 500 ps; seven of these are shown in Figure 4-15. Immediately, different behaviours with time delay are apparent, while many of the peaks stay relatively intense and are still observed at 500 ps, peak C quickly loses a lot of its initial intensity.

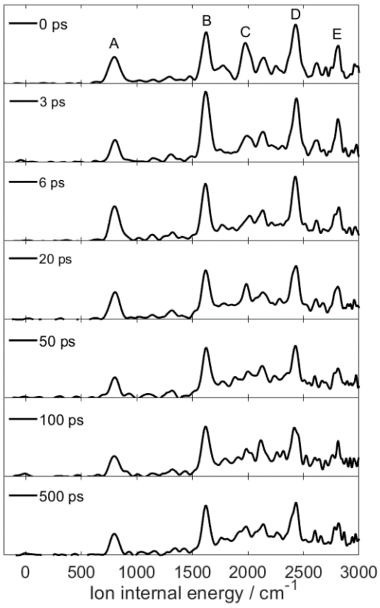

Figure 4-15: Photoelectron spectra measured via ~1600 cm^{-1} in S_1 at seven pump probe time delays when exciting at ~1600 cm^{-1}.

The intensities of photoelectron peaks A-E have been plotted as a function of time delay to give the time profiles shown in Figure 4-16, for peaks above ~1700 cm^{-1} the increasing congestion underneath has been subtracted. The data points up to 500 ps have been fit to either equation 2.5 or 2.6 (chapter 2) depending on the behaviour shown, with the results of the fits shown in Table 4-17. Further time-dependent behaviours become apparent from the time profiles in Figure 4-16. While photoelectron peaks A and B show oscillations, with an average τ_{osc} period of 6.6 ± 0.1 ps, on top of a small overall decrease in intensity, photoelectron peaks D and E appear to only show a small loss of overall intensity. The τ_1 and τ_2 lifetimes (where available) of all four fits (A, B, D, E) have relatively large associated error bars, so little can be stated about the agreement between the four fits. The values and error bars could be improved by measuring additional spectra at later time delays to more reliably fit the behaviour at long time delays because there are relatively few data points after 50 ps. While the lifetimes determined from the fits are less conclusive, a similarity shared by each peak A, B, D and E is that none lose more than half of their initial intensity so are all still observed with significant intensity by 500 ps. This suggests a bright state still populated at 500 ps.

This observation is pertinent when comparing to time dependent behaviour of peak C. In contrast, peak C loses most of its initial intensity over the first 9 ps, and by 500 ps only a small feature is seen in the spectrum which is relatively swamped by baseline structure, with congestion increasing in this region up to 500 ps. Also of note is that in the time profile of peak C in Figure 4-16, following the sharp loss of intensity over the first ~9 ps there are some relatively small recurrences in intensity. Two full oscillations are observed in the data points but they do not share a common oscillation period and both are much larger than the oscillation periods of peaks A and B. The first ‘oscillation’ occurs between 0 ps to ~20 ps, the second ‘oscillation’ occurs over the next ~12 ps and these cannot be correctly reproduced in the fit. These may be the result of overlapping vibrational levels but there is not enough information to unravel these here.

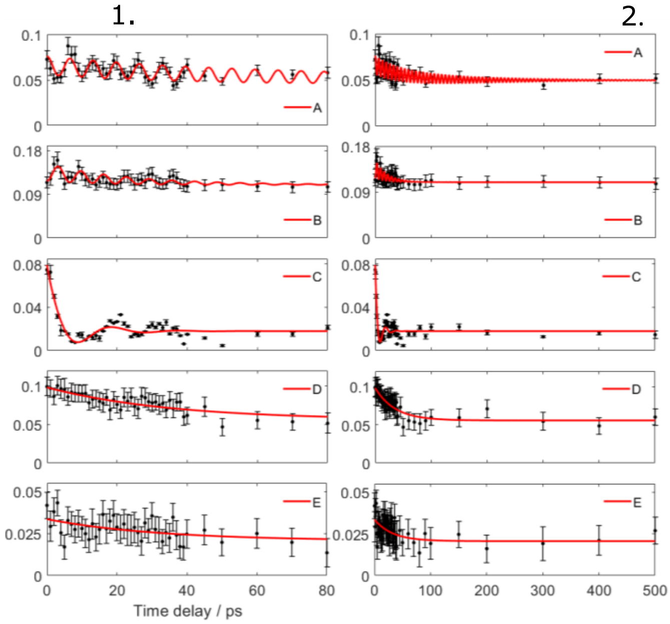

Figure 4-16: Time profiles showing the fits of the time-dependent intensities of photoelectron peaks A-E. Column 1 shows 0-80 ps and column 2 shows 0-500 ps. Plots are labelled A-E corresponding the photoelectron peak measured.

Peak/plot	A	B	C	τ_1	τ_2	τ_{osc}	Rsq
A	0.45	0.15	0.10	48 ± 38	173 ± 325	6.6 ± 0.1	0.71
B	1.00	0.23	-0.17	21 ± 13	26 ± 21	6.5 ± 0.1	0.65
C	0.16	0.29	0.27	2 ± 1	9 ± 8	19 ± 3	0.83
D	0.51	0.39		35 ± 13			0.76
E	0.19	0.12		32 ± 29			0.33

Table 4-17: Values determined from the fits to the time-dependent intensity of photoelectron peaks A-E. Columns A, B and C are normalised

The difference in intensity at time delays >300 ps suggests that the transition resulting in photoelectron peak C originates from a different S_1 vibrational level than the S_1 vibrational level(s) giving rise to photoelectron peaks A, B, D and E. The S_1 vibrational level giving rise to peak C appears to couple more efficiently to a large bath of dark states in a dissipative IVR scheme which is why photoelectron peak C shows a large exponential loss of intensity. This coupling is likely to be largely responsible for the increase in baseline intensity because large numbers of unresolved ion states will originate from the bath of dark states in S_1. Unfortunately, in this case it is not possible to measure the increase in baseline intensity because there is no clear featureless region of the baseline. If photoelectron peak C originates from the $\Delta v = 0$ transition from S_1 to the ion, and therefore is assignable to the same vibrational modes as the S_1 bright state, then it is possible to assign the S_1 vibrational level initially prepared. This is considered a reasonable assumption because (as discussed in the previous section) peak C at ~1970 cm^{-1} is one of the strongest peaks in the SEVI spectrum (see Figure 4-14). In Table 4-15 four vibrational levels were found which had predicted energies in reasonable agreement with the experimental S_1 and ion vibrational wavenumbers of ~1600 cm^{-1} and ~1970 cm^{-1} respectively, these were levels $10a^2 10b^2$, $10b^2 11a^2$, $10b^1 16b^2 17b^1$ and $1^1 10a^1 16a^1$. However, at this stage there is no strong evidence to favour one over the others; higher resolution spectra with more precise vibrational wavenumbers is required to unravel this further.

Considering that photoelectron peaks A, B, D and E all show similar weak losses of intensity and that peaks A, B and D can be assigned to the series 1^1, 1^2, 1^3 respectively, it seems likely that all four photoelectron peaks result from the same S_1 bright state: 1^2 (for assignments see analysis in section 4.4.1). The fact that peaks D and E do not show oscillations (whereas A and B do) is inconsistent with this conclusion but there are alternative explanations as to why oscillations may not be clearly observed for some photoelectron peaks. For example, if a photoelectron peak consists of multiple overlapping cation vibrational levels with opposing time-dependent behaviours then the net intensity of the photoelectron peak may not exhibit obvious oscillations. To determine this conclusively, the individual cation levels would need to be resolved and the time-dependent behaviour disentangled. Alternatively, the cation vibrational levels might have similar favourable Franck-Condon factors from both the bright and dark state in S_1 so overall only weak changes in intensity are observed. In Figure 4-16 some irregular fluctuations in the intensity of peaks D and E are apparent which could be evidence of additional behaviour alongside the decay. As a rough estimate which will be used in chapter 7, all four τ_1 values (of peaks A,B,D,E) are averaged to give a lifetime of 34 ± 14 ps, the τ_2 values are excluded because of the much higher value for peak A which is likely due to uncertainty about whether oscillations continue up to 500 ps.

The S_1 vibrational level 1^2 must strongly couple to a dark state in order to give rise to the oscillations in intensity observed for peaks A and B. This dark state appears to act as a doorway state, although not very efficiently, facilitating coupling to a larger bath of dark states because peaks A, B, D and E all show a small loss of intensity overall. This would also contribute to the increase in baseline intensity observed with increasing time delay. Peak A oscillates with maximum intensity at 0 ps so reflects the population of the bright state 1^2. Peak B oscillates out of phase, showing minimum intensity at 0 ps which increases to ~3 ps; at 0 ps the intensity is due to level 1^2 in the cation but this increase in intensity up to 3 ps suggests a coincident photoelectron peak must grow in which results from a transition from the dark state in S_1. At 3 ps, half the oscillation period, peak B at ~1610 cm^{-1} remains the most intense feature. Based on the propensity rule, it seems likely then that the $\Delta v=0$ transitions from both the bright state 1^2 and dark state are coincident at B. A search was conducted for vibrational levels with a wavenumber of ~1600 cm^{-1} and ~1610 cm^{-1} ±60 cm^{-1} in the S_1 and ion states respectively. Vibrational levels matching these wavenumbers are shown in Table 4-18, ordered according to increasing ΔN relative to 1^2, with only $\Delta N \leq 7$ shown.

Unfortunately, of the levels shown in Table 4-18, none can confidently be assigned as the dark state. Most vibrational levels in Table 4-18 involve large changes in quanta relative to the bright state 1^2, the only exception is level $1^1 15^2$ which requires ΔN = 3. Based on this, $1^1 15^2$ would the preferred assignment, however it is difficult to comment on the agreement between the predicted and experimental wavenumbers because of the disagreement over the wavenumber of mode 15 which is discussed in chapter 3. Using a calculated value for mode 15 in the cation, the predicted wavenumber of $1^1 15^2$ in the S_1 and ion states is in reasonable agreement to the experimental wavenumbers. However, wavenumbers from multiple sources are shown in Table 4-18, some studies suggest extremely poor agreement (~170 cm^{-1})[4] to the calculated wavenumber of mode 15 in the cation which would mean the predicted wavenumber of $1^1 15^2$ could be very far out from experimental values. This is unexpected though considering the good agreement between calculations and experimental wavenumbers for other aniline cation modes (including NH_2 localised) and the good agreement between calculated and experimental wavenumbers for mode 15 in other substituted benzene molecules shown in other studies which used similar levels of theory.[13] Due to the discrepancy, vibrational levels involving mode 15 can only be valid assignments if wavenumbers from certain sources and calculations are used, therefore it is not possible to make a conclusive assignment here. In the future, it would be necessary to measure the dispersed fluorescence resulting from vibrations within this energetic region of the S_1 electronic state to investigate the discrepancies in previous photoelectron studies.

Vibrational level	Predicted S_1 wavenumber / cm^{-1}	ΔE relative to ~1600 cm^{-1}	Predicted cation wavenumber / cm^{-1}	ΔE relative to ~1610 cm^{-1}	ΔN relative to 1^2
$1^1 15^2$	1564^a, 1562^b	36, 38,	1580^a, 1909^b, 1561^c,1912^d,	30, 299, 49, 300	3
$10b^1 16b^1 19a^1$	$1544^{a,b}$	56	$1611^{a,b}$, 1619^d	1, 9	5
$6a^2 10b^1 16b^1$	$1540^{a,b}$	60	$1660^{a,b}$, 1668^d,	50, 58	6
$6a^1 10b^2 15^2$	1630^a, 1602^b	30, 2, 38	164)1^a, $1977^{b/d}$,	31, 367	7

Table 4-18: Potential dark state assignments. Predicted wavenumbers are based on fundamental wavenumbers from a) calculations, b) Ref 4, c) Ref 9 , d) Ref 1.

4.5. Summary and conclusion

This chapter includes time-resolved photoelectron and SEVI spectra measured *via* four positions in S_1: (i)~1260 cm^{-1}, (ii)~1300 cm^{-1}, (iii)~1450 cm^{-1} and (iv)~1600 cm^{-1}. It has not been possible to fully unravel the time-dependent behaviour and coupling pathways in some of these studies so clearly further experiments are necessary. Some difficulties in the analysis process were related to the energy resolution and/or pump laser bandwidth achieved; firstly, multiple $S_1 \leftarrow S_0$ transitions were excited which complicated the photoelectron spectra, secondly the peak widths obscured wavenumber shifts in positions with time delay and thirdly, overlapping/coincident transitions from S_1 to the ion (which may or may not be related to the first point) meant it was difficult to disentangle the contributions to the time-dependent behaviour of photoelectron features.

Although analysis is incomplete, comparison of the time-dependent photoelectron spectra measured *via* different S_1 vibrational levels does provide some insight into the dynamics in aniline. The IVR dynamics of the vibrational levels excited at (ii)~1300 cm^{-1}, (iii)~1450 cm^{-1} and (iv)~1600 cm^{-1} in S_1 show an expected trend; when exciting the two lower wavenumber positions, the energy remains localised between a few levels whereas exciting the highest wavenumber position, energy dispersal to bath states is identified. This is in line with what would be predicted considering the increasing S_1 wavenumber and likely increase in density of states. However, this trend is not followed when exciting the lowest wavenumber position, (i) ~1260 cm^{-1}, where energy dispersal was determined with the photoelectron features showing losses of intensity with increasing time delay. This was unexpected considering the two higher wavenumber positions show restrictive IVR, suggesting the possibility of mode specific IVR with a coupling mechanism not available to other bright states, this is discussed in chapter 7. Notably, ~1260 cm^{-1} is the lowest wavenumber at which either intermediate or dissipative energy dispersal is apparent; below this threshold, IVR is only restrictive so ~1260 cm^{-1} is taken as the 'IVR onset energy'.

4.6. References

---

[1] X. Song, M. Yang, E. R. Davidson and J. P. Reilly, *J. Chem. Phys.,* 1993, **99**, 3224-3233

[2] N. Mikami, A. Hiraya, I. Fujiwara and M. Ito, *Chem. Phys. Lett.,* 1980, **74**, 531-535

[3] R. Scheps, D. Florida, and S. A. Rice, *J. Chem. Phys.,* 1974, **61**, 1730-1747

[4] X. Zhang, J.M. Smith, J.L. Knee., *J. Chem. Phys*, 1992, **97**, 2843-2860

[5] J.T. Meek, E. Sekreta, W. Wilson, K.S. Viswanathan, J.P. Reilly, *J. Chem. Phys*., 1985, **82**, 1741-1749

[6] J.C.D. Brand, D.R. Williams, T.J. Cook, *J. Mol. Spec.*, 1966, **20**, 359-380

[7] A. M. Gardner, W. D. Tuttle, L. E. Whalley, T. G. Wright, *Chem. Sci*., 2018, **9**, 2270-2283

[8] J. A. Davies, A. M. Green, A. M. Gardner, C. D. Withers, T. G. Wright and K. L. Reid, *Phys. Chem. Phys. Chem*., 2014, **16**, 430-443

[9] M. A. Smith, J.W. Hager and S. C. Wallace, *J. Chem. Phys*., 1984, **80**, 3097-3105

[10] J. A. Davies and K. L. Reid, *Phys. Rev. Lett*., 2012, **109**, 193004

[11] P. M. Felker and A. H. Zewail*, J. Chem. Phys*. 1985, **82**, 2994-3002

[12] J. A. Davies and K. L. Reid, *Phys. Rev. Lett.,* 2012, **109**, 193004

[13] W. D. Tuttle, A. M. Gardner, L. E. Whalley and T. G. Wright, *J. Chem. Phys.,* 2017, **146**, 244310

5. Investigation of IVR dynamics above 1700 cm^{-1} in the S$_1$ electronic state of aniline.

5.1. Chapter overview

This chapter focuses on the SEVI and time-resolved photoelectron spectra (tr-PES) measured *via* five wavenumber positions over the three broad features in the ~1650-2200 cm^{-1} region of the aniline S$_1$←S$_0$ REMPI spectrum. Figure 5-1 shows the region of the S$_1$ electronic state studied in this chapter with the five intermediate wavenumber positions labelled.

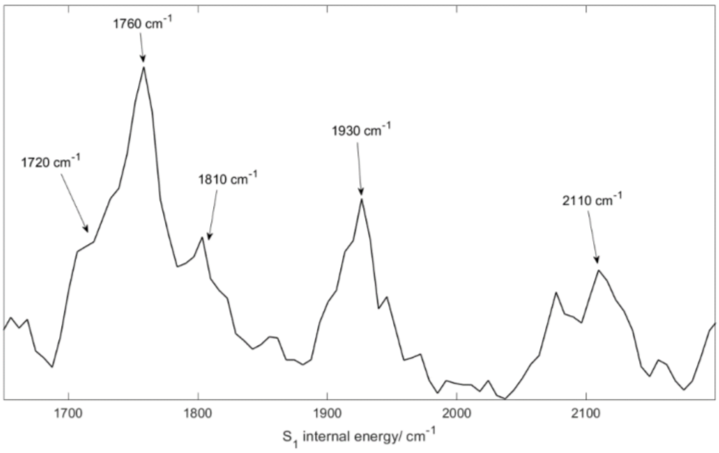

Figure 5-1: S$_1$←S$_0$ REMPI spectrum showing the 1650-2200 cm^{-1} region. Experimental wavenumbers are rounded to nearest 10 cm^{-1}.

Analysis of the tr-PES has enabled the determination of IVR lifetimes and eigenstate energy separations, revealing three examples of dissipative IVR at the highest wavenumber positions: ~1810 cm^{-1}, ~1930 cm^{-1} and ~2110 cm^{-1}. The tr-PES measured *via* the two lowest wavenumber positions: ~1720 cm^{-1} and ~1760 cm^{-1}, show more complex time-dependent behaviour which has proved difficult to unravel however, there is evidence to suggest the involvement of doorway states. Comparison of the SEVI and time-dependent photoelectron spectra has been used to suggest assignments for doorway states in these cases.

5.2. REMPI feature at S_1 0^0 + 1700-1850 cm^{-1}

5.2.1. Identifying unresolved vibrational levels

The S_1 REMPI feature at ~1700-1850 cm^{-1} is very broad, with prominent shoulders on either side, indicating that there are likely to be multiple unresolved vibrational levels contributing to the intensity of the feature. It is for this reason that the pump laser was stepped over the REMPI feature to selectively photo-excite different regions of the absorption profile. In Figure 5-2 the pump laser positions chosen are labelled I, II, II; these labels correspond to the SEVI spectra in Figure 5-3 i.e. excitation at I resulted in SEVI spectrum I.

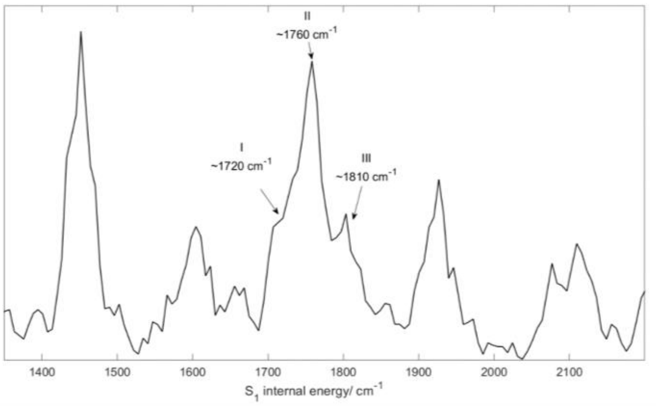

Figure 5-2: REMPI spectrum showing three wavenumber positions I-III excited by the pump laser.

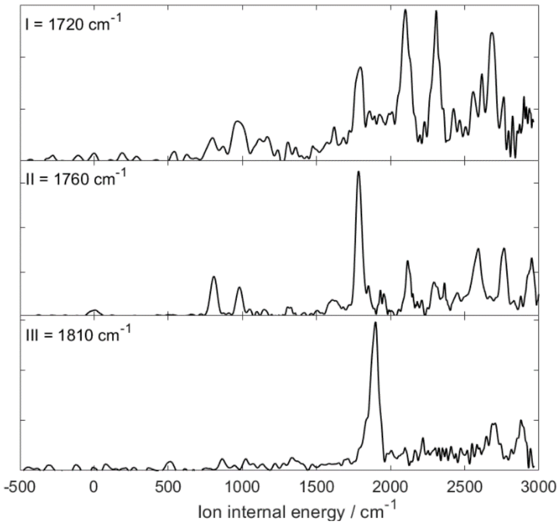

Figure 5-3: SEVI spectra showing the changing spectral profile as the pump laser is stepped over the broad feature at 1700-1850 cm^{-1} in the S_1 REMPI spectrum.

As the SEVI spectra were measured at a pump-probe time delay of 0 ps, they should all show a Franck-Condon projection of the initially excited S_1 bright state onto the cation vibrational levels and therefore should appear identical if the same bright state is always excited. However, the three SEVI spectra in Figure 5-3 are distinctly different; peaks appear at different wavenumbers and with different relative intensities at each of the three excitation positions. This means the pump pulse must populate different vibrational levels in S_1 as the pump wavelength is tuned across the feature. The changing profile of the SEVI spectra with excitation energy indicates at least three vibrational levels contribute to the intensity of the REMPI feature between ~1700-1850 cm^{-1}. Proposed assignments for the S_1 and cation vibrational levels are reported in the following sections where the tr-PES measured at each of the three excitation positions I, II and III will also be shown.

5.2.2. Photoelectron spectra *via* position I/ S_1 0^0 + ~1720 cm^{-1}

5.2.2.1. Assignment of vibrational levels

Figure 5-4 shows the SEVI spectrum measured *via* position I in the S_1 REMPI spectrum which is at ~1720 cm^{-1}. The intensity of SEVI peaks C, D and E which lie above ~2000 cm^{-1} are consistent with one of these peaks originating from the $\Delta v = 0$ transition from S_1. If this is the case, it means the vibrational level prepared involves modes whose vibrational wavenumbers change by at least ~300 cm^{-1} upon ionisation.

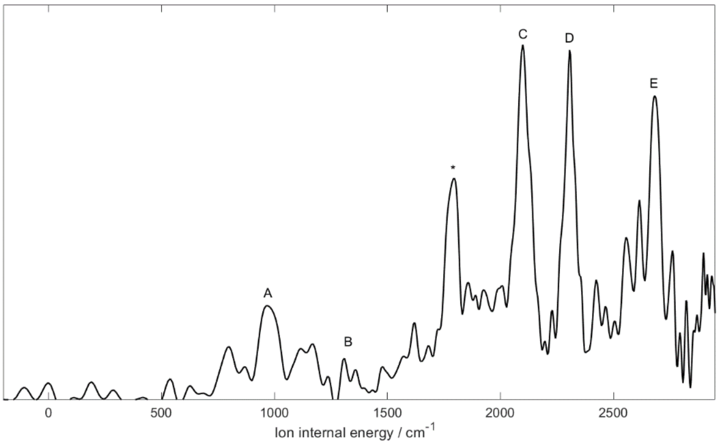

*Figure 5-4: 0 ps SEVI spectrum measured via ~1720 cm^{-1} in S_1 with peaks assigned A-E. The peak labelled * is not clear in tr-PES and only resolved when using long probe wavelengths -discussed further in section 5.2.5.*

Chapter 3 assigned the lower wavenumber REMPI feature at ~800 cm^{-1} which has a shoulder at ~750 cm^{-1}; it is possible that the S_1 vibrational level(s) at ~1720 cm^{-1} result from the levels at ~800 cm^{-1} and/or 750 cm^{-1} in combination with level

12^1, which has an S_1 vibrational wavenumber of 956 cm^{-1}.[1] In Chapter 3, it was concluded that I^2 was prepared when exciting at ~750 cm^{-1} in S_1; notably, this vibrational level shows a difference of ~560 cm^{-1} upon ionisation (see Table 3.1 in Chapter 3). Based on experimental wavenumbers for the fundamental modes, the combination level $\mathrm{I}^2 12^1$ is predicted at ~1718 cm^{-1} in S_1 and 2306 cm^{-1} in the cation.[1] These values are in excellent agreement to the pump laser wavenumber of ~1720 cm^{-1} and the experimental wavenumber of SEVI peak D at ~2310 cm^{-1} in Figure 5-4. In support of this assignment, both the constituent vibrational levels, I^2 and 12^1, were assigned at lower energies in the S_1 REMPI spectrum in Chapter 3, suggesting that the combination level $\mathrm{I}^2 12^1$ may be observed. Further, this combination band has previously been assigned in the literature.[3,4,5] Additionally, there is a peak at ~980 cm^{-1} in the SEVI spectrum which is in good agreement with the predicted wavenumber of 12^1 which was assigned at 983 cm^{-1} by Knee and co-workers.[1] However, there is only a weak feature at ~1330 cm^{-1} in the SEVI spectrum which is where the overtone of the inversion, I^2, is expected based on the wavenumber of 1323 cm^{-1} provided by Knee et al.[1] This will be discussed further following the introduction of the time dependent spectra. Chapter 3 also concluded that at 750 cm^{-1}, the $S_1 \leftarrow S_0$ $\mathrm{I}^1_1 6a^1_0$ transition was excited alongside I^2_0; however, while the SEVI spectrum in Figure 5-4 shows evidence of the $D_0^+ \leftarrow S_1$ I^2_2 transition, there is no strong ion peak at ~2160 cm^{-1} assignable to $\mathrm{I}^1 6a^1 12^1$ indicating that the $S_1 \leftarrow S_0$ $\mathrm{I}^1_1 6a^1_0 12^1_0$ transition is not excited.

The S_1 and cation vibrational wavenumbers for $\mathrm{I}^2 12^1$ are summarised in Table 5-1; however, if SEVI peak D does originate from the $D_0^+ \leftarrow S_1$ $\Delta v=0$ transition, there are two additional vibrational levels which are potential assignments, although these show poorer agreement to the experimental wavenumbers compared to $\mathrm{I}^2 12^1$. The predicted wavenumbers of these levels are shown in Table 5-1.

Vibrational level	Predicted S_1 wavenumber / cm^{-1}	ΔE to the experimental wavenumber ~1720 cm^{-1}	Predicted cation wavenumber / cm^{-1}	ΔE to the experimental wavenumber ~2310 cm^{-1} (peak D)
$\mathrm{I}^2 12^1$	1718^b,1713^c, 1710^d, 1714,^{e} 1709^f	2,7,10,6,11	$2306^{b/g}$, 2291^c,	4, 18
$\mathrm{I}^2 19a^1$	$1750^{a,b}$	30	2316^b	6
$\mathrm{I}^2 6a^2$	1746^b, 1744^c, 1733^d	26, 24,13	2365^b, 2347^c, 2369^g	55, 37, 59

Table 5-1: Predicted S_1 and ion state wavenumbers are based on fundamental wavenumbers from a) calculation, b) Ref 1, c) Ref 2 or wavenumbers in d) Ref 3, e) Ref 4, f) Ref 5, g) Ref 6.

One alternative assignment is $I^{2}6a^{2}$; supporting this is the fact that both $6a^{1}$ and I^{2} were assigned in the REMPI spectrum at lower wavenumbers suggesting the combination level may also be observed, plus this level was assigned by Scheps and co-workers to an S_1 band observed at 1733 cm^{-1},[3] which is likely encompassed by the excitation laser pulse used in this work. However, other than the assignment of peak D to $I^{2}6a^{2}$, there is no additional evidence from the SEVI spectrum in Figure 5-4 for this assignment because there are no obvious peaks at ~521 cm^{-1} or ~1042 cm^{-1} which is where the $6a^{1}$ and $6a^{2}$ cation levels are predicted respectively.[1] The other possible assignment is $I^{2}19a^{1}$; the fact that level $19a^{1}$ was not assigned in the REMPI spectrum at lower wavenumbers in this work or in the literature, suggests this assignment is less likely.[1,4,5] Knee assigned a cation fundamental wavenumber of 993 cm^{-1} to level $19a^{1}$, this is close to peak A in Figure 5-4, however this was not confirmed by pumping a specific intermediate level in S_1.[1] So of the three possibilities, $I^{2}12^{1}$ is considered more reasonable; assuming this assignment is correct, vibrational level assignments for the other relatively intense SEVI peaks in Figure 5-4 are suggested in Table 5-2.

Ion internal energy / cm^{-1}	Cation vibrational level	Predicted wavenumber of cation vibrational level/ cm^{-1}
A - 980	**12^{1}** $19a^{1}$	983^{a} 993^{a}
1790	**$1^{1}12^{1}$** $1^{1}19a^{1}$	1790^{a},1794^{c} 1800^{a}
C - 2100	$6a^{1}10a^{2}$ $6a^{1}11^{2}$ $10a^{1}12^{1}16a^{1}$ (See text)	$2125^{a,b}$ $2091^{a,b}$ $2140^{a,b}$
D - 2310	**$I^{2}12^{1}$** $1^{1}6a^{1}12^{1}$ (See Table 5-1 and text)	$2306^{a/c}$ 2301^{b}, 2311^{a}, 2315^{c}
E - 2680	I^{4} $I^{2}1^{1}6a^{1}$	2646^{a}, 2650^{c} 2651^{a}, 2661^{c}

Table 5-2: Wavenumber of SEVI peaks, alongside potential assignments and their predicted wavenumbers based on fundamental wavenumbers from a) Ref 1 and b) calculations or wavenumbers from c) Ref 6. In Ref 2 Meek commented they observed a 'remarkably harmonic progression' in the inversion mode in the aniline cation so the wavenumber of I^{4} is estimated as 2x the I^{2} value. Experimental wavenumbers rounded to nearest 10 cm^{-1}. Preferred assignments are in bold.

Obviously the discussion above assumes SEVI peak D results from the $\Delta v = 0$ transition from S_1; however, at the start of this chapter it was noted that the intensity of peaks C, D and E were comparable. Despite its intensity, it is considered likely that peak E only results from a $\Delta v \neq 0$ transition from S_1 because no plausible vibrational levels were found which have vibrational wavenumbers of ~1720 cm^{-1} in the S$_1$ electronic state and ~2680 cm^{-1} in the ion state (the experimental wavenumber of peak E) and this was not unexpected given the wavenumber difference between S$_1$ and the cation. However, it is possible that peak C may originate from a Δv = 0 transition from S$_1$ to the ion, this could be either instead of or as well as (meaning additional vibrational level(s) initially prepared in S$_1$ alongside I^{2}12^1) peak D. Several vibrational levels were identified which have S$_1$ and cation wavenumbers of ~1720 ± 60 cm^{-1} and 2100 ± 60 cm^{-1} (experimental wavenumber of peak C) respectively; these are shown in Table 5-3.

Vibrational level	Predicted S$_1$ wavenumber / cm^{-1}	ΔE to the experimental wavenumber ~1720 cm^{-1}	Predicted cation wavenumber / cm^{-1}	ΔE to the experimental wavenumber ~2100 cm^{-1}
6a^{1}10a^2	1742^{a,b}	22	2125^{a,b}	25
6a^{1}11^2	1764^{a,b}	44	2091^{a,b}	9
10a^{1}12^{1}16a^1	1758^{a,b}	38	2140^{a,b}	40

Table 5-3: Assignments for SEVI peak C. Predicted wavenumbers are based on fundamental wavenumbers from a) calculations and b) Ref 1 where possible

One vibrational level in Table 5-3, involves the fundamental 12^1 in combination with the vibrations 10a^1 and 16a^1. As mentioned above, based on their predicted wavenumbers, both vibrations 12^1 and 19a^1 are potential assignments for SEVI peak A in Table 5-4, although 12^1 is more probable. Other than this there is little evidence in the SEVI spectrum to recommend any of the vibrational levels over the others. Additionally, the three vibrational levels included in Table 5-3 are all combination bands involving vibrational modes which have not previously been assigned in the S$_1$ electronic state either as fundamentals or overtones. None of the vibrational levels show particularly good agreement to both the S$_1$ and cation state experimental vibrational wavenumbers, at least not comparatively better than the agreement shown by vibrational levels in Table 5-1 which are assignments for SEVI peak D. Although, importantly as some of the vibrations have not been assigned in the S$_1$ electronic state, many of the predicted wavenumbers in Table 5-3 are largely based on calculated wavenumbers.

While analysis of the 0 ps SEVI spectrum in this section strongly suggests the bright state I^{2}12^1 is excited and provides little evidence to support any alternative or additional assignments making multiple S$_1$ bright states seem unlikely, comparison to the time-dependent spectra, which is presented in the following section, reveals this must be the case. As will be shown below, more than one type of time-dependent behaviour is apparent indicating that another S_1 vibrational level has been excited alongside $I^2 12^1$.

5.2.2.2. Time-resolved photoelectron spectra

Photoelectron spectra were measured *via* ~1720 cm^{-1} in S_1 at selected pump-probe time delays between 0 ps - 500 ps; six of these are shown in Figure 5-5. With increasing time delay, a loss of structure is apparent with photoelectron peaks A-E all decreasing in intensity, this is accompanied by an increase in the intensity of the baseline above ~1800 cm^{-1}. However, notably, there is congestion already present at 0 ps; this suggests some eigenstates, which contain bright state character, lie outside of the bandwidth of the laser.

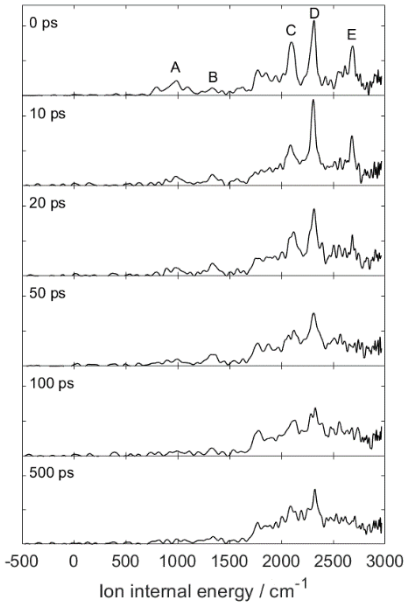

Figure 5-5: Photoelectron spectra measured via ~1720 cm^{-1} in S_1 at pump-probe time delays of 0 ps, 10 ps, 20 ps, 50 ps, 100 ps and 500 ps.

To further investigate the time-dependent behaviour, the intensities of peaks A-E and the baseline between 2420-2530 cm^{-1}, where there are no resolved vibrational features, have been measured and plotted as a function of pump-probe time delay to give the time profiles shown in Figure 5-6. As peaks C, D and E lie in a region of the spectrum where there is increasing congestion in the baseline, it was necessary to subtract this. Depending on the time-dependent behaviour, the data points (0-500 ps) were fit to either equation 2.5, 2.7 or 2.6 (see chapter 2) with the results shown in Table 5-4.

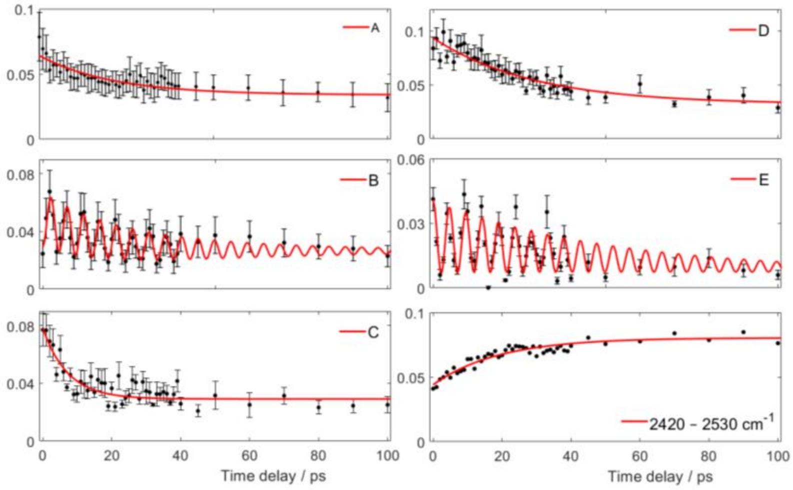

Figure 5-6: Time profiles showing fits to the time-dependent intensity of photoelectron peaks A-E and the baseline region between 2420 – 2530 cm^{-1} where there are no peaks. Labels correspond to photoelectron peak measured.

As briefly mentioned at the end of the previous section, two different types of time-dependent behaviour are shown in the time profiles of the peaks: i) photoelectron peaks A, C and D show an overall loss of intensity although the lifetimes differ, and ii) photoelectron peaks B and E show oscillations in intensity alongside an overall loss of intensity. The final time profile of the 2420-2530 cm^{-1} region of the baseline shows an exponential increase in intensity.

Coefficients							
Peak	**A**	**B**	**C**	τ_1**/ps**	τ_2**/ps**	τ_{osc}**/ps**	**Rsq**
A	0.55	0.49		21 ± 7			0.79
B	0.43	0.36	-0.32	17 ± 8	46 ± 24	4.74 ± 0.03	0.84
C	0.47	0.79		7 ± 3			0.75
D	0.52	1.00		29 ± 7			0.88
E	0.12	0.27	-0.32	53 ± 44	52 ± 38	4.75 ± 0.04	0.75
Baseline 2420-2530 cm^{-1}	0.72	0.59		19 ± 4			0.91

Table 5-4: Results obtained from fits of the time dependent intensity of peaks A-D and baseline region 2420 – 2530 cm^{-1} in the photoelectron spectrum. Column A and B are normalised.

There is more than one possible explanation for the different time-dependent behaviours. Firstly, more than one zero order bright state could have been excited at ~1720 cm^{-1} in S_1; the photoelectron spectra will then be a superposition of the individual photoelectron spectra measured via each bright state. If one bright state is strongly coupled to a dark doorway state and the other bright state only weakly coupled to dark bath states, then the time-dependent behaviour shown by different photoelectron peaks would be different depending on which bright state in S_1 the photoelectron peak originated from. Given the relatively high S_1 wavenumber and the width of the REMPI feature (see Figure 5-2), it is reasonable that there are multiple close lying $S_1 \leftarrow S_0$ transitions which could have been excited; indeed multiple assignments were found. Alternatively, it is possible that there is only one bright state excited yet for some reason, some photoelectron peaks do not exhibit intensity oscillations. This could be because either: i) the cation vibrational level has similar Franck-Condon factors from both the bright and dark S_1 vibrations or ii) there are overlapping cation vibrational levels which exhibit opposing time-dependent behaviours so the oscillations are obscured. Finally, the simultaneous excitation of multiple bright states in S_1 could lead to time-dependent behaviour irrespective of the involvement of any coupled dark states because of the phase evolution of the eigenstates making up the prepared vibrational wavepacket. However, this is inconsistent with the out of phase intensity oscillations observed for photoelectron peak B (see below).

The results here are somewhat inconclusive, excluding photoelectron peak C, the $\boldsymbol{\tau_1}$ lifetimes for the fits potentially do agree within error bars however, as the error bars for some of the fits (particularly those showing oscillations) are very large it is not possible to be confident in this. Given that the lack of oscillations observed for photoelectron peaks A and D can be explained in other ways, there is currently insufficient evidence to suggest photoelectron peaks A, B, D and E originate from different bright vibrational levels in the S_1 electronic state. To be more conclusive it would be necessary to measure spectra at similar wavenumbers using an excitation laser with a smaller bandwidth and determine if A, B, D and E are all observed when exciting at varying S_1 wavenumbers. Assuming photoelectron peaks A, B, D, E do originate from the same S_1 vibrational level, based on the assignment for peak D in section 5.2.2.1, the bright state is likely assignable to $\mathrm{I}^2 12^1$. Further, the intensity oscillations alongside the exponential loss of intensity apparent for photoelectron peaks B and E in Figure 5-6, indicates that $\mathrm{I}^2 12^1$ is strongly coupled to another S_1 vibrational level which acts as a doorway state and facilitates coupling to a large bath of dark states. The increasing population of bath states in S_1 is reflected by the growing congestion in the photoelectron spectrum which is captured by the time profile of the 2420-2530 cm^{-1} baseline region of the photoelectron spectra. Due to the disparity in the τ_1 lifetimes shown in Table 5-4, the estimated IVR lifetime for the S_1 bright state $I^2 12^1$ is based on the τ_1 lifetime determined for peak D assigned $I^2 12^1$ (the $\Delta v = 0$ transition) which is 29 ± 7 ps. The fit of peak D shows the best signal-to-noise, has a high rsq value and relatively small error bars.

Photoelectron peaks B and E oscillate out of phase with each other. Peak E shows maximum intensity at 0 ps indicating it reflects the population of the bright state, $I^2 12^1$. Peak B shows minimum intensity at 0 ps with intensity growing with increasing time delay up to ~2 ps; this indicates peak B reflects the population of the dark state that is strongly coupled to $I^2 12^1$, and acts as a doorway state. An average $\boldsymbol{\tau_{osc}}$ is determined from the fits of peaks B and E to be 4.75 ± 0.01 ps, which corresponds to an eigenstate separation of 7.03 ± 0.01 cm^{-1}. In Figure 5-7 the 0 ps and 2 ps photoelectron spectra are plotted on the same axes; 2 ps is approximately half the oscillation period so the photoelectron spectrum should largely be a Franck-Condon projection of the strongly coupled dark/doorway state.

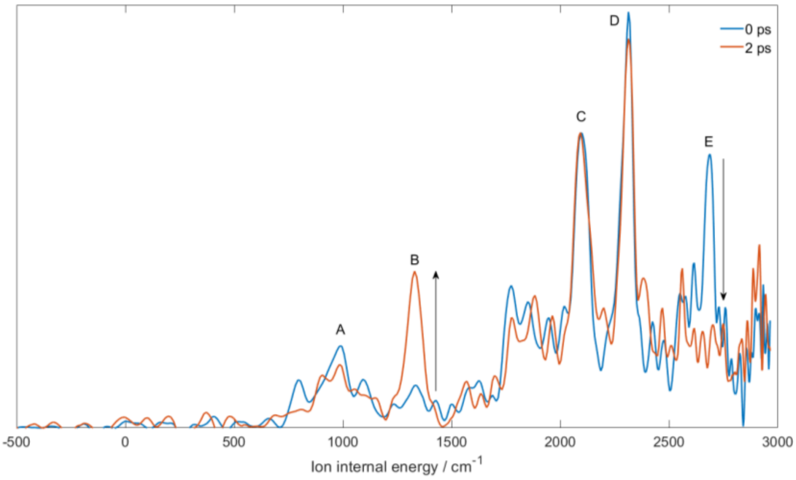

Figure 5-7: Photoelectron spectra measured via ~1720 cm^{-1} in S_1 at pump-probe time delays of 0 ps (blue) versus 2 ps (red)

While B at ~1330 cm^{-1} is the only photoelectron peak more intense at 2 ps, it is unlikely to originate from the $D_0^+ \leftarrow S_1$ $\Delta v = 0$ transition from the dark state because of the difference in wavenumber required upon ionisation (~1720 cm^{-1} in S_1 to ~1330 cm^{-1} in D_0^+); in aniline no vibrational levels are predicted at significantly lower wavenumbers in the ion state compared to the S_1 electronic state. As D at ~2310 cm^{-1} is the most intense photoelectron peak at 2 ps, it is possible that the $\Delta v = 0$ transitions from both the bright and dark states in S_1 may have coincident wavenumbers (within the experimental resolution) of peak D. This would be consistent with the small difference in intensity between 0 ps and 2 ps relative to peak B and could also explain why oscillations are not apparent in the time profile of D. If this is the case, photoelectron peak B would originate from a $\Delta v \neq 0$ transition from the dark state in S_1.

A search was conducted to determine if any vibratonal levels exist which have wavenumbers of ~1720 cm^{-1} and ~2310 cm^{-1} (wavenumber of peak D) ±60 cm^{-1} in the S_1 and cation states respectively. Table 5-5 shows the vibrational levels which match these energy constraints and involve $\Delta N \leq 4$, where ΔN is the change in the total number of vibrational quanta relative to the bright state, because anharmonic coupling strength is expected to decrease as ΔN increases.[7,8]

Vibrational level	Predicted S_1 wave-number / cm^{-1}	ΔE to the experimental wavenumber ~1720 cm^{-1}	Predicted cation wavenumber / cm^{-1}	ΔE to the experimental wavenumber ~2310 cm^{-1}	ΔN relative to $I^2 12^1$
$I^2 19a^1$	1750^{a,b}	30	2316^{b}	6	2
$I^2 6a^2$	1746^{b}, 1744^{c}	26, 24	2365^{b}, 2347^{c}	55, 37	3
$12^1 16a^1 17a^1$	1692^{a,b}	28	2325^{a,b}	15	4

Table 5-5: Assignments for the dark state in the S_1 electronic state. Predicted wavenumbers are determined from fundamental wavenumbers from a) calculations, b) Ref 1 and c) Ref 2.

If the bright state assignment of $I^2 12^1$ is correct, then based on the smallest change in vibrational quanta, the most likely assignment of the dark state would be $I^2 19a^1$ as this is the only level involving ΔN=2. In the 0 ps spectrum (see Figure 5-7) the broad photoelectron feature A at ~975 cm^{-1} is assigned to the vibration 12^1 and results from a $\Delta v \neq 0$ transition from the bright state; although the breadth of this feature indicates transitions to other vibrations may be present. At 2 ps, there is still significant intensity in this spectral region and although the profile has changed, given the resolution it is not possible to determine if there has been a definite shift in peak position. Notably, the 12 and 19a vibrations have similar fundamental vibrational wavenumbers in both the S_1 and D_0^+ electronic states. As a result, it would be useful to measure higher resolution SEVI spectra at 2 ps to determine if the intensity of feature A at later time delays is due to $19a^1$ rather than 12^1; this would support the involvement of $I^2 19a^1$ in the IVR dynamics.

A search has also been conducted to assign photoelectron peak B at ~1330 cm^{-1}; if it does not have the same vibrational identity as the dark state (i.e. a $\Delta v = 0$ transition) then it at least results from some $\Delta v \neq 0$ transition from the dark state and so could suggest whether the dark state assignment of $I^2 19a^1$ is likely or not. At ~1330 cm^{-1}, the wavenumber of photoelectron peak B is consistent with the vibrational wavenumber of I^2 in the cation reported by Knee and co-workers as ~1323 cm^{-1}. Meek and co-workers stated the inversion mode tends not to be excited in the ion unless deliberately excited in the S_1 electronic state, which led them to conclude that the ion and $^1B_2$ state are both planar or nearly planar.[2] This suggests that the dark state involves the inversion mode, supporting an assignment of $I^2 19a^1$. In the 0 ps SEVI spectrum in Figure 5-4 there is low intensity at ~1330 cm^{-1}. This means that either 1) the bright state does not involve the inversion mode bringing the earlier assignment of $I^2 12^1$ into question or 2) the bright state is $I^2 12^1$ but for some reason this vibration has poor overlap with the I^2 vibration in the cation. Only photoelectron peak E, which is at ~2680 cm^{-1}, oscillates in intensity showing maximum intensity at 0 ps, therefore assigning this level is important in confirming an assignment of the bright state in S_1. Two assignments were suggested in Table 5-3; both I^4 and $I^2 1^1 6a^1$, which notably involve the inversion mode, are in reasonable agreement with the wavenumber of peak E given the resolution of the picosecond laser. Despite the weak intensity of the feature assignable to the I^2 vibration at 0 ps spectrum, the fact that both possible assignments for peak E involve the inversion mode lends support to the assignment of the bright state to $I^2 12^1$. Realistically, complimentary higher resolution studies are needed to confirm assignments here.

Until now photoelectron peak C has been excluded from discussions; this is because although the time profile of C in Figure 5-6 shows an exponential loss of intensity, the lifetime is only 7 ± 3 ps. This is much shorter than the lifetimes of peaks A, B, D and E, outside of error bars and in fact the error bar shown in Table 5-4 for peak C is surprisingly small. Further, peak C is shown to be relatively intense in Figure 5-4; the good signal-to-noise and reasonably high Rsq value for the fit suggests the $\boldsymbol{\tau_1}$ lifetime determined from the fit of peak C should be reliable. The difference in IVR lifetime suggests that photoelectron peak C originates from a different bright state in S_1 compared to the other photoelectron peaks. Further, the exponential loss of peak intensity suggests dissipative IVR where the bright state is coupling, more efficiently based on the shorter IVR lifetime, directly to a large bath of dark states. If photoelectron peak C results from a $\Delta v \neq 0$ transition, assigning the S_1 vibrational level excited would be challenging however, given the intensity of peak C there is reason to believe it could originate from the $\Delta v = 0$ transition from S_1 to the ion. Vibrational levels which have predicted vibrational wavenumbers of ~1725 cm^{-1} and ~2100 cm^{-1} in the S_1 electronic and cation states respectively (± 60 cm^{-1}) were shown in Table 5-3, however as mentioned above there is still no reason to favour one assignment over the others based on current evidence. As discussed previously further experiments are needed to unravel the vibrational levels and coupling schemes in this region of the S_1 electronic state.

5.2.3. Photoelectron spectra *via* position II/ S_1 0^0 + ~1760 cm^{-1}

5.2.3.1. Assignment of vibrational levels

Figure 5-8 is the SEVI spectrum measured *via* ~1760 cm^{-1} which is the maximum of the S_1 REMPI peak and labelled position II in Figure 5-2. In S_1, this is 960 cm^{-1} above the ~800 cm^{-1} REMPI feature which was assigned 1^1 in Chapter 3 and ~810 cm^{-1} above the 950 cm^{-1} REMPI feature which was assigned 12^1 in chapter 3. This suggests that the combination level $1^1 12^1$ may be responsible for the intensity at ~1760 cm^{-1} in the S_1 electronic state; this vibration has previously been assigned in literature.[3,4,5] Consistent with this assignment, $1^1 12^1$ has a predicted wavenumber of 1790 cm^{-1} in the cation (see Table 5-6) and this is in very good agreement to the vibrational wavenumber of SEVI peak H which is at ~1780 cm^{-1} in Figure 5-8. If peak H originates from the $D_0^+ \leftarrow S_1$ $\Delta v = 0$ transition, this would explain its greater intensity relative to other peaks. In support of this assignment, the peaks at ~810 cm^{-1} (F) and ~980 cm^{-1} (G) in the SEVI spectrum can be assigned to the constituent fundamental vibrations 1^1 and 12^1 respectively. Further, there is a small origin peak and in chapter 3, the 12^1 vibration was observed in the SEVI spectrum measured via the origin.

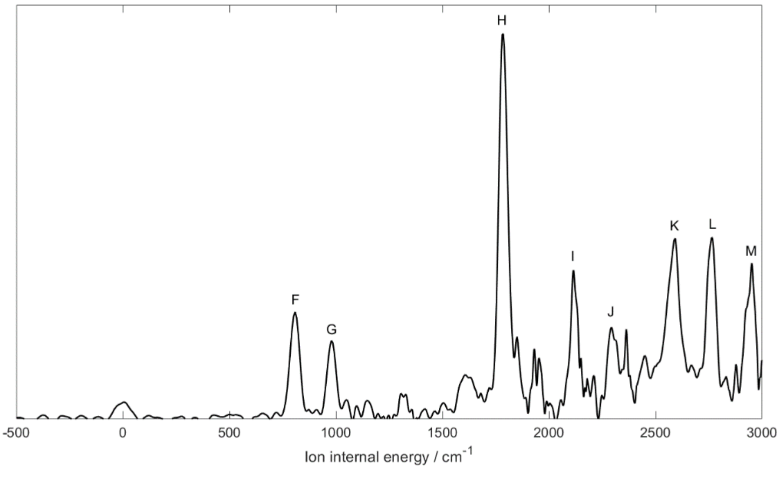

Figure 5-8: 0 ps SEVI spectrum measured via ~1760 cm^{-1} in S_1.

However, there is one alternative assignment. Level $19a^1$ is calculated to be at 985 cm^{-1} and 991 cm^{-1} in the S_1 electronic and cation states respectively, these vibrational wavenumbers are similar to those of level 12^1 meaning that $1^1 19a^1$ is an alternative assignment for the S_1 bright state and SEVI peak H and SEVI peak F could be assigned to $19a^1$. Table 5-6 compares both $1^1 12^1$ and $1^1 19a^1$.

Vibrational level	Predicted S_1 wavenumber / cm^{-1}	ΔE to the experimental wavenumber ~1760 cm^{-1}	Predicted cation wavenumber / cm^{-1}	ΔE to the experimental wavenumber ~1780 cm^{-1}
$1^1 12^1$	1773[a], 1756[b], 1750[c/g], 1751[d/e], 1746[f]	13, 4, 10, 9, 14	1782[a], 1790[b], 1774[d]	2, 10, 6
$1^1 19a^1$	1796[a,b]	36	1801[a], 1800[b]	21, 20

Table 5-6: Predicted S_1 and ion state wavenumbers are based on fundamental wavenumbers from a) calculations, b) Ref 1, c) Ref 4, d) Ref 2 or wavenumbers from e) Ref 3, f) Ref 5, g) Ref 4.

However, the facts that (i) 1^1 and 12^1 were assigned at lower wavenumbers in the S_1 REMPI spectrum in Chapter 3 but level $19a^1$ was not and (ii) there is poorer agreement between the predicted and experimental wavenumbers for level $1^1 19a^1$ compared to level $1^1 12^1$ indicates $1^1 12^1$ is more likely to be the bright state. Assignments for other peaks in the SEVI spectrum are shown in Table 5-7, where multiple vibrations are listed the preferred assignments are in bold.

Ion internal energy / cm^{-1}	Cation vibrational level	Predicted wavenumber of cation vibrational level/ cm^{-1}
0	0^0	0
F - 810	1^1	810[a], 807[b]
G - 980	**12^1** $19a^1$	972[a], 983[b], 981[d] 991[a], 993[b]
H - 1780	**$1^1 12^1$** $1^1 19a^1$	1782[a], 1790[b], 1794[d] 1801[a], 1800[b]
I - 2120	$1^2 6a^1$	2139[a], 2135[b], 2147[d]
J - 2300	**$1^1 6a^1 12^1$** $1^1 6a^1 19a^1$ $1^1 18a^1$	2311[b], 2290[c], 2315[d] 2320[a], 2319[a,b] 2306[a], 2234[c]
K - 2580	$1^2 12^1$ $9a^1 12^1$ $1^2 19a^1$	2592[a], 2597[b], 2607[d] 2579[a], 2576[b], 2575[d] 2611[a], 2607[b]
L - 2760	**$1^1 12^2$** $1^1 19a^2$	2754[a], 2773[b], 2774[d] 2792[a], 2793[b]
M - 2940	**12^3** $19a^3$ $12^2 19a^1$ $12^1 19a^2$	2916[a], 2949[b], 2940[d] 2973[a], 2979[b] 2935[a], 2959[b] 2954[a], 2969[b]

Table 5-7: Experimental wavenumbers of SEVI peaks, alongside potential assignments and their predicted wavenumbers based on fundamental wavenumbers from a) calculations, b) Ref 1, c) Ref 2 and energies from d) Ref 6. Experimental wavenumbers rounded to nearest 10 cm^{-1}.

5.2.3.2. Time-resolved photoelectron spectra

Figure 5-9 shows a selection of the photoelectron spectra measured *via* ~1760 cm^{-1} in S_1 at multiple pump-probe time delays between 0 – 500 ps. Some loss of intensity is apparent for most of the peaks with increasing time delay along with an increase in congestion above ~1900 cm^{-1}. However, notably, most of the peak can still be observed up to 500 ps.

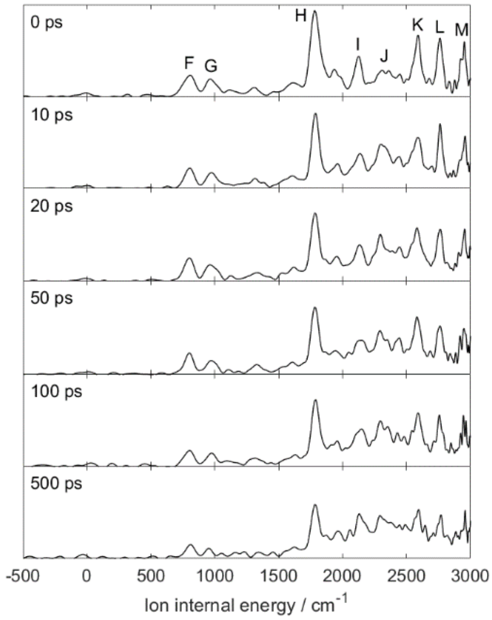

Figure 5-9: Photoelectron spectra measured via ~1760 cm^{-1} in S_1 at selected pump-probe time delays between 0-500 ps.

The intensities of photoelectron peaks F-M have been measured in two ways: i) the full area of each peak has been measured, the importance of this will be discussed and ii) the intensity underneath the peaks has been subtracted from the full peak area in cases where peaks lies in a region of the spectrum where congestion increases with time delay. Above ~1900 cm^{-1} there is no obvious featureless region of the photoelectron spectrum meaning it is not possible to measure the increasing congestion. The data points up to 500 ps have been fit to equations 2.5 or 2.6 depending on the time-dependent behaviour shown and the resulting time profiles are shown in Figure 5-10 and Figure 5-12.

Figure 5-10 shows the full area (no subtraction) of photoelectron peaks F-M up to 70 ps in order to focus on the early time-dependent behaviour. Very weak intensity oscillations are apparent for most of the peaks, in some cases these are unclear outside of error bars however the error bars, which are added after the fit (see chapter 2) are often conservative. The exception is peak G which does not show regular time-dependent behaviour although there are some fluctuations in intensity. This is attributed to the fact G is a particularly weak feature so any potential oscillations in intensity are very small and difficult to measure. Excluding peak G, the τ_{osc} values determined from the fits of the other peaks are in good agreement as shown in Table 5-8, this suggest the oscillations are real. An average oscillation period of 8.35 ± 0.21 ps is determined corresponding to an eigenstate separation of 4.00 ± 0.10 cm^{-1}.

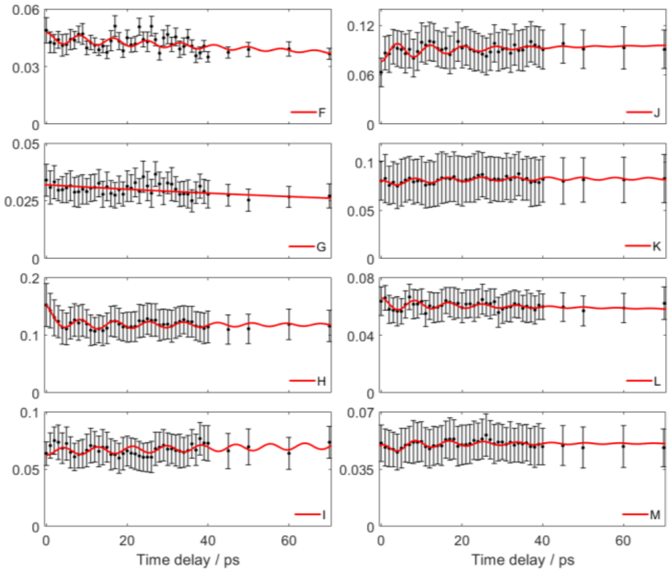

Figure 5-10: Time profiles showing fits to the time-dependent intensity of photoelectron peaks F-M up to 70 ps. Labels correspond to peaks measured. The full peak area was measured.

Peak	τ_{osc}	Rsq
F	8.31 ± 0.42	0.70
H	8.47 ± 0.28	0.76
I	8.52 ± 0.11	0.62
J	8.14 ± 0.34	0.53
K	8.24 ± 0.25	0.46
L	8.35 ± 0.33	0.69
M	8.45 ± 0.29	0.50

Table 5-8: τ_{osc} values determined from the fits of photoelectron peaks F-M up to 500 ps excluding peak G, which does not show clear time-dependent behaviour.

The intensity oscillations indicate the initially excited vibrational level, $1^1 12^1$, is coupled to another S_1 level. As photoelectron peaks F, H, K, L, M all show maximum intensity at 0 ps with intensity decreasing up to ~4 ps, this suggests they reflect the population of the initially excited bright state. Photoelectron peaks I and J show out of phase oscillations with minimum intensity at 0 ps which increases up to ~4 ps, this suggests there are transitions from the dark state in

S_1 at these wavenumbers. Peaks I and J are at ~2120 cm^{-1} and ~2300 cm^{-1} in the photoelectron spectrum respectively, while they are the only peaks more intense at 4ps versus 0 ps, they are still relatively weak which suggests they may not result from the $D_0^+ \leftarrow S_1$ $\Delta v = 0$ transition. As shown in Figure 5-11, the most intense peak at 4 ps is photoelectron peak H at ~1780 cm^{-1}, it is possible that the $\Delta v = 0$ transitions from both the bright and dark state in S_1 have coincident wavenumbers (within the experimental resolution) of peak H. In this case the out of phase oscillations observed for peaks I and J would be the result of $\Delta v \neq 0$ transitions from the dark state in S_1.

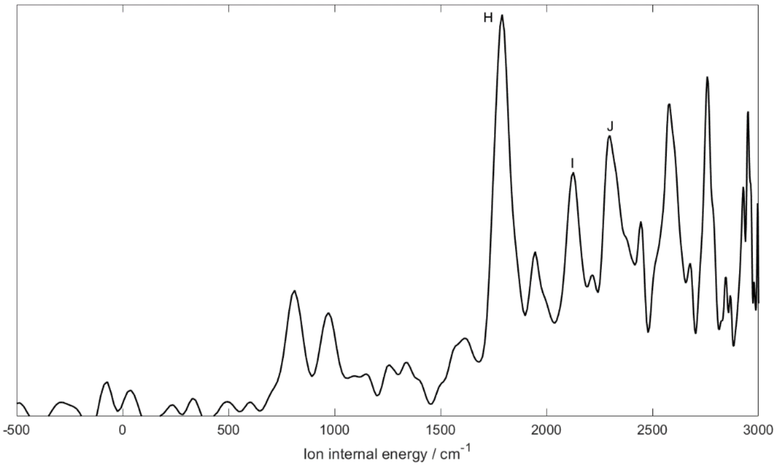

Figure 5-11: 4 ps photoelectron spectrum measured via ~1760 cm^{-1} in S_1.

A search has been conducted for any vibrational levels which have wavenumbers of ~1760 cm^{-1} in the S_1 electronic state (position of pump laser) and either ~2120 cm^{-1} (wavenumber of peak I), ~2300 cm^{-1} (wavenumber of peak J) or ~1780 cm^{-1} (wavenumber of peak H) in the cation. Levels which match these energy constraints (± 60 cm^{-1}) and involve a change in vibrational quanta of $\Delta N \leq 3$ relative to $1^1 12^1$ are shown in Table 5-9; no vibrational levels shown match the wavenumber of photoelectron peak J at ~2300 cm^{-1}. Based purely on the change in vibrational quanta relative to the bright state $1^1 12^1$, the most reasonable assignment for the dark state is $1^1 19a^1$ as it requires $\Delta N = 2$. In the cation, $1^1 19a^1$ has a predicted vibrational wavenumber of ~1800 cm^{-1}, meaning the $D_0^+ \leftarrow S_1$ $\Delta v = 0$ transition would result in a peak at H, which is consistent with the intensity of peak H at 4 ps. Further supporting the dark state assignment of $1^1 19a^1$, several vibrational levels involving mode 19a have predicted vibrational wavenumbers in good agreement to photoelectron peaks I and J which at 4 ps would originate from $\Delta v \neq 0$ transitions from the dark state. These levels are shown in Table 5-10.

Vibration -al level	Predicted S_1 wave-number / cm^{-1}	ΔE to the experimental wavenumber ~1760 cm^{-1}	Predicted cation wavenumber / cm^{-1}	ΔE to the experimental wavenumber ~1780 cm^{-1}	ΔN relative to $12^1 1^1$
$1^1 19a^1$	$1788^{a,b}$	28	1800^{b}	20	2
$12^1 15^2$	1721^{a}, 1718^{b}, 1657^{e}, 1656^{c}	39, 42, 103, 104	1742^{a}, 1729^{c}, 2085^{b}, 2079^{d}	38, 51, 305, 299	3
$1^1 6b^1 15^1$	$1707^{a,b}$	53	1774^{a}, $1789^{a,c}$, $1937^{a,b}$, 1945^{d}	6, 9, 157, 165	3
				ΔE to the experimental vibrational wavenumber ~2120 cm^{-1}	
$10a^1 12^1 16a^1$	$1758^{a,b}$	2	$2140^{a,b}$	20	3

Table 5-9: Assignments for the dark state in S_1. Predicted wavenumbers based on fundamental wavenumbers from a) calculations, b) Ref 1, c) Ref 9, d) Ref 6, e) Ref 5. Discrepancy regarding the reported wavenumber of mode 15 is discussed in Chapter 3.

Assignments for photoelectron peak I (~2120 cm^{-1})		Assignments for photoelectron peak J (~2300 cm^{-1})	
Vibrational level	Predicted wavenumber in the ion state / cm^{-1}	Vibrational level	Predicted wavenumber in the ion state / cm^{-1}
$6b^2 19a^1$	$2151^{a,b}$	$10b^2 19a^2$	2340^{b}
$10a^1 16a^1 19a^1$	$2150^{a,b}$	$16a^1 17a^1 19a^1$	$2335^{a,b}$
$1^1 10b^2 19a^1$	2154^{b}	$1^1 6a^1 19a^1$	2321^{b}
$10b^1 17b^1 19a^1$	$2097^{a,b}$	$10b^2 12^1 19a^1$	2330^{b}
$4^1 10b^3 19a^1$	$2144^{a,b}$	$10b^3 11^1 19a^1$	$2309^{a,b}$

Table 5-10: Vibrational level assignments for photoelectron peaks I and J at ~2120 cm^{-1} and ~2300 cm^{-1} respectively. Predicted wavenumbers are based on fundamental wavenumbers from a) calculations, b) Ref 1 and c) Ref 9

In Chapter 3, time-resolved photoelectron spectra measured *via* ~800 cm^{-1} indicated coupling between S_1 levels 1^1 and $10a^1 16a^1$, where level $10a^1 16a^1$ is the dark state. It follows then that $10a^1 12^1 16a^1$ could potentially be coupled to $1^1 12^1$ rather than $1^1 19a^1$. The predicted wavenumbers of this level are shown in Table 5-9. Although 12^1 and $19a^1$ have similar energies (see Table 3.1), $10a^1 16a^1 19a^1$ is excluded because there would be a change in vibrational quanta of 5 relative to the bright state $1^1 12^1$. The oscillation period measured here (8.35 ± 0.21 ps) is similar to the oscillation period resulting from the coupling of 1^1 and $10a^1 16a^1$ which is also ~8 ps (see Chapter 3). However, the fact that in the cation, $10a^1 12^1 16a^1$ has a predicted vibrational wavenumber of 2140 cm^{-1} so is an assignment for photoelectron peak I, provides some uncertainty because of its weak relative intensity. To conclusively assign the dark state, it would be useful to record higher resolution SEVI spectra at later time delays including 4 ps in order to observe small changes in peak positions which would allow more confidence in assigning transitions from the S_1 dark state. More precise experimental vibrational wavenumbers at 4 ps would also allow vibrational levels to be ruled out because the predicted wavenumbers in Table 5-9 span quite a large wavenumber range.

The time profiles in Figure 5-10 permit observation and analysis of the weak intensity oscillations however, the congestion underneath photoelectron peaks I-M which increases with time delay really needs to be subtracted in order to accurately measure the intensity of the photoelectron peaks, particularly at longer time delays. The time profiles in Figure 5-12 show the 'subtracted' intensity of photoelectron peaks I-M as a function of time delay allowing discussion of the behaviour at long time delays. For some peaks, the weak intensity oscillations are still apparent but for other peaks the intensity changes appear somewhat irregular so that either it is not possible to fit oscillations at all or the rsq value of the fit is relatively poor. This is attributed to the fact that the oscillations in the intensity of the photoelectron peaks are very weak and in some cases the intensity changes are obscured when attempting to subtract the rising background.

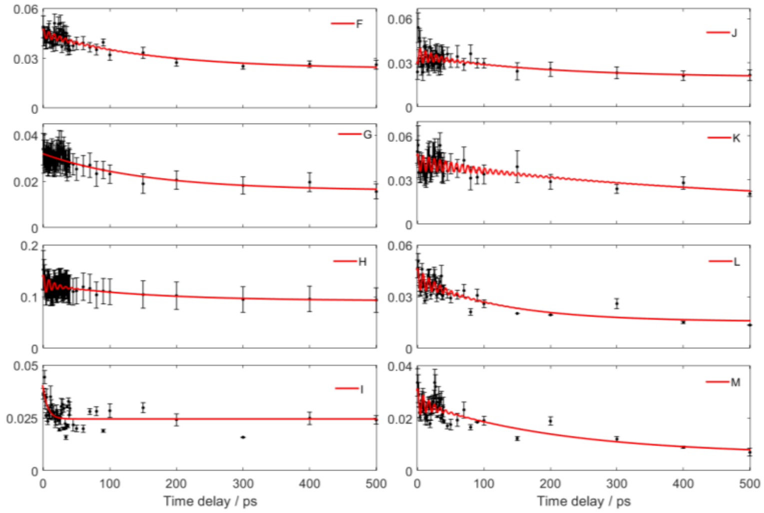

Figure 5-12: Time profiles showing fits to the time-dependent intensity of photoelectron peaks F-M up to 500 ps. Labels correspond to peaks measured. The subtracted area is shown.

An overall loss of intensity is apparent for all the photoelectron peaks F-M alongside the oscillations that were discussed earlier. This type of behaviour could suggest that the dark state, discussed above, is acting as a doorway state facilitating coupling to bath states, known as intermediate IVR. Although, the fact none of the time profiles drop to 0 suggests the bright state is still partially populated by 500 ps and that the doorway state does not couple efficiently to the bath states and is therefore not a "true" doorway state. As a further complication, the congestion already present in the 0 ps photoelectron spectrum suggests that there may be bath states which lie outside the bandwidth of the pump laser, this means their impact on the time-dependence would not be observed.

	Coefficients						
	A	**B**	**C**	$\boldsymbol{\tau_1}$	$\boldsymbol{\tau_2}$	$\boldsymbol{\tau_{osc}}$	**Rsq**
Peak F	0.26	0.23	0.03	165 ± 117	47 ± 124	8.31 ± 0.42	0.70
Peak G	0.17	0.17		155 ± 91			0.73
Peak H	1.00	0.35	0.20	159 ± 117	17 ± 10	8.47 ± 0.28	0.76
Peak I	0.27	0.15		7 ± 5			0.38
Peak J	0.22	0.16	-0.07	188 ± 48	35 ± 64	8.00 ± 0.35	0.39
Peak K	0.12	0.33	0.07	499 ± 1407	90 ± 202	8.42 ± 0.18	0.58
Peak L	0.17	0.27	0.07	130 ± 72	34 ± 41	8.48 ± 0.26	0.77
Peak M	0.07	0.22	0.06	215 ± 206	21 ± 26	8.51 ± 0.48	0.67

Table 5-11: Results from fits of the time-dependent intensity of peaks F-M. Column A, B and C normalised

Table 5-11 shows the lifetimes determined from the fits of photoelectron peaks F-M. It is difficult to confidently draw any conclusions from the lifetimes in this case because the error bars are very large, although there are a few notable points. Excluding peaks G and I, which only have a τ_1 value, for each photoelectron peak there is a trend where the τ_1 values tend to be 100s of picoseconds but the τ_2 values are 10s of picoseconds. Excluding photoelectron peak I which is significantly different, the average τ_1 value is 216 ± 283 ps and the average τ_2 value is 41 ± 49 ps. The τ_1 and τ_2 values of peak K and the associated error bars are much larger than for any other peak, if these are excluded, the average τ_1 and τ_2 lifetimes become 169 ± 46 ps and 31 ± 16 ps. Without further evidence, the difference between the τ_1 and τ_2 lifetimes could be attributed to error caused by difficulty in accurately measuring and fitting very small recurring changes in peak intensity against noise. Measuring additional spectra may improve the fits because it would provide more data points, however, while further spectra at later time delays may improve the accuracy of the τ_1 values, given that the recurrences in intensity are very small the oscillations will always be difficult to measure accurately against the noise.

The fact that photoelectron peak I has a much shorter τ_1 lifetime of 7 ± 5 ps, could mean photoelectron peak I originates from a second bright state in S_1 which has exhibits different time-dependent behaviour. However, in Figure 5-10 the time profile of photoelectron peak I showed oscillations in intensity with a period in very good agreement to the other photoelectron peaks. Due to this, the poor fit of peak I and the fact that all the τ_1 values have large error bars, it is not suggested that peak I results from a different bright state at this time. As a rough estimate, the IVR lifetime of the initially excited vibrational level, $1^1 12^1$, is taken to be the average of the τ_1 lifetimes excluding peak K and I which is 169 ± 46 ps. While there is uncertainty about this value, it is apparent in this case that decay occurs on a much slower timescale than for other S_1 vibrational levels prepared, so this value is sufficient to represent this in the discussion in Chapter 7.

5.2.4. Photoelectron spectra *via* position III/ S_1 0^0 + ~1810 cm^{-1}

5.2.4.1. Assignment of vibrational levels

Figure 5-13 shows the 0 ps SEVI spectrum measured *via* ~1810 cm^{-1} in S_1 which is position III in the REMPI spectrum in Figure 5-2. There are three clear peaks in the spectrum which all appear above ~1800 cm^{-1}; SEVI peak N at ~1890 cm^{-1} dominates the spectrum, being almost three times more intense than the other two peaks.

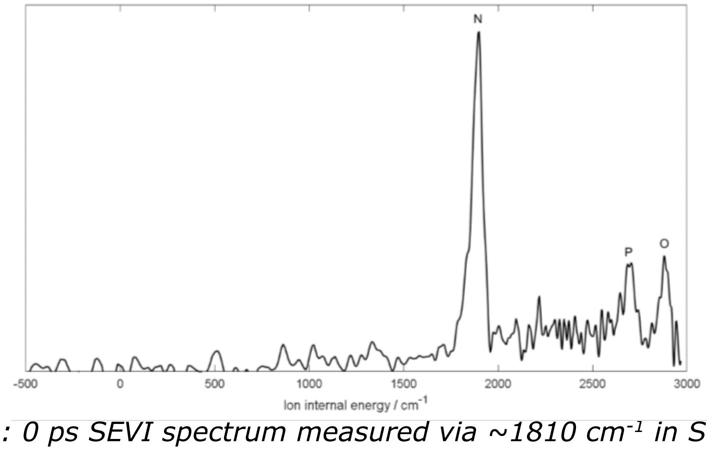

Figure 5-13: 0 ps SEVI spectrum measured via ~1810 cm^{-1} in S_1.

The REMPI feature at ~1810 cm^{-1} which was excited here is 510 cm^{-1} above another REMPI feature at ~1300 cm^{-1}; in Chapter 4 this lower feature was assigned to either level $1^1 6a^1$ or 13^1 with the time-dependent spectra suggesting $1^1 6a^1$ was more likely. A difference of 510 cm^{-1} is in good agreement to the experimental wavenumber of level $6a^1$ which is 492 cm^{-1},[1] this suggests the combination levels $1^1 6a^2$ and $6a^1 13^1$ as potential assignments for the REMPI feature at ~1810 cm^{-1}. The predicted S_1 and cation wavenumbers for both vibrational levels are summarised in Table 5-12; further supporting one of these assignments, both 1^16a^2 and $6a^113^1$ are reasonable assignments for photoelectron peak N. If peak N originates from the $D_0^+ \leftarrow S_1$ $\Delta v = 0$ transition, this would explain the dramatic difference in relative intensities.

Vibrational level	Predicted S_1 wavenumber / cm^{-1}	ΔE to the experimental wavenumber ~1810 cm^{-1}	Predicted cation wavenumber / cm^{-1}	ΔE to the experimental wavenumber ~1890 cm^{-1}
$6a^113^1$	1822[a], 1800[c], 1797[e], 1795[f]	12, 10, 13, 15	1897[a], 1909[b/d], 1863[c]	7, 19, 27
1^16a^2	1820[a], 1784[b], 1779[e]	10, 26, 31	1848[a], 1849[b]	42, 41

Table 5-12: Predicted wavenumbers of 13^16a^1 and 1^16a^2 in the S_1 electronic state and ion state based on fundamental wavenumbers from a) calculations, b) Ref 1 and c) Ref 2 and wavenumbers from d) Ref 6, e) Ref 3, f) Ref 5

There are no peaks in the SEVI spectrum below ~1800 cm^{-1}, meaning none of the constituent fundamental vibrational levels e.g. 13^1, $6a^1$, 1^1 are assigned. Notably, a similar situation was observed in the SEVI spectrum measured at ~1300 cm^{-1} in S_1; given the tentative assignment of the ~1300 cm^{-1} REMPI feature to 1^16a^1, this might indicate an assignment of 1^16a^2 here rather than $6a^113^1$. However, contrary to this, the predicted S_1 and cation wavenumbers of level $6a^113^1$ are in better agreement to the experimental vibrational wavenumbers. Both levels have been assigned in literature, Mikami and co-workers assigned the highest energy band in their fluorescence excitation spectrum at 1795 cm^{-1} to $6a^113^1$,[5] and Scheps and co-workers assigned $6a^212^1$ at 1779 cm^{-1} where 12^1 corresponds to 1^1 in this labelling scheme and $6a^17^1$ at 1797 cm^{-1} where 7^1 corresponds to 13^1 in this labelling scheme.[3] Without more precise experimental vibrational wavenumbers, a tentative assignment of $6a^113^1$ is currently suggested based on the better agreement between predicted and experimental wavenumbers. Assignments for the other SEVI peaks in Figure 5-13 are shown in Table 5-13.

Peak	Ion internal energy / cm^{-1}	Assignment	Predicted wavenumber in the ion / cm^{-1}
N	1890	**$6a^113^1$** 1^16a^2	1897[a], 1909[b/d], 1863[c] 1848[a], 1849[b]
P	2690	**$6a^18a^112^1$** $8a^118a^1$	2675[a], 2691[b], 2687[d] 2680[a], 2606[b],
O	2880	**$6a^112^113^1$** $6a^18a^2$ 13^118a^1	2869[a], 2892[b], 2887[d] 2887[a], 2895[b], 2898[d] 2874[a], 2783[b]

Table 5-13: Assignments for SEVI peaks N, P, O. Predicted wavenumbers of ion states are determined from a) calculations, b) Ref 1, c) Ref 2 and wavenumbers from d) Ref 6. Experimental wavenumbers rounded to nearest 10 cm^{-1}.

5.2.4.2. Time-resolved photoelectron spectra

Photoelectron spectra were measured *via* ~1810 cm^{-1}at selected pump-probe time delays between 0 ps and 500 ps; several of these are shown in Figure 5-14. Each photoelectron peak loses intensity with increasing time delay so that little structure is remains by 500 ps. This is accompanied by growing intensity or congestion in the baseline.

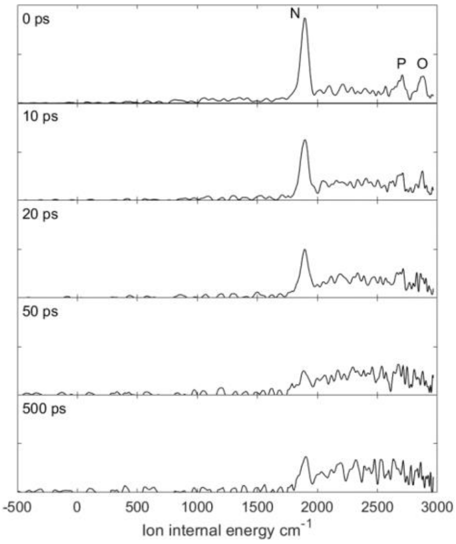

Figure 5-14: Photoelectron spectra measured via ~1810 cm^{-1} in S_1, at pump-probe time delays of 0 ps, 10 ps, 20 ps, 50 ps and 500 ps.

The intensity of photoelectron peaks N and O (following subtraction of the increasing congestion) have been plotted as a function of time delay to give the time profiles in Figure 5-15; the data points are fit to equation 2.5. To capture the growing congestion, the intensity of the baseline between 2045 – 2532 cm^{-1} has been measured and fit to equation 2.7. The results of all fits are shown in Table 5-14. Data points at later time delays (above 100 ps) when the peak intensity is negligible in most cases, have been excluded from the fits, as they could erroneously influence the lifetime calculated by the fit.

In Figure 5-15, the time profiles of peaks N and O both show an exponential decrease in intensity with τ_1 lifetimes of 19 ± 4 and 15 ± 9 respectively. This suggests that both photoelectron peaks are reflecting the population of the initially excited bright state, $6a^1 13^1$, in S_1 which is coupled to numerous bath states. This is known as dissipative energy dispersal. The time profile of the 2045 –2532 cm^{-1} spectral region shows an exponential increase in intensity, opposite behaviour to peaks N and O, with a τ_1 lifetime of 19 ± 6. The good agreement between lifetimes is consistent with the increasing congestion being the result of transitions from numerous bath states in S_1 that are populated through coupling to bright state $6a^1 13^1$. An average IVR lifetime of 18 ± 3 ps is determined from all three fits.

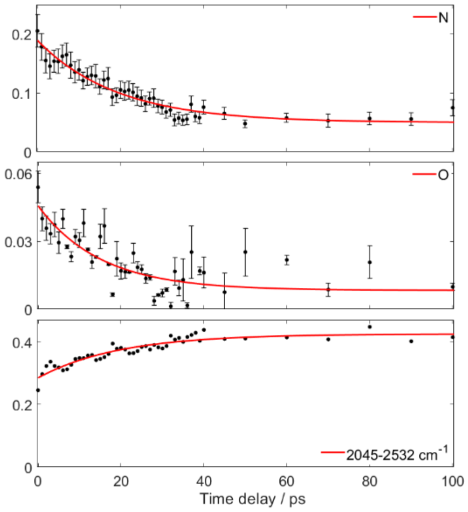

Figure 5-15: Time profiles showing fits to the time-dependent intensity of photoelectron peaks N, O and the 2045 – 2532 cm^{-1} region of the baseline where there are no peaks. Plots labelled according to feature measured.

	Coefficients			
Peak	**A**	**B**	τ_1	**Rsq**
N	0.17	0.49	19 ± 4	0.92
O	0.03	0.13	15 ± 9	0.62
Baseline 2045-2532 cm^{-1}	1	0.49	19 ± 6	0.86

Table 5-14: Results from fits of peaks N and O and baseline region 2045-2532 cm^{-1} in the photoelectron spectrum. Column A and B are normalised.

Photoelectron peak P at ~2690 cm^{-1} in Figure 5-14, has been excluded from the analysis. In comparison to peak N at ~1890 cm^{-1}, peaks P and O that appear above ~2500 cm^{-1} in the 0 ps spectrum are much weaker with poorer signal-to-noise. As a result, it was more difficult to accurately measure the small differences in signal against noise, quickly the error becomes comparable to the signal itself. This is the reason given the for larger error bar associated with the fit of peak O, although, this has apparently affected the integrals measured for peak P to a greater extent because even though the photoelectron spectra in Figure 5-14 show peak P loses intensity and cannot be observed after ~50 ps, this trend is not clearly observed when the time-dependent intensity of P is plotted as a function of time in Figure 5-16. Any fit of this data to a decay curve would be poor with a large uncertainty in the lifetime so provide no reliable quantitative information.

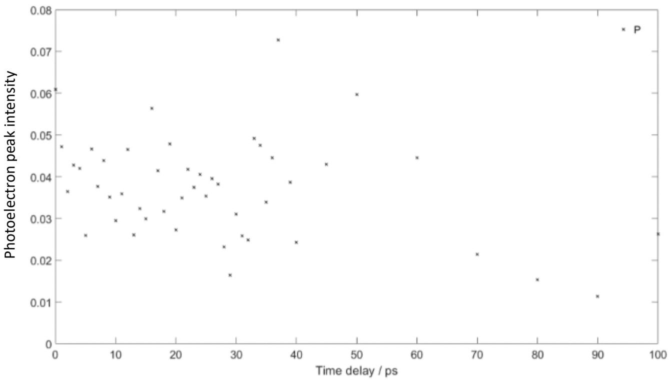

Figure 5-16: Time-dependent intensity of photoelectron peak P plotted as a function of pump-probe time delay.

5.2.5. Comparison of SEVI spectra via S_1 0^0 + (I)~1720 cm^{-1}, (II)~1760 cm^{-1} and (III)~1810 cm^{-1}

The 0 ps SEVI spectra measured *via* I) $I^2 12^1$ at ~1720 cm^{-1}, II) $1^1 12^1$ at ~1760 cm^{-1} and III) $6a^1 13^1$ at ~1810 cm^{-1} in S_1 are shown together in Figure 5-17. Notably, there is significantly more congestion in spectrum I) measured via $I^2 12^1$ at ~1720 cm^{-1} compared to the other two. Congestion present at 0 ps can be an indication of eigenstates, which are involved in the coupling scheme, lying outside the bandwidth of the pump laser. Considering that in all three cases, the time profiles indicated the bright state was coupled to bath states in S_1, it is interesting that the vibrational levels at I) ~1720 cm^{-1} apparently couple to more bath states lying much further away in wavenumber.

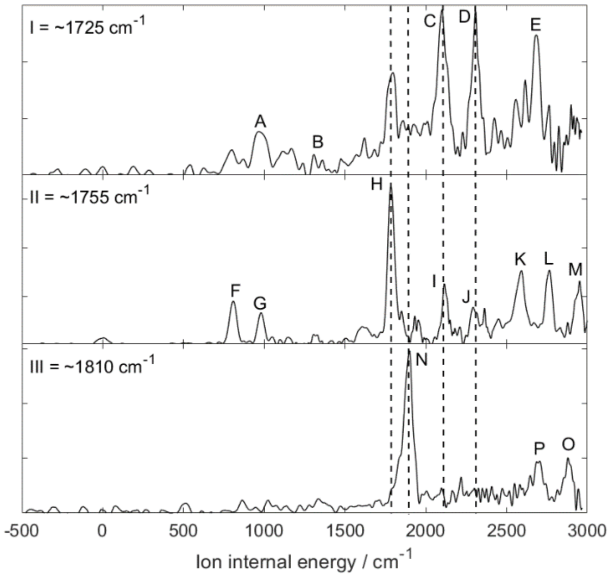

Figure 5-17: 0 ps SEVI spectra measured via I) ~1720 cm^{-1}, II) ~1760 cm^{-1} and III) ~1810 cm^{-1} in S_1. Peaks are labelled A-P, the same labels as used in the individual SEVI spectra presented in previous sections. Dotted lines are drawn through the peaks originating from $\Delta v=0$ transitions from S_1.

In Figure 5-17 dotted lines are drawn at the wavenumbers of peaks C, D, H, N which all originate from $D_0^+ \leftarrow S_1$ $\Delta v = 0$ transitions. The third SEVI spectrum, which was measured *via* ~1810cm^{-1} (position III) in S_1, shows no peaks in common with the other two SEVI spectra. The lack of similarity combined with the time-resolved spectra suggests no coupling occurs between level $6a^1 13^1$ (excited at III ~1810 cm^{-1}) and the S_1 vibrational levels excited at either I) ~1720 cm^{-1} or II) ~1760 cm^{-1}. This is not unexpected given the energy differences involved. However, there may be some similarities in peak positions between the SEVI spectra measured *via* $I^2 12^1$ at I) ~1720 cm^{-1} and $1^1 12^1$ at II) ~1760 cm^{-1}. Close inspection reveals SEVI peaks C and D at ~2100 cm^{-1} and ~2310 cm^{-1} respectively are slightly shifted in wavenumber compared to SEVI peaks I and J at ~2120 cm^{-1} and ~2300 cm^{-1} respectively. Although, given the broadness of the bands, there is some uncertainty as to whether these peaks are truly at the same position. Additionally, peak H, assigned $1^1 12^1$, is at ~1780 cm^{-1}; there is also a peak at the same wavenumber in the spectrum measured *via* I) ~1720 cm^{-1} in S_1 which could also be level $1^1 12^1$. This peak is only resolved in the SEVI spectrum not the time-dependent photoelectron spectra so it was not assigned a label in section 5.2.2.2. For the purposes of the following discussion this peak will be designated 'X'. The small wavenumber differences between peaks C/I and D/J respectively suggest different cation vibrational levels and indeed different assignments were suggested for the peaks. If this is true then the two SEVI peaks observed at ~1780 cm^{-1} in the two sets of spectra (X,H) could be a coincidence also.

As the peaks are broad and there is some uncertainty as to whether the peaks are at the same position and have the same vibrational identity or not, it would be valuable to record higher resolution photoelectron spectra where narrower peaks and more precise vibrational wavenumbers could be obtained. If the three peaks observed at ~1780 cm^{-1} (X), ~2100 cm^{-1} (C) and ~2310 cm^{-1} (D) in the SEVI spectrum recorded at S_1 0^0 + ~1720 cm^{-1} are the same cation vibrational levels as observed at ~1780 cm^{-1} (H), ~2120 cm^{-1} (I) and ~2300 cm^{-1} (J) in the SEVI spectrum recorded at S_1 0^0 + ~1760 cm^{-1}, then this could either indicate coupling between the S_1 vibrational levels at ~1720 cm^{-1} and ~1760 cm^{-1} or that the pump laser excited vibrational levels in common (e.g. $I^2 12^1$ and $1^1 12^1$) at both S_1 wavenumbers. The relative intensities of SEVI peaks X, C/D and H, I/J switch when exciting at ~1720 cm^{-1} versus exciting at ~1760 cm^{-1}, which may suggest a Fermi resonance between vibrational levels in S_1.

However, this is not obvious from the time-resolved photoelectron spectra, as shown in Table 5-15 different behaviour is largely observed for both sets of peaks. Although, of interest are the lifetimes observed for SEVI peaks C and I, while in good agreement to each other, for both peaks the lifetime determined is much shorter than for other peaks in the same spectrum. It was concluded that peak C originated from excitation of a second bright state in S_1 (see section 5.2.2.2) which coupled efficiently to bath states. However, for peak I it was somewhat inconclusive, while the lifetime was much shorter compared to other SEVI peaks in the same spectrum, large error bars were determined for lifetimes and importantly peak I showed oscillations with a similar period to all the other peaks.

SEVI peak	Position / cm^{-1}	Time-dependent behaviour	Lifetime τ_1 / ps	Lifetime τ_2 /ps	τ_{osc} / ps	Rsq
Observed in SEVI spectrum recorded at S_1 0^0 + ~1720 cm^{-1}						
*	~1780	Not observed in tr-pes	-	-	-	-
C	~2100	Exponential decay	7 ± 3	-	-	0.75
D	~2310	Exponential decay	29 ± 7	-	-	0.88
Observed in SEVI spectrum recorded at S_1 0^0 + ~1755 cm^{-1}						
H	~1780	Oscillations alongside overall decay	159 ± 117	17 ± 10	8.47 ± 0.28	0.76
I	~2120	Oscillations alongside overall decay	-	-	8.52 ± 0.11	0.62
			7 ± 5	-	-	0.38
J	~2300	Oscillations alongside overall decay	-	-	8.14 ± 0.34	0.53
			188 ± 48	35 ± 64	8.00 ± 0.35	0.39

Table 5-15: Energies, lifetimes and oscillation periods determined from the fits to the time-dependent intensity of photoelectron peaks discussed in text. The intensity of photoelectron peaks I and J was determined using two methods resulting in two fits, this is discussed in section 5.2.3.2

It is possible though that the time resolution of the experiment is not sufficient to capture the oscillations in intensity resulting from this possible Fermi-resonance. The vibrational levels excited at I) ~1720 cm^{-1} and II) ~1760 cm^{-1}, $I^2 12^1$ and $1^1 12^1$ respectively, are predicted to be ~40 cm^{-1} apart which would correspond to an oscillation period of less than 1 ps if these vibrational levels coupled. Further, as the time-resolved photoelectron spectra indicates that each vibrational level couples to other dark states, any time-dependent behaviour resulting from the Fermi-resonance may just be overshadowed and not immediately noticeable. Additionally, a difference of ~40 cm^{-1} may mean that the pump pulse does not fully overlap both bright states, in which case the true time-dependent behaviour is not observed and only time-independent eigenstates are observed. It may be of use to record time-resolved photoelectron/SEVI spectra when exciting at ~1740 cm^{-1} in S_1. If there is a Fermi-resonance, excitation in the middle of the two previous wavenumber positions may allow the pump pulse to coherently excite both vibrational levels and reveal any dynamics.

5.3. Photoelectron spectra *via* ~1930 cm^{-1}

5.3.1.1. Assignment of vibrational levels

Figure 5-18 shows the SEVI spectrum measured *via* ~1930 cm^{-1} in S_1 at a pump-probe time delay of 0 ps. The bright state initially excited is assigned as 12^2 because i) the ~1930 cm^{-1} REMPI feature is at close to double the wavenumber of the ~950 cm^{-1} REMPI feature assigned to level 12^1 in Chapter 3 and ii) 12^2 is at 1966 cm^{-1} in the cation,[1] consistent with the wavenumber of peak B at ~1980 cm^{-1} which is the most relatively intense. Further, photoelectron peaks A and D, which are the most intense after B, can be assigned to vibrational levels 12^1 and 12^3 respectively meaning there is a progression of mode 12.

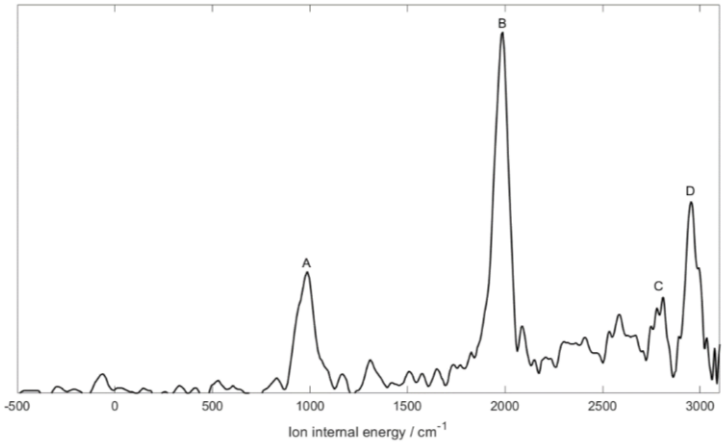

Figure 5-18: 0 ps SEVI spectrum measured at ~1930 cm^{-1} in S_1.

As shown in Table 5-16, three alternative assignments were found based on agreement to experimental wavenumbers; all four vibrational levels would be assignments for peak B in the cation. However, these levels were not assigned in literature, whereas level 12^2 was assigned,[3,4] and the constituent fundamental vibrations $19a^1$ and $8a^1$ were not assigned at lower wavenumbers in the S_1 REMPI spectrum in this work. Further, there is no evidence from the time-resolved photoelectron spectra (shown in the next section) to suggest more than one vibrational level has been excited.

Vibrational level	Predicted S_1 wavenumber / cm^{-1}	ΔE to the experimental wavenumber ~1930 cm^{-1}	Predicted cation wavenumber / cm^{-1}	ΔE to the experimental wavenumber ~1980 cm^{-1}
12^2	1930^a, 1912^b, 1905^c, 1904^d	0, 18, 25, 26	1944^a, 1966^b, 1959^e	36, 14, 21
$19a^2$	1976^a	46	1982^a, 1986^b	2, 6
$12^1 19a^1$	1953^a, $1941^{a,b}$	23, 11	1963^a, 1976^b	17, 4
$1^1 8a^1$	1940^a, $1932^{a,b}$	10, 2	$1994^{a/b}$, 2001^e	14, 21

Table 5-16: Predicted wavenumbers vibrational in the S_1 electronic state and cation based on fundamental wavenumbers from a) calculation, b) Ref 1 and wavenumbers from c) Ref 4, d) Ref 3, e) Ref 6.

Suggested assignments for each of the main peaks in the SEVI spectrum in Figure 5-18 are summarised in Table 5-17, preferred assignments are in bold.

Peak	Observed ion wavenumber / cm^{-1}	Assignment	Predicted wavenumber in the ion / cm^{-1}
A	980	$\mathbf{12^1}$ $19a^1$	972^a, 983^b 991^a, 993^b
B	1980	$\mathbf{12^2}$ $1^1 8a^1$ $19a^2$ $12^1 19a^1$	1944^a, 1966^b, 1959^c 1994^a, 1994^b, 2001^c 1982^a, 1986^b 1963^a, 1976^b
C	2780	$\mathbf{1^1 12^2}$ $1^2 8a^1$ $8a^1 9a^1$	2754^a, $2773^{b/c}$ 2804^a, 2801^b 2791^a, 2780^b
D	2950	$\mathbf{12^3}$ $19a^3$	2916^a, 2949^b, 2940^c 2973^a, 2979^b

Table 5-17: Vibrational level assignments for SEVI peaks. Predicted wavenumbers are based on fundamental wavenumbers from a) calculations, b) Ref 1 and wavenumbers from c) Ref 6. Experimental wavenumbers are rounded to nearest 10 cm^{-1}.

5.3.1.2. Time-resolved photoelectron spectra

Photoelectron spectra were measured *via* ~1930 cm^{-1} in S_1 at selected time delays between 0 ps and 500 ps, several of these are shown in Figure 5-19. Each of the peaks A-D decreases in intensity with increasing time delay so by 500 ps most structure has been lost from the spectrum. Above ~2000 cm^{-1} the intensity of the baseline is also observed to increase with increasing time delay.

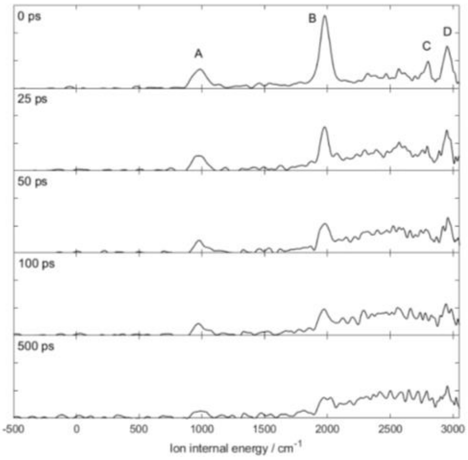

Figure 5-19: Photoelectron spectra measured via ~1930 cm^{-1} in S$_1$ at pump-probe time delays of 0 ps, 25 ps, 50 ps, 100 ps and 500 ps

The intensity of each photoelectron peak A-D along with two featureless regions of the baseline have been measured and plotted as a function of time delay to give the time profiles shown in Figure 5-20. The increasing baseline congestion has been subtracted and depending on the time-dependent behaviour, the data points up to 150 ps have been fit to equations 2.5 or 2.7. The results of the fits are shown in Table 5-18. As expected from the photoelectron spectra in Figure 5-19, the time profiles of photoelectron peaks A, B and D all show an exponential loss of intensity. An overall loss of intensity is also seen for peak C although there is more variation in data points which is attributed to much poorer signal to noise. The two time profiles showing the intensity of different baseline regions both show exponential increases in intensity. These behaviours are typical of dissipative IVR and indicates the bright state 12^2 couples to many bath states.

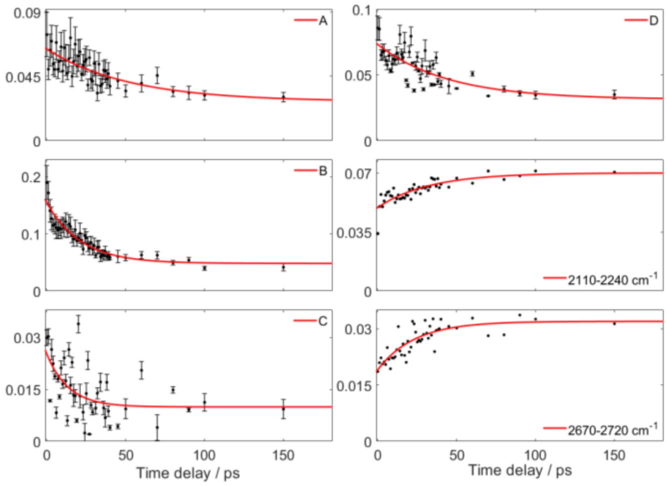

Figure 5-20: Time profiles showing the time-dependent intensity of photoelectron peaks A-D and baseline range (1) 2110-2240 cm^{-1} and (2) 2670-2720 cm^{-1} where there are no peaks. Plots labelled according to feature measured.

	Coefficient			
Peak/Region	**A**	**B**	**τ_1**	**Rsq**
A	0.26	0.35	52 ± 46	0.56
B	0.46	1.00	21 ± 6	0.88
C	0.09	0.14	14 ± 15	0.30
D	0.30	0.39	44 ± 37	0.55
Baseline 2110-2240 cm^{-1}	0.47	0.19	33 ± 13	0.73
Baseline 2670-2720 cm^{-1}	0.18	0.12	23 ± 12	0.69

Table 5-18: Results from fits of the time-dependent intensity of photoelectron peaks A-D and baseline regions (1) 2110-2240 cm-1 and (2) 2670-2720 cm^{-1}. Column A and B are normalised

The τ_1 value of 21 ± 6 ps determined from the fit of peak B is taken to be the IVR lifetime because i) peak B results from the $D_0^+ \leftarrow S_1$ $\Delta V=0$ transition from the bright state, ii) peak B shows good signal to noise and the fit shows the highest Rsq value and iii) there is some disparity between the different τ_1 lifetimes from all the fits. Little can be really be concluded about the agreement between the lifetimes because although there is some disparity, the error bars associated with the fits are relatively large. While large differences in decay lifetimes could be could be indicative of a second bright state, in this case, any disparity is attributed to peaks A, C and D being considerably weaker in intensity and significant growth in baseline intensity resulting in poorer signal-to-noise. This would explain the larger error bars and lower Rsq values for the fits of A, C and D compared to fit B. The similarity between the τ_1 values of peak B and the two baseline regions is consistent with the congestion resulting from the growing number of bath states, although again error bars are large.

5.4. Photoelectron spectra *via* ~2110 cm^{-1}

5.4.1.1. Assignment of vibrational levels

Figure 5-21 shows the 0 ps SEVI spectrum measured *via* ~2110 cm^{-1} in S_1. Table 5-19 shows the five potential vibrational level assignments which were found for the REMPI feature. The $D_0^+ \leftarrow S_1$ $\Delta v = 0$ transition from each of these S_1 vibrational levels could account for peak B in the SEVI spectrum which is at ~2190 cm^{-1}; this would explain the greater intensity of peak B relative to the other peaks.

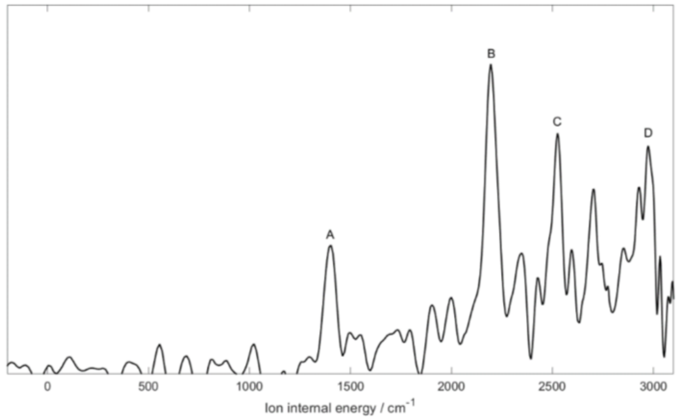

Figure 5-21: 0 ps SEVI spectrum measured via ~2110 cm^{-1} in S_1.

Vibrational level	Predicted S_1 wavenumber / cm^{-1}	ΔE to the experimental wavenumber ~2110 cm^{-1}	Predicted cation wavenumber / cm^{-1}	ΔE to the experimental wavenumber ~2190 cm^{-1}
$1^1 13^1$	2124[a], 2105[c]	14, 5	2188[a], 2195[b], 2145[c], 2197[d]	2, 5, 45, 7
$1^2 6a^1$	2122[a], 2092[b]	12, 18	2139[a], 2135[b], 2147[d]	51, 55, 43
$8a^1 19a^1$	2120[a]	10	2175[a], 2180[b/d]	15, 10
$8a^1 12^1$	2097[a], 2088[a,b]	13, 22	2156[a], 2170[b], 2165[d]	34, 20, 25
$6a^2 8a^1$	2144[a], 2116[a,b]	34, 6	2222[a], 2229[b]	32, 39

Table 5-19: Predicted S_1 and cation wavenumbers of vibrational levels mentioned in text based on fundamental wavenumbers from a) calculation, b) Ref 1, c) Ref 2 and wavenumbers from d) Ref 6.

Of the vibrational levels listed in Table 5-19, the most likely bright state assignment is concluded to be $1^1 13^1$. This is because i) this level this shows better agreement between predicted and experimental vibrational wavenumbers and ii) peak A at ~1390 cm^{-1} can be assigned to the constituent fundamental vibration 13^1, this mode has not been assigned in many other photoelectron spectra recorded following excitation of other low wavenumber S_1 vibrations. The other levels are considered less likely because although this REMPI feature is 810 cm^{-1} above the ~1300 cm^{-1} REMPI feature which was tentatively assigned to level $1^1 6a^1$ in Chapter 4, the fundamental levels 1^1 or $6a^1$ are not assigned in the SEVI spectrum here. Additionally mode 8a is involved in several potential assignments in Table 5-19 but this level has not been assigned in the S_1 REMPI spectrum as a fundamental or combination level. Table 5-20 shows assignments for other peaks in the SEVI spectrum.

Ion internal energy / cm^{-1}	Cation vibrational level	Predicted wavenumber of cation vibrational level / cm^{-1}
A – 1390	$\mathbf{13^1}$	1378^a, 1388^b, 1347^c, 1385^d
B - 2190	$\mathbf{1^1 13^1}$	2188^a, 2195^b, 2145^c, 2197^d
	$1^2 6a^1$	2139^a, 2135^b, 2147^d
	$8a^1 19a^1$	2175^a, $2180^{b/d}$
	$8a^1 12^1$	2156^a, 2170^b, 2165^d
	$6a^2 8a^1$	2222^a, 2229^b
C - 2520	$8a^1 13^1$	2562^a, 2575^b, 2517^c
	$1^1 10b^2 13^1$	2540^a, 2549^b
2700	$\mathbf{1^1 6a^1 13^1}$	2707^a, 2716^b, 2720^d
	$1^2 6a^2$	2658^a, 2656^b
	13^2	2756^a, 2776^b
D – 2960 - 2970	$\mathbf{1^2 13^1}$	2998^a, 3002^b, 2943^c

Table 5-20: Assignments for the main SEVI peaks. Predicted wavenumbers are based on fundamental wavenumbers in a) calculations, b) Ref 1, c) Ref 2 and wavenumbers from d) Ref 6. Experimental wavenumbers are rounded to nearest 10 cm^{-1}. Preferred assignments are in bold.

5.4.1.2. Time-resolved photoelectron spectra

Photoelectron spectra were measured *via* ~2110 cm^{-1} at selected pump-probe time delays between 0 and 500 ps, several of these are shown in Figure 5-22.

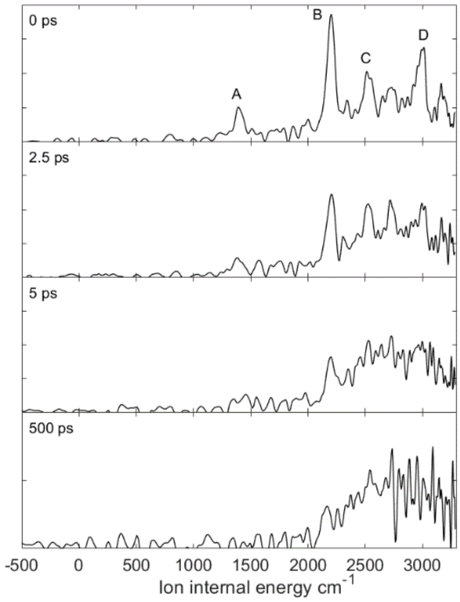

Figure 5-22: Photoelectron spectra measured at ~2110 cm^{-1} in S_1 at pump-probe time delays of 0 ps, 2.5 ps, 5 ps and 500 ps

As time delay is increased, the photoelectron peaks all quickly decrease in intensity with no obvious recurrences. By 5 ps only peak B, the most intense in the 0 ps spectrum, is observed and there is unstructured intensity above ~2000 cm^{-1} which increases further up to 500 ps. The intensity of each photoelectron peak A-D along with three featureless regions of the baseline have been plotted as a function of pump-probe time delay. Depending on behaviour, the data points are fit to either equation 2.5 or 2.7 and the resulting time profiles are shown in Figure 5-23. Given how quickly the photoelectron peaks lose intensity, photoelectron spectra have been measured every 0.5 ps in order to have enough data points to determine a reliable IVR lifetime. Further, only the intensities between 0 ps and 14 ps have been included in the fits because by 14 ps the peaks have lost most if not all intensity meaning that the signal to noise is no longer good. Variation in the data points at later time delays is likely just representative of noise or error in the experiment. The results of the fits are shown in Table 5-21.

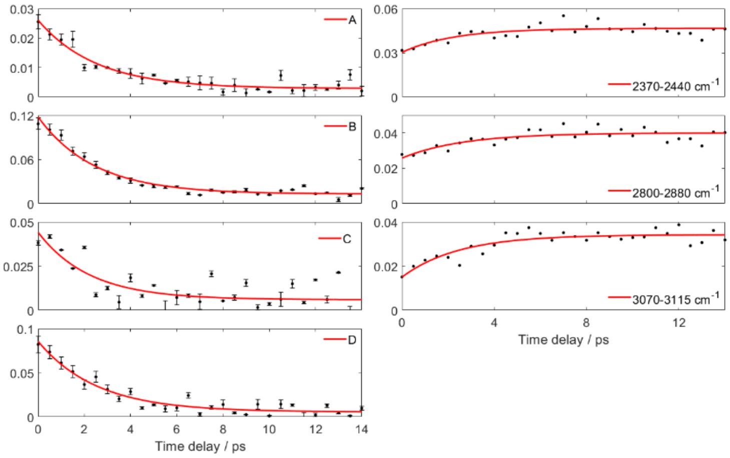

Figure 5-23: Time profiles showing the time-dependent intensity of peaks A-D and baseline regions: 1) 2370-2440 cm^{-1}, 2) 2800-2880 cm^{-1} and 3) 3070-3115 cm^{-1}. Plots are labelled according to feature measured.

	Coefficients			
Peak	**A**	**B**	**τ_1 / ps**	**Rsq**
A	0.03	0.22	2.5 ± 0.7	0.92
B	0.12	1.00	2.4 ± 0.4	0.97
C	0.06	0.36	2.2 ± 1.5	0.62
D	0.05	0.76	2.5 ± 0.6	0.93
Baseline 2370-2440 cm^{-1}	0.29	0.16	2.2 ±1.5	0.60
Baseline 2800-2880 cm^{-1}	0.25	0.14	2.6 ± 1.8	0.62
Baseline 3070-3115 cm^{-1}	0.14	0.18	2.5 ± 1.2	0.76

Table 5-21: Results of fits of the time-dependent intensity of peaks A-D and baseline regions in the photoelectron spectrum. Column A and B are normalised.

In Figure 5-23, the time profiles of photoelectron peaks A-D all show an exponential decrease in intensity which is typical of dissipative IVR. There is very good agreement between the τ_1 lifetimes, with an average lifetime of 2.4 ± 0.2

ps determined from all four fits A-D. This fast decay indicates that the initially excited S_1 vibrational level assigned $1^1 13^1$, couples efficiently to a large bath of dark states and rapidly loses population. The fit of peak C is worse in comparison to the fit of A, B and D with larger error bars and a lower Rsq value, this is attributed to peak C being relatively weak even at 0 ps and in a region of the spectrum where there is a rapidly increasing baseline intensity. This results in poorer signal-to-noise making it difficult to accurately measure the peak intensity, this is particularly true at longer time delays. The final three time profiles measure the unstructured congestion that grows in with increasing time delay; these profiles show an increase in intensity. The $\boldsymbol{\tau_1}$ lifetimes determined for these fits are all in very good agreement to the $\boldsymbol{\tau_1}$ lifetimes of peaks A-D which is consistent with increasing congestion being a result of coupling between level $1^1 13^1$ and bath states in S_1 and an increasing number of overlapping transitions from S_1.

5.5. Summary and conclusion

Time resolved photoelectron spectra have been measured *via* 5 intermediate wavenumber positions above ~1700 cm^{-1}. Assignments were made based on experimental vibrational wavenumbers determined from the higher resolution SEVI spectra, which have currently only been measured at 0 ps. Above, it has been noted that in some cases, it would be beneficial to compare to higher resolution spectra at later time delays in order to observed shifts in peak positions relative to 0 ps which has been inferred from the time-dependent data.

Excitation of these high energy vibrational levels has resulted in energy dispersal, in two cases being mediated by doorway states, being detected which is not unexpected given the relatively high internal energy. The IVR lifetimes are summarised in Table 5-22; these tend to decrease with increasing internal energy with the shortest IVR lifetime determined for S_1 $1^1 13^1$ at 2110 cm^{-1}. Notably, two results stand out: i) the first is the much longer IVR lifetime determined for the S_1 vibrational level at ~1760 cm^{-1} assigned $1^1 12^1$ which suggests coupling to bath states may not be very efficient and/or a small number of available bath states, and ii) the second is the much shorter IVR lifetime for the unassigned S_1 vibrational level excited at ~1720 cm^{-1}. The latter result could be an indication of mode-dependent dynamics, it is reminiscent of mode 7a in *para*-fluorotoluene.[10] Although further data is required to assign this level before the reason for the lifetime can be explored. Pertinent normal mode diagrams are shown in Figure 5-24.

Wavenumber excited by pump laser in S_1 / cm^{-1}	Initially excited vibrational level	Behaviour	IVR lifetime / ps
1720	$I^2 12^1$	Doorway	29 ± 7
	Not assigned	Dissipative	7 ± 3
1760	$1^1 12^1$	Doorway	169 ± 46
1810	$6a^1 13^1$	Dissipative	19 ± 6
1930	12^2	Dissipative	21 ± 6
2110	$1^1 13^1$	Dissipative	2.4 ± 0.2

Table 5-22: Summary of IVR lifetimes determined for vibrational levels excited in this chapter.

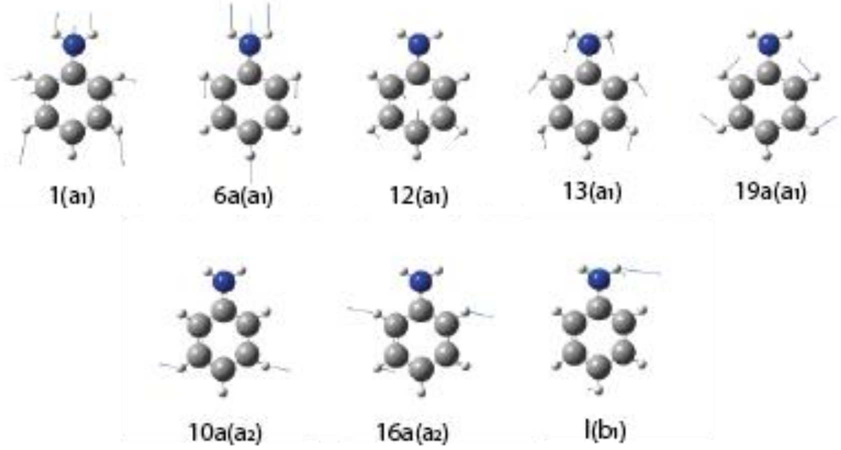

Figure 5-24: Pertinent normal vibrational modes.

5.6. References

---

[1] X. Zhang, J. M. Smith and J. L. Knee., *J. Chem. Phys.*, 1992, **97**, 2843-2860

[2] J. T. Meek, E. Sekreta, W. Wilson, K. S. Viswanathan, J. P. Reilly., *J. Chem. Phys.*, 1985, **82**, 1741-1749

[3] R. Scheps, D. Florida, and S. A. Rice, *J. Chem. Phys.,* 1974, **61**, 1730-1747

[4] J. C. D. Brand, D. R. Williams, T. J. Cook., *J. Mol. Spec.*, 1966, **20**, 359-380

[5] N. Mikami, A. Hiraya, I. Fujiwara and M. Ito, *Chem. Phys. Lett.,* 1980, **74**, 531-535

[6] X. Song, M. Yang, E. R. Davidson and J. P. Reilly, *J. Chem. Phys.,* 1993, **99**, 3224-3233

[7] A. M. Gardner, W. D. Tuttle, L. E. Whalley, T. G. Wright., Chem. Sci., 2018, **9**, 2270-2283

[8] J. A. Davies, A. M. Green, A. M. Gardner, C. D. Withers, T. G. Wright and K. L. Reid, *Phys. Chem. Phys. Chem*., 2014, **16**, 430-443

[9] M. A. Smith, J. W. Hager, S. C. Wallace., *J. Chem. Phys*., 1984, **80**, 3097-3105

[10] J. A. Davies, L. E. Whalley and K. L. Reid, *Phys. Chem. Chem. Phys.,* 2017, **19**, 5051-5062

6. A study of two near-isoenergetic vibrational levels in *para*-fluorotoluene.

6.1. Assignments of REMPI and SEVI spectra

This chapter discusses the SEVI and time-resolved photoelectron spectra measured following the selective photoexcitation of two near-isoenergetic S_1 vibrational levels in *para*-fluorotoluene (*p*FT), this analysis was published in reference 2. These vibrational levels are at ~1990 cm^{-1} and ~2030 cm^{-1} in S_1 and are labelled (i) and (ii) respectively in the REMPI spectrum in Figure 6-1 which shows the first 2200 cm^{-1} of the S_1 electronic state of *p*FT. The 1^1, 13^1, and $7a^1$ fundamental levels have also been assigned in the spectrum, normal mode diagrams are shown in figure 8.19 in the appendix.

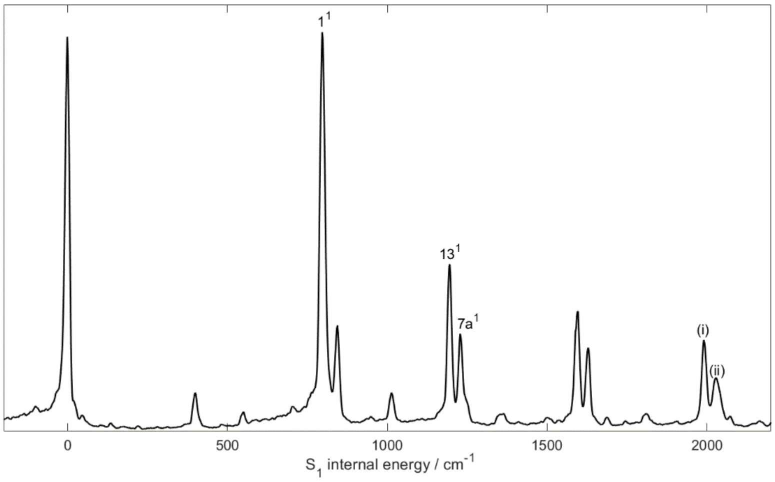

Figure 6-1: (1+1') REMPI spectrum of the S_1 electronic state at a pump-probe time delay of 10 ps.

i) SEVI spectrum *via* (i)/ S_1 0^0 + ~1990 cm^{-1}

Figure 6-2 shows the 0 ps SEVI spectrum measured *via* ~1990 cm^{-1} in S_1; three intense peaks are observed at ~1230 cm^{-1}, ~2050 cm^{-1} and ~2860 cm^{-1}. The intensities suggest one of these peaks originates from the $\Delta v = 0$ transition, given that the S_1 wavenumber of the vibrational level is ~1990 cm^{-1}, the SEVI peak at ~2050 cm^{-1} is a likely candidate because vibrational levels are expected to have similar S_1 and cation wavenumbers based on calculated and experimental S_1 and cation state wavenumbers in literature.[1]

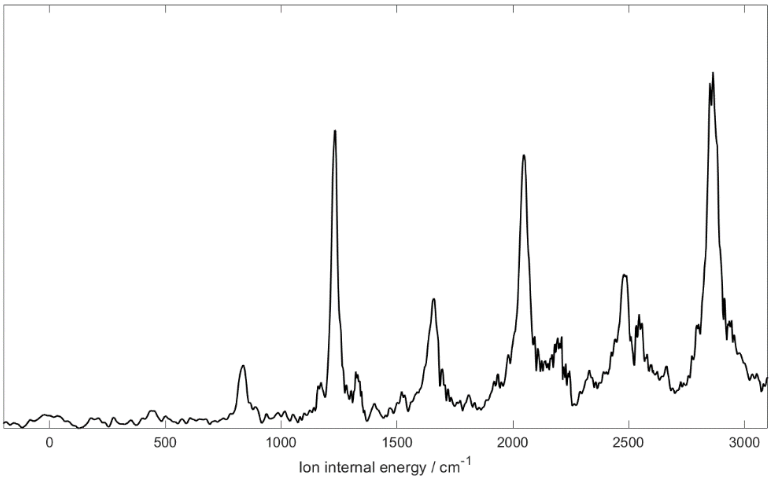

Figure 6-2: 0 ps SEVI spectrum measured via ~1990 cm^{-1} in S_1.

The predicted wavenumbers of level $1^1 13^1$ are in excellent agreement to these experimental vibrational wavenumbers; this is shown in Table 6-1. Mode 1 has ring breathing character and mode 13 has C-CH_3 stretching character (see figure 8.19 in appendix). Supporting this assignment, both the constituent 13^1 and 1^1 vibrations are assigned at lower wavenumbers in the REMPI spectrum in Figure 6-1 suggesting the combination level will be observed. Further, the two intense SEVI peaks at ~1230 cm^{-1} and ~2860 cm^{-1} are assigned to the fundamental of the contributing mode 13 and the combination level $1^2 13^1$ respectively meaning there is a progression in mode 1. Additionally, alongside 13^1, the 1^1 fundamental vibration can also be assigned at ~830 cm^{-1} in the SEVI spectrum meaning both constituent fundamental vibrations involved in the zero-order bright state, $1^1 13^1$, are assigned. Assignments for the SEVI peaks are summarised in Table 6-1 alongside the predicted vibrational wavenumbers; all assignments are to fundamentals, overtones or combination levels involving the same three A_1 modes 1, 13 and 6a, as a result all vibrational levels are totally symmetric.

Vibrational level	Predicted S_1 wavenumber / cm^{-1} ($1^1 13^1$ only)	S_1 wavenumber of REMPI peak / cm^{-1} ($1^1 13^1$ only)	Predicted cation wavenumber / cm^{-1}	Ion internal energy / cm^{-1}
1^1			824[a]	830
13^1			1230[a]	1230
$6a^1 13^1$			1670[a]	1660
$1^1 13^1$	1991[a]	1990	2054[a]	2050
$1^1 6a^1 13^1$			2494[a]	2480
$1^2 13^1$			2878[a]	2860

Table 6-1: Vibrational level assignments for each peak in the 0 ps SEVI spectrum in Figure 6-2. Predicted wavenumbers are based on experimental fundamental wavenumbers from a) Ref 1. Experimental wavenumbers are rounded to 10 cm^{-1}.

ii) SEVI spectrum *via* (ii)/ S_1 0^0 + ~2030 cm^{-1}

Figure 6-3 shows the 0 ps SEVI spectrum measured *via* the S_1 REMPI peak at ~2030 cm^{-1};[a] the most intense peak is at ~2150 cm^{-1} which is the closest in wavenumber to the S_1 vibrational level excited, however there are two other peaks of comparable intensity at ~1330 cm^{-1} and ~2970 cm^{-1}. Given that 1) both vibrations $7a^1$ and 1^1 can be assigned at lower wavenumbers in the REMPI spectrum in Figure 6-1 and 2) there is good agreement between predicted and experimental vibrational wavenumbers as shown in Table 6-2, the S_1 bright state and the SEVI peak at ~2150 cm^{-1} which results from the $\Delta v=0$ transition, are assigned to level 1^17a^1. Mode 1 has ring breathing character and mode 7a has C-F stretching character (see figure 8.19 in appendix).

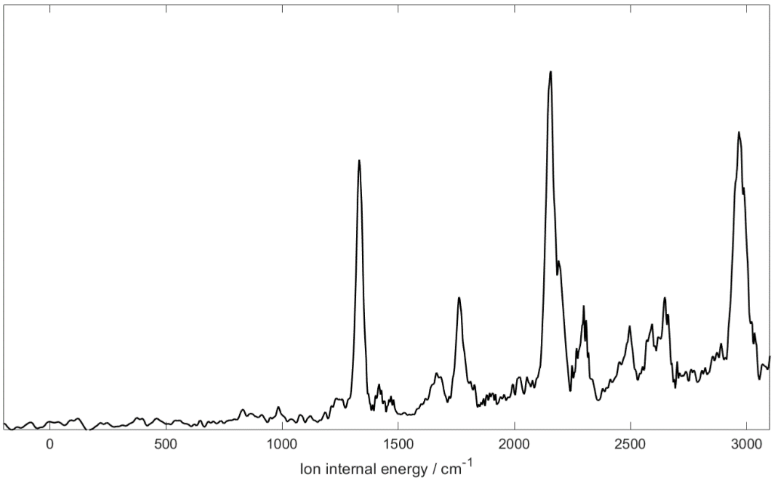

Figure 6-3: 0 ps SEVI spectrum measured via ~2030 cm^{-1} in S_1.

In support of this assignment, the two other intense SEVI peaks at ~1330 cm^{-1} and ~2970 cm^{-1} can be assigned to vibrational levels $7a^1$ and 1^27a^1 respectively; both assignments involve modes in common with the S_1 vibration level initially excited. Notably, the 1^1 vibration which is predicted at 824 cm^{-1} and is the other constituent fundamental vibration in the zero-order bright state,[1] is not observed. Assignments for the peaks observed in the SEVI spectrum in Figure 6-3 are summarised in Table 6-2 alongside predicted vibrational wavenumbers. All assignments are to totally symmetric fundamentals or overtone or combination levels involving the A_1 modes 1, 7a and 6a.

---

[a] In this thesis, the experimental vibrational wavenumbers have been rounded up to the nearest ~10 cm^{-1}, the published study (Ref 2) listed the S_1 vibrational wavenumber as 2026 cm^{-1}.

Vibrational level	Predicted S_1 wavenumber / cm^{-1} ($1^1 7a^1$ only)	S_1 wavenumber of REMPI peak / cm^{-1} ($1^1 7a^1$ only)	Predicted cation wavenumber / cm^{-1}	Ion internal energy / cm^{-1}
$7a^1$			1332[a]	1330
$6a^1 7a^1$			1772[a]	1760
$1^1 7a^1$	2027[a]	2030	2156[a]	2150
$1^1 6a^1 7a^1$			2596[a]	2590
$7a^2$			2664[a]	2650
$1^2 7a^1$			2980[a]	2970

Table 6-2: Vibrational level assignments for each peak in the 0 ps SEVI spectrum in Figure 6-3. Predicted wavenumbers are based on experimental fundamental wavenumbers from a) Ref 1. Experimental wavenumbers are rounded to 10 cm^{-1}.

iii) Comparison to published work

The results and analysis in this chapter were used to write the publication in reference 2, although the final photoelectron peak wavenumbers reported in that published work differ slightly from those listed here because the data was later reprocessed by another author. The wavenumbers of the photoelectron peaks reported in both cases are compared in Table 6-3; any differences between spectra are small (~10 cm^{-1} in most cases) and not considered to be significant considering that the best resolution achieved in the SEVI spectra is ~ 40 cm^{-1}. The differences are attributed to small differences in the process of reconstructing the spectra from raw data.

Excited level: $1^1 13^1$ (*p*FT)	Peak assignments	**13^1**	**$6a^1 13^1$**	**$1^1 13^1$**	**$1^1 6a^1 13^1$**		**$1^2 13^1$**
	Peak wavenumbers reported in this thesis:	1230	1660	2050	2480		2860
	Peak wavenumbers reported in Ref 2	1230	1670	2060	2490		2870
	Predicted wavenumber[1]	1230	1670	2054	2494		2878
Excited level: $1^1 7a^1$ (*p*FT)	Peak assignments	**$7a^1$**	**$6a^1 7a^1$**	**$1^1 7a^1$**	**$1^1 6a^1 7a^1$**	**$7a^2$**	**$1^2 7a^1$**
	Peak wavenumbers reported in this thesis	1330	1760	2150	2590	2650	2970
	Peak wavenumbers reported in Ref 2	1330	1770	2160	2610		2970
	Predicted wavenumber[1]	1332	1772	2156	2596	2664	2980

Table 6-3: Comparison of the wavenumbers of photoelectron peaks in the 0 ps SEVI spectra recorded via levels $1^1 13^1$ and $1^1 7a^1$ as shown in this work and reference 2. Also shown are predicted wavenumbers for these vibrations determined from experimental fundamental wavenumbers from ref 1.

6.2. Analysis of time-resolved photoelectron spectra measured *via* S_1 $1^1 13^1$

To investigate coupling involving the S_1 level $1^1 13^1$, photoelectron spectra were measured at selected pump-probe time delays between 0 ps and 500 ps via level $1^1 13^1$. Figure 6-4 shows spectra at six different time delays. The most intense peaks in the 0 ps spectrum have been labelled A-E, with the peak resulting from the $D_0^+ \leftarrow S_1$ $\Delta v=0$ transition, assigned $1^1 13^1$, labelled C.

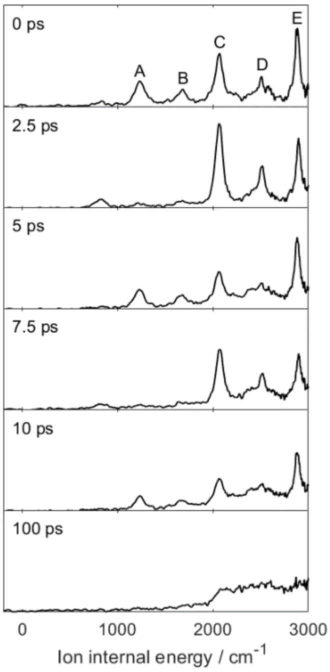

Figure 6-4: Photoelectron spectra measured via ~1990 cm^{-1} (level $1^1 13^1$) in S_1 at selected time delays, with the main peaks labelled A-E.

With increasing time delay, changes in the relative intensities of the photoelectron peaks are initially apparent, but by 100 ps only unstructured intensity is seen. To obtain oscillation periods and lifetimes, the intensity of each photoelectron peak A-E has been plotted as a function of pump-probe time delay to give the time profiles in Figure 6-5. The intensity underneath the peaks, which increases with time delay, has been subtracted in order to remove any signal from bath states. The time-dependent intensity of each peak has been fit to equation 2.6 and the results are shown in Table 6-4. The two subplots X and Y measure the intensity in the 2250-2350 cm^{-1} and 2650-2740 cm^{-1} regions of the spectrum in Figure 6-4 respectively. These spectral regions contain no features so these time profiles measure the congestion which increases with time delay. These plots are fit to equation 2.7 and the fit results are also shown in Table 6-4.

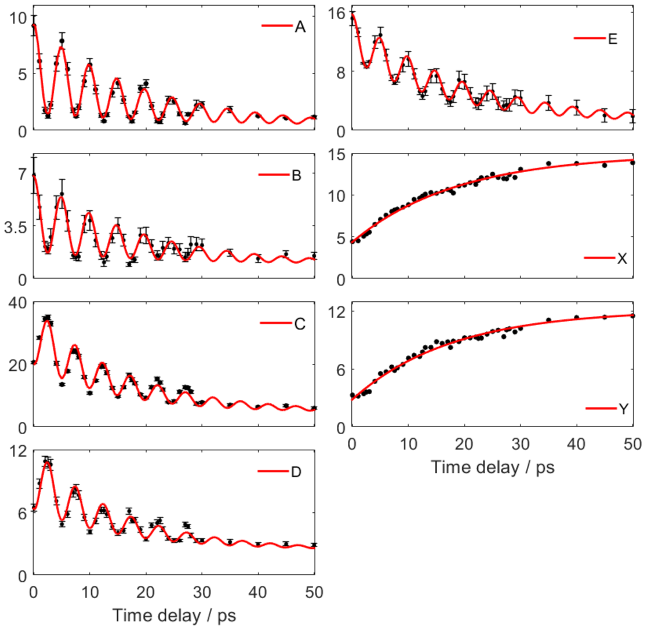

Figure 6-5: Time profiles showing the time-dependent intensity of peaks A-E and two featureless baseline regions X) 2250-2350 cm^{-1} and Y) 2650-2740 cm^{-1}.

	Coefficient						
Peak	**A**	**B**	**C**	τ_1	τ_2	τ_{osc}	**Rsq**
A: 13^1	0.43	4.98	4.00	19.8 ± 3.0	18.6 ± 2.6	4.94 ± 0.02	0.98
B: $6a^1 13^1$	0.97	3.31	2.50	18.4 ± 5.7	17.5 ± 4.9	4.92 ± 0.05	0.94
C: $1^1 13^1$	4.76	24.49	-9.53	15.4 ± 2.1	18.0 ± 5.3	4.93 ± 0.05	0.97
D: $1^1 6a^1 13^1$	2.40	6.86	-2.97	15.6 ± 2.3	15.1 ± 4.2	4.97 ± 0.06	0.97
E: $1^2 13^1$	1.11	11.57	3.01	18.7 ± 1.7	26.1 ± 6.8	4.91 ± 0.03	0.99
X: 2250-2350 cm^{-1}	4.38	10.51		18.6 ± 1.8			0.99
Y: 2650-2740 cm^{-1}	2.85	9.27		17.8 ± 1.7			0.98

Table 6-4: IVR lifetimes (τ_1/τ_2) and oscillation periods (τ_{osc}) determined from fits of peaks A-E and two featureless baseline regions (X,Y).

In Figure 6-5, the time profiles for photoelectrons peaks A-E all show oscillations in intensity, with some peaks beating out of phase to the others; this suggests that the initially excited vibrational level, $1^1 13^1$, is coupled to another level which is dark, resulting in the transfer of population. Additionally, the fact that peak C shifts from ~2050 cm^{-1} at 0 ps to ~2060 cm^{-1} at 2.5 ps suggests a different vibration is now observed meaning a transition from a different S_1 vibrational level. In Table 6-4 there is very good agreement between the oscillation periods suggesting coupling to a single dark level in S_1. An average $\boldsymbol{\tau_{osc}}$ value of 4.93 ± 0.04 ps is calculated from the five $\boldsymbol{\tau_{osc}}$ values which corresponds to an energy separation (Δ*E)* of 6.77 ± 0.05 ps between the two eigenstates resulting from the two strongly coupled ZOS. Peaks A, B and E show maximum intensity at 0 ps, which decreases up to 2.5 ps, then increases up to 5 ps, this behaviour indicates these peaks are reflecting the population of the initially excited level $1^1 13^1$. Peaks C and D show minimum intensity at 0 ps which increases up to 2.5 ps, then decreases up to 5 ps. This indicates there are features growing in which result from transitions from the 'dark' vibrational level.

In the time profiles of photoelectron peaks A-E, the oscillations in intensity actually appear superimposed on an exponential decay curve. Opposite behaviour, an exponential increase in intensity, is shown by time profiles X and Y which measure the congestion with time delay. There is fairly good agreement between the IVR lifetimes ($\boldsymbol{\tau_1}$ and $\boldsymbol{\tau_2}$) from each fit, with an average IVR lifetime ($\boldsymbol{\tau_{ivr}}$) of 18.3 ± 8 ps calculated from the twelve $\boldsymbol{\tau_1}$ and $\boldsymbol{\tau_2}$ values in Table 6-4**.** There is one outlier in the $\boldsymbol{\tau_2}$ value for peak E which is 26.1 ± 6.8 ps, although it does lie within error bars of some other peaks. This is attributed to the fact the intensity oscillations are quite shallow because peak E is relatively intense in both the 0 ps and 2.5 ps spectra. If this value is excluded, the average IVR lifetime ($\boldsymbol{\tau_{ivr}}$) is 17.6 ± 2.5 ps; the IVR lifetime drops by ~0.7 ps but the error bar is reduced by over half.

In previous work, the observation of both i) peaks showing oscillations in intensity alongside decay and ii) increasing congestion in the baseline have been attributed to intermediate IVR where the dark vibrational level acts as a doorway state facilitating coupling to bath states which themselves are only weakly coupled to the bright vibrational level (see Figure 1.3 in Chapter 1).[3,4,5] The fact that the lifetimes for peaks A-E and the baseline regions X and Y agree is consistent with the increasing congestion resulting from ionisation from these bath states because if the lifetimes and oscillation periods reflect the same IVR dynamics in S_1 then they should be the same for each fit, even if there are unresolved levels.

The photoelectron spectrum recorded at 2.5 ps (half the oscillation period) should be a Franck-Condon projection of the 'doorway state' strongly coupled to level $1^1 13^1$. At 2.5 ps, the peak at C has shifted to ~2060 cm^{-1} suggesting it is no longer assigned to $1^1 13^1$ nor originates from the $D_0^+ \leftarrow S_1$ transition from the bright state. In fact, as peak C is not only more intense at 2.5 ps than 0 ps but also the most relatively intense peak, it is likely that peak C at 2.5 ps originates from the $\Delta v=0$ transition from the dark level in S_1. This means that the $\Delta v=0$ transitions from both the bright and dark vibrational levels in S_1 are very close in wavenumber in the photoelectron spectrum. While peak D at ~2490 cm^{-1} is also more intense at 2.5 ps, it is only half the intensity of peak C at ~2060 cm^{-1} suggesting it originates from a $\Delta v \neq 0$ transition from the dark vibrational level in S_1.

To identify the doorway state, a search was conducted for vibrational levels with predicted wavenumbers within ±30 cm^{-1} of ~1990 cm^{-1} and ~2060 cm^{-1} in the S_1 electronic state and cation state respectively. The levels found are shown in Table 6-5; these are organised according to the required change in vibrational quanta, ΔN, relative to the bright state $1^1 13^1$ because coupling strength decreases as ΔN increases, although coupling selection rules and the difference in S_1 wavenumber between levels are also factors. Only $\Delta N \leq 3$ is considered.

Vibrational level	Predicted S_1 wavenumber / cm^{-1}	ΔE relative to ~1990 cm^{-1}	Predicted cation wavenumber / cm^{-1}	ΔE relative to ~2060 cm^{-1}	ΔN relative to $1^1 13^1$
$1^2 6a^1$	2002	12	2088	28	3
$9b^2 13^1$	1992	2	2062	2	3

Table 6-5: Predicted wavenumbers of vibrational levels $1^2 6a^1$ and $9b^2 13^1$ in the S_1 and ion states based on experimental fundamental wavenumbers from Ref 1.

Only two vibrational levels were found which match the above criteria; both are totally symmetric overall. Level $9b^2 13^1$ is expected to lie closest in wavenumber to $1^1 13^1$ in S_1 and shows better agreement to the wavenumber of photoelectron peak C at ~2060 cm^{-1}. Further, in the 2.5 ps SEVI spectrum in Figure 6-6, the peaks at ~830 cm^{-1} and ~1230 cm^{-1} can be assigned to vibrational levels $9b^2$ and 13^1 respectively. While the peak at ~830 cm^{-1} could also be assigned to the 1^1 vibration, the absence of a peak at ~440 cm^{-1} means $6a^1$ is not observed. Therefore, the dark state is assigned to $9b^2 13^1$. Notably, in a previous study anharmonic coupling was identified between the 1^1 and $9b^2$ with the populations of the zero-order states exhibiting oscillations in intensity.[6] Assignments for the other peaks in the 2.5 ps SEVI spectrum are shown in Table 6-6.

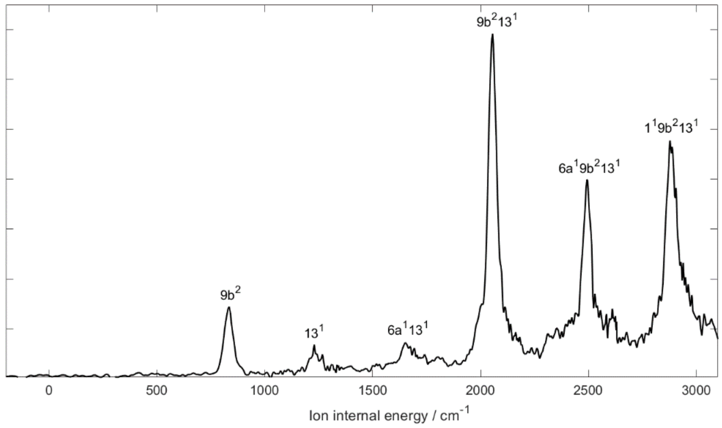

Figure 6-6: 2.5 ps SEVI spectrum measured via ~1990 cm^{-1} in S_1, the spectrum is a Franck-Condon projection of a dark state assigned $9b^2 13^1$.

Vibrational level	Predicted cation wavenumbers / cm^{-1}	Ion internal energy / cm^{-1}
$9b^2$	832^a	830
13^1	1230^a	1230
$6a^1 13^1$	1670^a	1670
$9b^2 13^1$	2062^a	2060
$6a^1 9b^2 13^1$	2502^a	2500
$1^1 9b^2 13^1$	2886^a	2880

Table 6-6: Vibrational level assignments for each peak in the 2.5 ps SEVI spectrum in Figure 6-6. Predicted wavenumbers are based on experimental fundamental wavenumbers from Ref 1. Experimental wavenumbers are rounded to 10 cm^{-1}.

6.3. Analysis of time-resolved photoelectron spectra recorded via S_1 $1^1 7a^1$

To investigate any coupling involving the S_1 level $1^1 7a^1$, photoelectron spectra were measured at selected pump-probe time delays between 0 ps and 500 ps; six of these are shown in Figure 6-7. With increasing time delay, the relative intensities of the peaks change and by 100 ps the peaks appear to have lost all intensity which is accompanied by a large increase in congestion in the baseline.

The five intense peaks in the 0 ps photoelectron spectrum are labelled A-E, with the peak originating from the $D_0^+ \leftarrow S_1$ $\Delta v=0$ transition assigned C. The intensity of each peak A-E has been plotted as a function of pump probe time delay to give the time profiles in Figure 6-8. The intensity underneath the peaks which increases with time delay has been subtracted in order to remove signal from bath states. The intensity of two featureless baseline regions have also been plotted as a function of time delay in Figure 6-8; time profile X measures the 2750-2850 cm^{-1} region of the spectrum and time profile Y measures the 2345-2425 cm^{-1} region of the spectrum. The time-dependent intensity of each peak has been fit to equation 2.6 and the intensities of the baseline regions are fit to equation 2.7. Table 6-7 contains the results of the fits.

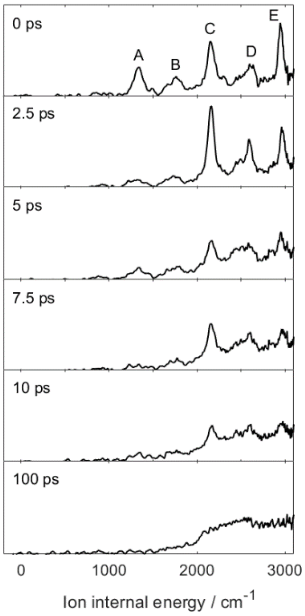

Figure 6-7: Photoelectron spectra measured via ~2030 cm^{-1} (level $1^1 7a^1$) in S_1 at selected time delays with the main peaks labelled A-E.

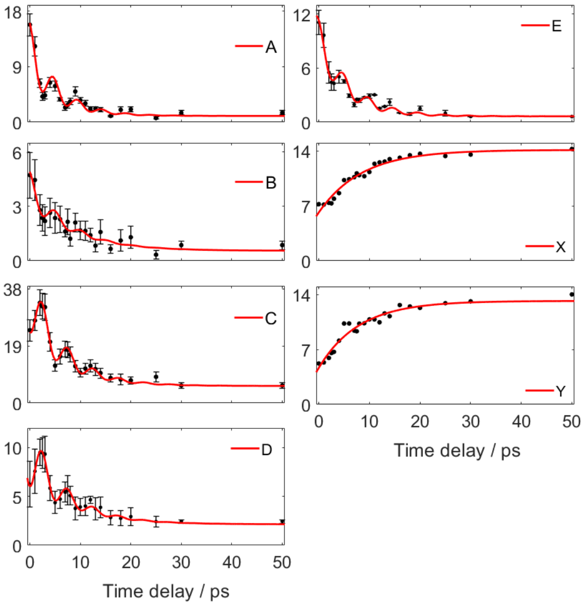

Figure 6-8: Time profiles showing the time-dependent intensity of peaks A-E and two featureless baseline regions X) 2750-2850 cm^{-1} and Y) 2345-2425 cm^{-1}.

	Coefficient						
Peak	**A**	**B**	**C**	τ_1	τ_2	τ_{osc}	**Rsq**
A: $7a^1$	1.00	10.57	4.50	5.4 ± 1.3	5.5 ± 3.1	4.79 ± 0.29	0.96
B: $6a^17a^1$	0.55	3.39	0.96	8.2 ± 2.5	5.2 ± 6.1	5.15 ± 0.76	0.92
C: 1^17a^1	5.68	29.1	-11.2	6.6 ± 0.8	6.1 ± 1.9	5.08 ± 0.16	0.99
D: $1^16a^17a^1/7a^2$	2.15	7.26	-3.36	7.7 ± 1.2	5.5 ± 1.9	5.05 ± 0.21	0.98
E: 1^27a^1	0.65	8.61	2.04	5.7 ± 1.2	7.5 ± 6.2	4.92 ± 0.31	0.97
X: 2750-2850 cm^{-1}	6.14	7.96		8.5 ± 1.4			0.97
Y: 2345-2425 cm^{-1}	4.65	8.52		7.9 ± 2.6			0.94

Table 6-7: Values including IVR lifetimes (τ_1/τ_2) and oscillation periods (τ_{osc}) determined from fits of peaks A-E and two unstructured regions of the baseline.

In Figure 6-8, the time profiles of photoelectron peaks A-E show oscillations in intensity with very good agreement between the oscillation periods determined from each fit. Therefore an average $\boldsymbol{\tau_{osc}}$ value of 5.00 ± 0.21 ps is determined from all five $\boldsymbol{\tau_{osc}}$ values included in Table 6-7. The time profiles of photoelectron peaks C and D show out of phase oscillations compared to photoelectron peaks A, B and E. The single oscillation period and appearance of out of phase oscillations indicate the transfer of population between two coupled S_1 vibrational levels, one of which is bright and one of which is dark. Peaks A, B and E show maximum intensity at 0 ps, which decreases up to 2.5 ps then increases up to 5 ps. This behaviour suggests these peaks are reflecting the population of the initially excited 'bright' vibrational level which was assigned 1^17a^1. Photoelectron peaks C and D show minimum intensity at 0 ps which increases up to a maximum at 2.5 ps. This suggests the growth of vibrational levels at these wavenumbers which result from transitions from the 'dark' vibrational level which is coupled to 1^17a^1. From the oscillation period an energy separation between the two eigenstates resulting from the two strongly coupled ZOS is determined to be (ΔE) of 6.68 ± 0.29 cm^{-1}.

The time profiles of peaks A-E show that the oscillations occur alongside an exponential decay in intensity. An exponential increase in intensity is shown by both time profiles X and Y which measure the congestion. There is fairly good agreement between the $\boldsymbol{\tau_1}$ and $\boldsymbol{\tau_2}$ lifetimes in Table 6-7, this allows for an average IVR lifetime, τ_{ivr}, of 6.7 ± 1.9 ps to be determined from all twelve $\boldsymbol{\tau_1}$ and $\boldsymbol{\tau_2}$ values. The Rsq values indicate the fits are all good however the τ_2 values for peaks B and E have much larger associated error bars which is attributed to the shallower oscillations observed for peaks B and E in Figure 6-8 and the fact that there are only ~3 oscillations to fit because they decay quickly. The appearance of oscillations alongside exponential decay is consistent with intermediate IVR where the dark vibrational level acts as a doorway state; this was observed previously in section 6.2. The exponential increase in intensity observed in time profiles X and Y is a result of overlapping transitions from bath states, which gain population from coupling to bright state $1^1 7a^1$, causing congestion in the spectrum.

Given that the oscillation period is ~5 ps, the 2.5 ps SEVI spectrum shown in Figure 6-9 should be a Franck-Condon projection of the strongly coupled doorway state. Only peaks C and D are more intense at 2.5 ps and oscillate out of phase. Given that peak C at ~2160 cm^{-1} is also the most relatively intense peak at 2.5 ps, it is assigned to the dark state $D_0^+ \leftarrow S_1$ $\Delta v=0$ transition. Therefore, a search has been conducted for vibrational levels with a predicted wavenumber of ~2030 cm^{-1} ± 30 cm^{-1} and ~2160 cm^{-1} ± 30 cm^{-1} in the S_1 and cation states respectively in order to assign the level which couples to level $1^1 7a^1$. Only one vibrational level was found which involves a change in vibrational quanta of $N \leq 3$ relative to level $1^1 7a^1$, therefore the doorway state is assigned to $9b^2 7a^1$. This level has a predicted wavenumber in the cation of ~2164 cm^{-1} which is in very good agreement to photoelectron peak C at ~2160 cm^{-1} and a predicted S_1 wavenumber of ~2028 cm^{-1} which is very close to the experimental S_1 wavenumber of $1^1 7a^1$ which is 2030 cm^{-1} in the REMPI spectrum. Further supporting this assignment, as mentioned in section 6.2, anharmonic coupling was previously identified between levels 1^1 and $9b^2$.[6] The normal mode diagram for 9b is also shown in section 8.2.2.

Vibrational level assignments for the other peaks in the 2.5 ps SEVI spectrum are shown in Table 6-8. Notably, in the 2.5 ps SEVI spectrum, the fundamental vibration $7a^1$ is assigned at ~1330 cm^{-1}, however the absence of a peak at ~832 cm^{-1} means the $9b^2$ vibration is not observed. Comparison of the time-dependent data shown here to that of the close lying level $1^1 13^1$ (shown in section 6.2) shows that both S_1 levels display evidence of coupling to a doorway state with the form $X^1 9b^2$ (where X= 13 or 7a). Therefore it is interesting that $9b^2$ is not observed here, yet it is assigned in the 2.5 ps SEVI spectrum measured *via* $1^1 13^1$ which is shown in Figure 6-6.

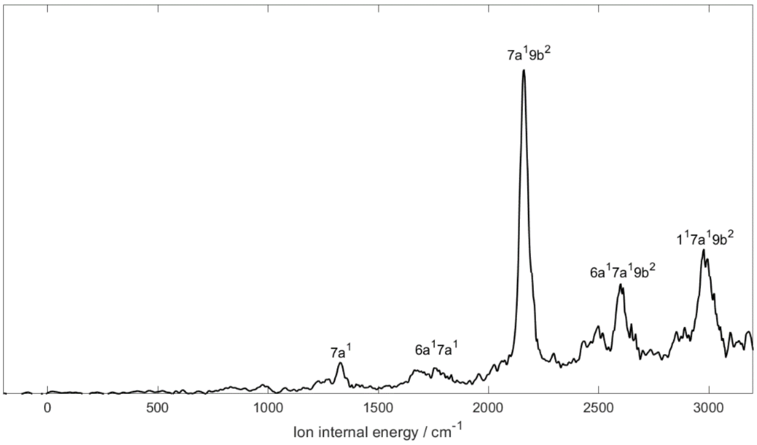

Figure 6-9: 2.5 ps SEVI spectrum measured via ~2030 cm^{-1} ($1^1 7a^1$) in S_1. The spectrum is a Franck-Condon projection of the dark state assigned $7a^1 9b^2$.

Vibrational level	Predicted S_1 wavenumber / cm^{-1} ($7a^1 9b^1$ only)	S_1 wavenumber of REMPI peak / cm^{-1} ($7a^1 9b^1$ only)	Predicted cation wavenumber / cm^{-1}	Ion internal energy / cm^{-1}
$7a^1$			1332^a	1330
$6a^1 7a^1$			1772^a	1780
$7a^1 9b^2$	2028^a	2030	2164^a	2160
$6a^1 7a^1 9b^2$			2604^a	2600
$1^1 7a^1 9b^2$			2988^a	2980

Table 6-8: Vibrational level assignments for each peak in the 2.5 ps SEVI spectrum in Figure 6-9. Predicted wavenumbers are based on experimental fundamental wavenumbers from Ref 1. Experimental wavenumbers are rounded to 10 cm^{-1}.

6.4. Mode-dependence: comparison between vibrational levels $1^1 13^1$ and $1^1 7a^1$

In the above, the dynamics of the two close lying vibrational levels, $1^1 7a^1$ and $1^1 13^1$, have been investigated. Mode 7a has C-F stretching character, whereas mode 13 has C-CH_3 stretching character. Comparison of the time-dependence following excitation of these S_1 vibrational levels therefore gives insight into the effect of the mode character on energy dispersal. There is considerable similarity between the SEVI spectra and time-resolved photoelectron spectra recorded *via* both vibrational levels, for example a similar series of peaks are observed in the 0 ps spectra, with the four most intense peaks being assigned to X^1, $6a^1 X^1$, $1^1 X^1$

and 1^2X^1 where X is either 13 or 7a. Table 6-9 summarises the average oscillation periods and lifetimes determined for both vibrational levels $1^1 13^1$ and $1^1 7a^1$. In both cases, doorway states mediated the dynamics and an average oscillation period of ~5 ps was determined corresponding to an eigenstate energy separation of ~6.68 cm^{-1} .

Vibrational level	S_1 wavenumber / cm^{-1}	Doorway state	τ_{ivr} / ps	τ_{osc} / ps	ΔE / cm^{-1}
$1^1 13^1$	1990	$9b^1 13^1$	17.6 ± 2.5	4.93 ± 0.04	6.77 ± 0.05
$1^1 7a^1$	2030	$7a^1 9b^1$	6.7 ± 1.9	5.00 ± 0.21	6.68 ± 0.29

Table 6-9: A summary of the fit results for both bright states.

Notably, the IVR lifetimes differ by almost a factor of three. Often the IVR lifetime is rationalised based on internal energy and therefore the density of states and opportunity for coupling, however in this case both vibrational levels have very similar wavenumbers, being separated by only ~35 cm^{-1}, meaning the density of states is likely similar for both. This suggests the difference in lifetime could be due to the vibrational character of the modes with mode 7a promoting the redistribution of vibrational energy more effectively than mode 13.

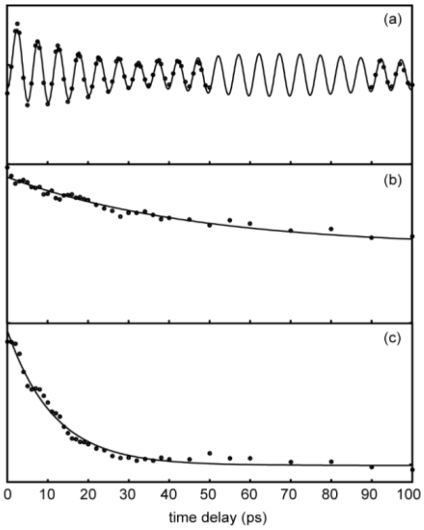

Figure 6-10: Subplots a, b, c show the time-dependent intensity of the Δv = 0 peak in photoelectron spectra recorded via three fundamental vibrations, a) 1^1, b) 13^1 and c) $7a^1$, in S_1.[2,4,6,] Taken from Ref 2.

In previous work time-resolved photoelectron spectra were measured *via* the fundamental vibrations 1^1, 13^1 and $7a^1$ in S_1 *p*FT.[4,6,7,] Figure 6-10 shows the time-dependent intensity of the $D_0^+ \leftarrow S_1$ Δv = 0 photoelectron peak in each case. The results of the fits such as lifetimes and oscillation periods (where appropriate) are shown in Table 6-10 alongside the lifetimes and oscillation periods that were determined for vibrational levels $1^1 13^1$ and $1^1 7a^1$ in this chapter.

Vibrational level	S_1 wave-number / cm^{-1}	Symmetry	τ_{ivr} / ps	τ_{osc} / ps	ΔE / cm^{-1}
1^1	~800	A_1	restrictive IVR	5.0^c	6.7^c
13^1	1194	A_1	50^b	-	-
$7a^1$	1230	A_1	13^d	-	-
$1^1 13^1$	1990	A_1	17.6^a	4.93^a	6.77^a
$1^1 7a^1$	2030	A_1	6.7^a	5.00^a	6.68^a

*Table 6-10: IVR lifetimes, oscillation periods and energy separations determined for five bright vibrational levels in S_1 p*FT*. a) From this work, b) From Ref 4, c) From Ref 6, d) From Ref 2*

Notably, there are several similarities in the time dependent behaviour observed following excitation of the three fundamentals and the $1^1 13^1$ and $1^1 7a^1$ combination levels. Firstly, the oscillation period observed for the level 1^1 is ~5 ps,[6] almost identical to the oscillation periods determined for both the $1^1 13^1$ and $1^1 7a^1$. Secondly, both the $7a^1$ and 13^1 levels show an overall exponential decay in population which is also observed for levels $1^1 13^1$ and $1^1 7a^1$.[4,2] However, the IVR lifetime for the level $7a^1$ is almost 4 times shorter than the lifetime of level 13^1. Further, $7a^1$ has a shorter IVR lifetime than level $1^1 13^1$ despite the fact that in S_1, level $7a^1$ lies 760 cm^{-1} lower than level $1^1 13^1$, in a region with ~10 times lower density of states.[2] Applying Fermi's Golden rule which states that IVR lifetime (decay rate) is proportional to density of states and average coupling strength, then, assuming that the average coupling strengths are similar in both cases, the density of states suggests that the IVR lifetime of level $7a^1$ should be longer than that of level $1^1 13^1$. This further supports the hypothesis that mode 7a can promote energy redistribution more effectively than mode 13 in PFT.

Table 6-11 shows the lifetimes and oscillation periods reported here compared to those reported in reference 2 because the data was later reprocessed by another author before publication. There are some small discrepancies which is attributed to two factors, firstly the small differences in the methods for calculating the peak integrals and secondly, the way the average lifetimes and oscillation periods are calculated. In reference 2, weighted averages and errors were determined, reducing the impact of outliers on the final averages. However, in the results presented in this chapter non-weighted average lifetimes and oscillation periods were calculated because of the good agreement between different peaks. This does result in the error bars being slightly larger. For both vibrational levels, both sets of oscillation periods and lifetimes agree within error bars and any differences are less than 0.5 ps, which is lower than the temporal resolution achieved within the experiment, so are not considered significant.

	Vibrational level: $1^1 13^1$		Vibrational level: $1^1 7a^1$	
	This work	Published work[2]	This work	Published work[2]
S_1 wave-number / cm^{-1}	1990		2030	
$\boldsymbol{\tau_{ivr}}$ / ps	17.6 ± 2.5	18.1 ± 3.4	6.7 ± 1.9	7.0 ± 1.5
$\boldsymbol{\tau_{osc}}$ / ps	4.93 ± 0.04	4.94 ± 0.01	5.00 ± 0.21	5.07 ± 0.08
ΔE / cm^{-1}	6.77 ± 0.05	6.75 ± 0.02	6.68 ± 0.29	6.58 ± 0.10

Table 6-11: IVR lifetimes, oscillation periods and eigenstate energy separations determined from photoelectron spectra recorded via S_1 levels $1^1 13^1$ and $1^1 7a^1$ in this chapter and reference 2.

6.5. The influence of the methyl rotor: comparison to *para*-difluorobenzene.

In previous work by the group the vibrational level $1^1 7a^1$ in S_1 *para*-difluorobenzene was excited, and the resulting IVR dynamics studied.[8] Comparison of the time-resolved photoelectron spectra recorded via $1^1 7a^1$ in the

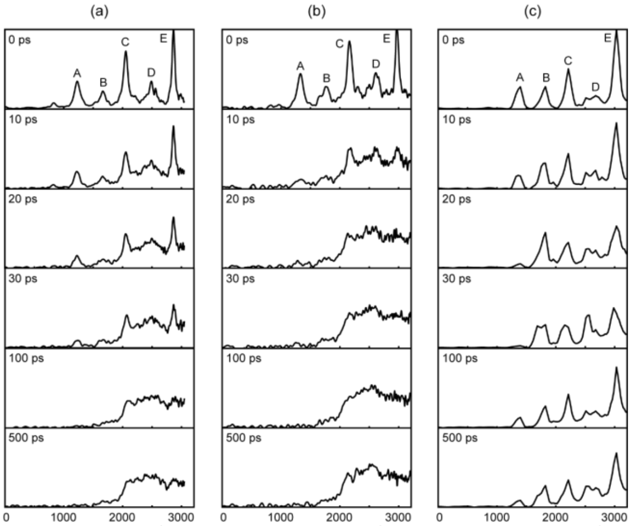

*Figure 6-11: Photoelectron spectra at several time delays recorded via vibrational levels a) $1^1 13^1$ in S_1 p*FT*, b) $1^1 7a^1$ in S_1 p*FT *and c) $1^1 7a^1$ in S_1 p*DFB*[8]. Figures taken from Ref 2.*

two related molecules *p*DFB and *p*FT allows the effect of the methyl rotor to be studied. Figure 6-11 shows photoelectron spectra recorded following excitation of levels $1^1 7a^1$ and $1^1 13^1$ in S_1 *p*FT (same as shown previously) and vibrational level $1^1 7a^1$ in S_1 *p*DFB at several time delays. The main peaks are labelled A-E.

Figure 6-12 shows the time profiles which result from plotting the intensity of peaks A and C in the three sets of photoelectron spectra in Figure 6-11 as a function of time delay. For all three vibrational levels, the time profiles show oscillations in intensity for both photoelectron peaks. In the case of *p*FT a single oscillation period of 5 ps was determined from the time-resolved photoelectron spectra recorded via both vibrational levels, $1^1 13^1$ and $1^1 7a^1$. In the case of *p*DFB, multiple oscillation periods have been reported (103 ps, 205 ps, 9.2 ps, 8.8 ps, 8.5 ps and 8.1 ps) and attributed to coupling between $1^1 7a^1$ and three other vibrational levels.[8]

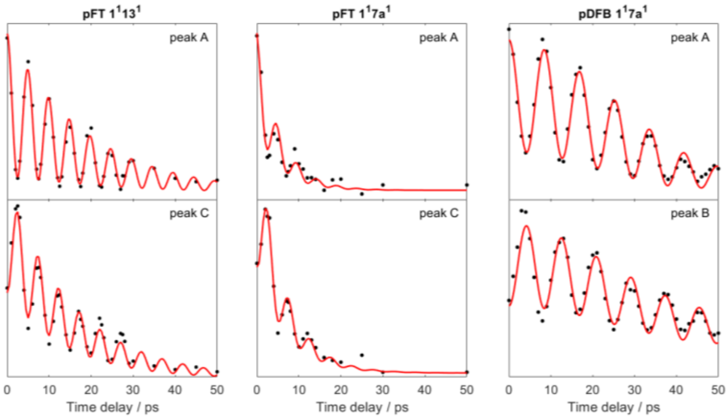

Figure 6-12: Time-dependent intensities of peaks A and C in the photoelectron spectra recorded via levels $1^1 13^1$ and $1^1 7a^1$ in pFT *and $1^1 7a^1$ in* pDFB*. The* pFT *time profiles are from this work. The* pDFB *plots originally from Ref 8 are adapted from Ref 2, peak A is assigned $7a^1$ and peak B is assigned $6a^1 7a^1$.*

Notably, whereas IVR lifetimes of <20 ps have been deduced for both *p*FT vibrational levels (see Table 6-10) due to a doorway state facilitating coupling to bath states, the *p*DFB spectrum remains well resolved to 500 ps with the time profiles showing extended quantum beating for at least 1 ns indicating restrictive IVR and coupling between only a few vibrational levels.[8] As there is no decay on the timescale of the experiment (although on longer timescale population will be lost through fluorescence) the τ_{ivr} value is taken to be infinity. The decrease in oscillation amplitude in the time profiles was attributed to rotational dephasing, previous work reported the amplitude increases again at later time delays.[8]

The fact that energy remains localised following excitation of level 1^17a^1 in *p*DFB yet intermediate energy dispersal occurs following excitation of level 1^17a^1 in *p*FT suggests a difference in the bath states available for coupling between the two molecules. One rationale is that the higher molecular symmetry in *p*DFB, together with the lack of a methyl group and therefore torsional modes, means there is simply a lower number of levels available for coupling compared to *p*FT. However, in *p*DFB the density of states of correct symmetry available for coupling is ~8 per cm^{-1}, in principle levels that are many wavenumbers apart could couple through anharmonicity suggesting that >100 states are available to couple.[2,9] Despite this, the time dependent behaviour indicates strong coupling between 1^17a^1 and only three other vibrational levels. Further, the lack of congestion in the 0 ps photoelectron spectrum recorded via level 1^17a^1 in *p*DFB (Figure 6-11) indicates no coupling to vibrational levels outside the laser bandwidth either which would not cause time-dependence (see below).[8] This suggests direct weak anharmonic coupling to bath states, although possible given the density of states, is not occurring. Considering that *p*FT and *p*DFB have similar energy level structures and anharmonicities, this suggests that similarly, little direct weak anharmonic coupling to bath states occurs in pFT either.[2] Instead it is likely that in *p*FT, torsion-vibration coupling is the mechanism for coupling to bath states because this cannot occur in *p*DFB which would explain why the initially excited vibrational level does not decay.

Therefore the shorter IVR lifetime of 1^17a^1 in *p*FT, combined with: 1) the increased congestion in the 0 ps spectrum compared to the 1^113^1 0 ps spectrum, and 2) the absence of any congestion in the spectrum of *p*DFB, suggests mode 7a promotes energy redistribution more effectively than mode 13 through the facilitation of torsion-vibration coupling to bath states, some of which lie outside of the laser bandwidth. The time profile for level 13^1 in *p*FT (Figure 6-10) shows that bright state population only decays to ~50% of the original intensity even up to 100 ps. This observation is consistent with only one torsional component undergoing IVR (owing to different nuclear spin symmetries of torsional levels), further evidence for torsion-vibration coupling being the mechanism facilitating IVR especially for levels involving 13^1.[4]

6.6. Interaction energy calculations

Torsion-vibration coupling requires an interaction between the methyl group and ring and therefore it is important to understand what happens to the interaction during the different vibrations. Moss et al. developed a model for this interaction which was used to explain spectral congestion observed in the first electronic state of *p*FT at low energies.[10] The model uses the van der Waals repulsion between the methyl hydrogens and ring carbon/hydrogens to account for torsion-vibration coupling.[10] The torsional potential is modulated by the distance between the methyl hydrogens and nearby ring atoms so vibrational motion changes the barrier to rotation[10] leading to mixing of the ring and methyl states.[10]

Using the van der Waals parameters (see Table 6-12) and equations provided by Moss et al,[10] the relative interaction energies expected following the excitation of vibrational modes 7a and 13 have been calculated by Katharine Reid and Julia Davies. In order to characterise the geometry in S_1 *p*FT, calculations were conducted at the CIS/6-311G** level of theory with the methyl group initially set in the staggered configuration; the lowest energy configuration. This allowed the separation between each of the methyl hydrogens and the nearby ring hydrogens/ring carbons (Hm-Hr and Hm-Cr) to be determined at each extreme position of vibrational motion associated with vibrational modes 7a, 13 and 1. These positions allow the net van der Waals interaction energies E_{vdW} to be calculated from the sum of pairwise interactions between the methyl and nearby ring atoms in pFT. The interaction between the methyl hydrogens and ring hydrogen/carbon atoms which are closest at the two extreme positions will be dominant. Equation 6.1, taken from reference 10, is used to calculate the van der Waals energy between two atoms a and b in terms of P and ϵ^*.

$$E_{ab} = \epsilon^* \left[2.9 \times 10^5 e^{\left(\frac{-12.5}{P}\right)} - 2.25 P^6 \right] \qquad \text{Equation 6.1}$$

ϵ^* is the well depth and can be expressed as:

$$\epsilon^* = (\epsilon_a \epsilon_b)^{\frac{1}{2}} \qquad \text{Equation 6.2}$$

where ϵ_a and ϵ_b are the individual atomic well depths. P is the reduced radius which is given by:

$$P = \frac{r^*}{R} \qquad \text{Equation 6.3}$$

where r^* is the sum of the van der Waals radii of the two atoms and R is the effective interatomic distance. R is the distance between the two nuclei, for hydrogen atoms the effective position of the atom is assigned to be approximately 0.915 of the bond length.[10] The results of the calculations are shown in Table 6-13.

Parameter in equation 6.1	Value
ϵ_{CH}^{*}	0.19 kJ/mol
ϵ_{HH}^{*}	0.20 kJ/mol
r_{CH}^{*}	3.34 Å
r_{HH}^{*}	3.0 Å

Table 6-12: List of parameters and values which are taken from reference 10

	Equilibrium	Mode 1		Mode 13		Mode 7a	
		(i)	(ii)	(i)	(ii)	(i)	(ii)
$R(C_r\text{-}H_m)_{min}$ / Å	2.67	2.78	2.60	3.07	2.27	2.74	2.60
$R(H_r\text{-}H_m)_{min}$ / Å	2.46	2.44	2.51	2.34	2.59	2.91	2.02
$E_{vdW}{}^{a}$ / kJ mol^{-1}	1.63	0.70	2.57	0.91	14.20	-0.55	16.95
$E_{vdW}{}^{a}$ / cm^{-1}	137	59	215	76	1187	-46	1417
$\Delta E_{vdW}{}^{b}$ / cm^{-1}	0	156		1111		1463	

Table 6-13: Calculation results: atomic separations and net van der Waals interaction energies (^{a} E_{vdW}) at equilibrium and the two extreme positions (i/ii) for modes 1, 13, 7a. Also shown is the maximum change in van der Waals energy occurring during vibrational motion (^{b} ΔE_{vdW}). Taken from Ref 2

For mode 1 the maximum E_{vdW} value calculated was 215 cm^{-1}, which is similar to the interaction energy at equilibrium which was calculated to be 137 cm^{-1}. However, for both mode 13 and mode 7a the maximum E_{vdW} value is over 1000 cm^{-1}, much higher than the equilibrium value. Notably, the maximum E_{vdW} value for mode 7a is 230 cm^{-1} higher than the equivalent value for mode 13. The ΔE_{vdW} term in Table 6-13 is the maximum change in van der Waals energy that occurs during a vibrational motion; when vibration 7a is excited the interaction energy is predicted to change by 1463 cm^{-1}, over 350 cm^{-1} higher than the ΔE_{vdW} value for vibration 13 which is 1111 cm^{-1}. The bigger change in the net interaction energy during the vibrational motion of mode 7a would result in a bigger change in the torsional potential during the vibration which would cause enhanced mixing of the vibrational and torsional levels. Therefore, this model predicts vibrational levels involving mode 7a are more likely than vibrational levels involving mode 13 to be involved in torsion-vibration coupling. The predictions of this model are consistent with the experimental observations: (1) the IVR lifetime of level $1^{1}7a^{1}$ is 3 times shorter than the IVR lifetime of the close lying $1^{1}13^{1}$ level and (2) the IVR lifetime of level $7a^{1}$ is shorter than the IVR lifetime of both 13^{1} and level $1^{1}13^{1}$ despite this level lying higher in wavenumber in a region with a higher density of states.[2]

6.7. Summary and Conclusion

Time-resolved photoelectron spectra were recorded following photoexcitation of close-lying S_1 vibrational levels $1^1 13^1$ and $1^1 7a^1$ at ~1990 cm^{-1} and ~2030 cm^{-1} respectively. In both sets of spectra, analysis revealed that both vibrational levels were each strongly coupled to a single doorway state assigned $9b^2 13^1$ and $7a^1 9b^2$ respectively. These doorway states facilitated the overall vibrational energy dispersal to weakly coupled bath states, although notably, the IVR lifetime of vibrational level $1^1 13^1$ was determined to be 17.6 ps whereas the IVR lifetime of vibrational level $1^1 7a^1$ was just 6.7 ps, almost 3 times smaller. Given the similarity of the S_1 wavenumbers, the difference in lifetime cannot be explained by density of states arguments. These results, together with the dynamics observed following population of the fundamental levels $7a^1$ and 13^1 where the IVR lifetime of level $7a^1$ was determined to be only 13 ps, suggest the dynamics are mode-dependent. Comparison to time-resolved photoelectron spectra recorded *via* vibrational level $1^1 7a^1$ in *p*DFB, which exhibits restrictive IVR and no congestion at 0 ps, suggests enhanced torsion-vibration coupling occurs when exciting mode 7a in *p*FT which accelerates IVR. The Van der Waals interaction energy between ring atoms and the methyl group is predicted to change more during the motion of mode 7a compared to mode 13 suggesting enhanced torsion-vibration mixing during the 7a vibration. Relevant normal mode diagrams are shown in the appendix.

6.8. References

---

[1] W.D. Tuttle, A. M. Gardner, L. E. Whalley and T. G. Wright., *J. Chem. Phys.,* 2017, **146**, 244310,

[2] J. A. Davies, L. E. Whalley, K. L. Reid., *Phys. Chem. Chem. Phys*, 2017, **19**, 5051-5062

[3] J. A. Davies and K. L. Reid., *J. Chem. Phys*., 2011, **135**, 124305

[4] J. A. Davies, A. M. Green, A. M. Gardner, C. D. Withers, T. G. Wright and K. L. Reid., *Phys. Chem. Chem. Phys*., 2014, **16**, 430-443

[5] Y. Yamada, N. Mikami and T. Ebata, *J. Chem. Phys*., 2004, **121**, 11530

[6] J. A. Davies and K. L. Reid., *Phys. Rev. Lett*., 2012, **109**, 193004

[7] C.J. Hammond, V. L. Ayles, D. E. Bergeron, K. L. Reid, T. G. Wright, *J. Chem. Phys.*, 2006, **125**, 124308

[8] J. Midgley, J. A. Davies, K. L. Reid., *J. Phys. Chem. Lett*., 2014, **5**, 2484-2487

[9] N. T. Whetton and W. D. Lawrance, *J. Phys. Chem*., 1989, **93**, 5377-5384

[10] D. B. Moss, C. S. Parmenter and G. E. Ewing, *J. Chem. Phys*., 1987, **86**, 51-61

7. Conclusions and future work

Picosecond laser pulses and velocity map imaging have been utilised to measure time resolved photoelectron spectra (tr-PES) which provide insight into energy dispersal within the S_1 electronic states of aniline and *para*-fluorotoluene. The REMPI spectrum of S_1 aniline has been presented and assignments made for observed S_1 vibrational levels up to ~2110 cm^{-1}. These assignments were made through comparison with SEVI spectra, which were recorded via each intermediate S_1 vibrational level. This technique provided better resolution in comparison to the photoelectron spectra obtained employing the VMI technique with a single energy ionisation photon. Finally, a systematic study of the IVR dynamics was conducted using time-resolved photoelectron imaging. Excluding the vibrationless origin, spectra were recorded via thirteen wavenumber positions in the S_1 electronic state and the IVR dynamics were followed for up to 500 ps. Additionally, two near degenerate S_1 vibrational levels at ~2000 cm^{-1} in *para*-fluorotoluene were excited and the ensuing IVR dynamics were followed up to 500 ps. As well as comparison between the two vibrational levels which provided information on mode dependent dynamics, comparisons were made to the related molecule, *para*-difluorobenzene, which provided insight into the role of the methyl torsional mode in accelerating IVR. In this chapter the most important results will be summarised, and conclusions drawn based on the comparison of IVR dynamics of different vibrational levels within a molecule and between different molecules. Suggestions for future work will also be discussed.

7.1. Spectroscopy of aniline

7.1.1. Summary of results

The IVR dynamics of the vibrational levels in S_1 aniline that were investigated in this work are summarised in Table 7-1. Chapter 3 showed time-resolved photoelectron spectra recorded via vibrational levels below ~1000 cm^{-1}; these low wavenumber vibrations exhibited either no IVR or restrictive IVR in which population remained localised in just a few coupled vibrational modes. Chapter 4 investigated the ~1000-1700 cm^{-1} region of the S_1 electronic state; notably, a range of dynamic behaviour was shown for these vibrational levels ranging from restrictive to dissipative IVR. Chapter 5 studied the high wavenumber vibrations above ~1700 cm^{-1}; the time-resolved photoelectron spectra indicated that 'dissipative' or 'intermediate' energy dispersal occurred following the initial excitation of each S_1 vibrational level; these IVR regimes were a result of coupling to large numbers of dark (bath) vibrational levels.

S_1 vibrational level	S_1 wavenumber / cm^{-1}	τ_{IVR} / ps	Regime
$6a^1$	490	-	No IVR observed
I^2	750	-	No IVR observed
$I^1 6a^1$ ($S_1 \leftarrow S_0$ $I_1^1 6a_0^1$)	750	-	No IVR observed
1^1	750	No decay observed	Restrictive
1^1	800	No decay observed	Restrictive
12^1	950	-	No IVR observed
$10a^2/11^2$ $I^2 6a^1$	1260	No decay 14 ± 3	Complex dynamics due to multiple ZOBS 1 = restrictive IVR 1 = dissipative IVR
$1^1 6a^1/13^1$	1300	No decay observed	Restrictive
$6a^1 12^1$	1450	No decay (rotational dephasing)	Restrictive
1^2	1600	34 ± 14	Intermediate
Assignment uncertain	1600	2 - 9 ps	Dissipative
$I^2 12^1$	1720	29 ± 7	Intermediate
Assignment uncertain	1720	7 ± 3	Dissipative
$1^1 12^1$	1760	169 ± 46	Intermediate
$6a^1 13^1$	1810	18 ± 3	Dissipative
12^2	1930	21 ± 6	Dissipative
$1^1 13^1$	2110	2.4 ± 0.2	Dissipative

Table 7-1: Summary of the IVR dynamics of vibrational levels in S_1 aniline that were studies in this work.

7.1.2. Comparison of S_1 dynamics

In many cases the different regimes can be rationalised using density of states arguments. At low wavenumbers where the density of states is low either no time-dependence or restrictive IVR is observed because there are few, if any, dark states of the correct symmetry which are close enough in wavenumber to couple to the initially excited bright state. At high wavenumbers, where there is a higher density of states due to the presence of fundamental, overtone and combination levels, dissipative energy dispersal is observed because there are more dark states available (due to symmetry and wavenumber proximity) for coupling to the initially excited bright state.

It has not been possible to completely unravel all IVR dynamics from the time-resolved photoelectron spectra. However, comparison of the IVR lifetimes and regimes at different S_1 wavenumbers suggests that in some cases there may be other factors which are influencing the IVR dynamics. Below ~1500 cm^{-1}, generally either restrictive IVR or no time-dependence is observed; notably, when exciting the S_1 vibration at 950 cm^{-1} no IVR is observed whereas when exciting at lower wavenumber positions (750 and 800 cm^{-1}) restrictive IVR was observed. This highlights the importance of accidental degeneracy in IVR processes. Considering the behaviour of the majority of vibrational levels below ~1500 cm^{-1}, there is one particularly unexpected result. The time-resolved photoelectron spectra measured *via* ~1260 cm^{-1} in S_1 were somewhat complicated because multiple vibrational levels were prepared in S_1. While one of the initially prepared S_1 vibrational levels exhibited quantum beats (restrictive IVR), a second initially prepared S_1 vibrational level decayed in an apparent dissipative regime over the timescale of the experiment, with an IVR lifetime of 14 ± 3 ps. This was an unexpected observation given that decay was not observed for close lying S_1 vibrational levels or for vibrational levels lying up to ~200 cm^{-1} higher in wavenumber. Notably, the photoelectron spectra do not show the obvious increase in congestion with pump-probe time delay which is typical of dissipative energy dispersal. However, it is possible that any increase is obscured by the fact that there is already significant congestion present in the spectrum at 0 ps (see Figure 7-1), which could either be a result of exciting multiple S_1 vibrational levels, or be an indication that the bright state is coupled to many dark states in S_1, some of which lie outside the bandwidth of the laser. This is not unusual for dissipative IVR which results from the coupling of numerous vibrational states. Further work is necessary to understand the coupling mechanism involved in this wavenumber region because the time-resolved photoelectron spectra showed numerous overlapping transitions. Comparison with higher resolution spectra and recording time-resolved SEVI spectra would be useful to provide more precise cation vibrational wavenumbers and resolve near-coincident cation vibrational levels.

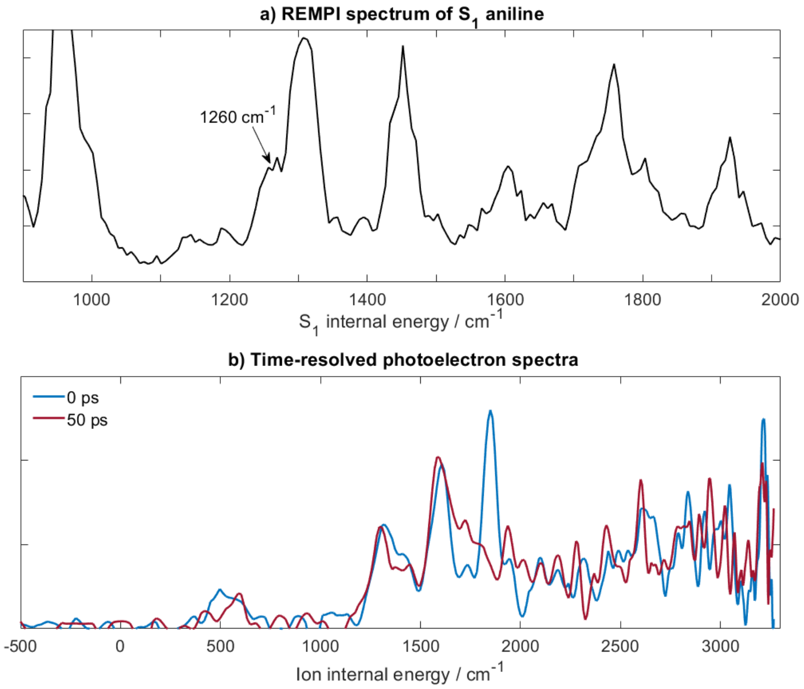

Figure 7-1: a) 900-2000 cm^{-1} region of the REMPI spectrum of S_1 aniline. b) Photoelectron spectra recorded via 1260 cm^{-1} at 0 ps versus 50 ps.

One suggested assignment for the S_1 bright vibrational level which decays is $I^2 6a^1$, where I is the inversion mode of the NH_2 group. It is possible that the involvement of the inversion mode accelerates IVR by permitting an energy dispersal pathway which is not available to the other bright vibrational states in this wavenumber region. Notably, most of the other observed vibrational levels below ~1500 cm^{-1} involve a_1 symmetry modes, which are in-plane. The out of plane large amplitude nature of the inversion mode could allow coupling to other out of plane and ring-localised vibrational modes. The fundamentals of these out of plane vibrational modes cannot anharmonically couple to the a_1 (in plane) bright vibrational states and so in these cases, these modes would only play a role if they are involved in overtone or combination bands.

If the inversion mode does facilitate coupling to a wider range of vibrational modes, this would be an example of mode specific IVR. Therefore, it is necessary to consider other vibrational levels involving the inversion mode, two of which were assigned in the energy region investigated in this study. (i) The time-resolved photoelectron spectra measured following preparation of the S_1 I^2 vibrational level at ~750 cm^{-1} showed no time-dependence. Given that this level lies at a relatively low S_1 vibrational wavenumber it is likely that the density of states is too low for dissipative IVR to occur. (ii) The time-resolved photoelectron spectra measured following preparation of the S_1 $I^2 12^1$ vibrational level at ~1720 cm^{-1}, showed decay with the dynamics potentially mediated by a doorway state. Again, unravelling the IVR dynamics is complicated by the fact that multiple S_1 bright vibrational levels appear to have been excited. Notably the IVR lifetime was determined to be 29 ± 7 ps, which is longer than the IVR lifetime determined for the lower wavenumber vibrational level at ~1260 cm^{-1}. This seems counter-intuitive based on density of states arguments, but with increasing wavenumber the increasing density of states is not necessarily uniform because there are 'clumps' of levels which become smoother at higher wavenumbers.[1] Thus, the higher wavenumber vibrational level may be accidentally non-coincident with the 'clump' of dark states.

The (potential) involvement of the inversion mode in the acceleration of IVR could result from the Franck-Condon activity of this vibration upon electronic excitation to S_1. Calculations predict that a planar structure is observed in the S_1 electronic state of aniline whereas the neutral ground state is nonplanar. An interesting comparison (if possible) would be with a molecule which possessed a centre of flexibility involving inversion of a substituent group, but where this mode was not particularly active owing to the similarity of geometries in the S_0 and S_1 electronic states.

Above ~1600 cm^{-1} each of the initially excited S_1 vibrational levels showed evidence of dissipative or intermediate IVR, where the dynamics in the latter were mediated by a doorway state (see Figure 7-2). The presence of a doorway state indicates that the initially excited bright vibrational state is accidently coincident with a strongly coupled close lying dark state with the same overall symmetry. The shortest IVR lifetime measured was for the highest wavenumber vibrational level, $1^1 13^1$, at ~2110 cm^{-1}. The rate of IVR varies as different vibrational levels are excited in S_1, however, it does not show a simple trend such as the IVR lifetimes decreasing with increasing vibrational wavenumber. This could be a result of bright states being involved in coupling mechanisms that permit coupling to only a subset of the total available dark vibrational levels or that in some cases many of the dark vibrational levels are too far away in wavenumber.

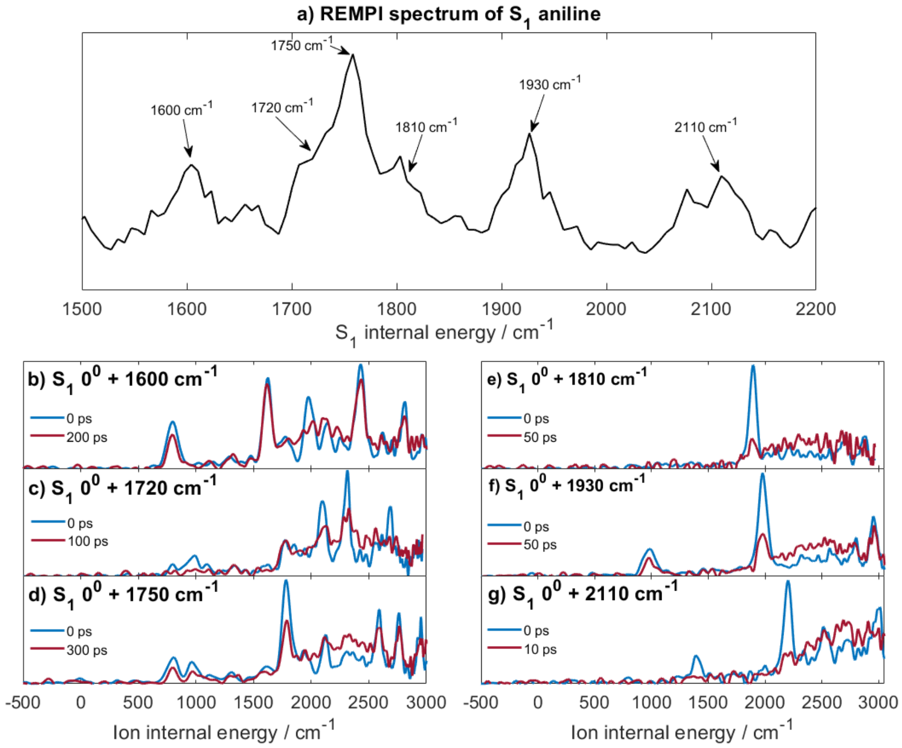

Figure 7-2: a) REMPI spectrum showing the 1500-2200 cm^{-1} region of S_1 aniline. b-g) Photoelectron spectra at selected time delays recorded via (b) 1600 cm^{-1}, (c) 1720 cm^{-1}, (d) 1750 cm^{-1}, (e) 1810 cm^{-1}, (f) 1930 cm^{-1}, (g) 2110 cm^{-1} in S_1.

7.2. Spectroscopy of *para*-fluorotoluene

7.2.1. Summary of time-resolved studies

The IVR dynamics of the S_1 vibrational levels $1^1 13^1$ and $1^1 7a^1$ in *p*FT make an interesting comparison, not only to each other but to the dynamics of the lower wavenumber fundamental vibrations 13^1 and $7a^1$. The IVR dynamics of both $1^1 13^1$ and $1^1 7a^1$ were found to be mediated by a doorway state of the form $X^1 9b^2$ (X = 7a or 13). However, despite the vibrations being only ~35 cm^{-1} apart, the IVR lifetimes differed by close to a factor of three. In previous work the IVR rate was also found to be accelerated for the $7a^1$ vibrational level compared with the 13^1 vibrational level, despite their similar S_1 wavenumbers. Notably, the IVR lifetime of level $7a^1$ is shorter than even level $1^1 13^1$, despite the latter being 760 cm^{-1} higher in S_1. It was therefore concluded that mode 7a promotes energy dispersal more effectively than mode 13.

Level	S_1 wavenumber / cm^{-1}	τ_{ivr} / ps	τ_{osc} / ps	ΔE / cm^{-1}
1^1	~800	restrictive IVR	5.0[c]	6.7[c]
13^1	1194	50[b]	-	-
$7a^1$	1230	13[d]	-	-
$1^1 13^1$	1990	17.6[a]	4.93[a]	6.77[a]
$1^1 7a^1$	2030	6.7[a]	5.00[a]	6.68[a]

*Table 7-2: IVR lifetimes, oscillation periods and energy separations determined following excitation of five vibrational levels in S_1 in p*FT*. a) From this work, b) From Ref 2, c) From Ref 3, d) From Ref 4*

In a previous study of *para*-difluorobenzene, it was found that energy remains localised following initial excitation of level $1^1 7a^1$ indicating coupling to a much smaller number of dark vibrational levels (compared to *para*-fluorotoluene).[5] It was concluded that torsion-vibration coupling is responsible for the energy dispersal in *para*-fluorotoluene because it is an additional mechanism allowing coupling to large numbers of dark vibrational levels which is not available in *para*-difluorobenzene. The higher level of congestion in the 0 ps photoelectron spectrum of level $1^1 7a^1$ in S_1 *para*-fluorotoluene alongside the faster IVR rate compared to level $1^1 13^1$, and the absence of congestion in the 0 ps spectrum of *para*-difluorobenzene, suggests that mode 7a promotes energy redistribution through the facilitation of torsion-vibration coupling to more distant dark vibrational levels. This is consistent with the bigger change in the torsional barrier occurring during the 7a vibrational motion leading to enhanced mixing of the ring and torsional levels.[4,11]

7.2.2. Higher resolution studies

In other, higher resolution, studies, vibrational coupling within S_1 *para*-fluorotoluene was investigated as part of my Ph.D. work by using two-dimensional laser induced fluorescence (2D-LIF) and dispersed fluorescence spectroscopy. These techniques utilised nanosecond laser pulses which meant that the temporal resolution was lost, but the spectra showed better frequency resolution. In these studies eigenstates were prepared rather than zero order states, although the eigenstates are often referred to by the dominant contribution from one of the ZOS. The full results of these studies have not been included in this thesis but one study is briefly discussed below to demonstrate how these techniques can provide additional complementary information to time-resolved studies which can help to unravel coupling mechanisms. Also, of relevance to the PFT study in this thesis, this frequency-resolved study highlighted the role of the methyl group and torsional levels in facilitating energy dispersal.[6]

In this frequency-resolved study, the focus was on a *p*FT S_1 band observed at ~847 cm^{-1}, the zero-order bright state was assigned to $2D_{18}$ (in Gardner-Wright notation). In a previous time resolved study, an intermediate IVR regime with an IVR lifetime of 17 ps that was observed following excitation of this band was concluded to be the result of a torsion-vibration coupling mechanism between the initially excited vibrational level and two doorway states.[7] One of the doorway states was assigned to $17a^1$ $m = 6$ which could couple to the m = 0 torsional component of the bright vibrational level.[7] In the frequency resolved study, because of the higher resolution of the 2D-LIF experiment, excitation across the band revealed coupling between this bright vibration ($2D_{18}$) and three dark vibration-torsional (vibtor) levels: $D_{11}D_{18}m=2$, $2D_{14}D_{18}m=2$ and $D_{18}D_{29}m=2$.[6] The complicated, congested appearance of the dispersed fluorescence spectra recorded via each of the resulting eigenstates, suggested that the three $m=2$ vibtor levels (mentioned above) may be coupling to each other, and also acting as doorway states, facilitating weak coupling between the initially excited vibration and a bath of other vibrational states.[6] Identification of these vibtor levels and their respective symmetries revealed that only the $2D_{18}m=1$ level was involved in coupling to these doorway states, suggesting that the $2D_{18}m=0$ level has limited role in energy dispersal.[6] The non-observation of a third doorway state in the time-resolved study was suggested to be a result of a weaker interaction between $2D_{14}D_{18}m=2$ and $2D_{18}m=1$.[6] The frequency resolution in this study allowed observation and assignment of the doorway states to vibtor levels which was not possible from time-resolved studies alone in this case.

7.3. Comparison of S_1 dynamics in related substituted benzene molecules

Shown below is a table comparing the IVR lifetimes and behaviour of different substituted benzene molecules as determined in this study (excluding vibrational levels with no IVR) or taken from previous literature.

Molecule	Level	S$_1$ wavenumber / cm^{-1}	τ_{IVR} / ps	Behaviour
aniline$^{(a)}$	1^1	800	-	Restrictive
*p*FT$^{(b)}$	1^1	800	-	Restrictive
*p*FT$^{(c)}$	13^1	1194	50	One torsional component 'decays'
Toluene$^{(c)}$	13^1	1195	12	Doorway states
*p*FT$^{(d)}$	$7a^1$	1230	13	Doorway states
aniline$^{(a)}$	Multiple levels excited: $10a^2/11^2$ $I^2 6a^1$	1260	- 14 ± 31	Restrictive Dissipative
aniline$^{(a)}$	$1^1 6a^1/13^1$	1300	-	Restrictive
aniline$^{(a)}$	$6a^1 12^1$	1450	-	Restrictive
aniline$^{(a)}$	1^2	1600	34 ± 14	Doorway states
aniline$^{(a)}$	Assignment uncertain	1600	2 - 9 ps	Dissipative
aniline$^{(a)}$	$I^2 12^1$	1720	29 ± 7	Doorway states
aniline$^{(a)}$	Not yet assigned	1720	7 ± 3	Dissipative
aniline$^{(a)}$	$1^1 12^1$	1760	169 ± 46	Doorway states
aniline$^{(a)}$	$6a^1 13^1$	1810	18 ± 3	Dissipative
aniline$^{(a)}$	12^2	1930	21 ± 6	Dissipative
*p*FT$^{(a)}$	$1^1 13^1$	1990	18 ± 6	Doorway states
*p*FT$^{(a)}$	$1^1 7a^1$	2030	6 ± 2	Doorway states
*p*DFB$^{(e)}$	$1^1 7a^1$	2068	-	Restricted
aniline$^{(a)}$	$1^1 13^1$	2110	2.4 ± 0.2	Dissipative

Table 7-3: Comparison of the IVR lifetimes determined for aniline, pFT, pDFB and toluene taken from a) this work, b) Ref 3, c) Ref 2, d) Ref 4, e) Ref 5

In terms of an IVR 'onset' energy above which energy dispersal is observed and below which energy remains localised, clearly *p*DFB is at one extreme with only restrictive IVR observed even at energies as high as 2068 cm^{-1}. At the other extreme, both toluene and *p*FT show energy dispersal either mediated by a doorway state or dissipative at only ~1200 cm^{-1}. Aniline lies in between these limits; there was evidence for dissipative IVR when exciting at ~1260 cm^{-1} although the circumstances where somewhat difficult to unravel because there was also evidence of multiple bright states. After this, dissipative or intermediate (mediated by doorway states) energy dispersal was observed above ~1600 cm^{-1}. Regardless of which 'onset' energy is assigned to aniline, it remains between *p*DFB and the toluenes.

Two factors which may affect the observed trend are the nature of the substituent group and the symmetry of the molecule. Many studies have discussed the role of the methyl group and torsion-vibration coupling,[1,2,6,8,9,10,11] and it has been shown to provide coupling routes to vibrational modes of different symmetry thus accelerating IVR. A ZEKE study by Wright and co-workers compared the spectra of *para*-xylene (*p*Xyl), which has two methyl groups, with *p*FT, which has one methyl group, following excitation of one quantum in the C-CH_3 stretching mode 5 (or 13 in Varsányi notation).[1] Congestion was more pronounced in the spectrum for *p*Xyl due to increased coupling and energy dispersal attributed to a more rapid increase in the density of states with energy due to larger number of torsional levels and vibtor levels.[1] This explains the lower IVR onset energy and fast IVR rates in toluene and *p*FT as both contain a methyl group. Neither aniline nor *p*DFB contain a methyl group and so a different factor must be changing between these molecules in order to cause the observed differences outlined above. Aniline has an extra degree of freedom in the six NH_2 localised motions; involvement of the out of plane NH_2 motions (inversion and torsion) could help provide routes to vibrations of other symmetry classes increasing access to bath states allowing accelerated energy dispersal. However, these are not low frequency modes; in the S_1 electronic state four of these vibrations are calculated between 276 cm^{-1} and 1608 cm^{-1} and the other two (NH_2 stretches) are over 3500 cm^{-1}. Thus, only the lowest energy modes are likely to be relevant in the studies presented here.

Other studies have considered how symmetry could affect the energy dispersal within molecules, with the expectation being that higher symmetries lead to lower density of levels (of correct symmetry) available for coupling and lower likelihood of coupling.[1,10,12,1310] Moving between *p*DFB and aniline means a change from a symmetrically substituted molecule of D_{2h} symmetry to an asymmetrically substituted molecule of C_{2v} if aniline is planar, or C_s if not. So, the lower IVR onset energy in aniline is in line with the expectation that comes from the lower symmetry. It is difficult to separately consider the impact of a change of symmetry and a change of substituent group as different substituents will alter the vibrational wavenumbers, number of vibrations and possibly the symmetries of vibrations as well as potentially adding an extra degree of freedom. So, it is unclear whether the acceleration in energy dispersal in aniline in comparison with other molecules is an influence of vibration-inversion/torsion coupling even though the NH_2 localised vibrations are high in wavenumber, as is the case when there is a methyl substituent, or whether the lower symmetry plays any role.

For a more complete comparison, it would be interesting to conduct a time-resolved study of fluorobenzene. This asymmetrically substituted molecule is also of C_{2v} symmetry but less flexible than *p*FT and aniline, the absence of a methyl group would remove the torsional levels from consideration leaving the focus on symmetry and the NH_2 group of aniline. A nanosecond ZEKE study of *para*-chlorofluorobenzene (*p*ClFB) has been conducted by Wright and co-workers, who found that spectra recorded via different intermediate levels tended to show flat baselines with little congestion.[14] The authors showed evidence for Fermi resonances but concluded that 'no large-scale IVR was seen'.[14] *p*ClFB belongs to the C_{2v} point group, as does planar aniline; a lack of energy dispersal for *p*ClFB could therefore indicate that energy dispersal in aniline is related to the presence of the NH_2 group. In addition, considering a molecule which is of definite *Cs* symmetry in the S_1 electronic state such as a meta or ortho-chlorofluorobenzene which lacks either a methyl group or NH_2 group would provide further evidence for the effect of symmetry on IVR generally and specifically in aniline.

7.4. Future work

Chapters 3, 4 and 5 presented data from the systematic study of aniline. In a number of cases the benefits of recording additional data were discussed; generally these were additional photoelectron spectra recorded at further time delays to improve the fits of time dependence or additional higher resolution SEVI spectra at further time delays to help assignments and identify changes in the vibrational wavenumber of peaks with increasing time delay. In terms of further work, these should be the first set of experiments.

In aniline, excitation at some S_1 wavenumbers (~750 cm^{-1}, ~1260 cm^{-1} and ~1600 cm^{-1}) showed evidence that multiple bright vibrational levels had been prepared. This complicated the subsequent analysis because the SEVI and photoelectron spectra were a combination of the individual spectra recorded via each bright vibrational level and thus there were multiple overlapping transitions, giving rise to poorly resolved peaks. Further, due to each S_1 level undergoing different coupling, the photoelectron peaks showed different time-dependent behaviours because they were manifestations of different couplings. In these experiments, pulses were used which were ~1 ps in duration and had bandwidths of ~34 cm^{-1}, whereas previous studies using this system show it to be capable of bandwidths of ~13 ps.[2,3,15,] If the bandwidth of the laser could be reduced to regain the frequency resolution, it would be useful to rerecord the REMPI spectrum and repeat experiments when exciting S_1 wavenumbers of ~750 cm^{-1}, ~1260 cm^{-1} and ~1600 cm^{-1} to attempt to individually excite the multiple bright vibrational levels.

Section 7.2.2 also highlighted the value of using time-resolved photoelectron spectroscopy alongside complementary higher resolution frequency-resolved techniques such as 2D-LIF which automatically excites every allowed (ro)vibrational level within the excitation window. These can be used to probe rovibronic structure and thus provide more precise vibrational wavenumbers. This would be useful for some of the cases discussed in chapters 3-5 in which multiple assignments were proposed for the bright vibrational states. Such studies would also aid in the assignment of coupled levels and doorway states if congestion is sufficiently low. These can be difficult to conclusively identify from time-resolved photoelectron spectra if the small change in photoelectron peak position with time delay is obscured by peak widths. This is a particular issue for the peak originating from the $\Delta v = 0$ transition from S_1 to the ion.

Further understanding of the factors affecting energy dispersal could be gained by comparing the IVR dynamics of the related molecules of different symmetry such as fluorobenzene, phenol, meta- or ortho-chlorofluorobenzene. These molecules would make for an interesting comparison to *p*DFB and aniline because none of these molecules contain a methyl group so would allow for other influencing factors such as symmetry to be uncovered through the comparison.

7.5. References

---

[1] W. D. Tuttle, A. M. Gardner, L. E. Whalley, D. J. Kemp and T. G. Wright, *Phys. Chem. Chem. Phys.,* 2019, **21**, 14133-14152

[2] J. A. Davies, A. M. Green, A. M. Gardner, C. D. Withers, T. G. Wright and K. L. Reid, *Phys. Chem. Chem. Phys.*, 2014, **16**, 430-443

[3] J. A. Davies and K. L. Reid., *Phys. Rev. Lett.,* 2012*,* **109**, 193004

[4] J. A. Davies, L. E. Whalley, K. L. Reid., *Phys. Chem. Chem. Phys*, 2017, **19**, 5051-5062

[5] J. Midgley, J. A. Davies and K. L. Reid, *J. Phys. Chem. Lett.,* 2014, **5**, 2484-2487

[6] A. M. Gardner, W. D. Tuttle, L. E. Whalley and T. G. Wright, *Chem. Sci.,* 2018, **9**, 2270-2283

[7] J. A. Davies and K. L. Reid, *J. Chem. Phys.,* 2011, **135,** 124305-124305

[8] D. B. Moss and C. S. Parmenter, *J. Chem. Phys.,* 1993, **98**, 6897-6905

[9] C. S. Parmenter and B. M. Stone, *J. Chem. Phys.,* 1986, **84**, 4710-4711

---

[10] P. J. Timbers, C. S. Parmenter and D. B. Moss., *J. Chem. Phys.,* 1994, **100,** 1028-1034

[11] D. B. Moss, C. S. Parmenter and G. E. Ewing, *J. Chem. Phys.,* 1987, **86,** 51-61

[12] C. S. Parmenter and B. M. Stone, *J. Chem. Phys.,* 1986, **84**, 4710-4711

[13] P. M. Felker, W. R. Lambert and A. H. Zewail, *J. Chem. Phys.,* 1985, **82**, 3003-3010

[14] D. J. Kemp, L. E. Whalley, W. D. Tuttle, A. M. Gardner, B. T. Speake and T. G. Wright, *Phys. Chem. Chem. Phys.,* 2018, **20**, 12503-12516

[15] J. A. Davies and K. L. Reid, *J. Chem. Phys.,* 2011, **135**, 124305

8. Appendix

8.1. Details of SEVI spectra

The figures below show the individual photoelectron spectra measured at different probe wavelengths which were used to produce the SEVI spectra shown in chapters 3, 4, 5 and 6. Spectra are ordered according to their appearance in the chapters. Probe wavelengths used are shown in the legends. Each of the spectra shown were recorded at pump-probe time delays of 0 ps.

8.1.1. SEVI and photoelectron spectra in chapter 3

a. Excitation at S_1 0^0 + 0 cm^{-1} in aniline.

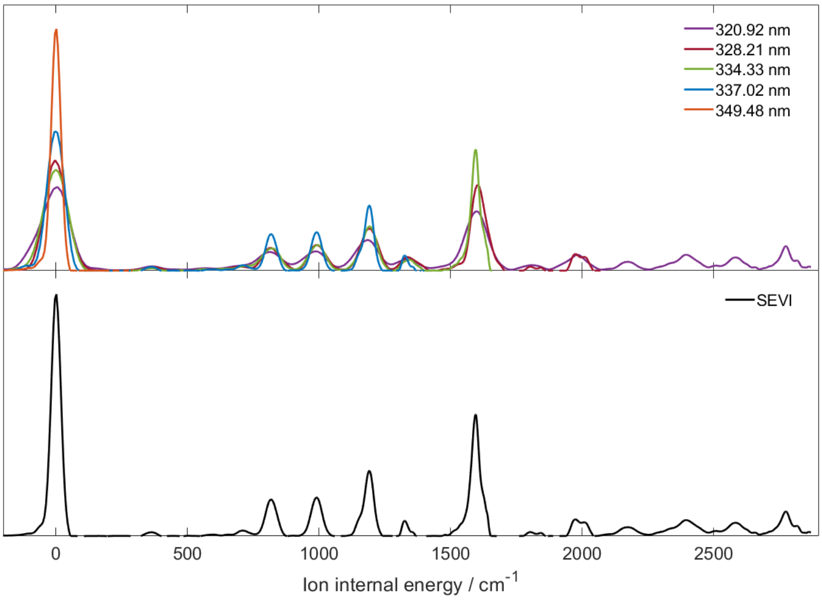

Figure 8-1: Top - Photoelectron spectra measured at S_1 0^0 *+ 0* cm^{-1} *at different probe wavelengths which are used to produce the SEVI spectrum. Bottom – SEVI spectrum resulting after splicing procedure*

b. Excitation at S_1 0^0 + 490 cm^{-1} in aniline.

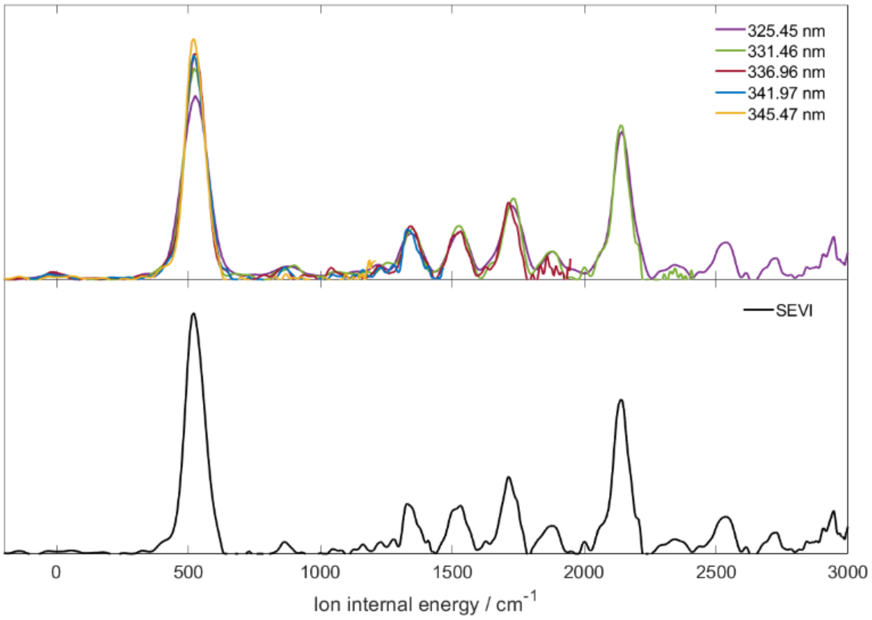

Figure 8-2: Top - Photoelectron spectra measured at S_1 0^0 + 490 cm^{-1} at different probe wavelengths which are used to produce the SEVI spectrum. Bottom – SEVI spectrum resulting after splicing procedure

c. Excitation at S_1 0^0 + 950 cm^{-1} in aniline.

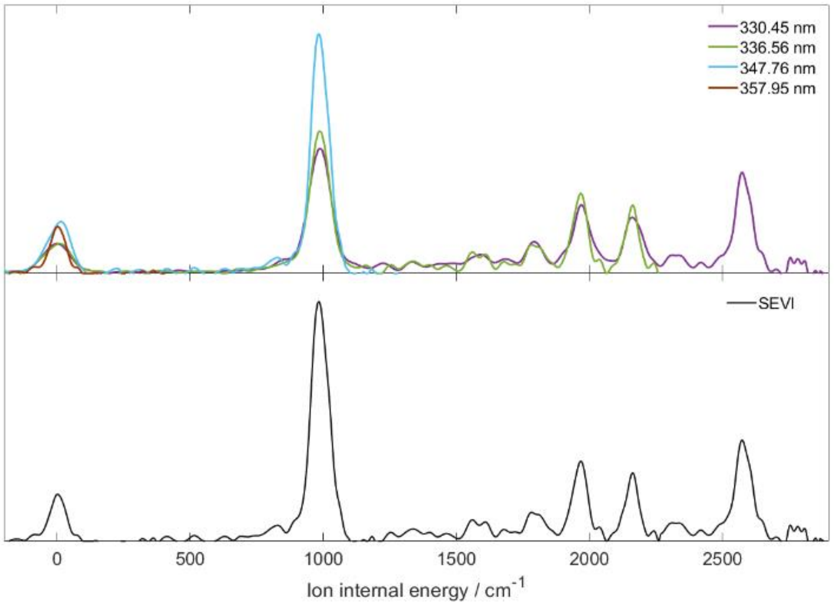

Figure 8-3: Top - Photoelectron spectra measured at S_1 0^0 + 950 cm^{-1} at different probe wavelengths which are used to produce the SEVI spectrum. Bottom – SEVI spectrum resulting after splicing procedure.

d. Excitation at S_1 0^0 + 800 cm^{-1} in aniline.

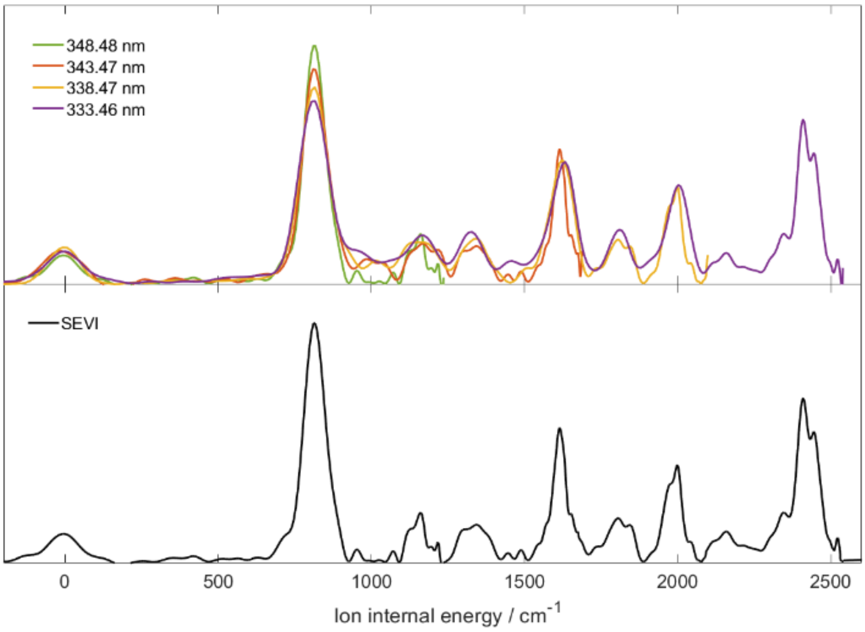

Figure 8-4: Top - Photoelectron spectra measured at S_1 0^0 *+ 800* cm^{-1} *at different probe wavelengths which are used to produce the SEVI spectrum. Bottom – SEVI spectrum resulting after splicing procedure.*

e. Excitation at S_1 0^0 + 750 cm^{-1} in aniline.

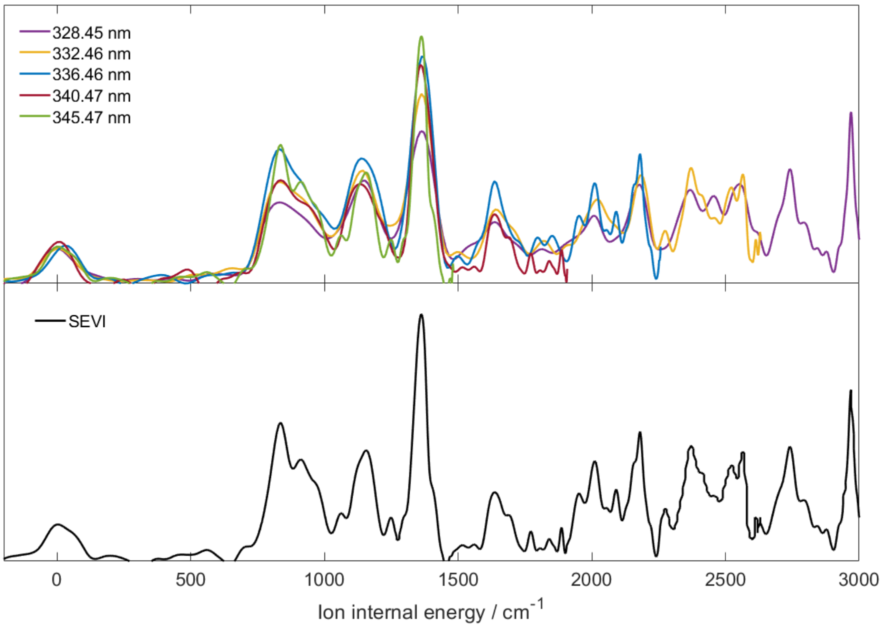

Figure 8-5: Top - Photoelectron spectra measured at S_1 0^0 *+ 750* cm^{-1} *at different probe wavelengths which are used to produce the SEVI spectrum. Bottom – SEVI spectrum resulting after splicing procedure.*

8.1.2. SEVI and photoelectron spectra in chapter 4

a. Excitation at S_1 0^0 + 1300 cm^{-1} in aniline.

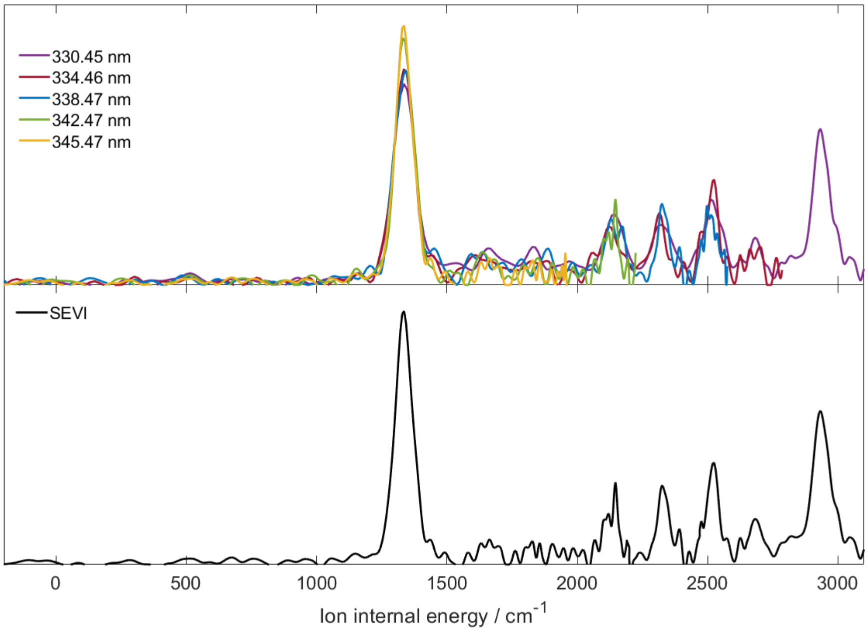

Figure 8-6: Top - Photoelectron spectra measured at S_1 0^0 + 1300 cm^{-1} at different probe wavelengths which are used to produce the SEVI spectrum. Bottom – SEVI spectrum resulting after splicing procedure.

b. Excitation at S_1 0^0 + 1260 cm^{-1} in aniline.

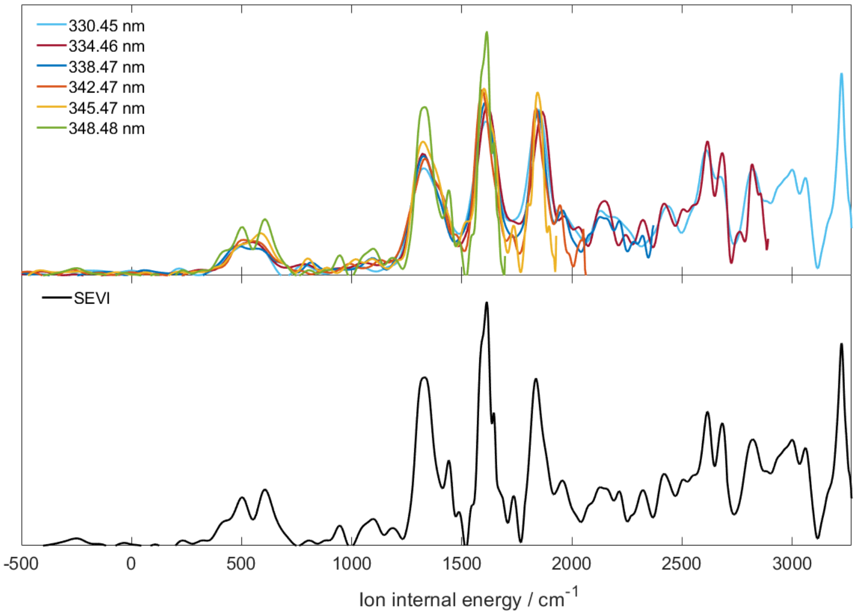

Figure 8-7: Top - Photoelectron spectra measured at S_1 0^0 + 1260 cm^{-1} at different probe wavelengths which are used to produce the SEVI spectrum. Bottom – SEVI spectrum resulting after splicing procedure.

c. Excitation at S_1 0^0 + 1450 cm^{-1} in aniline.

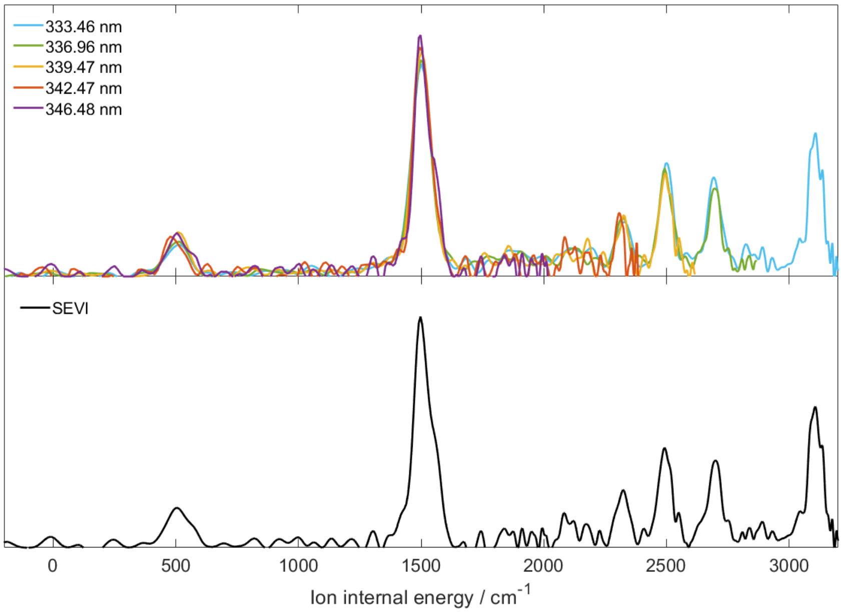

Figure 8-8: Top - Photoelectron spectra measured at S_1 0^0 + 1450 cm^{-1} at different probe wavelengths which are used to produce the SEVI spectrum. Bottom – SEVI spectrum resulting after splicing procedure.

d. Excitation at S_1 0^0 + 1600 cm^{-1} in aniline.

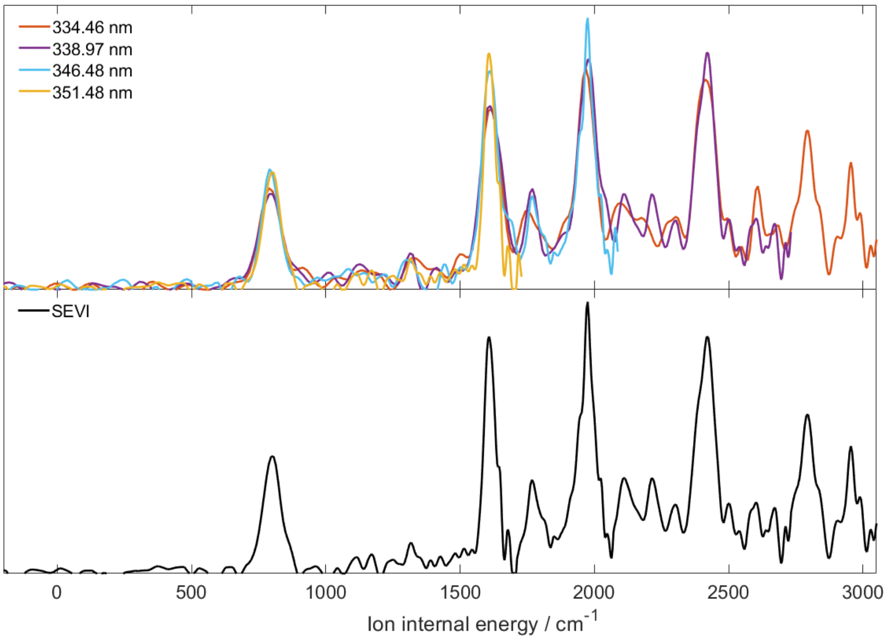

Figure 8-9: Top - Photoelectron spectra measured at S_1 0^0 + 1600 cm^{-1} at different probe wavelengths which are used to produce the SEVI spectrum. Bottom – SEVI spectrum resulting after splicing procedure.

8.1.3. SEVI and photoelectron spectra in chapter 5

a. Excitation at S_1 0^0 + 1720 cm^{-1} in aniline.

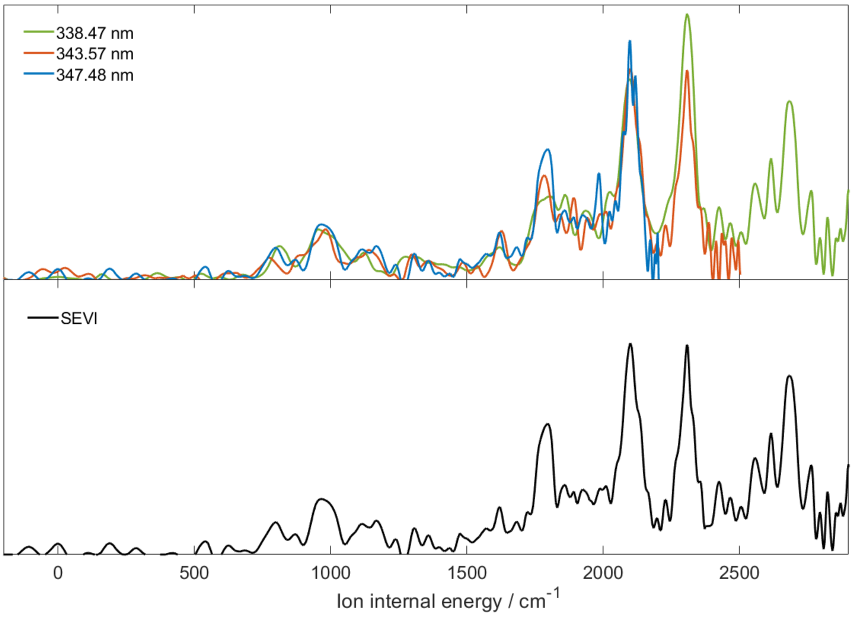

Figure 8-10: Top - Photoelectron spectra measured at S_1 0^0 + 1720 cm^{-1} *at different probe wavelengths which are used to produce the SEVI spectrum. Bottom – SEVI spectrum resulting after splicing procedure.*

b. Excitation at S_1 0^0 + 1760 cm^{-1} in aniline.

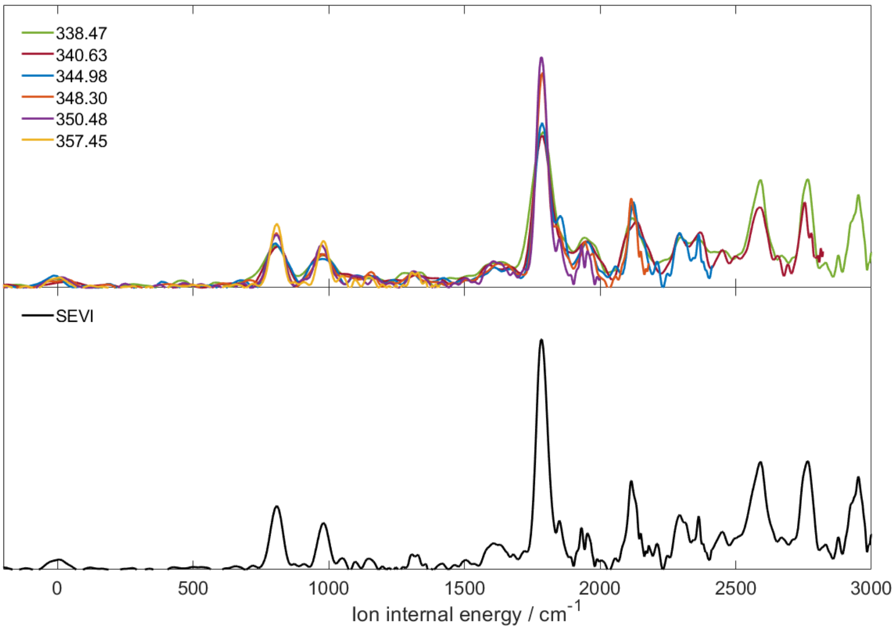

Figure 8-11: Top - Photoelectron spectra measured at S_1 0^0 + 1760 cm^{-1} *at different probe wavelengths which are used to produce the SEVI spectrum. Bottom – SEVI spectrum resulting after splicing procedure.*

c. Excitation at S_1 0^0 + 1810 cm^{-1} in aniline.

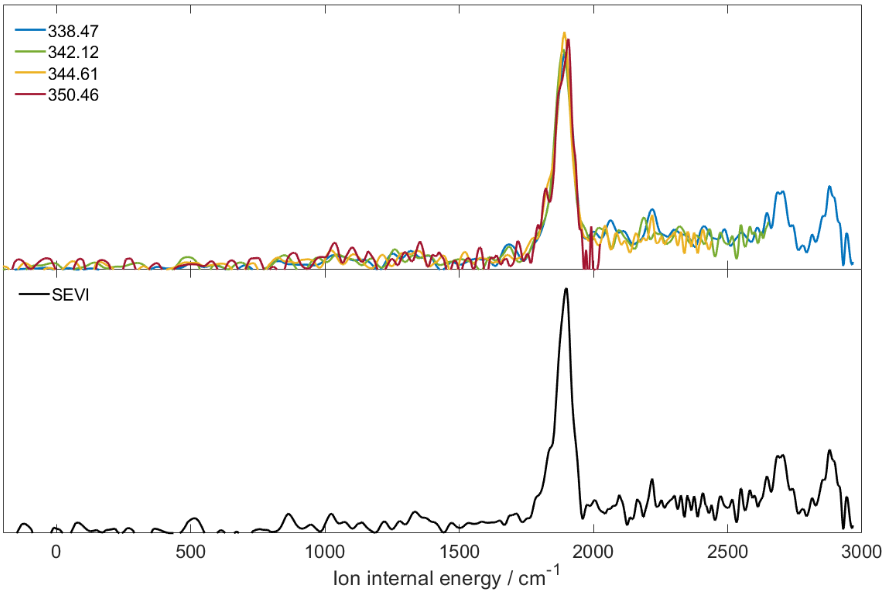

Figure 8-12: Top - Photoelectron spectra measured at S_1 0^0 + 1810 cm^{-1} at different probe wavelengths which are used to produce the SEVI spectrum. Bottom – SEVI spectrum resulting after splicing procedure.

d. Excitation at S_1 0^0 + 1930 cm^{-1} in aniline.

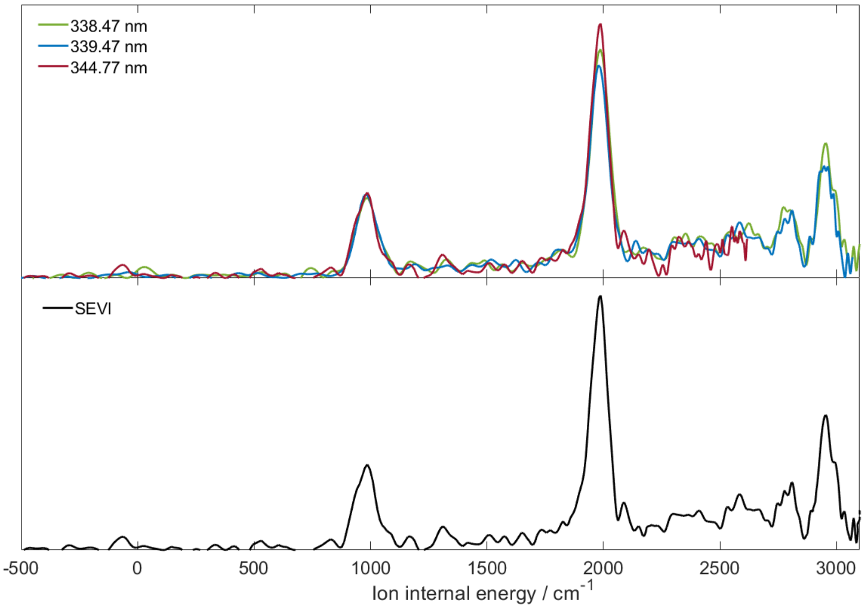

Figure 8-13: Top - Photoelectron spectra measured at S_1 0^0 + 1930 cm^{-1} at different probe wavelengths which are used to produce the SEVI spectrum. Bottom – SEVI spectrum resulting after splicing procedure.

e. Excitation at S_1 0^0 + 2110 cm^{-1} in aniline.

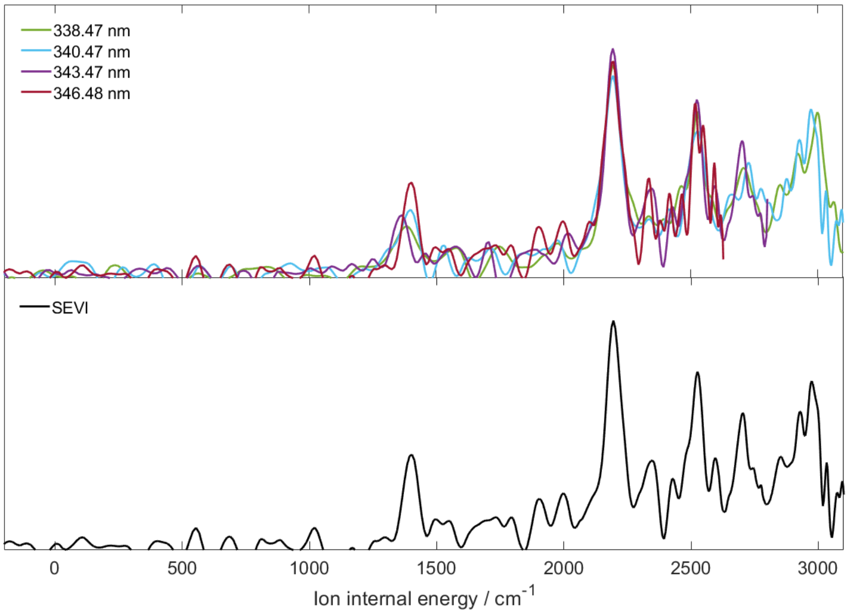

Figure 8-14: Top - Photoelectron spectra measured at S_1 0^0 + 2110 cm^{-1} at different probe wavelengths which are used to produce the SEVI spectrum. Bottom – SEVI spectrum resulting after splicing procedure.

8.1.4. SEVI and photoelectron spectra in chapter 6

a. Excitation at S_1 0^0 + 1990 cm^{-1} in *para*-fluorotoluene.

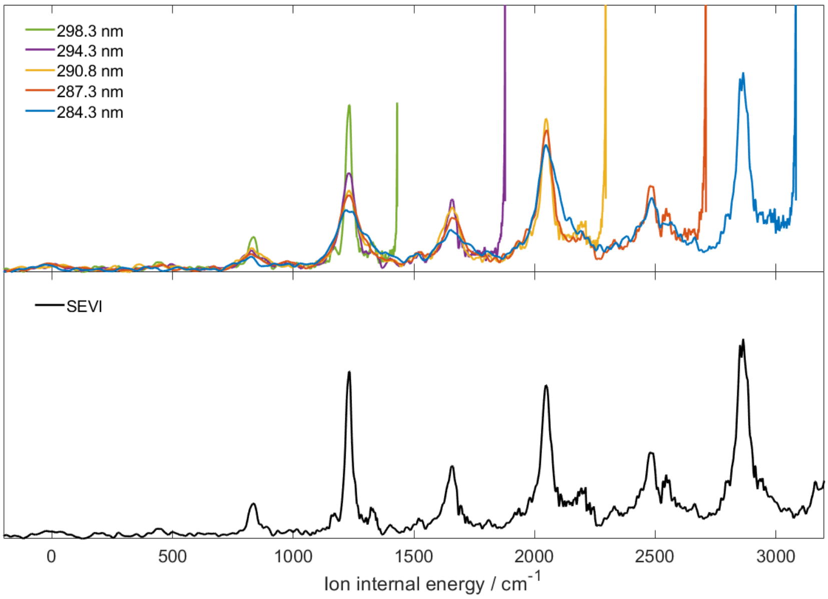

Figure 8-15: Top - Photoelectron spectra measured at S_1 0^0 + 1990 cm^{-1} at different probe wavelengths which are used to produce the SEVI spectrum. Bottom – SEVI spectrum resulting after splicing procedure.

b. Excitation at S_1 0^0 + 2030 cm^{-1} in *para*-fluorotoluene.

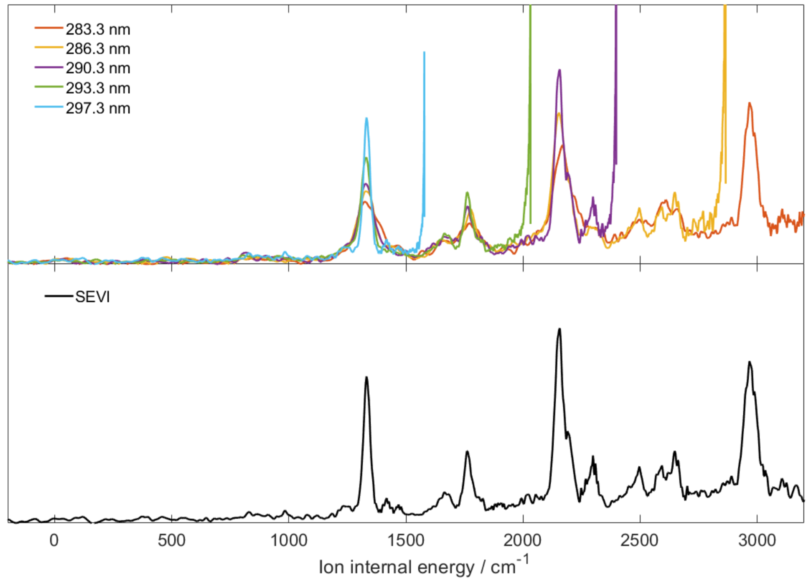

Figure 8-16: Top - Photoelectron spectra measured at S_1 0^0 + 2030 cm^{-1} at different probe wavelengths which are used to produce the SEVI spectrum. Bottom – SEVI spectrum resulting after splicing procedure.

8.2. Normal mode diagrams

8.2.1. Aniline

Shown in Figure 8-17 are the calculated normal mode diagrams for vibrations in the S_1 electronic state of aniline, refer to section 3.3 in Chapter 1.

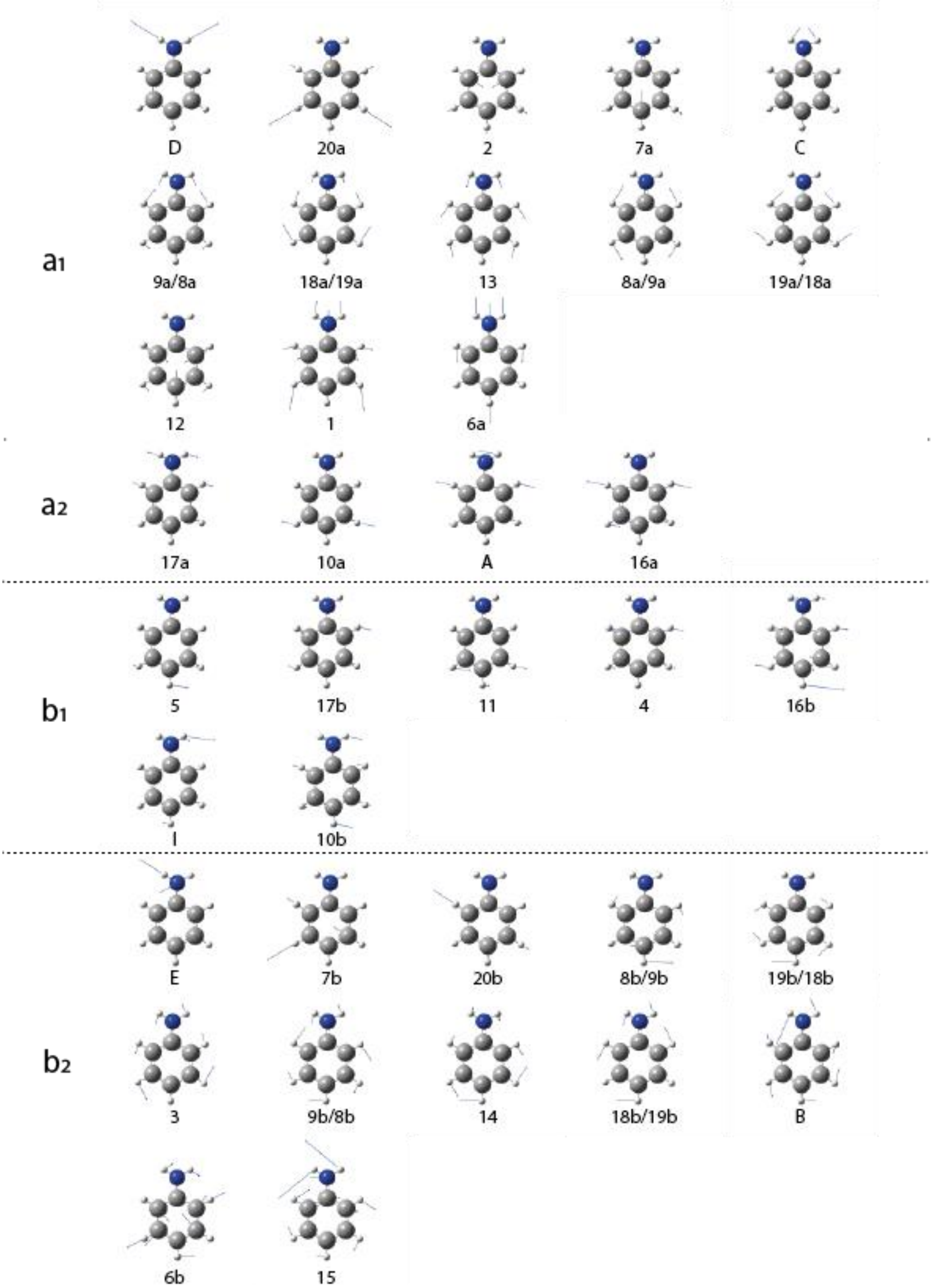

Figure 8-17: Calculated normal mode diagrams for aniline in the S_1 electronic state.

Shown in Figure 8-18 are the calculated normal mode diagrams for vibrations in the D_0^+ electronic state of aniline, refer to section 3.3 in Chapter 1.

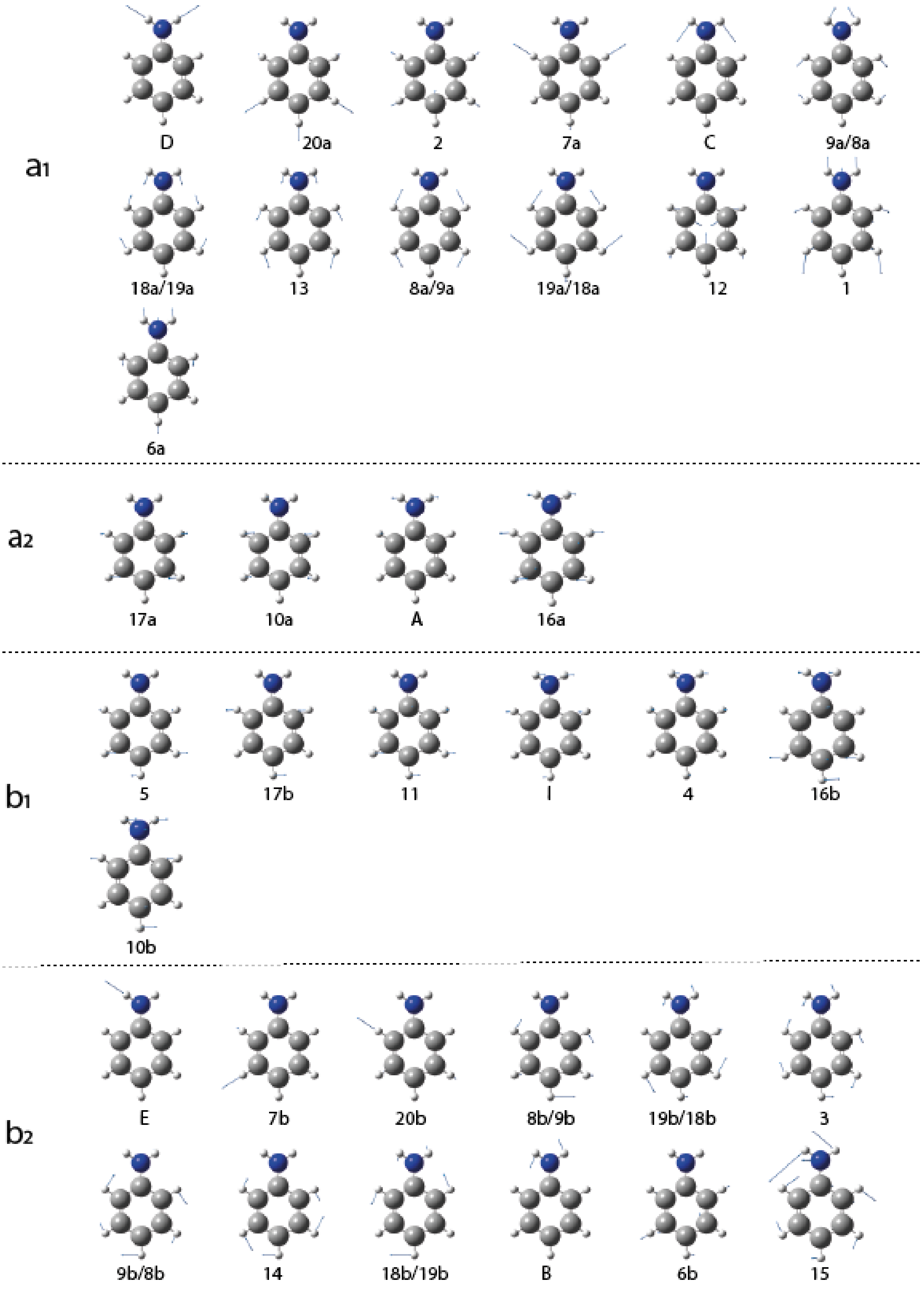

Figure 8-18: Calculated normal mode diagrams for aniline in the D_0^+ electronic state.

8.2.2. *Para*-fluorotoluene (PFT)

Shown in Figure 8-19 are the calculated normal mode diagrams for modes 1, 7a, 9b and 13 in S_1 *para*-fluorotoluene, refer to Chapter 6. These diagrams are taken from reference 1 and were labelled according to Gardner-Wright notation, the corresponding Varsányi labels are shown in Table 8-1.

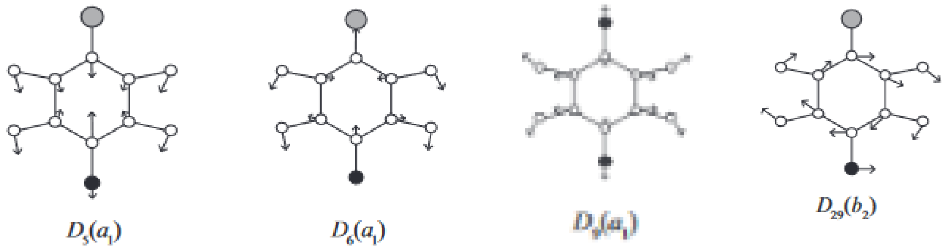

$D_5(a_1)$ $D_6(a_1)$ $D_9(a_1)$ $D_{29}(b_2)$

Figure 8-19: Calculated normal mode diagrams from Ref 1 for the four pFT modes discussed in Chapter 6, labelled using the Gardner-Wright notation scheme.

Gardner-Wright notation	Varsányi notation
5	7a
6	13
9	1
29	9b

Table 8-1: Corresponding labels in the Gardner-Wright and Varsányi notation schemes.

8.3. References

---

[1] A. Andrejeva, A. M. Gardner, W. D. Tuttle, T. G. Wright, *J. Mol. Spec.,* 2016, **321**, 28-49